# SHOCK DEFORMATION AND VOLCANISM ACROSS THE CRETACEOUS-TERTIARY TRANSITION

Volume I

A Dissertation

by

ALAN ROYCE HUFFMAN

Submitted to the Office of Graduate Studies of
Texas A&M University
in partial fulfillment of the requirements for the degree of

DOCTOR OF PHILOSOPHY

May 1990

Major Subject: Geophysics

# SHOCK DEFORMATION AND VOLCANISM ACROSS THE CRETACEOUS-TERTIARY TRANSITION

Volume I

A Dissertation

by

ALAN ROYCE HUFFMAN

Approved as to style and content by:

Neville L. Carter
(Co-Chair of Committee)

Richard L. Carlson
(Co-Chair of Committee)

Andreas K. Kronenberg
(Member)

James E. Russell
(Member)

Stanley A. Mertzman
(Member)

Joel S. Watkins
(Head of Department)

May 1990

# ABSTRACT

Shock Deformation and Volcanism Across The Cretaceous-Tertiary Transition
(May 1990)
Alan Royce Huffman, B.A. Franklin and Marshall College
Co-Chairs of Advisory Committee: Neville L. Carter
Richard L. Carlson

The cause of the Cretaceous-Tertiary (K/T) transition and other mass extinctions remains one of the most controversial scientific topics in the geosciences. Paleontologic, mineralogic, geochemical, and geophysical evidence associated with the K/T boundary have been used to argue that the extinctions were caused by meteor impact or volcanism. To assess the viability of a volcanic model for the K/T transition, a study was undertaken to: (1) determine the character of shock-induced microstructures in silicates from the K/T boundary, known volcanic rocks, known impactites, and samples previously shocked experimentally; (2) complete a series of shock-recovery experiments on granite and quartzite at elevated temperatures and variable pulse duration to determine temperature- and rate-dependent effects on microstructural development; (3) determine the distribution of shocked minerals at DSDP Site 527, Walvis Ridge, and ODP Holes 689B and 690C, Maud Rise, Wedell Sea; and (4) develop a volcanic model that can account for all of the evidence at the K/T transition.

Comparison of natural and experimentally-shocked quartz and feldspar using optical and transmission electron microscopy (TEM) revealed that the optical and statistical character of shock-induced microstructures in volcanic rocks are different from both classic impact microstructures, and from the Raton K/T samples. Comparison of the Manson and Raton samples reveals similarities sufficient to support the contention of Izett (1987b) that Manson is a possible source for shocked quartz in the Raton deposits.

A series of 31 high-explosive (HE) shock-recovery experiments at pressures to 25 GPa and temperatures to 750°C were completed on samples of Westerly granite and Hospital Hill quartzite. TEM and optical microscopy reveal that both pre-shock temperature and pulse duration have a first-order effect on the nature and development of shock-induced microstructures in

quartz and feldspar. Application of the experimental results to natural shock-induced microstructures indicates that the volcanic microstructures are probably produced at elevated temperatures and shock pressures that do not exceed 15 GPa. The results also suggest that the Raton K/T deposits probably represent a moderate impact event at pressures below about 25 GPa.

Analysis of samples from the K/T transition at DSDP Site 527 suggests that multiple events are recorded at this site including at least two enrichments of chalcophile elements possibly related to basaltic volcanism. A major event, coincident with the paleontological K/T boundary, is marked by a strong Ir anomaly and high frequency of shock deformation in quartz and feldspar at all three localities. Correlations between biostratigraphy, isotopes, and the data from this study suggest that the decline in marine productivity over an extended period of time may be due to climate changes induced by basaltic volcanism.

The results from this study were combined with the other lines of evidence across the K/T transition to develop an endogenous model for mass extinctions. The eruption of the Deccan Traps is a viable mechanism for the K/T extinctions, and the correlation of flood basalts with every major biotic crisis in the last 250 Ma supports the link between these two phenomena. Eruption of flood basalts enriched in F, Cl, $CO_2$, and $SO_2$, could disrupt the terrestrial ecosystem, and could produce effects including elevated $pCO_2$, acid rain, ozone depletion, lower ocean alkalinity, and climatic change, which can explain the observation of stepped or gradual extinction.

# DEDICATION

It is with the deepest love that I dedicate this dissertation to the memory of my beloved father, Mr. E. Royce Huffman. Throughout my childhood, he always worked as hard as humanly possible to provide our family with the comforts that make life enjoyable, and the education that he never had the opportunity to achieve for himself. His endless zest for life, sense of fairness and justice, work ethic, and love of God, Country, and his fellow man, have been instilled in me. I thank him gratefully for these invaluable gifts.

On June 10, 1987, while on his first vacation in over 20 years, E. Royce Huffman passed away peacefully aboard a cruise ship in Bermuda. It is said that the Earth bemoans the loss of one of her children, and so it was with Royce. Twelve hours after his death, a magnitude 5.0 earthquake rocked the valley where he was born in 1924. Although he did not live to see me graduate from Texas A&M, I know that he had every confidence that I would finish. To you, Dad, I dedicate this work, the fulfillment of all your dreams and aspirations for your son.

Alan R. Huffman

March 7, 1990

# ACKNOWLEDGEMENTS

In the course of my graduate education at Texas A&M University, I have had the pleasure and privilege of working with many fine people. It is difficult to do justice to the professionalism and high caliber of my colleagues because words cannot express totally my deep feelings toward them. The research contained in this dissertation is the product of a team effort. Although my name is placed at the top, I wish to present the research as a result of an integrated program involving several of my colleagues and myself. Without our collaborative efforts, and the many discussions and brainstorming sessions, I am sure that this work would be much less than it has turned out to be.

First to my committee as a whole, including Neville Carter, Rick Carlson, Andreas Kronenberg, Stan Mertzman, Jim Russell, and Lonnie Jones, I extend my thanks for their support and guidance throughout the project. In particular, I would like to thank Andreas for teaching me the use of the transmission electron microscope and the techniques for analyzing and interpreting TEM images and diffraction patterns. To Stan, I offer my thanks for helping me through a particularly difficult period during my bachelor's program, and for believing in me when other people might have called it quits. Finally to my dear friends, mentors, and colleagues, Neville and Rick, my deepest thanks. Their supportiveness, collaboration, and friendship have made my graduate research enjoyable, exciting, and very rewarding. Their willingness to share their ideas, philosophies, and sound advice have helped me to grow as a person and a scientist. Any heights that I achieve in my career will be due greatly to them, and I salute them.

Much of the work reported herein is the result of collaborations with colleagues from other institutions. Particular thanks go to J. Michael Brown for his collaboration in the experimental shock-recovery work. Without his guidance and insights, this work would not have been completed. Also thanks to Jim Crocket for his analyses of iridium on the Maud Rise and Walvis Ridge samples. Thanks also go to Kevin McCartney and Marian Tredoux, who worked with me diligently as a team to develop the new paradigm for endogenous causation of mass extinctions. Special thanks go to Chuck Officer, without

whose efforts and dogged determination to resist blind impact dogma, none of this work would ever have been started, let alone completed. I also offer sincere thanks to my colleagues Dave Loper, Chuck Drake, Tony Hallam, Stefan Gartner, and Buck Sharpton, without whose comments, constructive criticism, and assistance, many of the ideas in this work would not exist in their present form.

Sincere thanks go to my colleagues who provided unselfishly many of the samples used in this study. These include Carl Orth (Raton K/T sediment), Glenn Izett (Raton shocked mineral separates), Bill Rose and Craig Chesner (Toba eruptive material), Chuck Officer (too many samples to list here), Peter Borella (Walvis Ridge samples), Uve Reimold and Fred Horz (shocked Hospital Hill quartzite), Haraldur Sigurdsson (Tambora eruptive samples), A. V. Murali (Lameta Bed samples), Don Swanson (Mt. St. Helens samples), Ted Bunch (Manson Core samples), and Peter Hooper (samples of Deccan, Greenland, and Columbia River basalts).

Many of the analyses reported in this work were completed with the support and assistance of several research groups within Texas A&M and Los Alamos National Laboratory. Thanks go to Dennis James of the Center for Chemical Characterization and Analysis (TAMU) for the use of his INAA facility, and to Dennis James and Tracy Woods for taking the time to teach me the NAA method. Thanks also go to John Krohn of the Nuclear Science Center (TAMU), and also to Jim Petish, Greg Stasney, and the rest of the reactor staff who assisted in performing the irradiations on my samples. Also thanks to Carl Dufner, Randy Scott, and Lisa Doneghy of the Electron Microscopy Center (TAMU) for their assistance with my TEM work. And last but not least, thanks to John Shaner and Group M-6, Los Alamos National Lab, and to Austin Bonner and Robert Medina, without whose expert assistance on the firing table our shock recovery experiments could not have been completed.

I would also like to acknowledge those who made the progress and preparation of my research as easy as possible, including Robin McNeely, Jack Magouirk, Cathy Littleton, and Michele Beal. Their help has made my life at Texas A&M much easier and I will miss their assistance greatly when I leave.

Also, thanks to Lilly Lyddon for a superb job of drafting the figures for this work.

I would like to acknowledge the College of Geosciences, The Department of Geophysics, and The Center for Tectonophysics, who have consistently provided financial support for me and my research. This support enabled me to devote my full attention to the research, and is responsible in part for the quality and quantity of work that I have completed over the last several years. Additional support for my research was provided by the Texas Engineering Experiment Station, and Jack Gallagher of the Atlantic Richfield Company. This support is acknowledged gratefully.

I would also like to thank Mel Friedman, Dean of the College of Geosciences at TAMU, for giving me the unique opportunity to work with him on various Department of Energy panels and committees, and as his assistant in the Texas A&M Petroleum Recovery Research Program. These activities allowed me to meet many prominent scientists, and permitted me to gain insights into how science policy is established in the United States. These experiences will undoubtedly serve me well in my career.

I would also like to thank my friends, in particular Bob and Judy Hendrickson and family, Mark and Kim LaVern and family, Neville and Susan Carter and family, Rick and Karen Carlson and family, Ted and Arian Oldham, Ken Wilks, Fred and Judy Chester, Tom and Diane Hilde, Tony Gangi, Chris Mathewson, Norm Tilford, Pat Domenico, Vaughn Bryant, Dale Morgan, and all our other friends and acquaintances who have made life in College Station enjoyable. I will always remember fondly my years as a graduate student.

To my parents, Royce and Alice, who struggled financially to give me the best education possible, I extend my deep and undying gratitude. Their only request was that I try to be the best at what I selected as my profession. I hope that I have accomplished that task. I thank them for the opportunity to explore the world and the edges of the unknown; the trip has truly been worth the cost. My only regret is that my father did not live to be with me at graduation in May. However, I know that he will be watching.

Last and most deeply, I wish to thank my wife, Beverly, for loving me when times were good or bad, for bearing with me when I was unbearable, and for making our home a place of warmth and caring during these difficult years. I also thank her for her devotion to our daughter, Andrea, and to me, and for her never-ending support of all my efforts to make our lives better. All that I have done over the last seven years, I have done with all my heart and soul for Beverly and Andrea, for they are the wind beneath my wings.

Alan R. Huffman
March 7, 1990

# TABLE OF CONTENTS

TABLE OF CONTENTS (continued)

TABLE OF CONTENTS (continued)



Volume II

# LIST OF FIGURES

Volume I

LIST OF FIGURES (Continued)

LIST OF FIGURES (Continued)

LIST OF FIGURES (Continued)

LIST OF FIGURES (Continued)

LIST OF FIGURES (Continued)

LIST OF FIGURES (Continued)

LIST OF FIGURES (Continued)

# LIST OF TABLES

## Volume I

# CHAPTER I

# INTRODUCTION: THE CRETACEOUS-TERTIARY BOUNDARY DEBATE: ANATOMY OF A SCIENTIFIC CONTROVERSY

## Introduction

Throughout the Phanerozoic, life on earth has evolved on land and in the seas from simple forms to more complex ones. This evolutionary process has always involved the replacement of older families of organisms with new forms through the process of extinction. In general, the extinction process proceeds at a steady pace, and has decreased in intensity through the Phanerozoic as families have matured (Boyajian, 1986). However, this steady process has been interrupted episodically by sudden increases in the rate of extinction (Raup and Sepkoski, 1984). This sudden and large increase in extinction rates above the background extinction level, followed by recovery of the global ecosystem, is called a mass extinction (figure 1-1). Mass extinctions and less severe changes in the biota have played a major role in geology, since changes in fossils were used as the basis for relative dating of strata through the concept of faunal succession. Without these rapid changes in the biota, early geology would have been hampered greatly in its attempts to date and correlate geologic strata.

Among the many extinction events of the last 570 Ma of earth history, two events stand out as particularly intense. These events, which mark the end of the Paleozoic and Mesozoic Eras, are known as the Permo-Triassic and Cretaceous-Tertiary mass extinctions. These events marked major changes in

---

This dissertation follows the format and style of Tectonophysics.

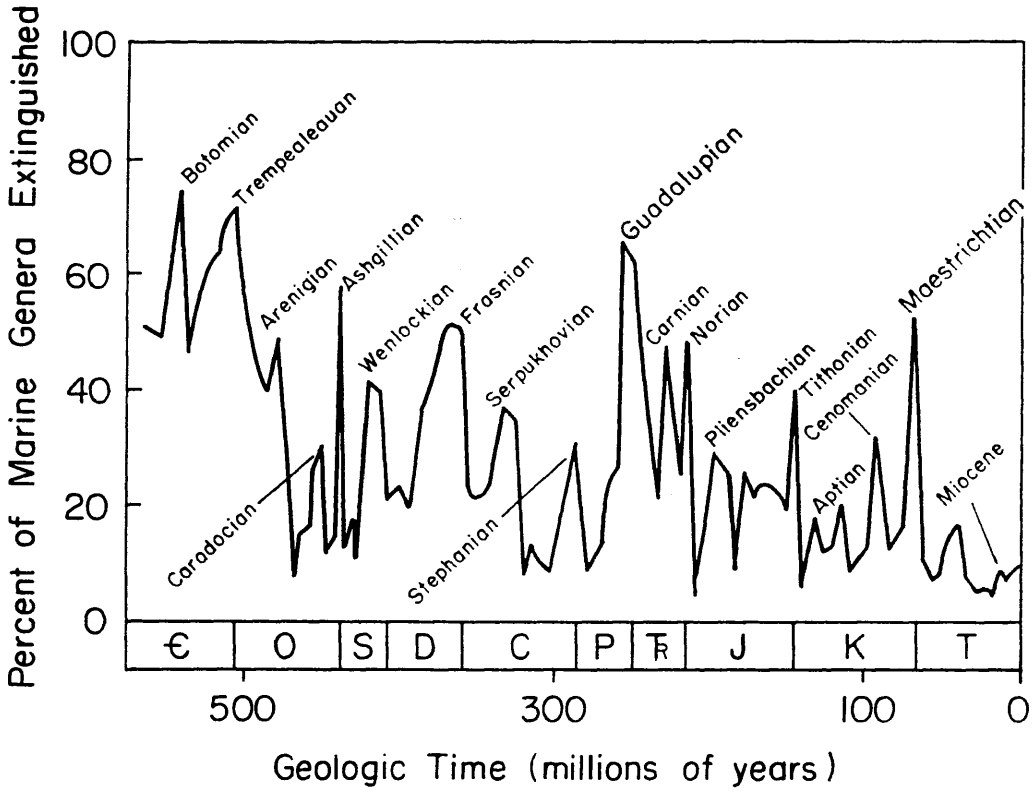


Figure 1-1: Intensity of extinction at the generic level throughout the Phanerozoic. Major extinction events are denoted by large spikes, and names are assigned to the major stage boundaries. Diagram after Sepkoski (1985).

the character of life on earth, and hence were used to divide the Phanerozoic into three Eras. The intensity of these two events, along with the Ashgillian (Ordovician-Silurian) event, suggested that something "catastrophic" must have occurred to cause such dramatic changes in the biota.

## The Cretaceous-Tertiary Extinction Event

Among the many extinction events in the Phanerozoic, the Cretaceous-Tertiary (K/T) event has received most of the attention. This is owing to several factors including, (1) the K/T event marks the transition from dominance of the dinosaurs to dominance of mammals, (2) the K/T boundary (KTB) is well exposed in Europe and North America where much early geology was done, and (3) humans have always been excited by the life, times, and death of the dinosaurs.

Russell (1979) reviewed the state of knowledge on the K/T extinctions. He noted that the extinction of the dinosaurs was not preceded by any precursory changes in the biota, which supported the idea of a sudden catastrophic event. The K/T event was clearly more severe in the marine realm (Table 1-1) as indicated by the relative levels of extinction. Although significant debate centers to this day on whether the marine and nonmarine extinctions were synchronous (e.g. Rampino, 1988), it was evident that a severe trauma of some sort was inflicted on the earth's ecosystem at the end of the Cretaceous. This trauma, either directly or indirectly caused about half of the extant Cretaceous genera to be extinguished (Table 1-1), with some groups such as the ammonites and belemnites suffering complete extinction. This

Table 1-1: Estimates of extant genera before and after the K/T extinction event, and the percent change in genera across the boundary. Negative numbers in column three imply a decrease in extant genera. Data from Russell (1979).

| | Late Cretaceous | Early Paleocene | % Change |
|---|---|---|---|
| Fresh Water Organisms | | | |
| Cartilaginous fishes | 4 | 2 | -50 |
| Bony fishes | 11 | 7 | -36 |
| Amphibians | 9 | 10 | +11 |
| Reptiles | 12 | 16 | +33 |
| | 36 | 35 | -3 |
| Terrestrial Organisms (excluding fresh water forms) | | | |
| Higher plants | 100 | 90 | -10 |
| Snails | 16 | 18 | +13 |
| Bivalves | 10 | 7 | -30 |
| Mammals | 22 | 25 | +14 |
| | 148 | 140 | -5 |
| Floating Marine Microorganisms | | | |
| Acritarchs | 28 | 10 | -64 |
| Coccoliths | 43 | 4 | -91 |
| Dinoflagellates | 57 | 43 | -25 |
| Diatoms | 10 | 10 | -0 |
| Radiolarians | 63 | 63 | -0 |
| Foraminifera | 18 | 3 | -83 |
| Ostracods | 79 | 40 | -49 |
| | 298 | 173 | -42 |

Table 1-1 continued

| | Late Cretaceous | Early Paleocene | % Change |
|---|---|---|---|
| Bottom-dwelling Marine Organisms | | | |
| Calcareous algae | 41 | 35 | -15 |
| Sponges | 261 | 81 | -69 |
| Foraminifera | 95 | 93 | -2 |
| Corals | 87 | 31 | -64 |
| Bryozoans | 337 | 204 | -39 |
| Brachiopods | 28 | 22 | -21 |
| Snails | 300 | 150 | -50 |
| Bivalves | 399 | 193 | -52 |
| Barnacles | 32 | 24 | -25 |
| Malacostracans | 69 | 52 | -25 |
| Sea Lillies | 100 | 30 | -70 |
| Echinoids | 190 | 69 | -64 |
| Asteroids | 37 | 28 | -24 |
| | 1976 | 1012 | -49 |
| Swimming Marine Organisms | | | |
| Ammonites | 34 | 0 | -100 |
| Nautiloids | 10 | 3 | -30 |
| Belemnites | 4 | 0 | -100 |
| Cartilaginous fishes | 70 | 50 | -29 |
| Bony fishes | 185 | 39 | -79 |
| Reptiles | 29 | 3 | -90 |
| | 332 | 99 | -70 |

50% change at the generic level translates to a species extinction of over 75% across the KTB (Russell, 1977). The origin, character, and severity of this trauma has been a point of heated debate for many years. At the time Russell (1979) wrote his review, a variety of theories had been put forth to explain the K/T extinctions.

Trophic Effects

The most obvious way to explain extinctions is by mechanisms intrinsic to the biota themselves. In particular, the collapse of the phytoplankton, which are the base of the oceanic food chain, could lead to the extinction of fauna that were higher up in the chain. At the K/T transition, the marine realm lost the base of its food chain in the phytoplankton (e.g. Gartner, 1977), along with many larger fauna. In stark contrast, the terrestrial and fresh-water communities were the least affected with their food chain remaining essentially intact despite some extinctions and floral change in the terrestrial flora (Tschudy, 1971; Hickey, 1984; Johnson and Hickey, 1988).

One problem with the idea of trophic extinction is the observation that some marine macroorganisms, such as the inoceramids (Sloan et al, 1986) suffer total extinction before the phytoplankton, suggesting that other forcing agents may have been at work before the terminal K/T event. It appears that the extinctions may have actually occurred on two time scales with a long decline in global habitat causing the death of macroorganisms, followed by an abrupt terminal event that destroyed the microorganisms. The observations at the KTB indicates that a trophic cause for the extinctions may not be viable.

## Marine Regressions

A viable way to explain the early death of the inoceramids before the terminal K/T event would be by habitat destruction. Hallam (1977) proposed that the pre-boundary extinctions of macroorganisms were due to sea-level decline, which wiped out large areas of continental shelf habitat. The climatic changes that would accompany such a sea-level change would also cause increased stress on the biota. The causes of eustatic changes are poorly understood, and may include changes in spreading rate, glaciation events, volcanism, global isostatic changes, and other causes (Hallam, 1987). In addition, a serious problem exists in distinguishing between true eustatic change and tectonic and other influences on apparent sea level.

## Temperature and Climate Change

Climatic and temperature changes have long been postulated as a cause of extinction. The oxygen isotope record for the late Cretaceous and early Paleocene reveals that the late Cretaceous was a period of warming (Stevens and Clayton, 1977), with an apparent global maximum in the early Upper Cretaceous (McLean, 1978). The isotopic evidence from the South Atlantic (Boersma, 1984) suggests a thermal rise across the K/T transition in surface waters, while the terrestrial plant record from the northern hemisphere (Hickey, 1984; Johnson and Hickey, 1988; and Krassilov, 1975) indicates a cooling across the transition as evidenced by changes in leaf morphology and an increase in the dominance of ferns over angiosperm plants at middle to high latitudes. The data suggest that the K/T transition was a period of relative climatic instability, with changes in temperature, rainfall, and global climate

circulation. The observation that a thermal minimum occurred at different times in various regions suggests that the earth's atmosphere was in a state of rapid flux.

Crowley and North (1988) have postulated that the earth's climate system can be perturbed by very small forcing factors intrinsic to the climate system itself. They argue that extrinsic forcing factors, although important, are not necessary to cause abrupt climate transitions. If this model is correct, then it is quite possible that subtle changes in landmass distribution, albedo, and other climatic factors could cause global catastrophes, and that the following extrinsic factors such as volcanism, meteor impact, and galactic effects may not be needed to explain the extinction record.

## Volcanism

Vogt (1972) proposed that volcanic activity across the K/T transition may have been sufficiently intense to cause the extinctions. Since this mechanism was proposed, significant work has been done on the effects of both basaltic and explosive silicic volcanism (Tazieff and Sabroux, 1983). It is now recognized that the emissions from basaltic eruptions such as the historic Laki eruption of 1783 (Devine et al, 1983). are quite devastating to the environment. Evidence from eruptions such as Krakatau (1883), Tambora (1815), Agung (1963), and El Chichon (1983) demonstrates clearly that the effects of explosive volcanism are also potentially damaging. The main weakness of the volcanic models has been the perception that rates of eruption are insufficient to cause global effects.

## Meteoroid and Comet Bombardment

It has long been recognized that the earth-moon system has been bombarded by meteoroids and comets throughout its history. Urey (1973) suggested some possible effects from the collision of a large comet or meteoroid with the earth. As the size of the impactor increases, so should the severity of the effects. The calculations of Urey indicated, however, that an impactor would have to be extremely large to produce global effects. McLaren (1970) argued that the effects of such an impact in the oceans would be particularly devastating to the affected ocean basin. In contrast, however, the evidence from craters on land suggests that the largest craters show no evidence of correlated extinctions (Officer and Grieve, 1986).

## Ultraviolet Radiation

Recent concern over the Antarctic ozone hole has re-emphasized the risk of a diminished ozone layer (El-Sayed, 1988). It has been suggested that an extreme increase in solar flare activity, or the presence of a nearby supernova could partially or totally destroy the terrestrial ozone layer. In the aftermath of such an event, the biosphere would be subjected to intense solar radiation, climatic instability, reduction of visible light transmission in the atmosphere, and global cooling (Russell, 1979). Although these effects would be severe, they would only last for a short period (~10 years, Reid, 1977; Hunt, 1978). It is possible, however, that the effects of such a loss of ozone could account for significant increases in extinction rates (Clark et al, 1977).

Ionizing Radiation and Supernova Activity

It has been postulated that a nearby supernova would have significant effects on the earth's ecosystem. In addition to destruction of the ozone layer by ultraviolet rays, a supernova would cause elevated background radiation in the earth's atmosphere (Tucker, 1977). Such increases could reach up to 300 roentgens per year in the first 10 years, which would prove detrimental or lethal to most large organisms on land. The presence of large concentrations of radioactive minerals in late Cretaceous fossils (Salop, 1977) has been used to support this idea. In addition to immediate effects of a supernova, the ecosystem would also be subjected to a prolonged period of radiation exposure of about 10 roentgens per year over a period of $10^3$ to $10^4$ years (Tucker, 1977). Although the astrophysical evidence suggests that a supernova should occur within 50 light years of the earth about every 70 Ma (Clark et al, 1977), there is no evidence of a supernova of K/T age to support this hypothesis (Feldman, 1977).

Galactic Orbit Effects

As our solar system revolves around the Milky Way every 200 Ma, our system crosses the galactic plane about every 30 Ma. During this crossing, the levels of cosmic radiation on earth increase for a period of about 1 Ma (Hatfield and Camp, 1970). In addition, the solar system could also be exposed to other stresses during passage through a spiral arm of the galaxy. These stresses would include increased exposure to supernovae, climatic effects of interstellar dust clouds, and other effects (Talbot et al, 1976; Clark et al, 1977).

The problem with such effects is that they would probably not leave any evidence of their presence to prove or disprove the proposed causes.

## Arctic Spillover

Gartner and Keany (1973) and Gartner and McGuirk (1979) proposed an oceanographic solution to the K/T extinction event. They proposed that the Arctic Ocean evolved as an isolated fresh to brackish water body during the late Cretaceous, and that rifting of the North Atlantic ocean basin at K/T time caused the lighter Arctic waters to spill over into the Atlantic Ocean. Meanwhile, the heavier Atlantic waters intruded into the Arctic. The spread of this cold, low salinity water over the top of the Atlantic Ocean caused the extinction of planktonic marine organisms, along with the benthic and nektonic organisms through depletion of dissolved oxygen in the water column (Kauffman, 1977) and food chain collapse. Gartner and McGuirk (1979) note further that isotopic data from late Cretaceous fauna in North American, Greenland, and North Atlantic deep-sea sites supports this model.

## A Scientific Revolution: The Alvarez Bolide Hypothesis

In 1978, a team of researchers from the University of California were trying to determine sedimentation rates at several classic localities at Gubbio, Italy. This team, led by Nobel Laureate Luis Alvarez, was attempting to use the assumption of a constant flux of extraterrestrial exotic elements, along with actual analyses for these elements in sedimentary rocks, to determine actual rates of sedimentation at Gubbio. The analyses for the platinum-group

element (PGE) iridium (Ir) revealed a large anomaly coincident with the K/T boundary layer. Upon examination of the data, the team concluded that this large Ir anomaly could not be accounted for by sedimentation rates, and that the assumption of a constant flux of cosmic matter must be incorrect. This conclusion led to the publication of a landmark paper (Alvarez et al, 1980) that changed profoundly the course of extinction research.

Alvarez et al (1980) proposed that the K/T extinctions were caused by the impact of a 10±4 km diameter asteroid on the earth. They proposed that the effects of this event would include global darkness, acid rain, devastation of plants by atmospheric heating and firestorms, and complete collapse of the global ecosystem. Although no recognized impact crater is of sufficient size (200-300 km) and the correct age (66±1 Ma) to be the "smoking gun", the Alvarez team argued that the presence of excess Ir and the elemental ratios between other elements and Ir, virtually ruled out other sources and supported exclusively the bolide hypothesis. The fundamental importance of the Alvarez hypothesis was two-fold. First, the bolide hypothesis was the first extinction model that had some hard evidence to support it over the other models. Second, it was the impetus for a tremendous amount of new research on extinction as a process.

## The Impact Scenario

In the bolide hypothesis, a 10-km diameter chondritic asteroidal object enters the earth's atmosphere at a velocity of 15-20 km/sec. As the bolide transits the atmosphere, it produces an atmospheric shock wave that superheats the air and causes large scale conversion of $N_2$ and $O_2$ to NO and

$NO_2$ (Prinn and Fegley, 1987). Secondary reaction of these compounds with water vapor produces large amounts of nitric acid, leading to acid rains in the affected hemisphere. As the blast wave propagates outward from the entry point, a hole is created in the bolide's wake. This wake of low atmospheric pressure acts as a vaccuum which pulls ejecta and vaporized bolide material upward into the stratosphere and ionosphere. This atmospheric transit takes only about two seconds to occur. As the air wave travels outward from the entry point, it destroys vegetation at great distances.

After transiting the atmosphere, the bolide strikes the planetary surface, producing a shock wave with pressures on the order of a Megabar at the impact center (Melosh, 1989). The energy release for the impact event has been estimated at about $10^{23}$ Joules, which is roughly equivalent to $10^8$ Megatons of TNT (Jones and Kodis, 1982). The seismic coupling of the impact would likely be $10^{-1}$ to $10^{-2}$ so that only a small fraction of the total energy is expended in the planetary interior far from the impact site. The majority of the energy is expended in mechanical and chemical work in the atmosphere and at the site of the impact. Still, this seismic energy release is roughly equivalent to $10^6$ magnitude 8.0 earthquakes (Richter, 1958).

As the object penetrates the planet surface, the shock wave propagates into the planet and backward into the bolide itself, causing intense shock deformation of the target rocks. When the shock front reaches the back surface of the bolide, the reflected wave becomes a tension wave that causes the object to fragment and vaporize. At the same time, melted and vaporized target rock are jetted outward along with a large peripheral spall layer that develops into a base surge much like that observed during lateral volcanic

blasts (e.g. Mount Saint Helens). At the same time, the vaporized bolide is mixed with the target-rock ejecta, and is blown upward and outward into the stratosphere and ionosphere (e.g. Schultz and Gault, 1982).

The thermal release during the impact and vaporization process also generates a flash front much like that observed during nuclear tests (Jones and Kodis, 1982). The flash front mixes with the air wave, ejected target rock, and spall, to produce an expanding fireball that engulfs plants, soil, and air into a growing firestorm. This firestorm destroys everything on the planet surface for a distance of several hundred kilometers from the impact site, with diminishing effects at greater distances. The mixture of vaporized bolide and target rock is ejected in part into the stratosphere and ionosphere through the atmospheric hole, and spreads outward as a dust veil, leading to greatly decreased incoming solar radiation. Alvarez et al (1980) estimated that the effect of this dust veil would be to reduce incoming radiation to $10^{-13}$ of normal. This would cause a global darkness similar to the "nuclear winter" recently proposed as a possible effect of global nuclear war (Toon et al, 1982).

As the dust settles after the impact, a transient crater with a diameter of 200 to 300 km and initial depth of 10 to 20 km would remain. Surrounding the crater would be an ejecta blanket of mixed melt, spall blocks, soil, and pyrolized vegetation. At greater distances from the crater, the ejecta blanket would thin, and grain sizes of target material would decrease rapidly. At great distances from the impact site, the distal deposits would consist of fine target material combined with condensed bolide and other fines (e.g. Hörz, 1982).

On a global scale, the earth's atmosphere would cool rapidly and photosynthesis would be shut down nearly instantaneously from the dust veil effects (Gerstl and Zardecki, 1982). This would devastate the vascular plants and photosynthetic marine organisms, and would lead to food chain collapse. The rapidly cooling atmosphere would produce rains laced with nitric acid and condensed heavy metals from vaporized bolide. This would lead to further ecological deterioration, causing decreased pH in the oceans, intense leaching of soils and erosion on land, and rapid destruction of terrestrial ecosystems that are not buffered well against acid rains (e.g. Schindler, 1988). Recovery of the physical environment occurs rapidly in the bolide model, and takes from 10 to $10^4$ years, followed by rapid recovery of the global ecosystem.

For about four years following the publication of the Alvarez et al (1980) paper, a proliferation of K/T research led to publication of much new information on the geochemical, mineralogical, and geophysical character of K/T sites around the world. As the evidence mounted, it appeared to support the bolide hypothesis. The Ir layer almost always coincided with the extinction horizon, and was also found to be virtually global in its distribution (Alvarez et al, 1982).

The strongest line of evidence in support of the bolide hypothesis was discovered in the K/T sections in the western interior of the United States. Bohor et al (1984) reported the presence of quartz grains in the Raton Basin K/T boundary clay that contained shock-induced microstructures, which were believed to be unique to impact. Further search revealed that like the Ir, the shocked quartz was also distributed globally (Bohor et al, 1987) and coincided with the extinction horizon. The morphology of these quartz and feldspar

grains at Raton included large grain sizes and sutured grain boundaries indicative of a continental target (e.g. Izett, 1987b). Additionally, the grain sizes at sites around the world tended to decrease away from North America, suggesting that the impact site must have been on or adjacent to North America (Bohor et al, 1987).

Additional support for impact was found in the occurrence of sanidine and magnetite microspherules in the boundary clay (Smit and Klaver, 1981; Smit and Kyte, 1984). The spherules were similar to tektites and were proposed to represent impact melt of various compositions that was ejected into the atmosphere.

While the bolide hypothesis was gaining more support and momentum, several problems arose. First, the impact hypothesis failed in its original form, to account for the extinctions that preceded the Ir layer such as the inoceramids and other macroorganisms (e.g. Hallam, 1987). It also failed to explain the selectivity of the extinctions (Officer et al, 1987). Furthermore, some of the microorganism extinctions also appeared to not be synchronous (Smit and Romein, 1985), and also predated the boundary event (Brinkhuis and Zachariasse, 1988). In order to explain a sequence of extinctions by impact, Hut et al (1987) proposed a model of multiple cometary bombardment. Their model, which is unsupported by the geologic record, suggests that the Oort cloud of comets which encircles our solar system, released large numbers of comets over a short period of time and several of these comets struck the earth in rapid succession near K/T time.

Alvarez et al (1980) recognized another problem in the clay mineralogy of the KTB layer. The Mg-rich smectite clay that makes up most of the layer is more indicative of altered volcanic ash than of impact fallout (Rampino and Reynolds, 1983). Despite the argument that the high Mg content supported an impact origin (Kastner et al, 1984), the lack of other conclusive evidence in favor of an impact origin left serious questions regarding the origin of the deposit.

One of the basic tenets of the bolide hypothesis was the uniqueness of an extraterrestrial source for iridium. In a classic paper, Zoller et al (1983) demonstrated that Kilauea volcano was a terrestrial volcanic source of iridium, and that the iridium was produced as an aerosol that was borne on the winds. Zoller et al (1983) also observed elevated levels of As, Sb, Se, and other trace elements in Kilauea aerosols (see also Olmez et al, 1986; Crowe et al, 1987) that are also elevated in KTB sections around the world (e.g. Michel et al, 1981; Smit and tenKate, 1982).

## A Counter-Revolution: The Volcanic Hypothesis

In response to the problems associated with the bolide hypothesis, Officer and Drake (1983) proposed that the K/T event was actually a prolonged one. Using all the available evidence, they argued that the faunal record, the distribution of iridium across the transition, and the mineralogy of the boundary clay all supported an endogenous cause for the extinctions. Later, Officer and Drake (1985) reiterated their assertion of an endogenous cause for the K/T extinctions. They argued that the presence of other trace elements such as As, Sb, Se, and their ratios to Ir were more supportive of a mantle

origin for the chemistry across the K/T transition. They further argued that the volcanism probably lasted for $10^4$ to $10^5$ years.

In a third contribution, Officer et al (1987) solidified their working model, and suggested that the kill mechanism for the K/T event was a combination of silicic and flood basalt volcanism over a period of 1 x $10^5$ to 3 x $10^5$ years. In particular, they argued that the primary culprit was the main eruptive phase of the Deccan Traps flood basalt, which erupted synchronously with the K/T extinctions. They suggested that the aerosols from the Deccan Traps produced sufficient Ir and other trace elements to explain the chemical signatures across the KTB, while the microspherules and shocked quartz were produced by a silicic component of the volcanism. The longer term climatic deterioration caused by sulfur, halogens, and $CO_2$ included acid rain, a decrease in ocean alkalinity, ozone layer depletion, and climate change.

The Volcanic Scenario

In stark contrast to the impact hypothesis, the volcanic scenario for the K/T extinctions is built on the premise that a prolonged episode of particularly intense volcanism caused a deterioration of global climate. The onset of volcanism occurs as a combination of explosive silicic eruptions and basaltic fissure eruptions. This initial activity causes some climate perturbation due to dust veil effects from ash and stratospheric effects from aerosols of sulfur, halogens, and $CO_2$.

As the volcanic activity continues, the dominant activity shifts to the basaltic fissure eruptions. The large volumes of basalt extruded onto the

Deccan Plateau would contribute volumes of sulfur, $CO_2$, and halogens sufficient to cause severe climate distress. The proposed effects include (1) climatic cooling and decreased photosynthesis from stratospheric dust veils and sulfur aerosols, (2) acid rain from reactions between $CO_2$, $SO_2$, and halogens in the eruptive plumes, (3) ozone depletion by stratospheric aerosols of F and Cl, (4) heavy metal toxicity from chalcophile and siderophile elements that precipitate from the aerosols, (5) increased erosion and runoff on the continents, and (6) decreased alkalinity in the oceans from acid rains.

This wide spectrum of environmental effects adds to the severity of the direct climate effects, and leads directly and/or indirectly to selective and sequential extinctions on land and in the oceans. The sequence and selectivity are related directly to the tolerances of each organism to the applied stresses. The recovery period for this scenario lasts up to several million years.

## Geochemical, Mineralogical, and Geophysical Evidence at The KTB

A wide variety of analytical techniques have been applied to K/T stratigraphic sections around the world. It is appropriate to discuss briefly the many lines of evidence that have been used in favor of the two competing hypotheses. A thorough review of the extensive body of literature is beyond the scope of this chapter, but an attempt will be made to point out the significance of each piece of evidence. Both hypotheses call on these lines of evidence, and try to use them in different ways. Therefore, a table (Table 1-2) has been constructed to facilitate this discussion.

Table 1-2: List of geochemical, mineralogical, and geophysical evidence from the K/T transition and the explanation given by the impact and volcanic hypotheses for each line of evidence.

| Evidence | Impact Model | Volcanic Model |
|---|---|---|
| Iridium & PGE | Extraterrestrial | Volcanic aerosols |
| Chalcophile Elements | Target rock | Volcanic aerosols |
| Carbon Isotopes | Productivity collapse | Productivity collapse |
| Oxygen Isotopes | Post-impact cooling (nuclear winter) | Sulfur aerosols and dust veil effects |
| Strontium Isotopes | Increased continental runoff/acid rain | Increased continental runoff/acid rain |
| Soot/Carbon Black | Impact-triggered fires | Volcanically-triggered fires |
| Rare Earth Elements | Nitric acid rains | Sulfur and Halogen acid rains |
| Shocked Minerals | Target rock ejecta | Silicic volcanic ejecta |
| Microspherules | Melted target rock | Volcanic ejecta |
| Clay Mineralogy | Impact fallout | Altered volcanic ash |
| Geomagnetic Reversals | Impact-induced | D" layer disturbance |
| Marine Regression | Unexplained | Pre-volcanic changes |
| Periodicity/Episodicity | Nemesis or impact recurrence | Mantle dynamics |
| Extinction Selectivity | Unexplained | Relative faunal tolerances |
| Extinction Sequence | Multiple impacts | Relative faunal tolerances |

Iridium and The PGE

After the initial discovery of excess Ir at Gubbio (Alvarez et al, 1980), analyses of iridium were performed on K/T sections around the world. Within a few years, Ir anomalies had been identified at 36 sites (Alvarez et al, 1982, their figure 1). At present, enriched levels of Ir have been reported from over 75 sites. The Ir values at these sites vary from a maximum of 87 ppb at Stevns Klint in Denmark, to 0.16 ppb in the South Atlantic Ocean.

More recently, Tredoux et al (1989) analyzed all of the PGE for several K/T sections. Their results reveal that all of the PGE display enrichments relative to their crustal average values. They further observe that the chondrite-normalized PGE trends show a chondritic signature in the northern hemisphere and a more basaltic signature in the southern hemisphere. This suggests that either a partitioning event of some kind caused changes in the hemispheric signatures, or that there are actually two sources of Ir across the K/T transition.

Chalcophile Elements

Michel et al (1981) and Smit and tenKate (1982) recognized that several chalcophile elements including As, Sb, and Se were also enriched in the KTB clay. Analyses from both marine and terrestrial sites around the world revealed that like the Ir, the other enrichments were also global in their extent (e.g. Izett, 1987b). In sharp contrast to the PGE trends, which showed a diluted chondritic signature, the chalcophile elements displayed an enrichment of $10^3$ to $10^4$ relative to C1 chondrite in the boundary layer.

Carbon Isotopes

It has long been recognized that decreases in marine productivity during biotic crises lead to sharp negative excursions in $\partial^{13}C$ in the oceans (e.g. Tappan, 1968). The marine record at the KTB is no exception. Although the intensity of the $\partial^{13}C$ decrease varies from one locality to another (e.g. Shackleton and Hall, 1984; Zachos et al, 1988), the general trend is a rapid lightening of $\partial^{13}C$ as primary productivity collapsed across the transition.

Oxygen Isotopes

The primary chemical evidence for climatic changes at the K/T transition comes from changes in $\partial^{18}O$ values in the oceans (e.g. Tappan, 1968). Oxygen isotopes, which are very sensitive to temperature changes, show differing responses to the KTB event at various localities. The general trend in $\partial^{18}O$, however, is toward heavier values, reflecting a cooling event across the KTB (Shackleton and Hall, 1984). Some sites display subtle precursory changes up to 2 x $10^5$ years before the boundary, while others show an abrupt increase in $\partial^{18}O$ at the KTB with no evidence of any precursors (Arthur et al, 1987).

Strontium Isotopes

A positive excursion in $\partial^{87}Sr$ occurs across the K/T transition (Hallam, 1987). This isotope anomaly, which displays an increase from 0.7077 in the late Cretaceous to a peak value of 0.7079 at the KTB, appears to represent increased

runoff from the continents due to a marine regression. Present debate centers not on the presence of the anomaly, but on the time that the anomaly begins to occur. Koepnick et al (1985) argue for initial changes in strontium isotopes up to 3 Ma before the KTB, while MacDougall (1988a) proposes that the isotopic excursion is coincident with the KTB, in response to the K/T impact.

Soot and Carbon Black

Wolbach et al (1988) observed the presence of soot and carbon black at the KTB at several localities and inferred that this evidence represented global wildfires which occurred immediately following the K/T impact event. The presence of the carbon, along with kerogen and retene (Gilmour et al, 1988) suggests that significant combustion of coniferous biomass occurred across the K/T transition. Carbon black has also been observed at Stevn's Klint (H. Hansen et al, 1987), and is distributed over 3.5 meters below the KTB, which implies large-scale production of reduced carbon by various mechanisms up to 50,000 years before the terminal extinction event. In addition, where carbon black and Ir have both been analyzed, it appears as though the data sets correlate very highly, indicating that carbon black may be a carrier and scavenger of Ir.

Rare Earth Elements (REE)

Smit and tenKate (1982) observed that the REE concentrations in KTB sediments at Caravaca, Spain, and Stevns Klint are lower than in the surrounding Cretaceous and Danian sediments. Also, a negative Ce anomaly has been identified in some marine sections (e.g. Schmitz, 1985). In contrast to

these observations, some continental sections (Hildebrand and Boynton, 1987) and the Brazos River section in Texas (Huffman et al, 1989) show REE patterns that reflect uninterupted influx of typical continental sediments.

Shocked Quartz and Microspherules

As mentioned above, one of the primary lines of evidence supporting the impact hypothesis is the presence of shocked quartz grains and microspherules in KTB sediments. The evidence for shocked quartz will be discussed in detail in chapter 2.

A variety of microspherules have been observed in KTB sediments at sites around the world. These microspherules vary in composition including sanidine (Smit and Klaver, 1981), magnetite (Smit and Kyte, 1984), kaolinite (Izett, 1987a), and magnesioferrite spinel (Kyte and Smit, 1986). In addition, H. Hansen et al (1987) observed that some spherules from Denmark, New Zealand, and Spain contain combinations of sanidine and goethite. Chemical analyses of spherules from several localities (Kyte and Smit, 1986) indicate that trace element compositions of similar spherules vary widely from one site to another. The magnetite spherules are also enriched in Ir (Cisowski, 1988a). Although the origin of the spherules in under debate, Sm-Nd and Rb-Sr systematics for the sanidine spherules (Shaw and Wasserburg, 1982) suggest that authigenic growth and a volcanic origin are both viable. Also, Cisowski (1988a) has suggested that the mineralogy, morphology, and chemistry of the magnetite spherules is more in line with a terrestrial combustion origin rather than an impact origin.

## Clay Mineralogy of the KTB "Ejecta " Layer

The clay mineralogy of the KTB layer is dominated by a Mg-rich smectite along with lesser amounts of illite (S/I ratio >9) and other clay minerals (Elliott et al, 1989). This mineralogy has been a major point of concern in the literature since smectite is normally interpreted as an alteration product of volcanic ash. The unusual chemistry of the smectite, along with other criteria, have been used (e.g. Kastner et al,1984) to argue in favor of an impact origin of the entire clay. However, the observation that this same smectite occurs well above and below the KTB (Christensen et al, 1973; Rampino and Reynolds, 1983) implies that it is not exotic and probably represents a terrestrial source. Although the KTB layer does appear to have a small fraction of impact debris, it is most likely dominated by volcanic and detrital material (Izett, 1987b).

## Marine Regressions

The K/T stratigraphic record in Europe supports the contention that a regression preceded the boundary event (Hallam, 1987; Stanley, 1988). In stark contrast, the Brazos River K/T section in Texas, which was an outer shelf environment at the KTB, shows no evidence of a regression (Jiang and Gartner, 1986). Furthermore, it has been argued that the South Atlantic margins generally show an environment of advancing seas, not regression (Reyment and Morner, 1977), which is reasonable since the South Atlantic was undergoing post-rifting subsidence at K/T time.

The confusion between the various sites around the world raises the issue of whether an apparent sea-level change at several localities in one region truly represents a global regression (Bond, 1976; Jeletzky, 1978), and whether eustatic and regional tectonic changes can be distinguished from each other? Despite this problem, however, the correlation between extinction events and relative sea-level change, both regressive and transgressive, in the Phanerozoic is probably significant (e.g. Hallam, 1989).

## Geomagnetic Reversals

Raup (1985) observed that changes in the frequency of geomagnetic reversals correlate well with extinction events. Later, Muller and Morris (1986) suggested that the changes in reversals could be due to impacts, although this idea is unsupported by current geophysical models of the geodynamo and the geologic record (Loper and McCartney, 1990). As an alternative, Loper and McCartney (1986) proposed that changes in reversal frequency are coupled to changes in the D" layer of the lower mantle, and that the timing of the reversals correlates better with an internal model for extinctions (Loper et al, 1988).

## Periodicity and Episodicity of Geophysical Phenomena

Since the discovery of Ir and the landmark paper by Alvarez et al (1980), the proposal has been put forth that the K/T event was not a unique occurrence, but was part of a process that occurs periodically. Raup and Sepkoski (1984) proposed that the K/T extinction is just one of a series of extinctions caused by periodic bombardment by comets or meteoroids, and that

this process occurs about every 26 Ma. The 26 Ma value was derived from a time-series analysis of the terrestrial extinction record; this has been criticized by many workers because of the statistics of small numbers (e.g. Hoffman, 1985), the weakness of the statistical methods used (e.g. Stigler and Wagner, 1987), and errors and poor age-date control in the geologic record (Hallam, 1984; Stothers, 1989). The primary concern with the statistical methods employed by Raup and Sepkoski (1984) was that the nature of the data set could produce numerical artifacts that would result in erroneous periodicities (Lutz, 1985).

Despite the barrage of criticisms surrounding the idea of extinction periodicity, the proposed link between impact and extinctions triggered a variety of studies on many geophysical phenomena to test for other periodicities in the geologic record. Initial work on cratering (Alvarez and Muller, 1984; Whitmire and Jackson, 1984; Davis et al, 1984, and Rampino and Stothers, 1984a, 1984b) led ultimately to the suggestion that extinction and cratering periodicities were linked to galactic phenomena (Clube and Napier, 1984), or to the presence of a solar companion star called "Nemesis" (e.g. Whitmire and Matese, 1986). After the existence of Nemesis was proposed, Hut et al (1987) proposed that the solar companion could perturb the Oort cloud, which would lead to intense cometary bombardment of the earth over short periods of time. The only problem with this model is that (1) no proof of the existence of Nemesis is available, (2) no evidence of multiple impacts across the K/T transition exists (Officer and Grieve, 1986), and (3) the terrestrial cratering record does not support the proposed periodicities (Grieve et al, 1986). In addition, none of the models take into account the role of nonlinear dynamics in geologic phenomena (e.g. Shaw, 1987).

Table 1-3: Results for statistical analysis of proposed periodicities of geophysical phenomena. Data taken from Rampino and Stothers (1984b). The N value is the number of events used to perform the analysis, the age range is the limit of the available data set, and the period is the dominant apparent periodicity observed in the data.

| Phenomenon | N | Age Range | Period |
|---|---|---|---|
| Mass Extinctions | 9 | 0-250 Ma | 30±1 |
| Tectonic Pulses | 18 | 0-600 Ma | 33±3 |
| Flood Basalts | 12 | 0-250 Ma | 32±1 |
| Low Sea Levels | 13 | 0-600 Ma | 34±1 |
| Plate Rate Changes | 7 | 0-180 Ma | 34±2 |
| Magnetic Reversals | 300 | 0-170 Ma | 30±1 |
| Carbonatites | 28 | 0-600 Ma | 34±1 |
| Kimberlites | 38 | 0-420 Ma | 35±1 |
| Impact Craters | 41 | 0-250 Ma | 31±1 |
| Galactic Plane Crossings | - | - | 33±3 |

Despite the apparent problems and limitations of time series and nonparametric methods, similar analyses have been performed on a variety of geophysical phenomena. Rampino and Stothers (1984a, 1984b) noted that the half-period of our solar system for crossing the galactic plane was 33±3 Ma. Similar apparent periodicities exist for a variety of phenomena with all the recurrence intervals falling between 30 to 35 Ma (table 1-3). Although the similarities in recurrence interval for the various phenomena may be fortuitous, it requires that serious thought be given to the concept of coupling between apparently unrelated geophysical events. Although the data appear to represent true periodicities, it is more likely that they represent an average recurrence interval for relatively episodic phenomena.

## Purpose of This Work

The primary line of evidence in support of the impact hypothesis has been the presence of shocked quartz in KTB sections around the world (Bohor et al, 1987). When Officer and Drake (1985) proposed that volcanism could explain the evidence at KTB, they were criticized, primarily because no evidence of shock deformation had ever been reported in terrestrial volcanic ejecta. Furthermore, it was argued that based on current eruption models, volcanic eruptions were incapable of producing pressures sufficient to produce shock damage in silicate minerals (de Silva et al, 1988).

To support the volcanic hypothesis, it had to be demonstrated that (1) shock-induced microstructures do exist in terrestrial volcanic ejecta; (2) shock waves produced under volcanic conditions (i.e. high temperatures and relatively long durations of loading) can produce pressures sufficient to cause

shock microstructures to form; and (3) the distribution of shocked silicates across the KTB extends above and below the boundary clay, which would support the concept of shock events of extended duration.

In order to address some of these problems, a study was undertaken by researchers at Texas A&M University and Dartmouth College. The first phase of this study (Chapter 2 of this work) included petrographic analysis of pyroclastics and lava samples from Toba caldera (Toba ash), Long Valley caldera (Bishop Tuff), Yellowstone caldera (Lava Creek ash), Mt. St. Helens (Mt. St. Helens ash), and Tambora caldera (Tambora diorite xenolith and pyroclastics). These samples were compared petrographically with known impact samples from Lac Couture, Manson, and Clearwater Lakes West impact craters, tectonic features from various environments, experimentally shocked silicates, samples from nuclear tests, and KTB deposits from the Raton Basin and Gubbio.

The second phase (Chapter 3) of this study involved the analysis of deep-sea cores spanning the KTB at DSDP Site 527, Walvis Ridge, South Atlantic Ocean and ODP sites 689B and 690C from the Queen Maud Rise, Wedell Sea. The goal was to correlate the occurrence of shocked silicates and changes in trace-element geochemistry that might yield new insights into the environmental changes across the KTB, as well as the origin and duration of the observed effects.

The third phase (Chapter 4 and 5) of the study included a series of shock-recovery experiments on quartzite and granite at elevated temperature and longer durations of loading than achieved in previous lab experiments.

The recovered materials were analyzed by optical and transmission electron microscopy to determine the structural state of quartz and feldspar as a function of pressure, pre-shock temperature, and pulse duration. The resulting microstructures were compared to other similar experiments performed at other labs, and also to natural materials from impact craters, volcanics, and KTB materials.

The fourth and final phase (Chapter 6) of the study included a detailed review of the evidence supporting impact and volcanism, and the proposal of an endogenous mechanism for mass extinctions that is in accord with the geochemical, mineralogical, and geophysical evidence across the K/T transition.

# CHAPTER II

# HIGH-STRAIN-RATE PROCESSES AND SHOCK DEFORMATION IN EXPERIMENT AND NATURE

## Introduction

One of the basic tenets of the impact theory for the K/T extinctions is the uniqueness of shock-induced microstructures as indicators of impact events. The counterproposal that volcanism can also produce such microstructures (Officer and Drake, 1985) was unsupported by observations until Carter et al (1986) reported the occurrence of shock-induced microstructures in samples from several volcanic centers. The presence of such features in known volcanic rocks suggests that either our understanding of volcanic eruption mechanisms is flawed and very high shock pressures are generated during eruptions, or that the formation of the observed microstructures is not only a function of peak shock pressure and may be controlled by other factors as well.

In light of the observations of Carter et al (1986), it is necessary to review the state of knowledge about shock damage in natural materials, and impact and volcanism as high strain-rate processes. The microstructures observed in known impacts and volcanic materials will be compared to samples from two classic KTB localities, and also to a set of shock-recovery experiments completed recently at the NASA Johnson Space Center (Reimold, 1988).

## Shock-induced Microstructures in Silicates

Microstructures induced by natural and artificial shock deformation were studied extensively during the mid 1960's to early 1970's (e.g. symposium edited by French and Short, 1968; Stöffler, 1972, 1974) following the discovery by McIntyre (1962) of shock-induced planar features (planar elements, shock lamellae) at Clearwater Lakes, Quebec. This flurry of activity was stimulated initially by the Bucher-Dietz controversy concerning the impact versus volcanogenic origin of certain enigmatic structures ("cryptoexplosion structures"), and was accelerated subsequently by the Apollo program. Apart from studies related to cratering dynamics (e.g. Robertson and Grieve, 1977), studies of shock metamorphism subsided until the bolide theory was proposed by Alvarez et al (1980). Most of the previous work on shock-induced microstructures has been done on the common target materials quartz and feldspar, and this discussion will be restricted to these minerals alone. For a detailed discussion of shock effects in other silicate minerals, the reader is referred to Chao (1968) and Stöffler (1972).

Shock damage in silicates is a function of many material properties, including bulk density, porosity, modal mineral composition, compressibility and shock-impedance variations between adjacent minerals, variations in thermal conductivity between minerals, volatile content, and macrostructural features such as joints and faults (Chao, 1968). Deformation associated with shock waves in known meteor impact craters (e.g. Melosh, 1989) reveals four general types of deformation including: (1) brittle response characterized by fracturing, fragmentation, and brecciation, (2) plastic deformation including formation of planar features, shock mosaicism, and hydrodynamic bulk flow,

(3) phase transformations to high-pressure polymorphs such as coesite and stishovite, and (4) thermal dissociation, melting, and vaporization (Stöffler, 1972, 1974). The general progression of these features is from (1) to (4) as the intensity of shock increases; however any combination of these types of deformation may occur in a single specimen because of the heterogeneous nature of shock deformation. Similarly, the peak pressure at which specific types of deformation occur is a complex function of the material properties coupled with the character of the shock event.

The Brittle Response

Most silicates shocked in nature display some form of brittle response including fracturing, fragmentation, and brecciation. In general, these types of deformation occur at shock states below or just above the Hugoniot Elastic Limit (HEL), which is roughly 3.0 GPa for K-feldspar (Grady and Murri, 1976), 3.0 to 4.0 GPa for plagioclase (Ahrens et al, 1973), and 4.5 to 14.5 GPa for quartz (Duvall and Graham, 1977). The large range of HEL values in quartz results from the strong anisotropy of the response of quartz to shock loading (Melosh, 1989). Brittle failure also occurs during the rarifaction and release phases of a shock event as the target material decelerates and reverberates. This phase of the shock event also produces intense fragmentation and brecciation of the target rocks.

The character of fracturing tends to change from random fracture at low shock states, to more preferentially oriented sets as the HEL is exceeded. The preferred crystallographic orientations of these fracture sets supports the contention that planar fracture and crystallographic faulting are produced in

shear during the compression phase of a shock event. The presence of similar features in static laboratory experiments with large compressive stresses (Christie et al, 1964) also supports the contention that organized fracturing occurs during compression, and some of these fractures originate by some type of shear failure mechanism (Hörz, 1968; Gratz et al, 1988). The intensity of planar fracture increases with shock intensity at pressures below the HEL, and is progressively suppressed in favor of plastic flow as shock pressures increase well above the HEL. The orientations of planar fractures are usually parallel to planes of low Miller indices, and are considered generally to be indicative of mild shock (Stöffler, 1972).

## Plastic Deformations

As a material is shocked to states above the HEL, plastic flow occurs and eventually predominates over fracturing. This plastic deformation includes the development of planar features, shock mosaicism, kink bands, deformation bands, and mechanical twins. The two plastic flow structures of primary interest to this work are shock mosaicism and planar features. For a thorough discussion of the other modes of plastic deformation, the reader is referred to Stöffler (1972).

### Shock Mosaicism

Carter et al (1968) first described shock mosaicism in olivine in shock-recovery experiments to 100 GPa, and in stony meteorites. Subsequently, Stöffler (1972) presented a thorough discussion of this type of microstructure, emphasizing that shock mosaicism represents the most common manifestation

of plastic deformation by high strain rate processes. The shock mosaic structure, which may or may not be accompanied by other phenomena indicative of high strain rate plastic deformation, is expressed optically as small, irregular, highly-distorted domains. The size and degree of disorientation of the domains is evidenced by asterism and broadening of Laue spots using X-ray single crystal techniques or by streakiness and line broadening using Debye-Scherrer Techniques (Stöffler, 1972; Hörz and Quaide, 1972). Increasing asterism, streakiness, and spot and line broadening are indicative of increasing disorientation and reduction of domain size, both of which are generally correlative with increasing shock pressure, provided that recovery processes have not been operative (Stöffler, 1972; Hörz and Quaide, 1972). Since partial recovery due to subsequent annealing is common both in silicates deformed by high-stress experimental and natural shock (post-shock temperatures are very high; e.g. Boslough, 1988), it is unlikely that the mosaic structure provides a reliable indicator of shock intensity (Carter et al, 1990). However, this worker believes that mosaicism in quartz and feldspar is diagnostic of high strain rate deformation, and even when partially recovered, can be easily distinguished optically from other subgrain-forming processes which occur during creep of natural rocks (e.g. Carter, 1976). For an alternate view, see Sharpton and Schuraytz (1989).

## Planar Features

Since their initial discovery at the Clearwater Lakes, Quebec impactite (McIntyre, 1962), the nature, properties and orientations of shock-induced planar features (planar elements, shock lamellae) have been described and discussed by many workers (e.g. several papers in French and

Short, 1968; Stöffler, 1972, 1974; Christie and Ardell, 1976). Like tectonic deformation or Böhm lamellae, planar features are commonly partially healed or annealed, and are frequently decorated with minute bubbles, voids or inclusions. Unlike tectonic lamellae, they are typically straight, sharp, continuous, and possess optical signatures that are very different and distinctive (e.g. Carter, 1968). TEM studies show that the planar features consist of thin zones of glass, separated by nearly dislocation-free quartz (Christie and Ardell, 1976; Gratz et al., 1988), along which very small shear displacements have taken place (< 0.1 micron, Carter, 1968, his figure 7). In sharp contrast, tectonic lamellae are composed primarily of dislocation tangles or minute elongate subgrains (e.g. White, 1973). Planar features commonly occur in two or more intersecting sets whose number, densities and orientations are an increasing function of peak shock pressure (Hörz, 1968; Grieve and Robertson, 1976).

Planar features can be divided into four classes based on their morphology, including (1) non-decorated fine optical discontinuities that are barely resolvable optically (except in phase-contrast illumination) but easily resolved by transmission electron microscopy (TEM), (2) homogeneous lamellae which differ slightly in orientation from the host crystal and show decreased refractive index, (3) lamellae filled with diaplectic glass and high pressure polymorphs, and (4) decorated elements containing vesicles or inclusions of fluid and gas caused either by thermal annealing or by emplacement of gas into the shocked grains during the shock event (Engelhardt and Bertsch, 1969). Planar features are usually oriented along densely-packed lattice planes with the shortest Bravais vectors (figure 2-1D) and are spaced 2 to 10 microns apart. They form at pressures above the HEL in

Figure 2-1: Crystallography of α–quartz. A. Crystal form showing the typical *r* rhombohedra, *m* first-order prism, and *c* and *a* directions. B. Cut away diagram showing the *a* and *c* directions, the *m*, *r*, *c*, *π*, and ω planes. C. Equal area projection (lower hemisphere) showing crystallographic orientation of poles to some crystal forms in quartz (right-handed). D. List of common forms in quartz along with their Miller indices and the angle between *c* and the form.

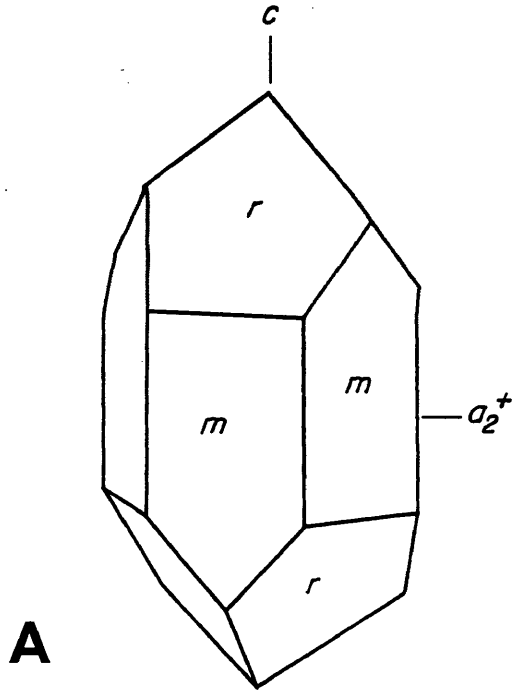


A

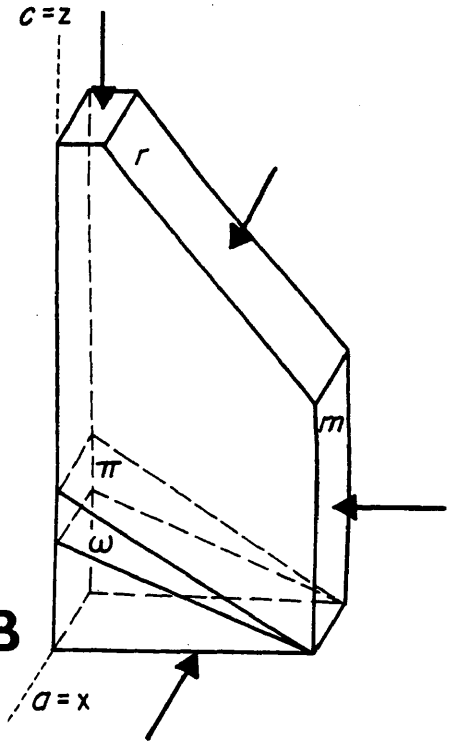


B

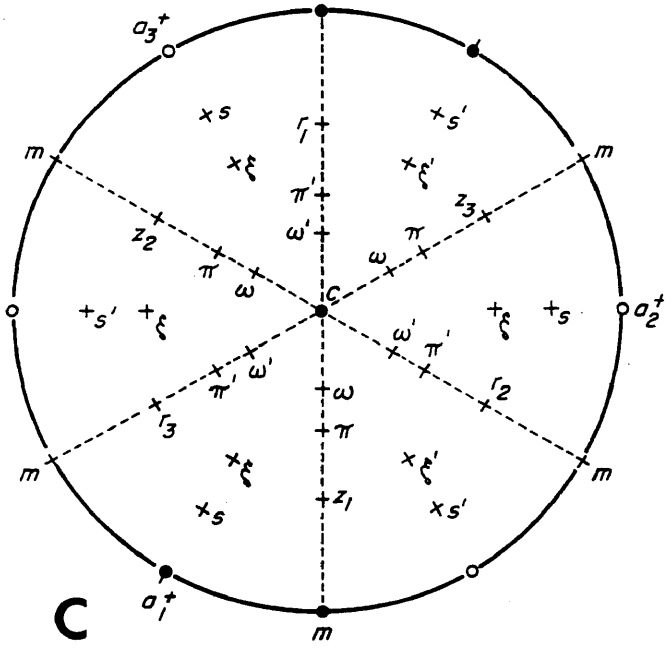


C

| Quartz Crystal Forms | | | C∧⊥ Form |
|---|---|---|---|
| c | {0001} | basal pinacoid | 0° |
| ω<br>ω' | {10$\bar{1}$3}<br>{01$\bar{1}$3} | rhombohedra | 22°57' |
| π<br>π' | {10$\bar{1}$2}<br>{01$\bar{1}$2} | rhombohedra | 32°25' |
| r<br>z | {10$\bar{1}$1}<br>{01$\bar{1}$1} | unit rhombohedra | 51°47' |
| s {11$\bar{2}$1} s'{2$\bar{1}\bar{1}$1}<br>ξ {11$\bar{2}$2} ξ'{2$\bar{1}\bar{1}$2} | | trigonal bipyramids | 65°33'<br>47°44' |
| m | {10$\bar{1}$0} | first order prism | 90° |
| a | {11$\bar{2}$0} | second order prism | 90° |

D

the two-phase region of the Hugoniot, and increase in number and orientation as a function of increasing shock pressure. In quartz, it is observed that the ω features are normally the first planar features to form at 15 to 17 GPa, followed by $\pi$ features at 20 GPa. Above 20 GPa, the $\pi$ features are the most common type of planar feature, along with other forms such as *s*, *a* , m, $\{11\bar{2}2\}$, $\{21\bar{3}1\}$, and $\{51\bar{6}1\}$.

The formation of planar features can be explained by several mechanisms. Among these mechanisms are shear failure and subsequent frictional heating to produce silicate melt along the failure surfaces (Grady, 1980), and collapse of quartz in compression to form high-pressure polymorphs followed by reversion of these polymorphs to diaplectic glass upon release of the shock wave. The first detailed set of shock-recovery experiments on oriented single-crystal quartz (Hörz, 1968) revealed that the general progression from the ω form, to $\pi$ form and other planar features is basically independent of the shock propagation direction. The results for crystals shocked in the *c*, *m*, and *r* directions (figure 2-1B) show that the ω planar features form at about 16 GPa in the *c* experiment, followed by the $\pi$ form at pressures above 20 GPa. The formation of the ω features occurs above 20 GPa in the other two orientations, suggesting that the features form in orientations where there is a net shear stress applied during the shock. The lower onset pressures for ω features in the *c* experiment indicates that the primary control on the formation of the planar features is the crystallography of the quartz. Hörz also observed some basal *c* planar features in the experiments which were most abundant in the *r* (ca. 9%) and the c (ca. 5%) experiments at about 26.5 GPa. Müller and Defourneaux (1968) also performed

recovery experiments on single crystal quartz shocked from 9.5 to 33 GPa in the *c* direction and obtained results similar to Hörz (1968).

Radiance measurements in shocked silica fitted to a gray-body temperature profile by Schmitt and Ahrens (1989) indicate that temperatures during shock may be sufficiently high to be explained by frictional heating and melting which supports the shear model. However, the observations of very small (< 0.1 micron) shear offsets along the features (Carter, 1968, his figure 7; Christie and Ardell, 1976, their figure 4), and that strongly-shocked quartz retains its rigidity in compression (J.M. Brown, personal communication, 1989) suggest that the model of heterogeneous solid-state collapse may be the more viable of the two.

A third mechanism for formation of planar features involving release melting after passage of the shock wave has been proposed by Gratz et al (1988). Their experiments on single crystal quartz shocked to 12 and 24 GPa in the *a* direction (i.e. perdendicular to *c* and *m* ) reveal that most planar features form in the *c* and $\pi$ directions. Gratz et al (1988) argue that the orientations of the features suggests that they form in tension during the release phase of the shock. Their results are at odds with the detailed and much more thorough work of Hörz (1968). The presence of high-pressure polymorphs in the planar features and in glassy areas of naturally-shocked materials (e.g. Kieffer et al, 1976) also tends to rule out the contention of Gratz et al. Their orientation data for planar features appear to be biased by a single thin section orientation used in their study, which was cut in the *a* plane (i.e. perdendicular to the shock direction).

Phase Transformations and Isotropization

As silicates, and particularly quartz, are shocked to pressures significantly above the HEL, the crystal structure collapses to more dense polymorphs such as coesite or stishovite. The formation of high-pressure phases should occur at all pressures above the lower stability limit for these phases (e.g. 3.0 GPa for coesite and 7.5 GPa for stishovite, Kieffer, 1971; Stöffler, 1971), although preservation of these phases becomes problematic at high shock states due to the high residual temperatures produced by strong shock waves (e.g. Boslough, 1988). Work on known impact target rocks reveals that the strong residual temperature problem does prevent the preservation of both stishovite and coesite at pressures above about 30 GPa (Kieffer et al, 1976). It also appears that the high-pressure polymorphs tend to form at the intersection of multiple sets of planar features and inside individual planar features, supporting the notion that the phase transformations are somehow related to the formation of glass or melt in the planar features.

It is also observed that the degree of isotropization and lowering of refractive index increases with shock pressure from the HEL up to about 35 GPa where total isotropization occurs in quartz (e.g. Grothues et al, 1989). This gradual increase in isotropization, which is also observed in static experiments in the diamond anvil cell (R. Jeanloz, personal communication, 1989) is believed to reflect the progressive conversion to short-range-order silicates with higher shock state, which may be related to the volume of quartz that has tried to convert to the high-pressure state. The progressive increase in the numbers and volume of planar features formed is directly related to this isotropization process as well.

## Melting and Thermal Dissociation

In addition to fracturing and brecciation, release from high shock states where residual temperatures occur can lead to melting and thermal dissociation of the target rocks. In general, the degree of melting observed increases with shock pressure, and manifests itself initially on fractures and in voids, and finally as massive melting. If shock pressures are sufficiently high (i.e. >50 GPa), the target rock may be melted during the compressional phase of the shock event as well, and subsequently vaporized upon release.

## Other Shock Microstructures

In addition to those plastic deformations not addressed above such as twinning and kink bands, it is important to note the distinction between *c* basal planar features and basal deformation lamellae in quartz. Basal quartz deformation lamellae are quite distinct from planar features, and are produced by long-range stresses from dislocation tangles and mixed arrays of dislocations (Christie et al, 1964; McLaren et al, 1967; Christie and Ardell, 1976). The optical signature of these features, which is quite different from planar features, is shown by Carter (1968; his figure 9C and 9D) in a single grain containing both types of feature. Carter (1965) first observed basal planar features in shattercones in the Witwatersrand quartzite, and also at Barringer Crater and Clearwater Lakes, Quebec. Later, Grieve and Robertson (1976) classified these features as type-A basal planar features with a mean onset stress around 9 GPa. Stöffler (1972) incorrectly classifies all basal structures as fractures. Provided that no alteration, post-event annealing, or fluid injection has occurred after deformation, the three types of basal quartz

structures are easily distinquished. However, once these processes have acted on a sample, all the features appear optically as planar arrays of inclusions or voids, which makes a distinction very difficult.

## Impact as a High-Strain-Rate Process

The role of planetesimal collisions and impacts in planetary formation and accretion has long been recognized (e.g. Shoemaker, 1977). More recently, Grieve (1982) has documented approximately one hundred terrestrial impact structures ranging in diameter from 140 km to less than 100 meters. These impact structures, which are all located on continents (Grieve, 1982, his figure 1 and table 2) attest to the importance of cratering as a terrestrial phenomenon. Among these craters, only three predate the Phanerozoic, with two of these (Vredefort and Sudbury, both 140 km) being the largest structures preserved in the crustal record. Since the publication of Grieve's 1982 list of structures, only two documented structures have been reported from a continental shelf environment in Nova Scotia (Jansa et al, 1989) and from the Cretaceous shelf in Texas (V. L. Sharpton, personal communication, 1989). In general, the young age of ocean floor makes its use as a long-term impact record impossible. However, Grieve (1982) used the available cratering data to estimate a size versus frequency-of-impact distribution for Phanerozoic impact structures. The resulting relationship suggests that for crater sizes greater than about 23 km, impacts are distributed as $N_C \sim D^{-2}$ where $N_C$ is the cumulative distribution and D is crater size. For crater sizes less than 23 km, the relationship breaks down, probably due to a combination of craters lost to erosion, and those that have been modified so severely as to be unrecognizable. In a similar fashion, Shoemaker et al (1979) estimated the

recurrence interval for impacts of objects of various sizes with earth. The data, which ranged from micrometeorite data from the space shuttle, to counts of identifiable earth-crossing asteroids, revealed that objects capable of producing Meteor Crater (100 meter object) should strike the earth about every 10,000 years, while objects capable of producing the Sudbury or Vredefort structures (10 km object) should strike the earth about every 100 Ma. Despite the suggestion that cratering may be periodic (Alvarez, 1989), Grieve et al (1985) have emphasized that the terrestrial cratering record is insufficient to support such an argument.

## Crater Evolution

The evolution of impact structures is a complex process. This is especially true as it pertains to the large-scale morphology and the micro-structures observed in the target rocks. Although the initial compression and excavation phases described in chapter 1 of this work are quite spectacular, they are only the brief first step in a lengthy, multistage process which includes compression and excavation, subsequent thermal metamorphism, and modification by tectonic rebound and erosion (Melosh, 1989).

Most of the energy of crater evolution is expended in the compression and excavation phases. After the impacting object strikes, a large bowl-shaped transient crater remains. The distribution of shock deformation caused by the impact is a strong function of the composition, size, velocity, and angle of incidence of the impactor, along with the composition and structural morphology of the target area. In addition to the transient crater and the shock deformation, the shock wave leaves behind a large amount of heat from

dissipative processes, which leaves the target rocks at elevated temperatures. Experimental data suggest that even weak shock in the 20 GPa range can produce residual temperatures up to 500°C (Boslough, 1988).

The presence of excess thermal energy in the target rocks leads to an episode of thermal metamorphism. The larger the impacting object is, the larger the spatial and temporal extent of the thermal event will be. During this subsequent thermal metamorphism, strains imparted during the compression and excavation phases are recovered through healing of fractures and annealing of plastic deformation features such as mosaicism and planar features. Fluids present in the target rocks will be quite mobile and chemically active during this phase, leading to bubble trails in crystals and hydrothermal alteration of the target rocks.

Following the thermal metamorphic phase, which is relatively short in duration, the long period of crater modification becomes important. In the case of small craters such as Meteor Crater, the transient crater is supported by the strength of the lithosphere so that only erosion is significant as a modifying agent. In the case of larger structures that the lithosphere cannot support, a phase of tectonic rebound occurs, which produces a central uplift. In the case of very large structures such as the Ries Crater, Germany, the crustal fracturing produced by the impact event leads to larger-scale tectonic adjustments, resulting in the development of a multi-ring basin structure. The significance of this phase of deformation is that the greatest amount of tectonic deformation again occurs near the central uplift region of the crater where most shock microstructures of interest occur. The large tectonic strains achieved during the modification phase can alter significantly the observed

microstructures. As the tectonic rebound slows down, erosion becomes the dominant modifying agent until the original crater morphology is completely lost.

Shock Microstructures and Impact Rocks

Considering the primary role that impact craters have played in understanding shock deformation, a brief discussion of the relationship between impact structures and shock-induced microstructures is appropriate. Early work on the Ries Crater, Germany (Engelhardt and Stöffler, 1968) and Canadian craters (Dence, 1968) revealed a clear relationship between the intensity of deformation and proximity to the center of a crater. This relationship was confirmed by hypervelocity impact studies in the laboratory (Gault et al, 1968). In general, the central uplift of most structures shows the strongest deformation with intense melting and dissociation of nearly all minerals. Further from the central uplift but still within the crater, intense deformation including partial melting, formation of planar features, and intense mosaicism predominates. Further from ground zero and at greater depths, the level of deformation decreases until only fracturing of the target rocks is observed (figure 2-2). It is important to note that the volume of material that is shocked to states above the HEL is quite small compared to the total volume of material that is affected by an impact event. In addition, very little of this material is ejected from the crater, which explains why distal deposits from impacts are often difficult to recognize. In fact, the largest portion of distal deposits from impacts are probably a mixture of spall from

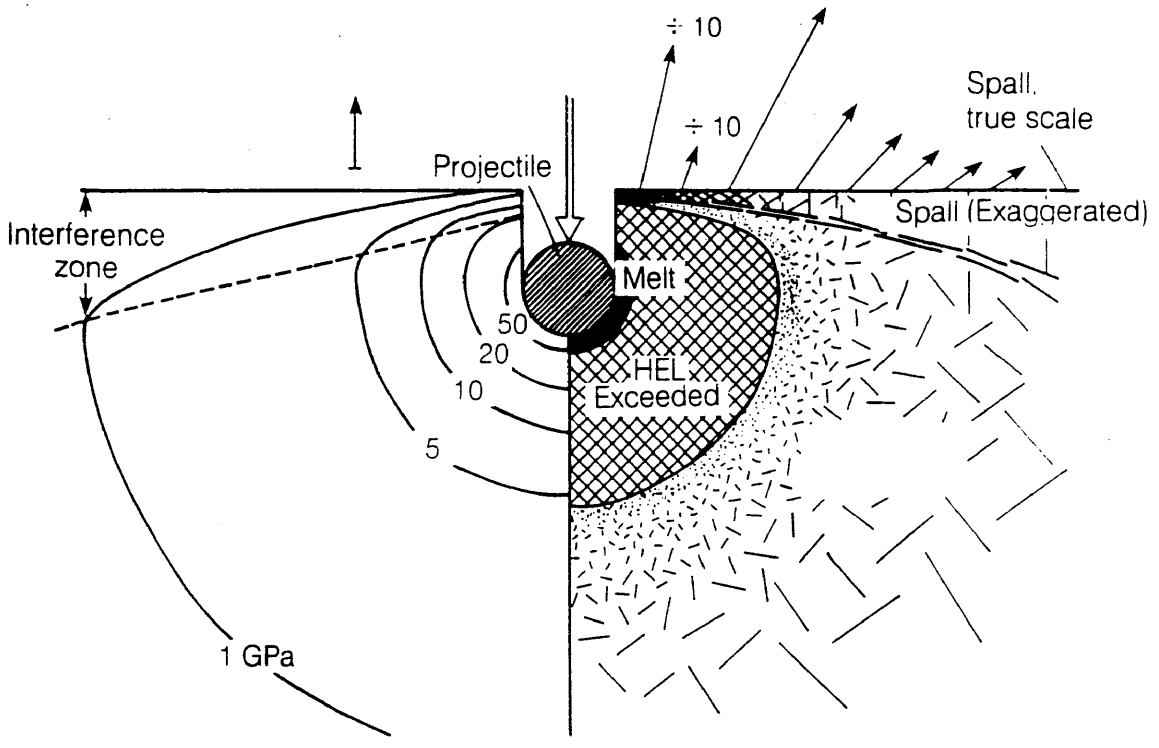


Figure 2-2: Illustration of the intensity of shock deformation and spalling during the compressional phase of an impact event. The projectile velocity is 10 km/sec. which produces a throw velocity on the free surface of the target of 200 m/sec. Below the target, which is assumed to be a homogeneous, isotropic silicate material, the pressure contours are roughly hemispherical and grade outward from vaporized and melted target, to plastic shock deformation above the HEL, and finally to shock states below the HEL dominated by fracturing and crushing. Tension waves produced by rarifaction off the free surface produce a spall sheet which is expelled as high-velocity ejecta. Diagram after Melosh (1989).

surface effects of the event, along with vaporized impactor and vaporized and melted target rock that is jetted out of the crater during the excavation phase. This suggests that the diagnostic feature for identifying distal impact deposits is the presence of tektites and microtektites, along with evidence of shock-induced microstructures in silicate minerals.

At the same time that crater studies were underway, samples subjected to nuclear tests were also being studied. The results of these studies (e.g. Short, 1968a; Cummings, 1968; and Borg, 1972) supported the data from impact craters, and showed that the level of shock damage decreased as the shock wave attenuated radially from ground zero.

## Explosive Volcanism as a High-Strain-Rate Process

The geologic and environmental impact of explosive volcanism has been brought to light by the recent eruptions of volcanos such as Mount St. Helens, El Chichon, Nevada Del Ruis, and Galunggung (Allard, 1983). These eruptions, along with many other devastating blasts during historic time including Mt. Vesuvius in 79 A.D. (~2000 dead; Barberi et al, 1983), Tambora in 1815 (~92,000 dead; Zen, 1983), Krakatau in 1883 (~36,000 dead; Zen, 1983), and Mt. Pelee in 1902 (~30,000 dead, Westercamp, 1983) emphasize strongly the need for a better understanding of the magmatic processes that lead to violent explosive eruptions. Although very destructive and costly in human terms, these historic eruptions represent the lower end of the energy and size range for explosive volcanic eruptions (Smith and Braile, 1984, see figure 2-3). Large calderas such as Long Valley, Valles, and Yellowstone have produced eruptions about one order of magnitude larger than Tambora, which was the

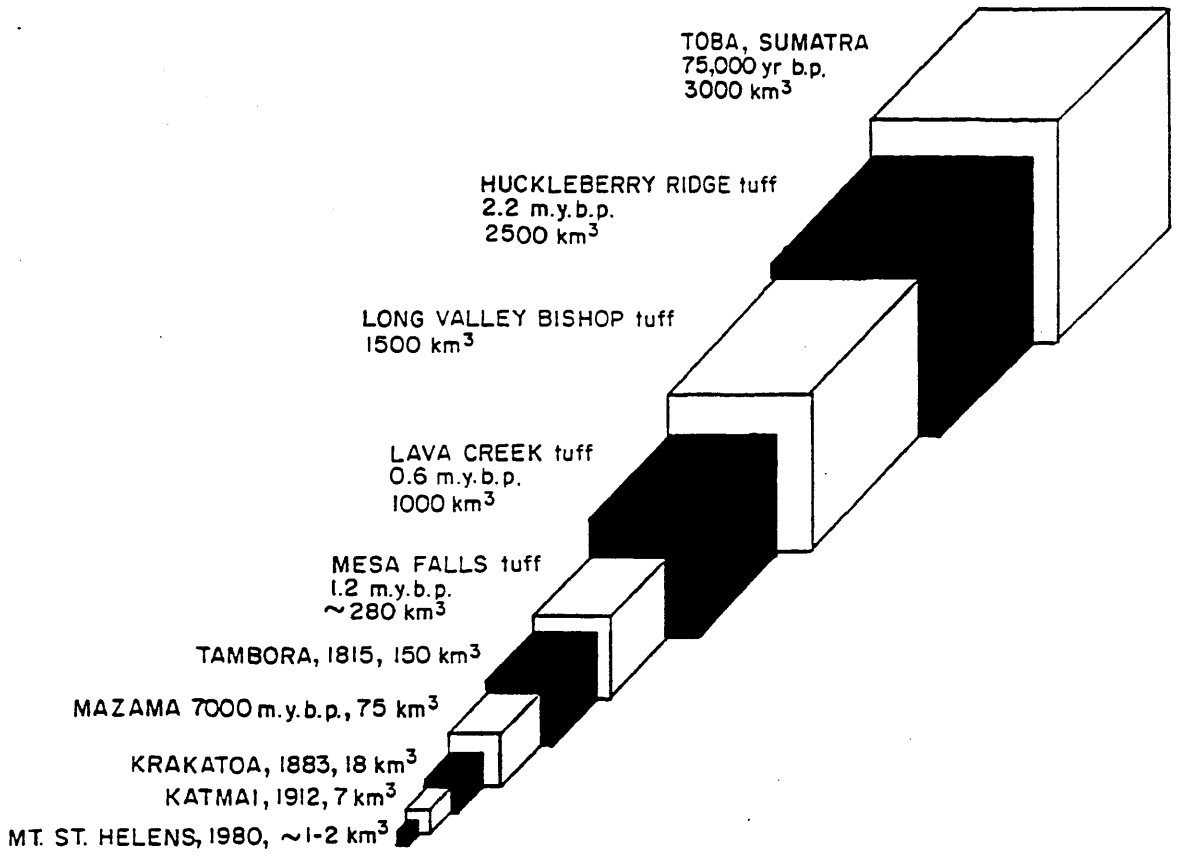


Figure 2-3: Relative sizes of explosive volcanic eruptions of known age in terms of their dense-rock-equivalent (DRE) eruptive volume.

largest eruption of the last 200 years with a total eruptive volume of about 150 $km^3$ Dense Rock Equivalent (DRE), and extremely large discharge rates (Sigurdsson and Carey, 1987). In comparison, the greatest known volcanic explosion at Toba, Sumatra, which occurred 75,000 years ago, had a volume of about 3,000 $km^3$ DRE, or nearly 20 times large than Tambora, 170 times larger than Krakatau, and more than 1000 times larger than Mt. St. Helens (Ninkovitch et al, 1978).

Shock-Induced Microstructures in Volcanic Rocks

Before Officer and Drake (1985) and Officer et al (1987) suggested a volcanic source for the KTB shocked quartz, no challenge had ever been issued to the concept of shock deformation as a unique indicator of meteor impact. Some workers (e.g. Schreyer, 1983) have argued that shock-induced microstructures are only indicative of high strain rates, and are not process-specific, although no reports of shock-induced microstructures from bonafide non-impact sources had been documented.

In a pioneering study, Carter et al (1986) searched for microstructural evidence of shock deformation in tephra deposits, ignimbrites, and deep-sea ash cores from the Toba eruption of 75,000 yr b.p. (figure 2-4). In their optical study of over 2500 grains of quartz and feldspar, they found evidence for widespread development of the shock mosaic structure, commonly partially recovered (Figure 2-5). Although some of the observed mosaicism in the Toba feldspars may be due to chemical zonation (Sharpton and Schuraytz, 1989) or disequilibrium crystallization (e.g. Lofgren, 1980), the presence of the mosaic structure in quartz still supports the idea of high pressures or rates of loading

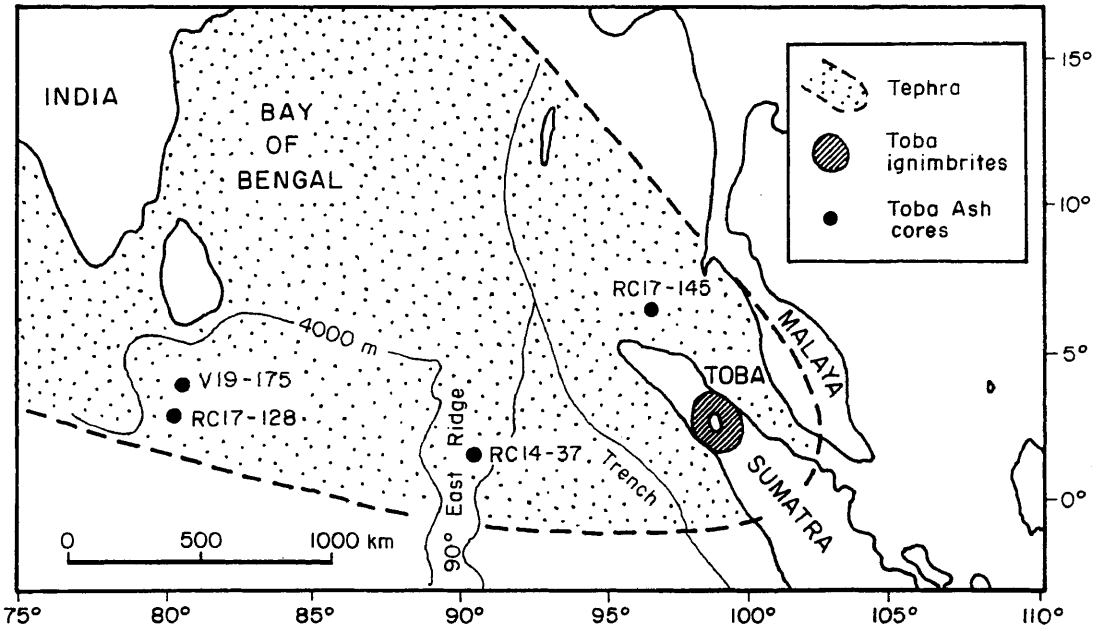


Figure 2-4: Regional map of the Northeast Indian Ocean showing the location of samples of Toba ash from deep sea cores, along with the extent of deposition of Toba ashes in relation to the caldera itself. Diagram from Carter and Officer, 1989)

in the Toba magmatic system either during or immediately prior to the eruption. Planar features were also observed in quartz and feldspar in the Toba ignimbrite samples (figure 2-6A & B), but only rarely (24 grains, <<1%), and only in single sets. Additional evidence of high-strain-rate deformation at Toba occurs in strongly kinked biotites (figure 2-6C & D). although these features are not diagnostic of shock.

Subsequent examination of volcanic samples from Long Valley caldera (Bishop Tuff), Mt. St. Helens (ash from the May 18, 1980 eruption), and Yellowstone caldera (Lava Creek ash) revealed a similar occurrence of the shock mosaic structure, and scarce single sets of planar features as at Toba. Carter et al (1986) argued that the paucity and presence of only single sets of planar features might be due to the high ambient temperatures (~750°C) of rocks in the magmatic system during eruption with quartz in the ß-stability field. Another possibility is that the character of high-strain-rate events in magmatic systems is quite different from impact, and favors the dominance of the mosaic structure and rare single sets of planar features. Based on data from impact rocks, shock events at the low pressure end of the plastic deformation regime (i.e. 10-15 GPa) coupled with high ambient temperatures in volcanic systems might be a viable explanation for the microstructures observed at Toba and the other volcanic centers.

The results from Toba and other volcanic centers discussed above were sufficiently encouraging to support further investigations. Recently, samples of ignimbrite and a diorite xenolith from the 1815 Tambora eruption on the island of Sumbawa were studied optically in search of evidence of high-strain-rate deformation. Although the fresh eruptive material did not show any

Figure 2-5: Optical micrographs showing the shock mosaic structure in quartz and plagioclase of Toba ignimbrites. All scale bars are in millimeters and all photos are in crossed nicols. A. Mosaic structure in quartz grain in section T-94B. B. Strong mosaicism and incipient recrystallization (small white grains in the center) in plagioclase in specimen 10.680. C and D. Partially-recovered mosaic structure in plagioclase in specimens T-65 and T-94B, respectively.

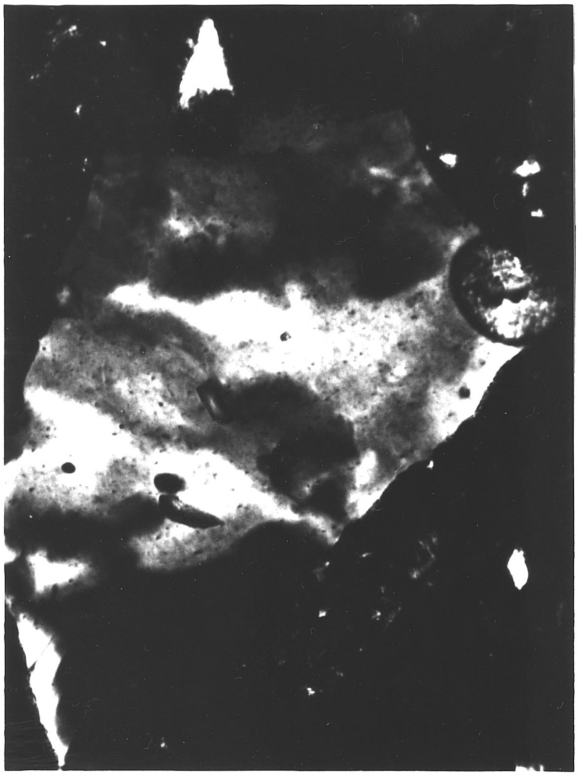

A

230 µm

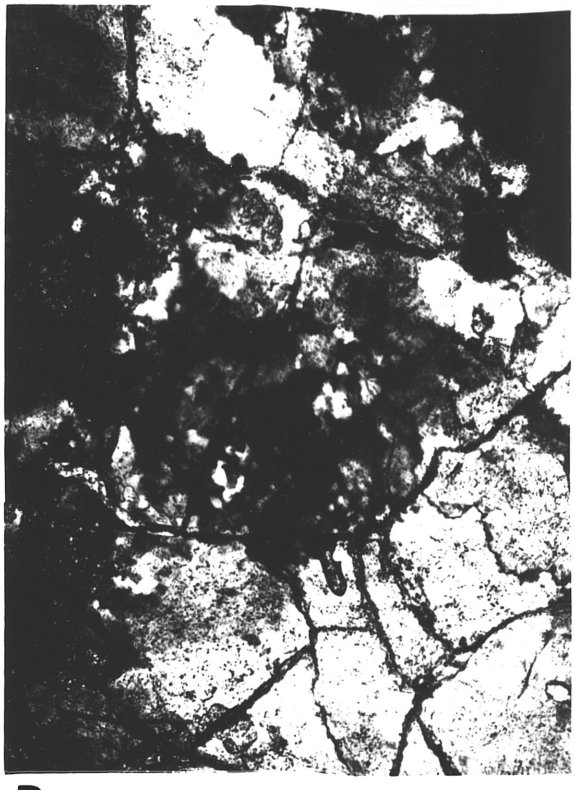

B

195 µm

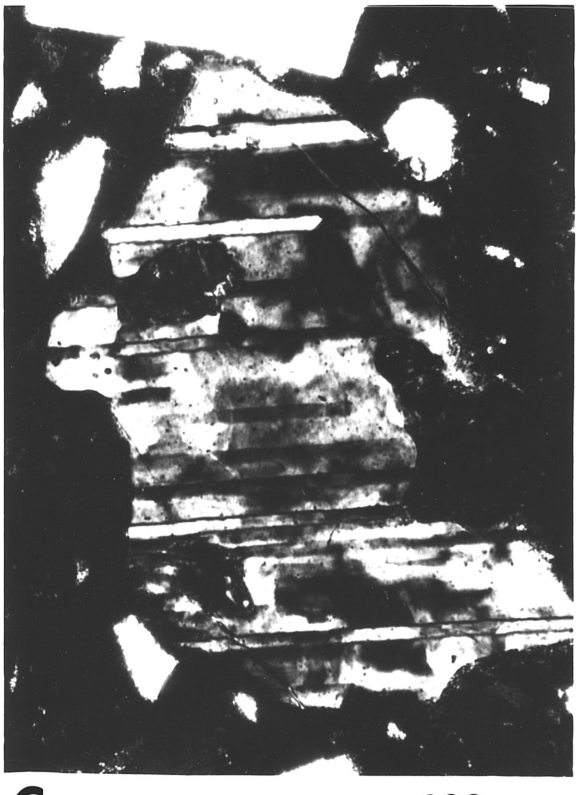

C

230 µm

D

280 µm

Figure 2-6: Optical micrographs of shock-induced microstructures in Toba ignimbrites. All scale bars are in millimeters. A and B. Planar features in quartz grains in specimens T-32 (NE trending features) and T-92 (N-S trending features) respectively; crossed nicols. C and D. Irregularly and highly kinked and fragmented biotite grains in T-94B and 10.680 respectively; plane polarized light.

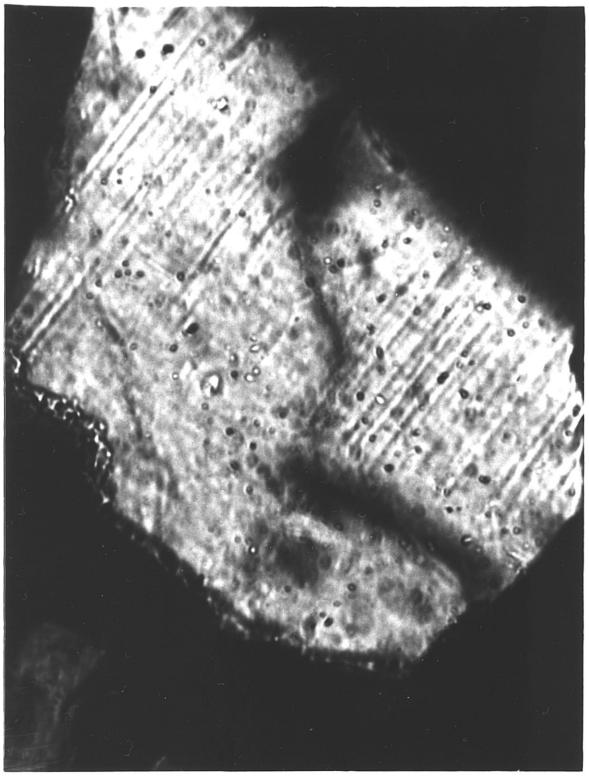

A

120 µm

B

200 µm

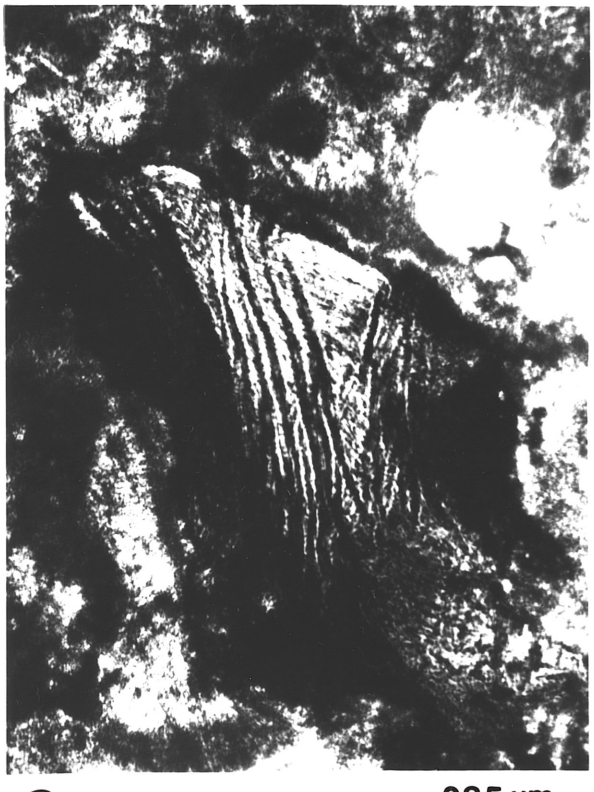

C

285 µm

D

360µm

evidence of high-strain-rate deformation, petrographic analysis of the diorite xenolith revealed the presence of planar features, the shock mosaic structure, and reduced birefringence in clinopyroxene (figure 2-7B, C, D). Additionally, unusual strings of fluid inclusions in plagioclase feldspar (figure 2-7A) may represent annealed planar features, although this is not definitive.

Universal-stage analysis of the clinopyroxene revealed that the planar features are oriented from 0° to 14° from the alpha direction with a mean orientation of 7° from alpha. This {h0l} orientation is identical to that reported for planar features in clinopyroxene in the breccias of the Ries crater in Germany (Stöffler, 1972), and is indicative of impact-equivalent shock pressures approaching 20 GPa. The {h0l} orientation also rules out the possibility that these features are some type of exsolution lamellae or other feature. Furthermore, the presence of the mosaic structure and reduced birefringence in the same region of the sample argue in favor of a high-strain-rate origin for the features in the clinopyroxene.

TEM and diffraction analysis of the clinopyroxene from Tambora (figure 2-8) confirm the presence of the high-strain-rate damage, including the shock mosaic structure (figure 2-8B), significant distortional strains and fracturing (figure 2-8C), and lamellar features oriented approximately parallel to {101}. These submicrostructures are in sharp contrast to undeformed clinopyroxene from other areas of the same sample (figure 2-8D) and emphasize the heterogeneity of high-strain-rate deformation, especially at the TEM scale.

Figure 2-7: Optical micrographs of deformation structures in a diorite xenolith (TB-199) from the 1815 eruption of Tambora volcano on the island of Sumbawa, Indonesia. A. Dense bubble trails in plagioclase indicative of deformation followed by an annealing phase. B. Shock mosaic structure and fracturing in clinopyroxene. C. Planar features with orientation {h0l} in clinopyroxene; plane polarized light. The features (NE-trending) are very fine (~1 micron in width) with spacing of about 5 microns. D. Clinopyroxene showing planar features, shock mosaic structures, and fracturing in crossed nicols.

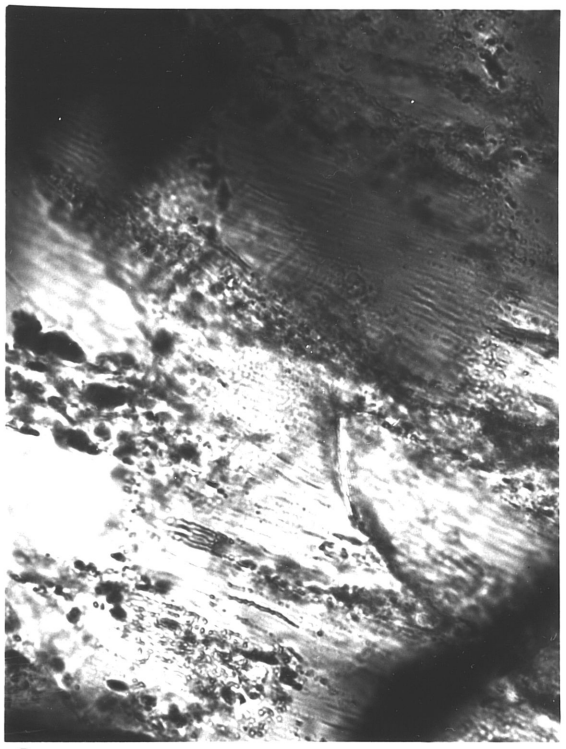

A

45 µm

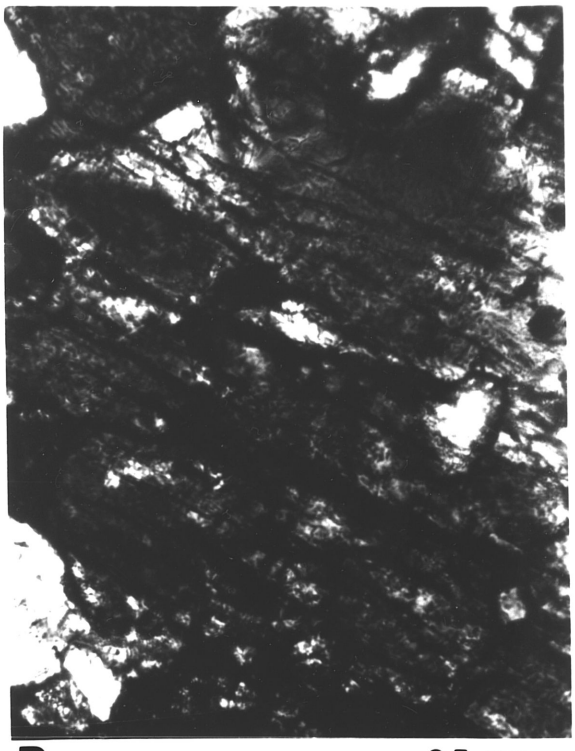

B

25 µm

C

65 µm

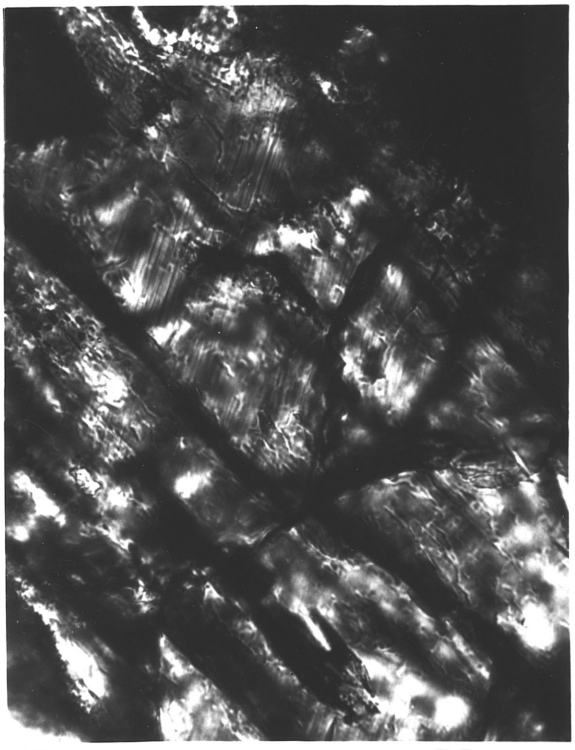

D

55 µm

Figure 2-8: Transmission electron micrographs of submicrostructures in clinopyroxene from diorite xenolith TB-199 from the 1815 eruption of Tambora. A. Planar defects that may contain small crystals of a second phase and are possibly related to the optical lamellae. B. Fracturing and distortional strain possibly reflecting subtle mosaicism; note the spot broadening in the diffraction pattern. C. Small twins in mildly-deformed host clinopyroxene. D. Area of undeformed clinopyroxene showing dislocations and bubble trails. All scale bars are 0.5 microns.

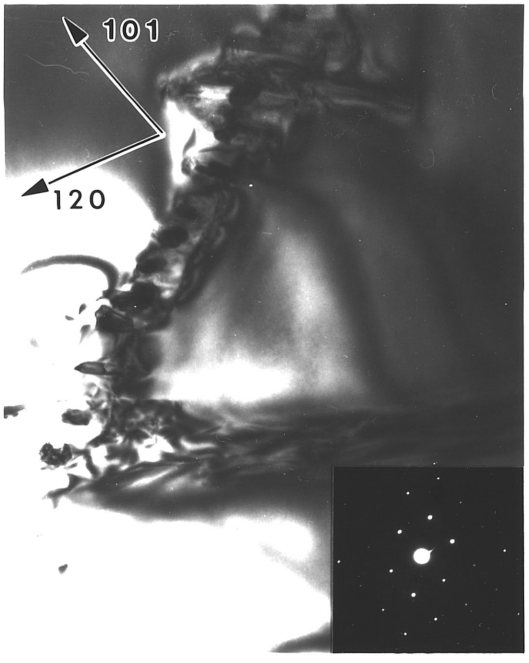


A

0.5μm


B

0.5μm

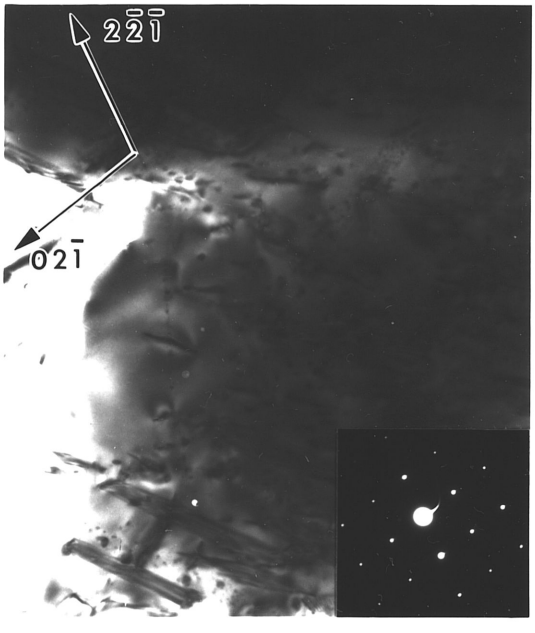


C

0.5μm

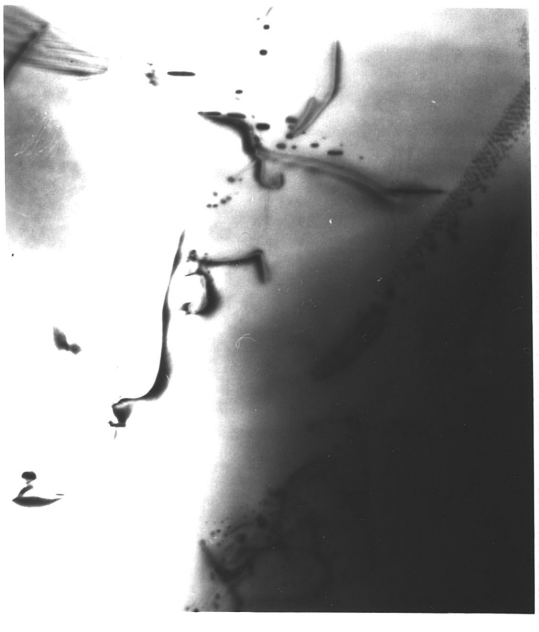

D

0.5μm

## Comparison of Volcanic and Other High-Strain-Rate Microstructures

The differences and similarities between microstructures in the Toba and other volcanics, those from impactites and man-made explosions, and tectonites are easily recognized based on the criteria defined at the beginning of this chapter. Like shock-induced planar features from known impact sites (figure 2-9A), the Toba features in quartz (figure 2-9C) and Bishop Tuff features in plagioclase (figure 2-9D) are straight, sharp, continuous, and develop along specific crystallographic planes. This is in stark contrast to tectonic (Böhm) lamellae in quartz from the Dry Creek Ridge Anticline in Montana (figure 2-9B) and other tectonites which do not fit the criteria above.

Likewise, the partially recovered shock mosaic structure observed in plagioclase from the Toba ignimbrites (figure 2-10C) is very similar to mosaicism observed in K-feldspars shocked to 15 GPa in a nuclear test (figure 2-10A), plagioclase shocked to 15 GPa in a chemical implosion experiment (figure 2-10C), and K-feldspar from the Clearwater Lakes impactite (figure 2-10D). All of these features are indicative of intense plastic deformation in the compressed state and bear no resemblance to microstructures produced by subgrain formation and recrystallization under tectonic conditions (Carter et al, 1990).

## Mechanisms For Generating Shock Waves in Volcanics

The presence of "shocked" minerals in such a wide range of explosive volcanics supports the theory that some silicic volcanic eruptions may occur occasionally by thermally-driven detonation as opposed to decompression and

Figure 2-9: Planar features and tectonic lamellae in quartz and feldspar. Scale bars are in mm. A. Planar features in quartz grain in Lac Couture, Quebec impactite. B. Tectonic (Böhm) lamellae in quartz grain from the Dry Creek Ridge anticline, Montana. C. Planar features in quartz fragment in Toba, Sumatra ignimbrite. D. Planar features in plagioclase crystal from the Bishop Tuff.

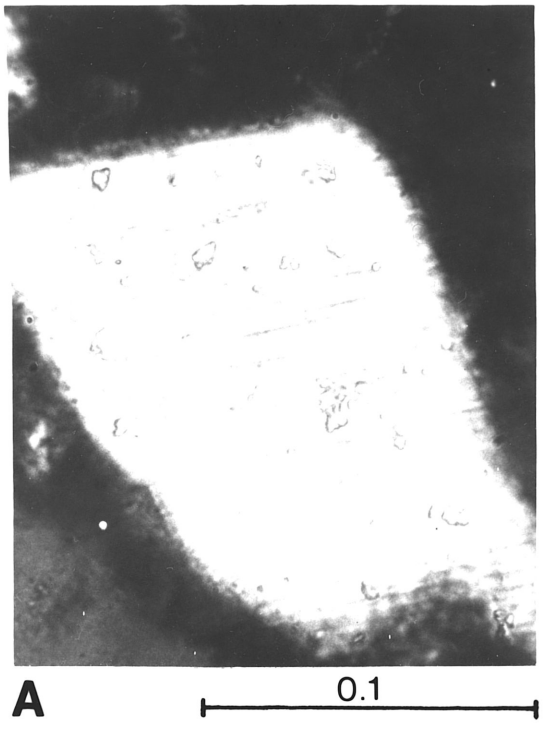
A
0.1


B
0.1


C
0.5


D
0.1

Figure 2-10: Shock mosaic structure in feldspar. Scale bars are in mm. A. K-feldspar grain in granodiorite shocked to 15 GPa in the Sedan nuclear test (Short, 1968a). B. Plagioclase crystal shocked to 15 GPa in a chemical implosion test (Short, 1968b). C. Partially recovered shock mosaic structure in the plagioclase grain from the Toba ignimbrite sample 10.680. D. K-feldspar grain from Clearwater Lakes impactite.


A
0.1


B
0.5

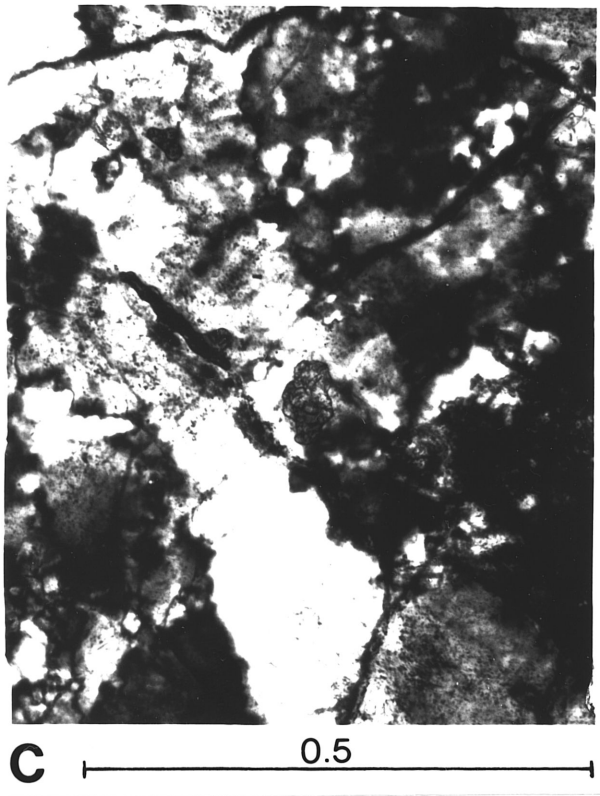
C
0.5


D
0.5

devolatization following the failure of a volcanic edifice (e.g. Rice, 1985, 1988). The mechanism for generating detonation explosions in a magmatic environment is poorly understood; studies of magma-water interactions leading to hydromagmatic explosions suggest that overpressures can exceed 350 bars with rise times of less than one second in laboratory experiments (Sheridan and Wohletz, 1983; Wohletz, 1986). Conventional volcanologic and rock mechanics experience suggests that magmatic overpressures greater than confining pressure are not attainable as tensile failure of the volcanic edifice will limit the internal pressure. Therefore, shock waves cannot be produced by sudden pressure drops during venting of gases, leaving the general theory of thermally-driven confined detonation as the only viable alternative for the generation of high shock pressures under relatively unusual circumstances.

Several mechanisms have been proposed for rapid development of overpressures in magmatic systems (Nelson, 1981; Sheridan and Wohletz, 1983; Blake, 1984; Wohletz and McQueen, 1984; Wohletz, 1986; Bardintzeff and Bonin, 1987; and Boslough, 1989), but most of these models indicate that overpressures do not develop rapidly enough to produce classic shock-induced microstructures. Keeping this apparent restriction on eruption dynamics in mind, several possible mechanisms for generation of internal volcanic shock waves may be viable and need further investigation.

Quench Supersaturation

Rice (1985, 1988) argued that production of a shock wave in a magmatic setting by internal detonation requires a very specific set of conditions,

including a closed system where dissolved volatiles reach a critical supersaturation, triggering the eruption process. Once nucleation and exsolution begins, a pressure front propagates exceedingly rapidly across the magma chamber, increasing in magnitude as it triggers further exsolution of volatiles and crystallization of silicates. Based on seismic data, the geometry, size, and energetics of the Mt. St. Helens May 18, 1980 explosion, and drawing on the extensive mining, explosives, and other industrial experience, Rice (1985, 1988) has proposed generation of peak shock pressures greater than 50 GPa. The sporadic presence of shocked plagioclase in the Mt. St. Helens dacite and ash (Carter et al, 1986) suggests that pressures were indeed much higher than the overburden pressure for the Mt. St. Helens magma chamber. The estimate of the explosive energy of the May 18 eruption was about 24 Megatons TNT equivalent (Kieffer, 1980). If direct scaling relations are used, this implies an explosive energy for the Toba eruption of about $3 \times 10^4$ Megatons. This is in agreement with the energy determinations of Sabroux (1983), where $10^6$ $m^3$ of erupted material is equivalent to 1 Megaton of total energy, yielding a total energy for Toba of $3 \times 10^6$ Megatons. Blast coupling of explosions is usually about $10^{-2}$, yielding a net explosive energy of about $3 \times 10^4$ Megatons (Yokoyama, 1988).

Loper and McCartney (1988) propose a mechanism somewhat similar to that of Rice which involves rapid exsolution of $CO_2$ in mantle plume material as it reaches shallow depth. The major weakness of the Rice and Loper and McCartney models is that they require a closed magmatic system that is supersaturated with volatiles and contains no phenocrysts before the eruption. The presence of nucleation surfaces in a melt presumably will cause volatiles to exsolve prematurely, preventing the proposed mechanism from

being viable. The problem is that most magmatic systems are believed to contain a significant volume of crystals before eruptions occur. In particular, the presence of large phenocryst plagioclase in the Mt. St. Helens material suggests that these models are not appropriate.

Catastrophic Dewatering (The Amphibole Effect)

Bardintzeff and Bonin (1987) have suggested that the breakdown and resorption of amphiboles and other hydrous phases during magma ascent can lead to rapid buildup of overpressures and explosive eruptions. This model proposes that the breakdown of hydrous phases along with the crystallization of anhydrous phases from the melt drives volatiles into the remaining melt at rates too great for the magmatic system to buffer effectively. As this process occurs at depths of 5 to 8 km, the residual melt oversaturates rapidly, leading to volatile pressures of several hundred bars. If such a process occurred catastrophically, the concomitant pressure spike would be on the order of kilobars, which might be sufficient to produce weak shock deformation. However, the kinetics of this process are most likely too slow to allow the dewatering process to outrun the buffering capacity of the magmatic system as Bardintzeff and Bonin (1987) propose.

Thermochemical Detonation

Following up on the early work of Kusnetsov (1966), Boslough (1989) has proposed that thermochemical detonations from catastrophic phase changes in volatile-saturated magmatic systems are possible. Calculations for a pure albite-water system at 0.1 GPa and 500°C reveal that a Chapman-Jouguet

detonation from 100% liquid to 95.6% crystals and 4.4% water vapor will produce a pressure of 0.6 GPa. The production of much higher pressures on the order of 10 GPa at 25°C required to produce classic shock microstructures is problematic, however, since pressures this high will tend to drive the system back into the liquid phase. Also, the higher temperatures encountered in most natural magmatic systems (700° to 800°C) exacerbate this problem and lower the pressure limits even further. Another problem with this model is kinetics, which are notoriously slow in silica-dominated systems. Such detonations involving rapid crystallization will require rapid chemical transport or high-strain-rate, shock-induced shear transport as proposed by Dremin and Breusov (1968). Since rapid chemical transport is unlikely in such systems, shear transport during the shock event is the only viable mechanism to allow the detonation to proceed.

Gas-Phase Explosions

Although the volcanic gas phase consists mainly of $CO_2$ and $H_2O$ (e.g. Allard, 1983), significant concentrations of other gases such as $H_2$, $H_2S$, $SO_2$, CO, COS, and rare gases are also commonly observed. The mixture of gases is a direct function of magmatic temperature, pressure, composition, and oxygen fugacity (e.g. Gerlach, 1983), and can change dramatically during ascent and eruption, making gas composition a useful volcanic monitoring parameter (Shimozuru, 1983).

The presence of explosive gases such as $H_2$ and CO in magmatic gas systems raises the question of whether magmatic conditions will permit these gases to combust, and if so, at what conditions? Recent results from the 1980

eruption of Mt. St. Helens (e.g. Lipman and Mullineaux, 1981) provide an excellent database for a specific eruption from which to make some estimates regarding the possibility of gas explosions in magmatic systems.

Stoiber et al (1981) estimated that a minimum of 2.4 x $10^5$ tons (3.63 x $10^{10}$ moles) of sulfur were emitted during the May 18 eruption of Mt. St. Helens. Gerlach and Casadevall (1986) evaluated the high-temperature gas emissions from fumeroles at Mt. St. Helens, and estimated that the sulfur content of the magmatic gas phase (both $SO_2$ and $H_2S$) was about 0.36 mole percent, which yields a total gas content for the eruption of 2.2 x $10^{13}$ moles, or about 2.2 x $10^{11}$ moles of $H_2$ and CO. Based on standard combustion reactions for these gases, the energy of reaction at 750°C is about 190 to 200 KJ per mole of gas. Using the estimate of 24 Megatons (9 x $10^{15}$ J) for the energy of the May 18 eruption, and dividing by the energy of reaction, the eruption would require 4.5 x $10^{10}$ moles of $H_2$ and/or CO at 750°C. As the temperature of the melt is increased to 1000°C, the required amount of gas increase to 5.1 x $10^{10}$ moles. Even for the highest magmatic temperatures acceptable for the Mt. St. Helens magmatic system, it is apparent that there was up to four times more gas energy available than is required to account for the eruption energy.

The other primary constraint on the combustion of $H_2$ and CO is the presence of sufficient $O_2$ to allow the reaction to proceed. Unfortunately, the gas phase data for Mt. St. Helens indicate that the $fO_2$ of the magmatic system before and after the May 18 eruption was at Ni-NiO or slightly above, i.e. $fO_2 \sim 10^{-16}$, $H_2/H_2O \sim 10^{-2}$, $CO/CO_2 \sim 10^{-2}$ at 750°C (Gerlach and Casadevall, 1986). This $pO_2$ is clearly insufficient to permit combustion to occur in the normal sense within the magmatic system. However, in light of the earlier discussion

on thermochemical detonation, a viable mechanism may exist for triggering the combustion of these explosive gases. Boslough (1989) did his calculations for a pure albite-water system with no additional reactive gases present. If a Chapman-Jouguet detonation is produced in a magmatic system, the propagating shock front produces a sudden increase in pressure and temperature, which tends to drive the magmatic system back into the liquid field. The gases which are subjected to this shocked state are heated rapidly, which causes fast-gas reactions to occur and drives the $pO_2$ up the Ni-NiO buffer line from a value of $10^{-16}$ at 750°C to $10^{-6}$ at 1300°C. This abruptly elevated $pO_2$, along with the higher pressures of the explosive gases in the compressed state, may permit the development of a shock-induced gas explosion or rapid gas reaction that will contribute some excess chemical energy to the propagating shock front. When the other possible chemical effects during a weak shock event are added, the possibility of a triggered gas detonation in a magmatic system becomes more acceptable.

Once such a driven chemical detonation occurs in a magmatic system, the overpressures that can be produced are a function of the detonation geometry, the materials involved (i.e. gas and magma chemistry), the thermodynamic state of the system at the time of detonation, and the efficiency and rate of the detonation process. Based on the available information in the shock literature, it is reasonable to assume that pressures significantly greater than the 0.6 GPa calculated by Boslough (1989) might be attainable.

## Experimental Analogs for High-Temperature Shock Deformation

The scientific data for shock deformation of rock-forming minerals initially at temperatures other than ambient are exceedingly few because of the conventional interpretation of volcanic eruptions discussed above and because in the mid 1960's, a very large group of scientists was convinced that virtually all cryptoexplosion structures resulted from asteroid or comet impact. However, because of this strong bias, there exists a wealth of information on the nature and origin of shock-induced microstructures produced at initially ambient temperature by natural impact and artificial high explosive, chemical, gas gun, and nuclear explosions, information which provide a very important base for comparison of structures induced in silicates initially at elevated temperature.

Hörz (1968) and Müller and Defourneaux (1968) performed a fundamental series of shock-recovery experiments on oriented quartz single crystals that has provided a basis for studying the development of shock-induced microstructures in quartzose rocks. Stöffler et al (1975) studied shock metamorphism in quartz sand targets using hypervelocity impact (5.9-6.9 km/sec) of projectiles. Quartz grains shocked up to 30 GPa accounted for only 4% of the mobilized target material in these experiments, and were concentrated within the craters produced by the projectiles. The resultant microstructures included comminuted quartz, cataclastic breccias, and glassy aggregates.

More recently, systematic shock-recovery experiments have been carried out on coherent, nearly randomly oriented, Hospital Hill

Witwatersrand quartzite in an attempt to determine the stress dependence of microstructural development in bonded polycrystalline aggregates (Reimold and Hörz, 1986a, b). The fourteen initial experiments were carried out at 25°C in a 20 mm powder gun in the pressure interval 5.1 to 35.5 GPa and crystallographic orientations of planar fractures and planar features were analyzed using universal-stage techniques (Reimold and Hörz, 1986a, b).

F. Hörz subsequently devised an external furnace to preheat the quartzite target to about 440°C and shocked six specimens in the pressure range 2.9 to 28.6 GPa. In comparing the general features and distinctions of the initially cold with the preheated samples, Reimold (1988) noted that pervasive fracturing, brecciation, and shock mosaicism are better developed at comparatively lower shock pressures in preheated specimens. As the development of mosaicism progresses, random fracturing decreases in abundance, planar fractures appear, and rare planar elements first appear at 16.8 GPa in the cold shocked sample, but are not observed at 17.5 GPa in the preheated one.

These suites of experiments have been analyzed still further for microstructures perceived to be more pertinent to the problem posed here. For both sets of experiments, the general progressive development (subjective) of microfractures, shock mosaicism, and planar features are shown as a function of peak shock pressure (figure 2-11A). Intensity of random microfracturing increases at both temperatures to about 10 GPa, whereupon the shock mosaic structure first appears in sporadic grains. At shock pressures near 20 GPa, microfracturing is suppressed as shock mosaicism becomes pervasive at both temperatures, the only detectable

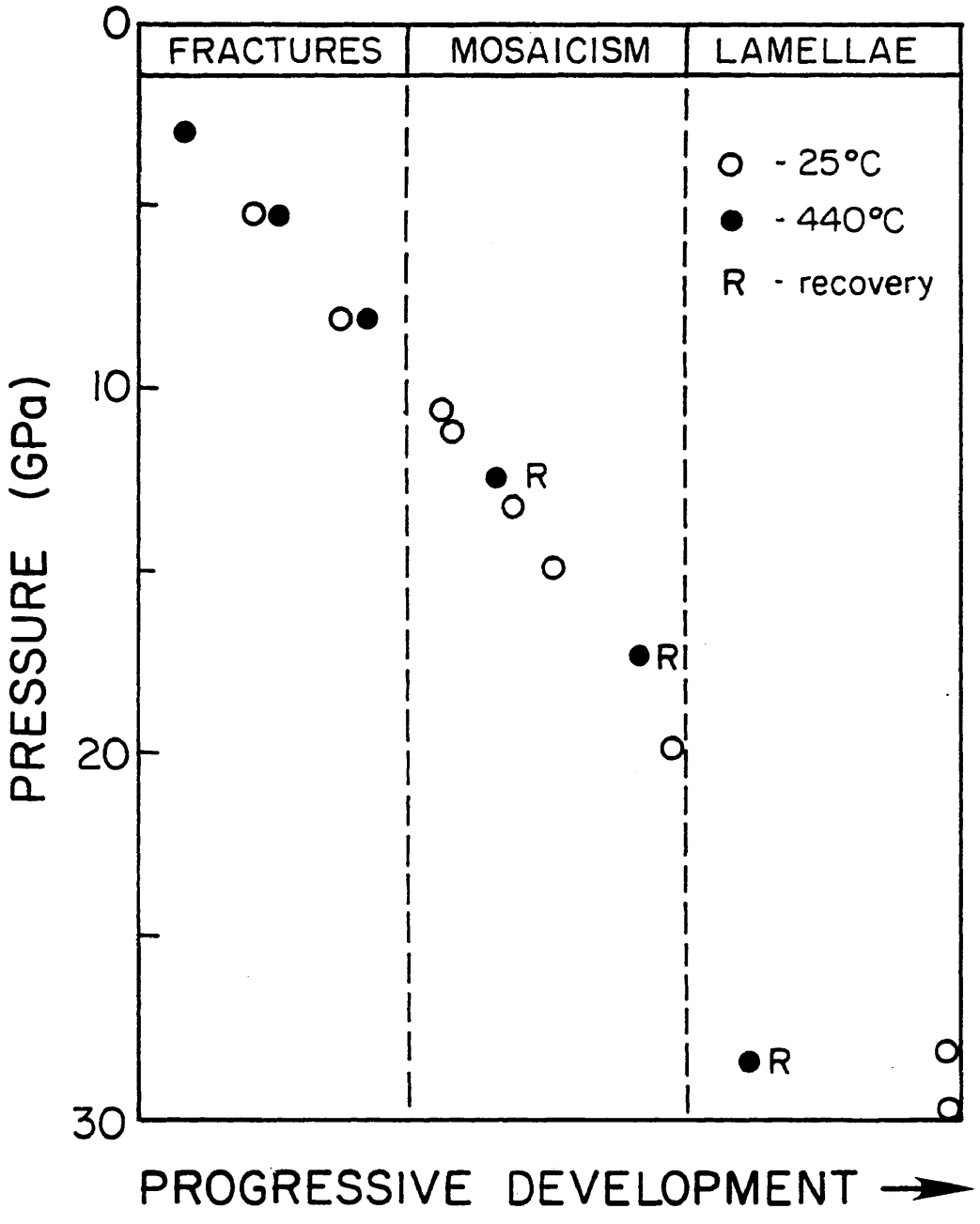


Figure 2-11: Results of optical analysis of shock-recovery experiments on Hospital Hill quartzite. A. (This page) Progressive development of fracturing, mosaicism, and planar features as a function of peak shock stress. The solid circles represent samples that were preheated to 440°C before being shocked. B. (Next page) Orientation data for planar features in the pair of experiments recovered from 28 GPa at 25° and 440°C pre-shock temperature. Diagram from Carter and Officer (1987).

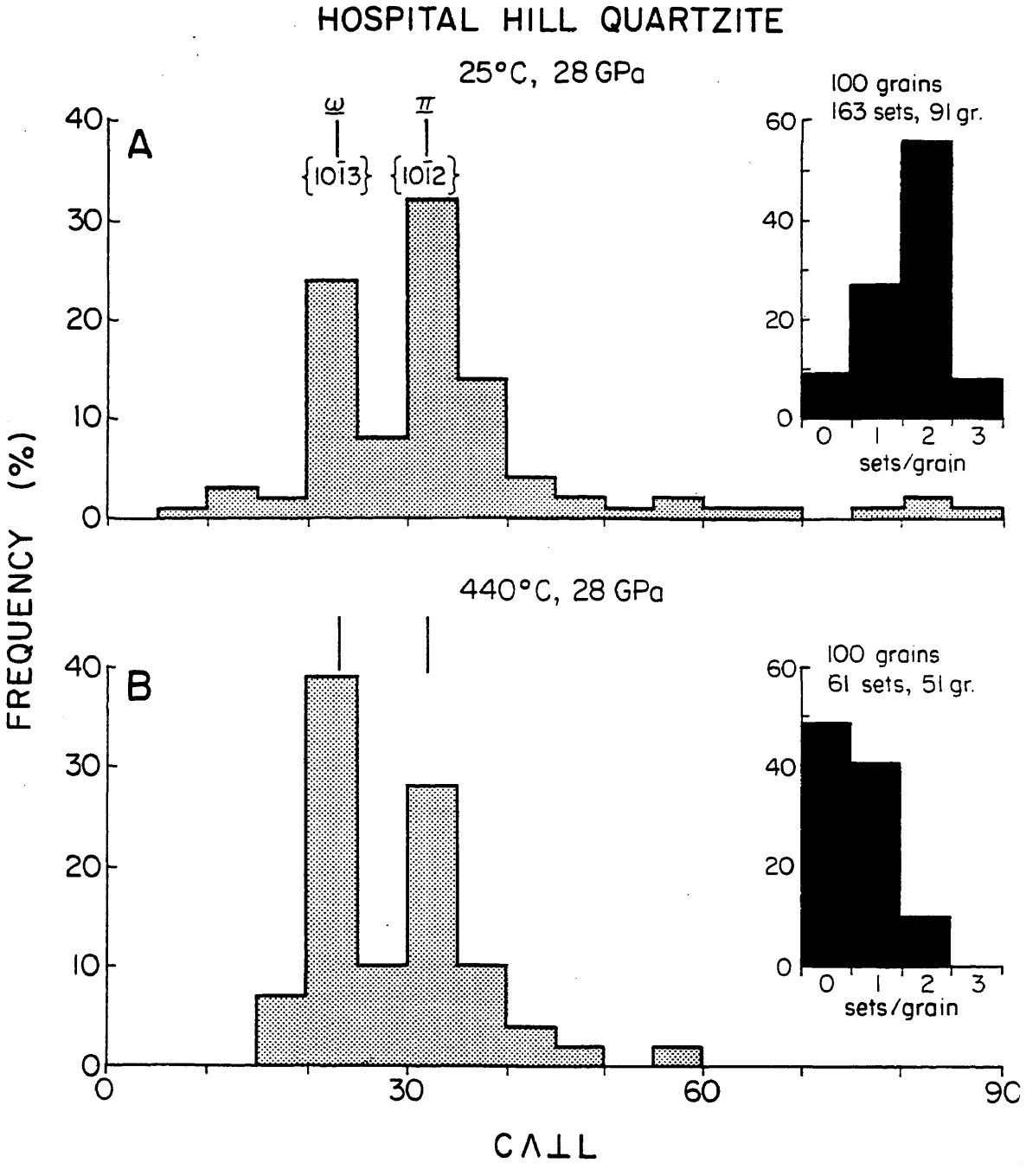


Figure 2-11 (continued)

difference being a higher degree of thermal recovery in specimens initially at 440°C. Unfortunately, there exists a shock pressure gap between 20 and 28 GPa, but at the latter pressure, shock mosaicism is still generally well-developed and planar features are evident. Again, comparing only the two samples shocked to 28 GPa, apart from planar feature development discussed below, the main difference lies again in the higher degree of partial thermal recovery of the higher temperature specimen.

The only samples containing planar features and shocked to nearly the same stress level at room and elevated temperature were analyzed in detail for the development and orientations of planar features (figure 2-11B). The most dramatic difference between the two sets of experiments is in the development of the planar features as shown in the inset of figure 2-11B. Of the 100 grains sampled (nearly the total recovered) for each specimen, only nine were devoid of planar features at 25°C whereas planar features were absent in 49 grains shocked at 440°C. A single set of planar features occurred in 41 grains in the high-temperature experiment and two sets occurred in only ten grains whereas, for the room-temperature experiments, 27 grains contained single sets, 56 grains contained duplex sets, and eight grains contained three intersecting sets.

The 100 grains sampled from each section shocked to 28 GPa were also plotted to show orientations of the optic axes and the normals to planar features. These data (figure 2-12) support the contention that planar features form at a wide range of orientations with respect to the shock direction. The nearly random orientations of both the quartz grains (figure 2-12B, D), and the planar features not excluding the U-stage blind spot (enclosed dashed

Figure 2-12: Orientation data for *c* and normals to planar features in 100 grains each of Hospital Hill quartzite shocked to 28 GPa at 25° and 440°C. A. Normals to planar features in the sample shocked at 25°C. S is the shock direction. Note the blind spot at angles greater than 50° from the plane of the section. B. Orientation of *c* in quartz in the 25°C experiment. Closed circles represent grains that contain planar features; open circles denote grains with no planar features. C. Normals to planar features in the sample shocked at 440°C. S is the shock direction. D. Orientation of *c* in quartz from the 440°C experiment with the same convention applied as in C.

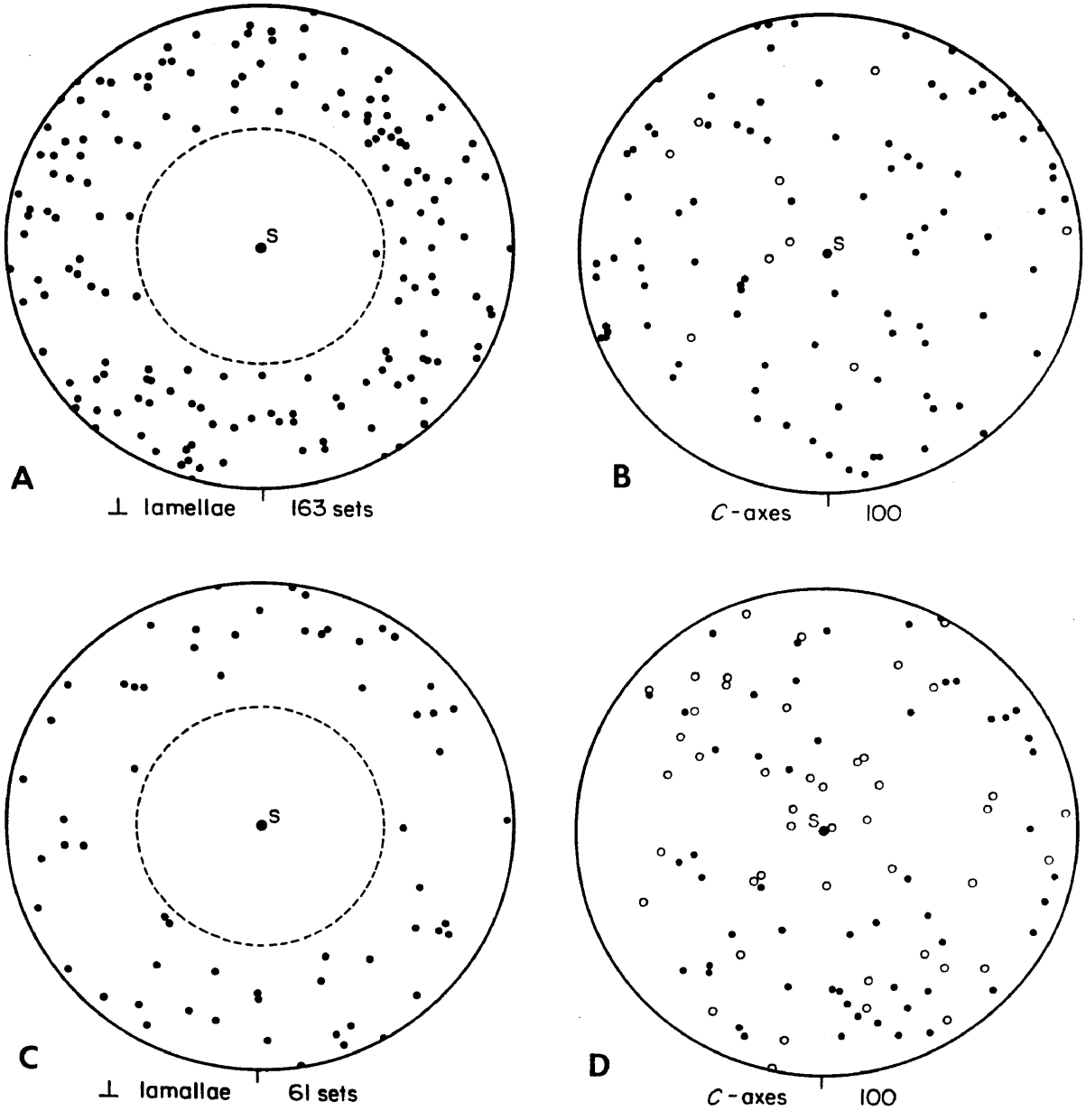
S
A
⊥ lamellae
163 sets
S
B
C-axes
100
S
C
⊥ lamallae
61 sets
S
D
C-axes
100

circle; figure 2-12A, C), suggest that the crystallography of quartz exerts the primary control on formation of planar features.

Some of the microstructures observed in these specimens include the shock mosaic structure, partially recovered, which is accompanied by some random fracturing at 17.5 GPa and 440°C (figure 2-13A). In contrast, the mosaic structure produced in a specimen shocked to 29.7 GPa at 25°C (figure 2-13B) shows no hint of recovery. Thin sharp ω planar features dominate the sample shocked to 28 GPa at 440°C (figure 2-13C), although small areas of $\pi$ features do occur on occasion. In contrast to the high temperature experiment, the specimen shocked to 28 GPa at 25°C displays multiple intersecting sets of planar features (figure 2-13D). Transmission electron micrographs from both specimens shocked to 28 GPa reveal the change from dominance of multiple sets of planar features (figure 2-14B) at 25 °C to well-developed single sets of features (figure 2-14C, D). In contrast to the optical orientation data for both specimens, however, the planar features observed in the TEM (magnification of 36,000X) show several orientations including *r*, *a*, *c*, $\pi$, and *s*. The most frequently observed orientation was *r* with no ω features observed in either case. This may reflect the actual formation process for planar features which probably includes several different orientations of submicrostructures that coalesce to produce optically visible features with specific orientations. Low magnification TEM (3600X) performed by Doukhan and Goltrant (personal communication, 1990) on naturally-shocked quartz reveals that the optical features are recognizable at this intermediate scale. Unfortunately, the thinning methods used and the low keV of the available microscope prevented low magnification work from being completed in this study. The lack of ω features at the higher magnifications is attributed to the

Figure 2-13: Shock-induced microstructures in experimentally shocked Hospital Hill quartzite. Scale bars are in mm. A. Partially recovered shock mosaic structure in quartz shocked to 17.5 GPa at 440°C. B. Shock mosaic structure associated with planar features in quartz shocked to 29.7 GPa at 25°C. C. Planar features parallel to $\omega$ in quartz grains shocked to 28 GPa at 440°C, with a small zone of features parallel to $\pi$ just to the left of center. D. Intersecting sets of planar features characteristic of quartz grains shocked to 28 GP at 25°C.


A
0.5

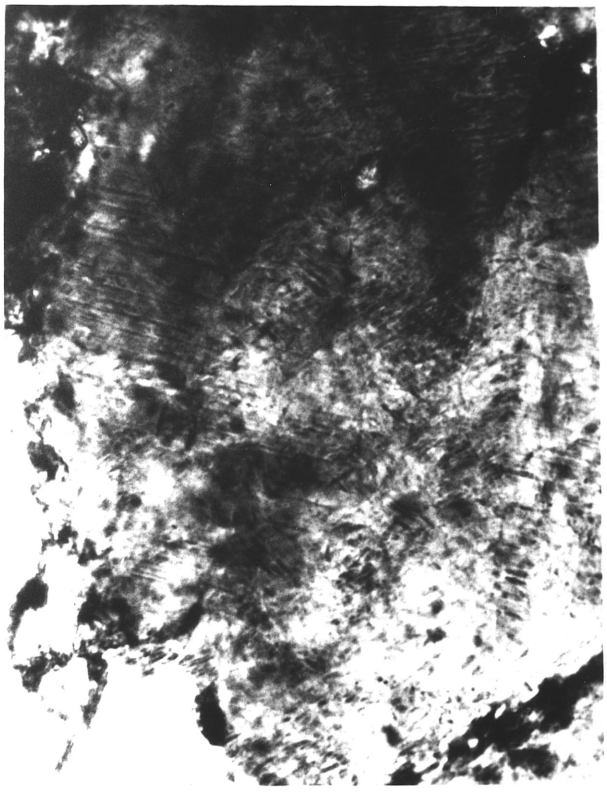
B
0.5

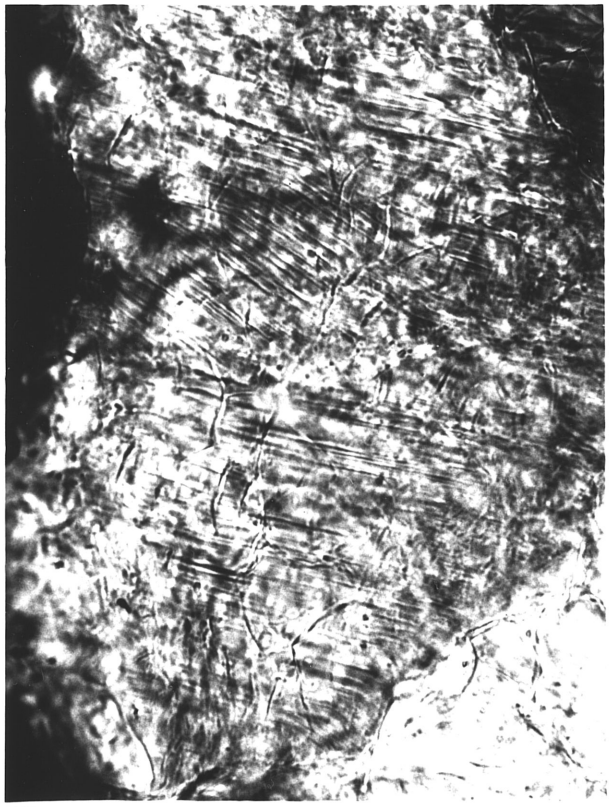
C
0.1

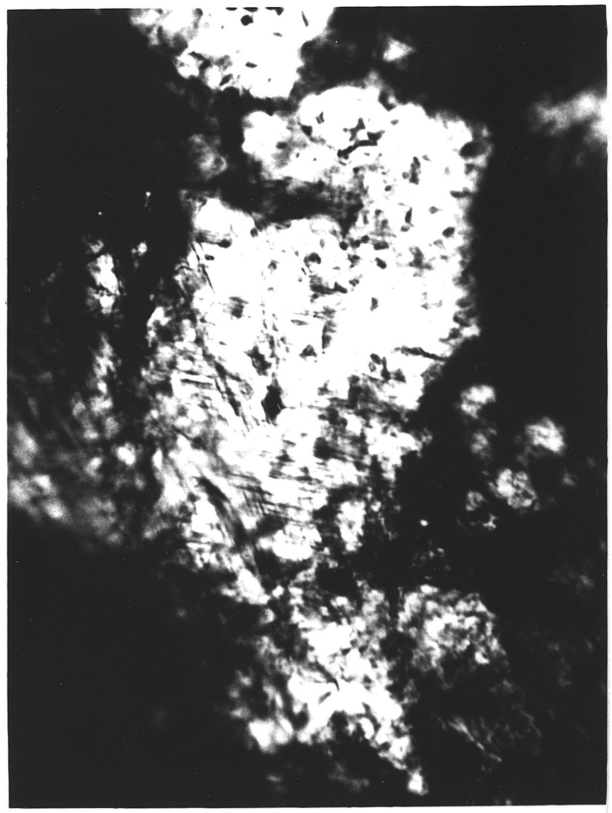
D
0.1

change in scale from the optical and low-magnification TEM to the higher magnification TEM.

Differences in planar feature orientations are not so dramatic, especially when considering the much smaller number of planar features in the high-temperature experiment. The usual forms $\omega$ and $\pi$ are well developed at both temperatures, with the $\omega$ being favored at 440°C and $\pi$ being slightly more abundant at 25°C. It is suggested that the paucity of planar features at the higher temperature and, where present, their preferential development in single sets may bear importantly on shock microstructures possibly generated during explosive silicic volcanism. These observations are also consistent with preliminary results for the few Toba and other volcanic samples discussed above where only single sets of planar features in rare quartz grains have been found to date (Carter et al, 1986). Much more prevalent in these volcanic specimens is the presence, as in the experiments, of partially recovered shock mosaicism. This very distinctive mosaic structure is associated with shock stresses in excess of 10 GPa and is the most common manifestation of strong shock deformation (Stöffler, 1972). It is well-developed in varying proportions in quartz and feldspar grains in the volcanic specimens and differs only in degree of recovery from the mosaic structure developed in silicates shocked at ambient temperature. Because of its prevalence in shock metamorphism, this manifestation of high-stress deformation should be much more thoroughly studied and documented than has been the practice in recent years. Since 1984, virtually all attention has been focused on multiple sets of planar features.

Figure 2-14: Transmission electron micrographs of submicrostructures in quartz from Hospital Hill quartzite shocked to 28 GPa. A. Well developed shock mosaic structure along with fine planar features parallel to $\pi$ (NE-trending features) in a sample shocked at 25°C. b. Multiple intersecting sets of planar features oriented parallel to *r* and *c* from a sample shocked at 25°C. Note that the crystalline quartz between the features shows no disorientation effects or evidence of shear displacement. C. A dominant single set of planar features (NE trending features) shocked at 440°C, with one planar feature trending East. Note the indications of disorientation in the remaining quartz crystal and the very rough boundaries of the features. D. A dominant single set of planar features shocked at 440°C. Note the greater width of the features and the evidence of disorientation in the diffraction pattern. All scale bars are 0.5 microns; G represents glass, and Q represents crystalline quartz.

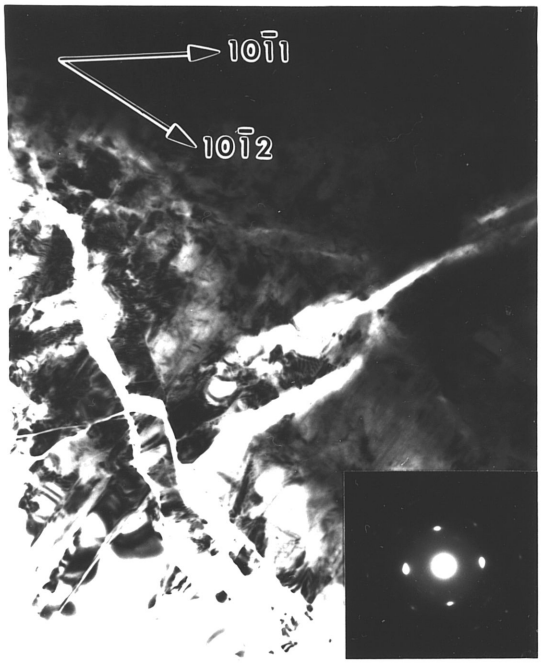


A

0.5μm

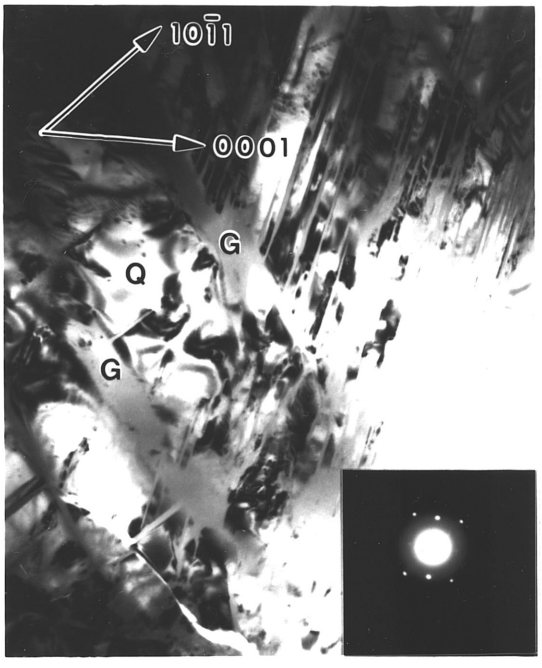


B

0.5μm


C

0.5μm

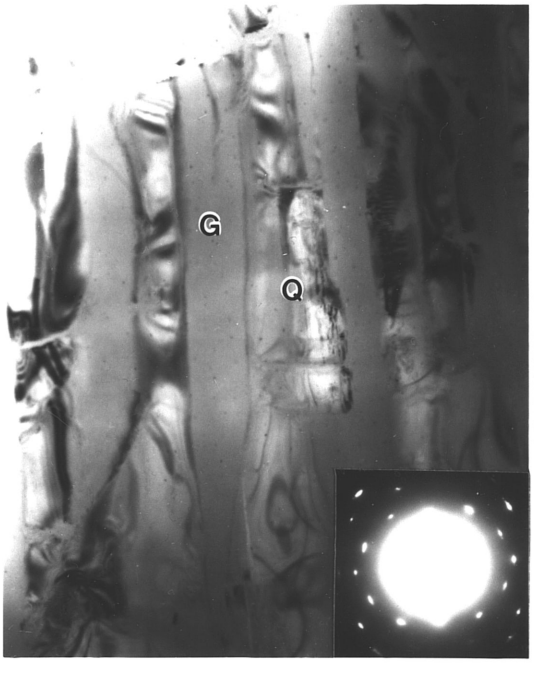


D

0.5μm

## Shocked Minerals at The Cretaceous-Tertiary Boundary

As discussed in chapter 1, the most crucial evidence in favor of an impact cause for the KTB event is the occurrence of quartz grains containing multiple intersecting sets of planar features at KTB sites around the world (e.g. Bohor et al, 1987). The presence of high-strain-rate microstructures in known volcanic rocks, along with the advent of several possible mechanisms for development of shock waves and/or high strain rates in magmatic systems, requires that the debate over the origins of shocked minerals at the KTB remain open.

The proposal of an extended period of intense volcanism across the K/T transition (Officer et al, 1987; Courtillot, 1988) implies that evidence of shock deformation should also be distributed well above and below the KTB clay layer, and should correlate approximately with the duration of volcanism. Differences in shock mosaicism and the development and orientations of planar features in the quartzite shocked to 28 GPa at 25° and 440°C (figure 2-11) along with the observations from the volcanic specimens and impactites suggests that statistical comparison of KTB deposits may allow a distinction to be made between impact and volcanically generated high-strain-rate microstructures.

## Shocked Minerals From The Raton Basin

Since the first report of shocked quartz from the Raton Basin (Bohor et al, 1984), virtually all photomicrographs of KTB shocked quartz from sites around the world have shown at least two intersecting sets of planar features.

This practice has led to the widely held belief that only multiple intersecting sets of planar features in quartz are diagnostic of shock deformation. It has also led many workers to ignore the other indicators of shock deformation that are so prevalent in the Raton deposits and elsewhere, including the shock mosaic structure, fused glasses, and the dominance of single sets of planar features.

Analysis of acid-washed clastic separates from the Starkville-South (STS) and Clear Creek North (CCN) localities in the Raton Basin reveal that a variety of shock-induced microstructures are present in these deposits. In particular, measured orientations of planar features in 100 grains encountered in linear traverses of thin sections of STS separates (figure 2-15A) show a distribution of planar features that are similar to the results from the Toba volcanics (figure 2-15C) and the 440°C experiment on quartzite (figure 2-15B). In the STS material, only 22% of the grains contained two sets of planar features. Planar features parallel to ω predominate (59%). In both the experiment and the Raton STS sample, only about 20% of the grains contained two sets of planar features. The orientation data for the STS locality are also very similar to the data of Izett (1987b, his figure 29) for the CCN locality; unfortunately, Izett fails to give the numbers of grains measured. Observational data for the CCN material from this study support the results of Izett (1987b), and indicate that the shock mosaic structure is common at both localities, along with single and multiple sets of planar features (figure 2-16 and 2-15). For both the STS and CCN samples used for this study, mosaicism in quartz and feldspar (figure 2-16C, D, and figure 2-17A), commonly partially recovered, is the prevalent shock-induced microstructure, and occurs in about one third of the quartz and feldspar grains.

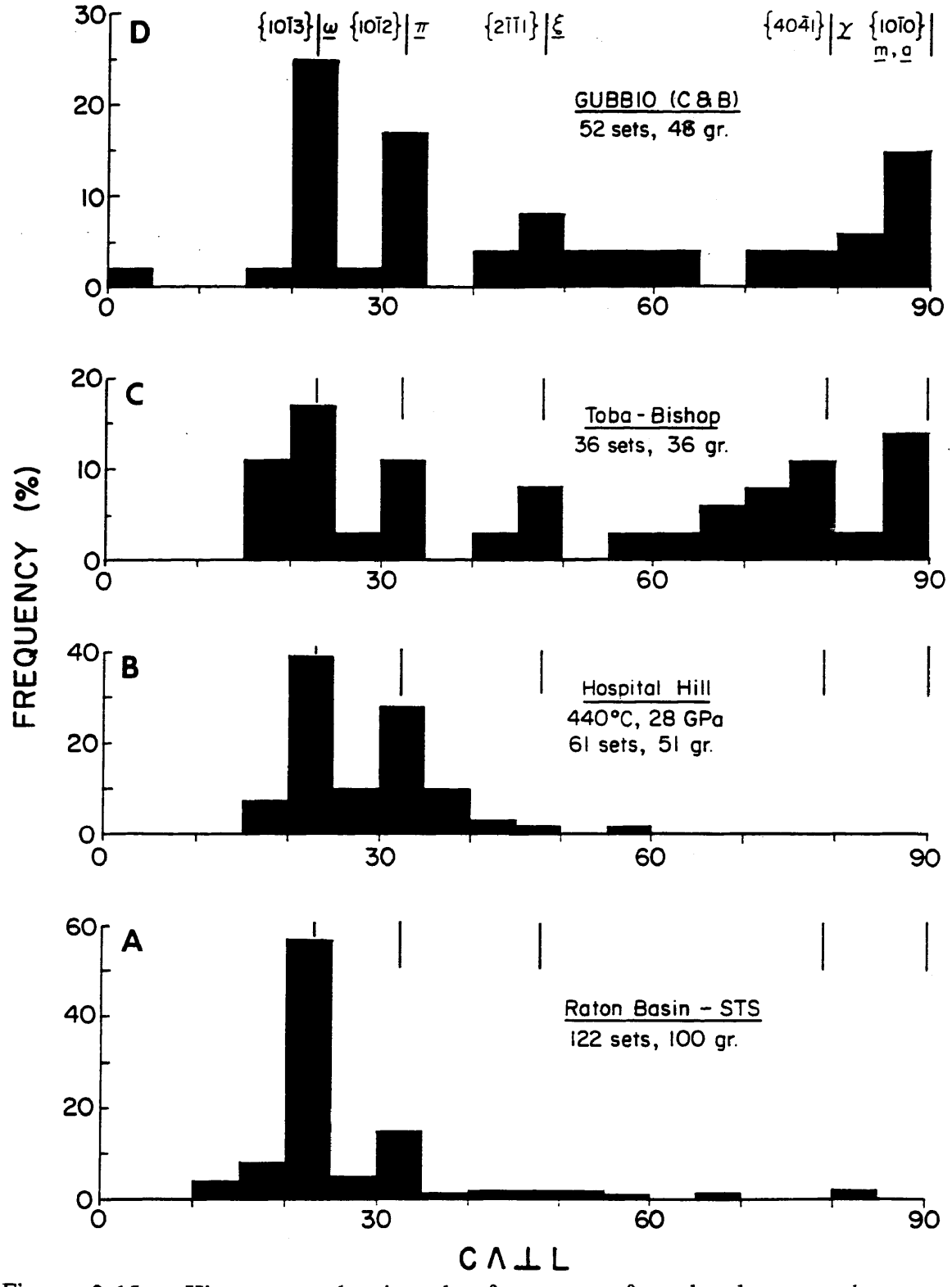


Figure 2-15: Histograms showing the frequency of angles between the quartz c-axis, and normals to sets of planar features in the samples indicated. Diagram from Carter and Officer (1989).

TEM analysis of the CCN material (figure 2-18) reveals that the KTB materials display a variety of submicrostructures including single sets of planar features (figure 2-18A), and shock-fused glasses that have recrystallized and annealed to a microcrystalline aggregate (figure 2-18B). Unlike the experimentally-shocked quartzite (figure 2-14), the KTB planar features represent either highly strained quartz or glass that subsequently devitrified into a microcrystalline form (figure 2-18A, C). The morphology of these features is changed dramatically by electron beam damage (figure 2-18C, D) which vitrifies the material in the planar features. TEM diffraction data for the CCN materials reveals a dominance of *a* and *r* planar features with occasional *s* features, which is very similar to the data for the Hospital Hill quartzite. Again, no $\omega$ or $\pi$ features were observed in the TEM foils studied.

Another point of concern over the shocked minerals in the Raton sediments has been the apparent lack of very intense shock, including the presence of high-pressure polymorphs such as coesite and stishovite which are common in impact ejecta (e.g. McHone and Dietz, 1988), and in cryptoexplosion structures (Martini, 1978). Samples of KTB material documented in the literature reveal only mosaicism and single and multiple sets of planar features, which may be due in part to cratering dynamics, in that the most intensely deformed material is usually deposited near the crater site (Melosh, 1989). Recent nuclear magnetic resonance (NMR) and x-ray diffraction analysis of mineral separates from the Raton sites, however, indicate the presence of stishovite (McHone et al, 1989), which supports the contention that an impact occurred at K/T time. The presence of stishovite and/or coesite may be problematic, however, since these phases should also form in non-impact environments at a range of pressures from equilibrium

Figure 2-16: Planar features and shock mosaic structure in quartz and feldspar grains in the Starkville South Raton Basin KTB layer. Scale bars are in mm. A. Single set of planar features (WNW trending) parallel to ω in quartz. B. Intersecting sets of planar features (NE and EW trending) both parallel to ω in quartz. C. Shock mosaic structure associated with planar features in quartz. D. Shock mosaic structure in plagioclase. Photos from Carter et al (1990).

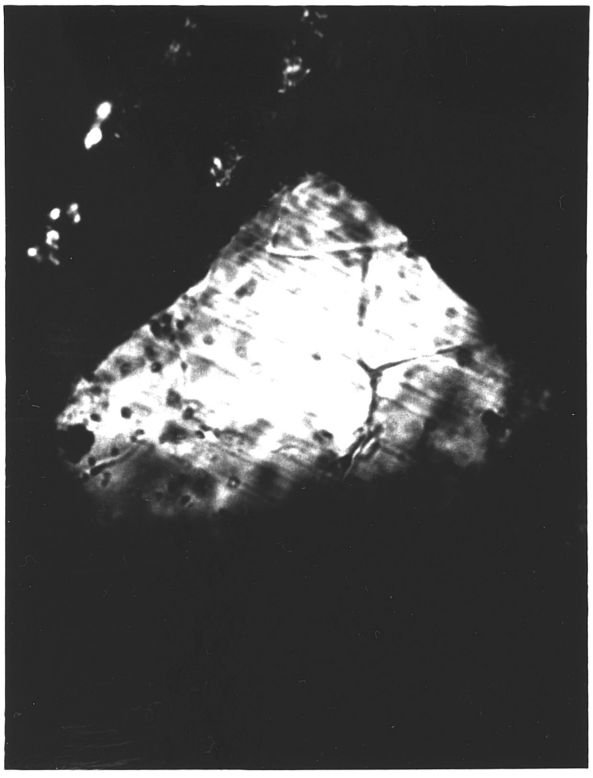
A
0.05


B
0.05

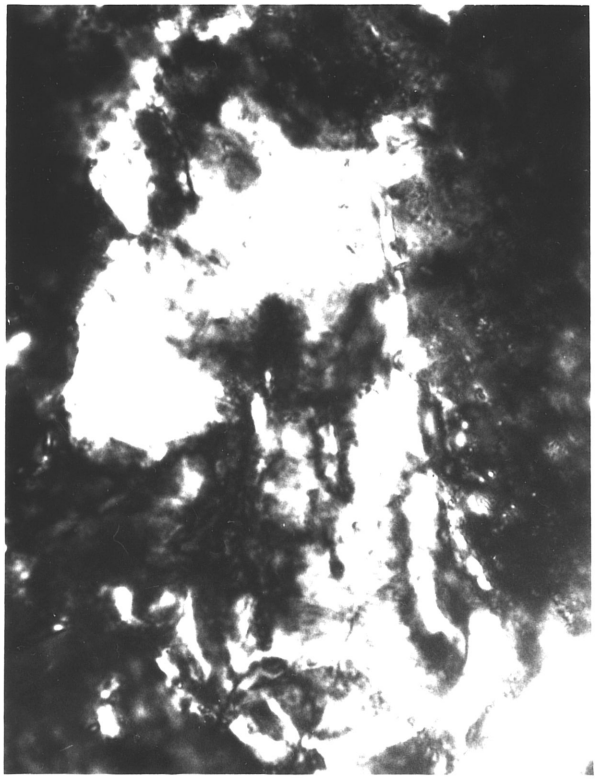
C
0.05

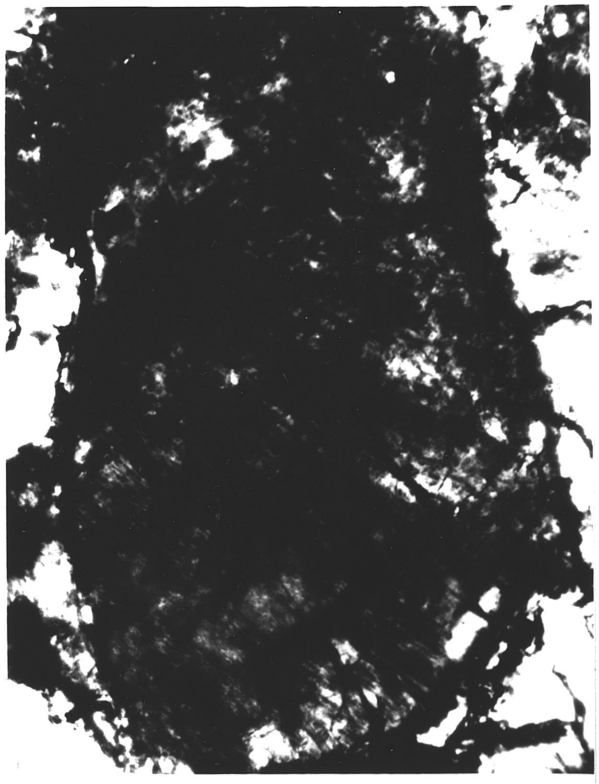
D
0.05

Figure 2-17: Planar features and shock mosaic structure in quartz and feldspar grains in the Clear Creek North, Raton Basin KTB layer. A. Intense shock mosaic structure associated with muliple sets of planar features. B. Multiple intersecting sets of planar features showing 5 different orientations. C. Single sets of planar features oriented parallel to ω. D. Duplex set of intersecting planar features, both parallel to ω.


A
65 µm

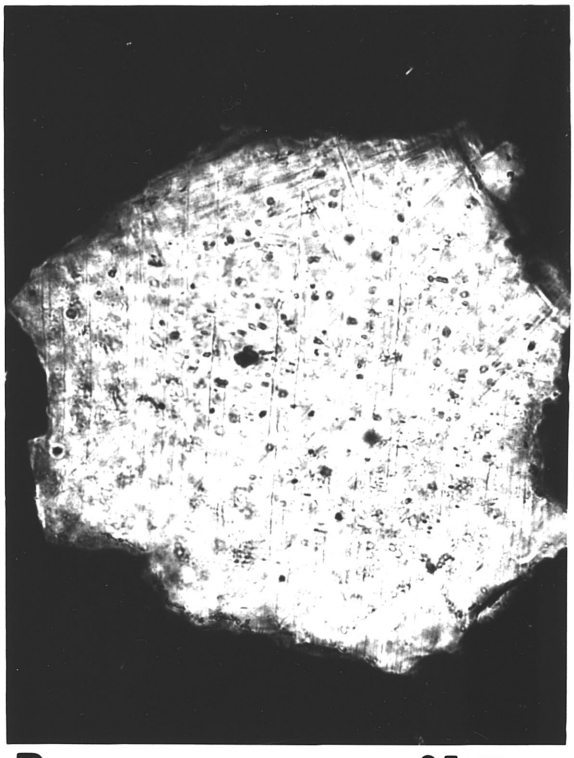
B
65 µm

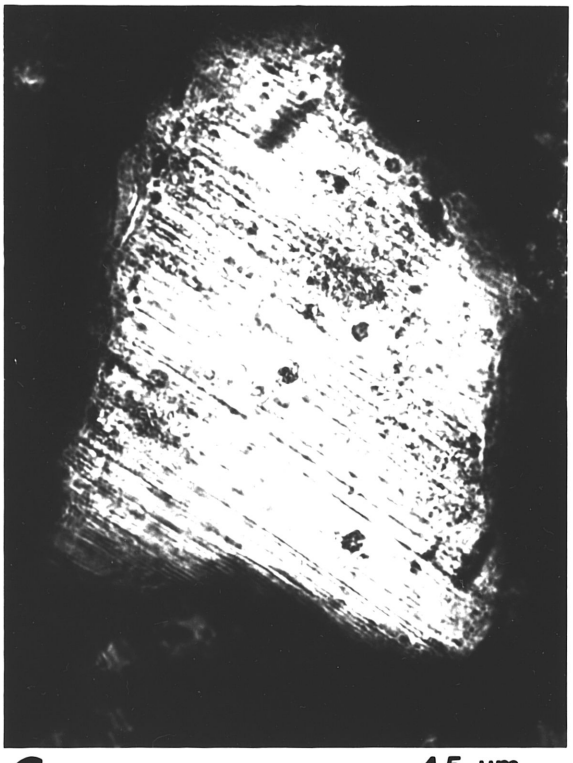
C
45 µm

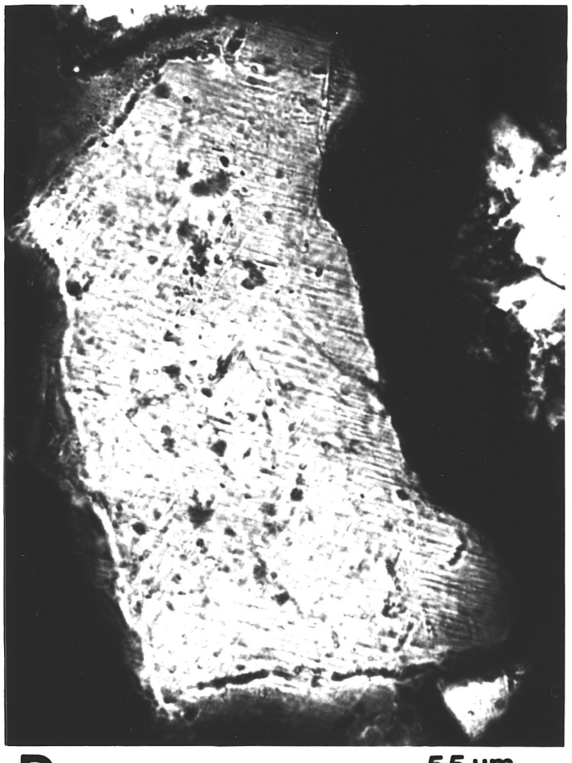
D
55 µm

Figure 2-18: Transmission electron micrographs of submicrostructures in quartz from the KTB, Clear Creek North, Raton Basin. A. Planar features oriented parallel to *r*, filled with very fine crystalline material and surrounded by relatively strain-free quartz. B. Recrystallized and annealed glass after fused quartz, showing classic grain boundary morphology, and disorientation of electron diffraction patterns indicative of recrystallization form a short range order glass. C. Intensely disrupted quartz containing a large amount of microcrystalline material and planar features (NNE trending) parallel to *a*. The microcrystalline material is >50% of the sample. D. Micrograph of 2-16C after vitrification of the microcrystalline areas by electron beam damage. All scale bars are 0.5 microns.

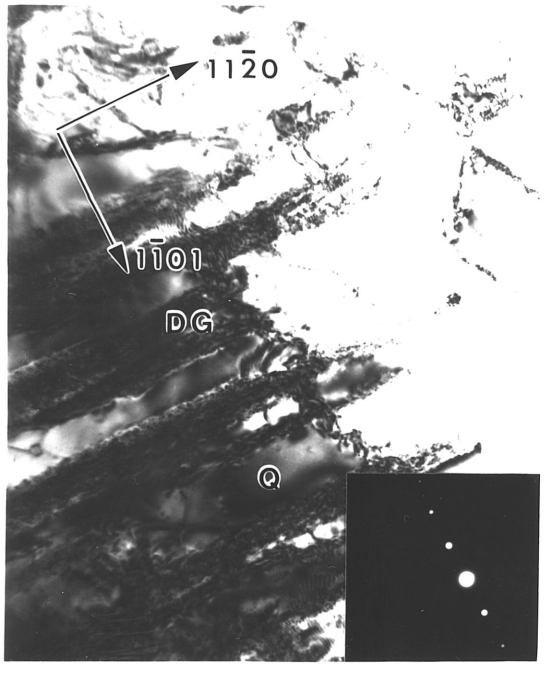


A

0.5μm

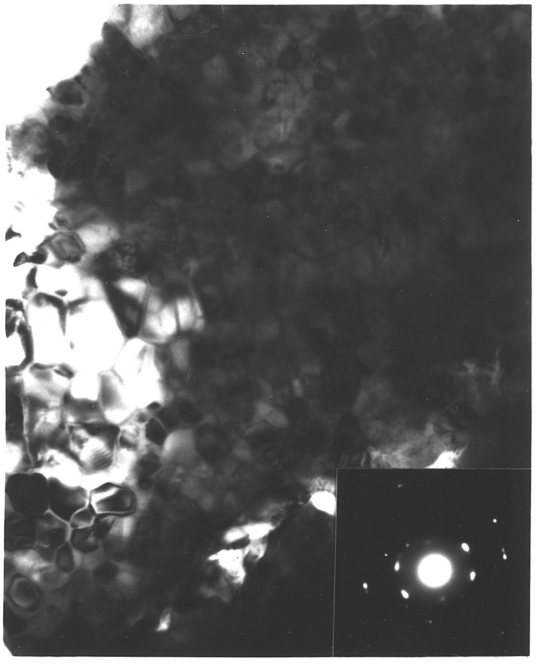

B

0.5μm

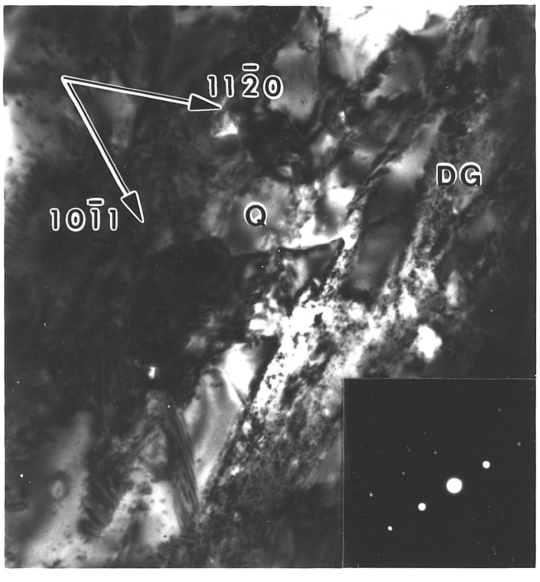


C

0.5μm

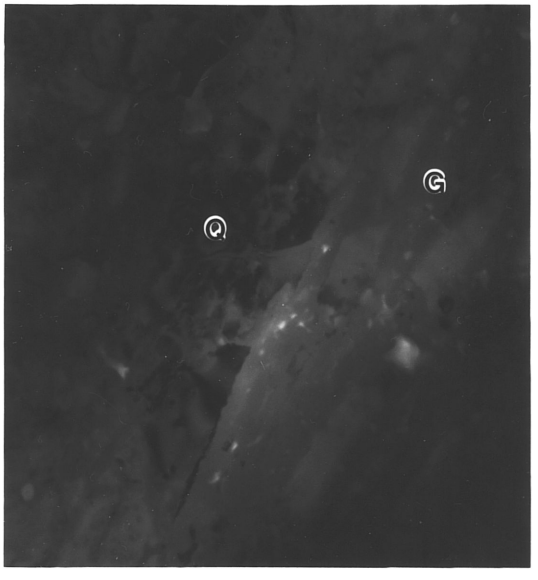


D

0.5μm

(static) pressures to the high pressures of short duration which are produced during impacts. The equilibrium pressures required to produce these polymorphs are >3.0 GPa for coesite and >7.5 GPa for stishovite (Kieffer, 1971; Stöffler, 1971). Based on the physics of deformation and transformation processes, these polymorphs can be expected to form at a wide variety of conditions between the equilibrium and shock end-members, as a function of the applied strain rate, duration of loading (i.e. total strain energy input), and ambient temperature.

## The Distribution of Shocked Minerals Across the K/T Transition at Gubbio

A glaring deficiency in nearly every shock deformation study at the KTB has been the tendency to focus only on the boundary layer itself. This practice resulted from the assumption built into the bolide hypothesis that the only place worth looking was the boundary layer, and was compounded by the "rush to publish" results as soon as they were available. As the complexity, selectivity, and sequencing of the K/T extinction have been documented, it has become clear that some events at the K/T transition may have occurred before and after deposition of the "Magic" layer. The proposals of multiple cometary impact (Hut et al, 1987) and volcanism (Officer et al, 1987) as alternatives to the single bolide theory have made the study of extended sections essential to a more thorough understanding of events across the K/T transition.

In a pioneering study at the Bottacione and Contessa sections from Gubbio, Italy, Carter et al (1990) analyzed thin sections of whole rock material and clastic separates from closely-spaced samples across the K/T transition. The nearly 3000 observations of quartz and feldspar grains from both localities

Figure 2-19: Frequency of shock mosaicism in quartz and feldspar as a function of the distance from the KTB at Gubbio. Main rock types are as indicated and separates are quartz and feldspar grains separated from the carbonate and clay fractions. Sample labels are given beside each bar and the number in parentheses represents the total number of quartz and feldspar fragments observed in each section. Thirty-nine thin sections and ~3000 observations are recorded.

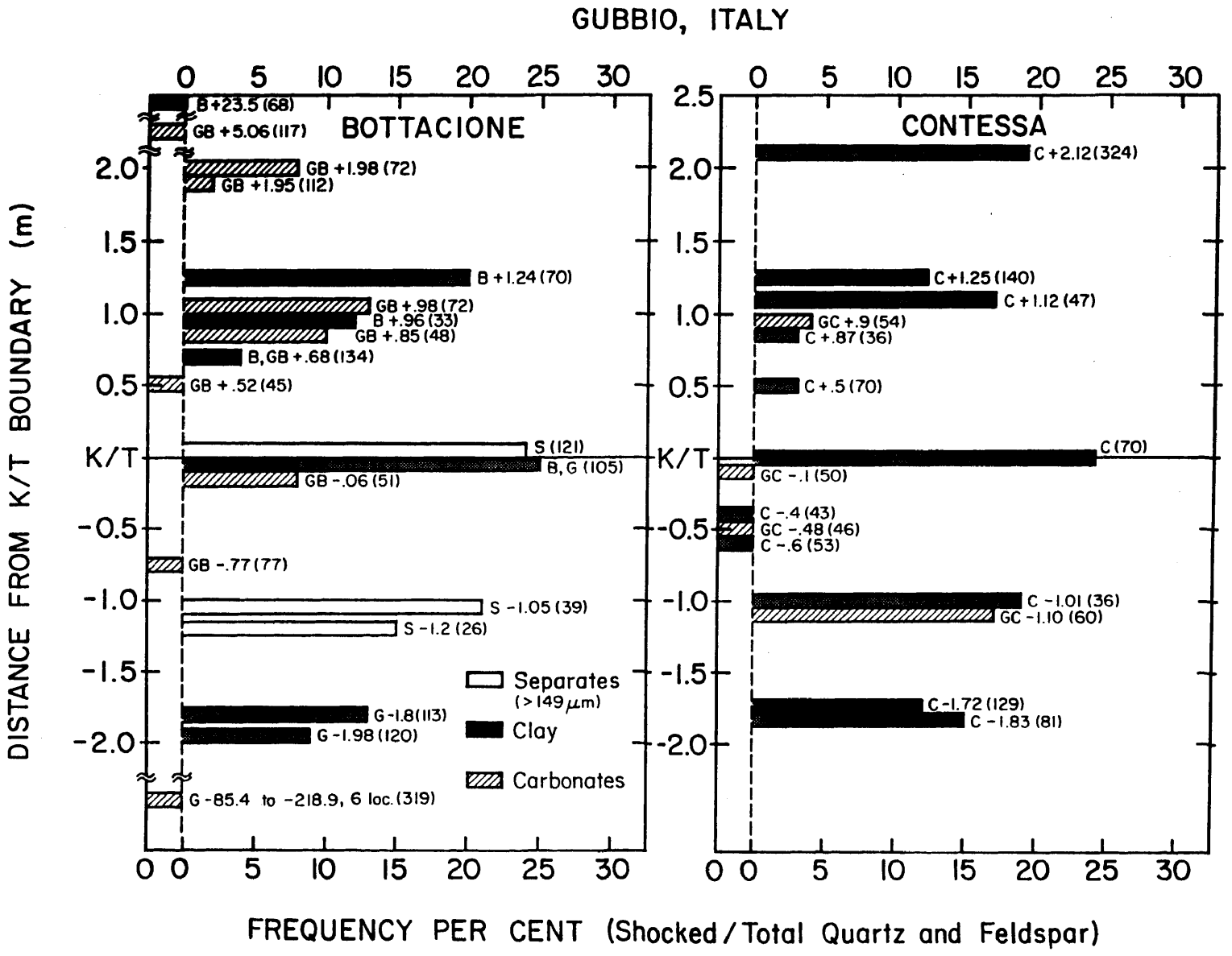
GUBBIO, ITALY
BOTTACIONE
CONTESSA
DISTANCE FROM K/T BOUNDARY (m)
FREQUENCY PER CENT (Shocked / Total Quartz and Feldspar)
B +23.5 (68)
GB +5.06 (117)
GB +1.98 (72)
GB +1.95 (112)
B +1.24 (70)
GB +.98 (72)
B +.96 (33)
GB +.85 (48)
B, GB +.68 (134)
GB +.52 (45)
S (121)
B, G (105)
GB -.06 (51)
GB -.77 (77)
S -1.05 (39)
S -1.2 (26)
G -1.8 (113)
G -1.98 (120)
G -85.4 to -218.9, 6 loc. (319)
C +2.12 (324)
C +1.25 (140)
C +1.12 (47)
GC +.9 (54)
C +.87 (36)
C +.5 (70)
C (70)
GC -.1 (50)
C -.4 (43)
GC -.48 (46)
C -.6 (53)
C -1.01 (36)
GC -1.10 (60)
C -1.72 (129)
C -1.83 (81)
Separates (>149 μm)
Clay
Carbonates
K/T

Figure 2-20: Shock mosaicism (A and B) and planar features (C and D) in quartz and feldspar grains at the Gubbio K/T transition. Scale bars are in mm. A. Partially recovered shock mosaic structure in K-feldspar from the KTB, Bottacione locality. B. Partially recovered shock mosaic structure in plagioclase from 1 m above the KTB, Bottacione locality. C. Single set of prismatic planar features (NW trending) in quartz from 1.72 m below the KTB, Contessa locality. D. Intersecting sets of planar features in quartz (NE trending set is $\pi$ and the NW trending set is prismatic) from 2.12 m above the KTB at the Contessa locality.

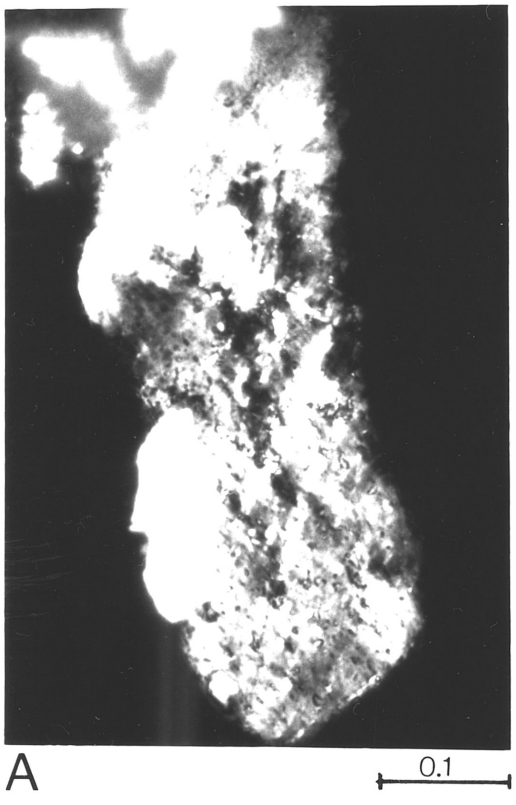
A
0.1
B
0.05
C
0.05
D
0.05

(figure 2-19) reveal evidence of shock deformation in the form of the shock mosaic structure, commonly partially recovered, well above and below the KTB proper. Planar features are very rare at Gubbio (e.g. Bohor et al, 1985), and make up far less than 1% of the clastic fraction. The small size of the grains studied (<50 microns), combined with technical difficulties in the thin sectioning process, made the obtaining of good quality micrographs; a few representative shock microstructures are shown in figure 2-20. Carter et al (1990) reported optical orientation measurements of 52 sets of planar features in 46 grains of quartz (figure 2-15D) from Gubbio. As in the volcanic samples, Raton separates, and experimentally-shocked quartzite, the ω form predominates at Gubbio, with secondary concentrations of the $\pi$, $m$, and $a$ forms. At Gubbio, as in the high-temperature experiment, only 13% of the quartz grains containing planar features had multiple sets.

Of the 52 total sets observed at Gubbio, only 6 sets occur at the KTB proper. The remaining 46 sets occur up to 2.0 m above and 1.8 m below the KTB at Bottacione, and up to 2.12 m above and 1.72 m below the KTB at Contessa. The 6 grains that do contain duplex sets of planar features are distributed at 2.12 m above the Contessa KTB (2 sets), 0.6 m above the Contessa KTB (1 set), 2.0 m above the Bottacione KTB (1 set), and at the Bottacione KTB (2 sets). In addition, samples well above and below the KTB at Bottacione were analyzed for shock with negative results. These analyses from 89.6 to 218.9 m below, and 5.06 to 23.5 m above the KTB revealed that the shock microstructures observed are significantly above background, although the shock deformation across the transition is spaced over several meters. The results of Carter et al (1990) reinforce the idea that careful searches for KTB phenomena must include considerable stratigraphic distances both above and below the KTB proper.

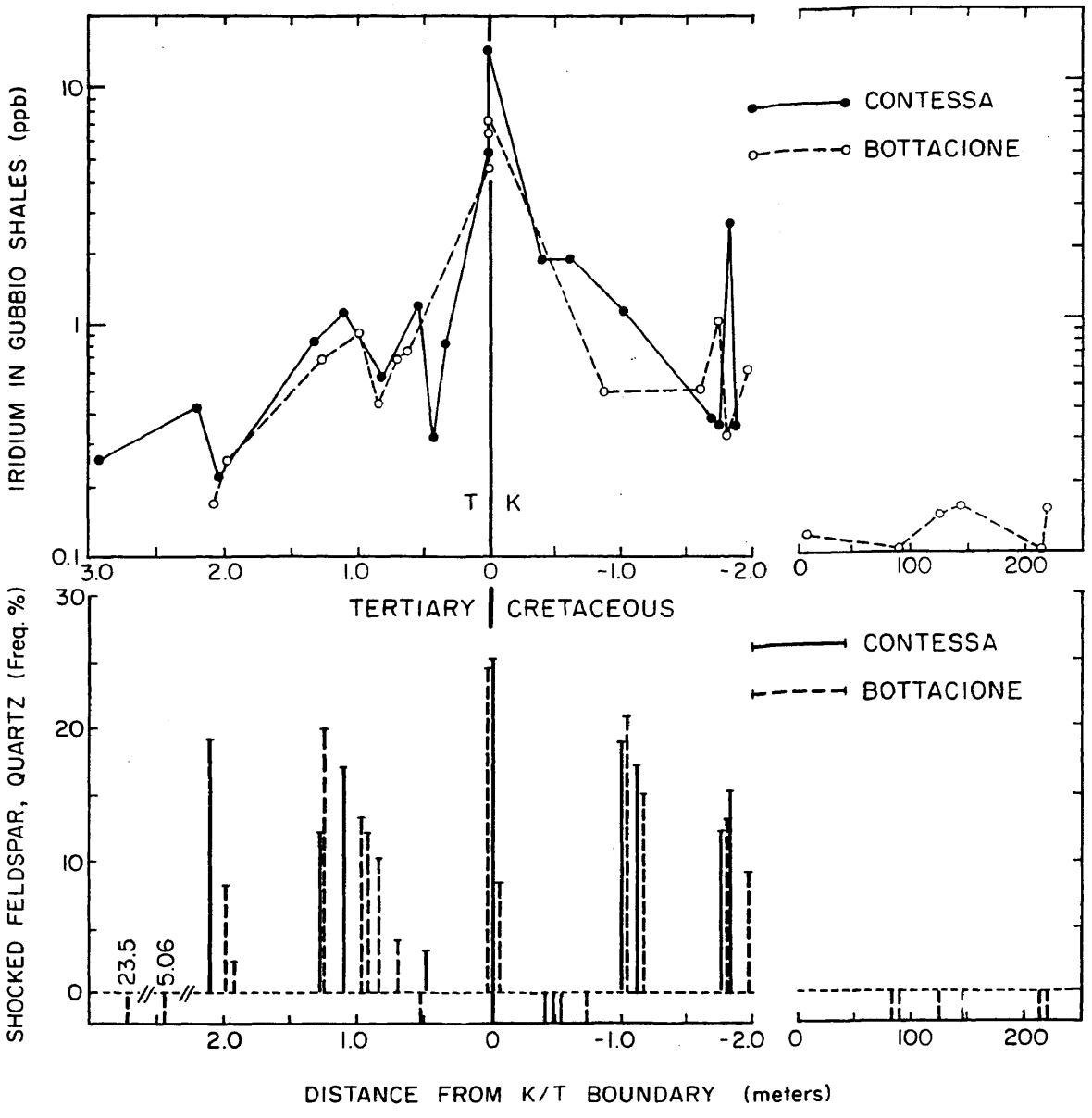


Figure 2-21: Iridium concentrations on a carbonate-free basis in clays from the Bottacione and Contessa localities as a function of distance from the KTB (Crocket et al, 1988). Summary of shock frequency versus stratigraphic position for all samples plotted at same scale for comparison.

In coordination with the work of Carter et al (1990), Crocket et al (1988) analyzed samples of Bottacione and Contessa material for Ir and other trace elements. Their data for the shale layers at both localities (figure 2-21A) reveal elevated levels of Ir in 13 samples from Bottacione and 16 samples from Contessa between 1.98 m below and 2.12 m above the KTB. These values, which range from 0.3 to 15 ppb, are significantly higher than the background values of 0.1 to 0.2 ppb observed from 6.3 to 218.9 m below the KTB, and also correlate nicely (within sampling limitations) with the shock frequency data of Carter et al (1990). The combined results of these two studies support the contention that explosive, episodic volcanism may have begun up to 0.2 Ma before the KTB, and lasted up to 0.2 Ma into the Paleocene (Officer et al, 1987). Similar zones of extended Ir-enrichment have also been documented at K/T sections in the N. Pacific (Michel et al, 1985), Denmark, Spain, and France (Rocchia et al, 1987), Germany (Graup et al, 1989), and New Zealand (Tredoux et al, 1989).

## Manson Crater as a K/T Candidate

One of the glaring problems with the Alvarez hypothesis has been the lack of a crater of sufficient size with an age date of 66 Ma. Izett (1987b) has proposed that the Manson structure in Iowa (figure 2-22) may be the source of the shocked quartz at the KTB. The Manson structure is about 35 km in diameter (Hoppin and Dryden, 1958; Hartung et al, 1988; Anderson and Hartung, 1988) and is buried under glacial till deposits, making direct study difficult. $^{40}Ar/^{39}Ar$ dating of shocked microcline from drill cores at Manson yields an age date of 65.7 ± 1.0 Ma (Kunk et al, 1989) which supports the assertion of Izett (1987b). However, paleomagnetic data (Cisowski, 1988b)

indicate that the Manson impact event occurred during a normal magnetic polarity interval, while the KTB occurs in reversed chron 29R.

The Manson structure consists of an uplifted Precambrian basement complex of gneiss and metagranite, with a diameter of 2 to 5 km and total uplift of about 6000 meters above the surrounding basement. Early petrographic work by Short (1966) and Bunch (1968) revealed the presence of multiple intersecting sets of decorated planar features with the ω orientation dominant. Surrounding the central uplift is a ring structure with a diameter of 32 to 35 km. Hoppin and Dryden (1958) suggested that thickening of lower Cretaceous shales and sandstones in the ring was indicative of as much as 340 meters of downward displacement in the late Cretaceous. This observation is most intriguing considering that the $^{40}Ar/^{39}Ar$ date for the structure post-dates the proposed tectonism. The lower Cretaceous strata within the ring structure appear to also be deformed severely and fractured as would be expected for the outer margins of an impact structure.

Gravity surveys over the Manson structure (Holtzman, 1970) revealed a large negative anomaly over the ring structure, which was attributed to the lower density of the Cretaceous units relative to the surrounding Paleozoic limestones and dolomites. Holtzman (1970) also noted that unpublished magnetic surveys across the structure suggested the presence of mafic to ultramafic rocks at fairly shallow depths below the structure.

Petrographic analysis of the Manson basement rocks (figure 2-23) reveals that the rocks in the central uplift are strongly to intensely shocked, showing strong mosaicism in quartz and feldspar, single and multiple sets of

Figure 2-22: Map of the Manson structure, Iowa, showing the regional geology and structural setting. symbols used in the map include: $X^2vg$ = Lower Proterozoic granitoid and volcanic rocks; XYg = Lower and Middle Proterozoic granite and gneiss; $Y^3v$ = Middle Proterozoic basalt, rhyolite, and volcanic/sedimentary rocks; $Y^3so$ = Middle Proterozoic red lithic sandstone, siltstone, and mudstone; and $Y^3s$ = Middle Proterozoic red to buff quartzose clastic rocks. Diagram after Izett (1987b).

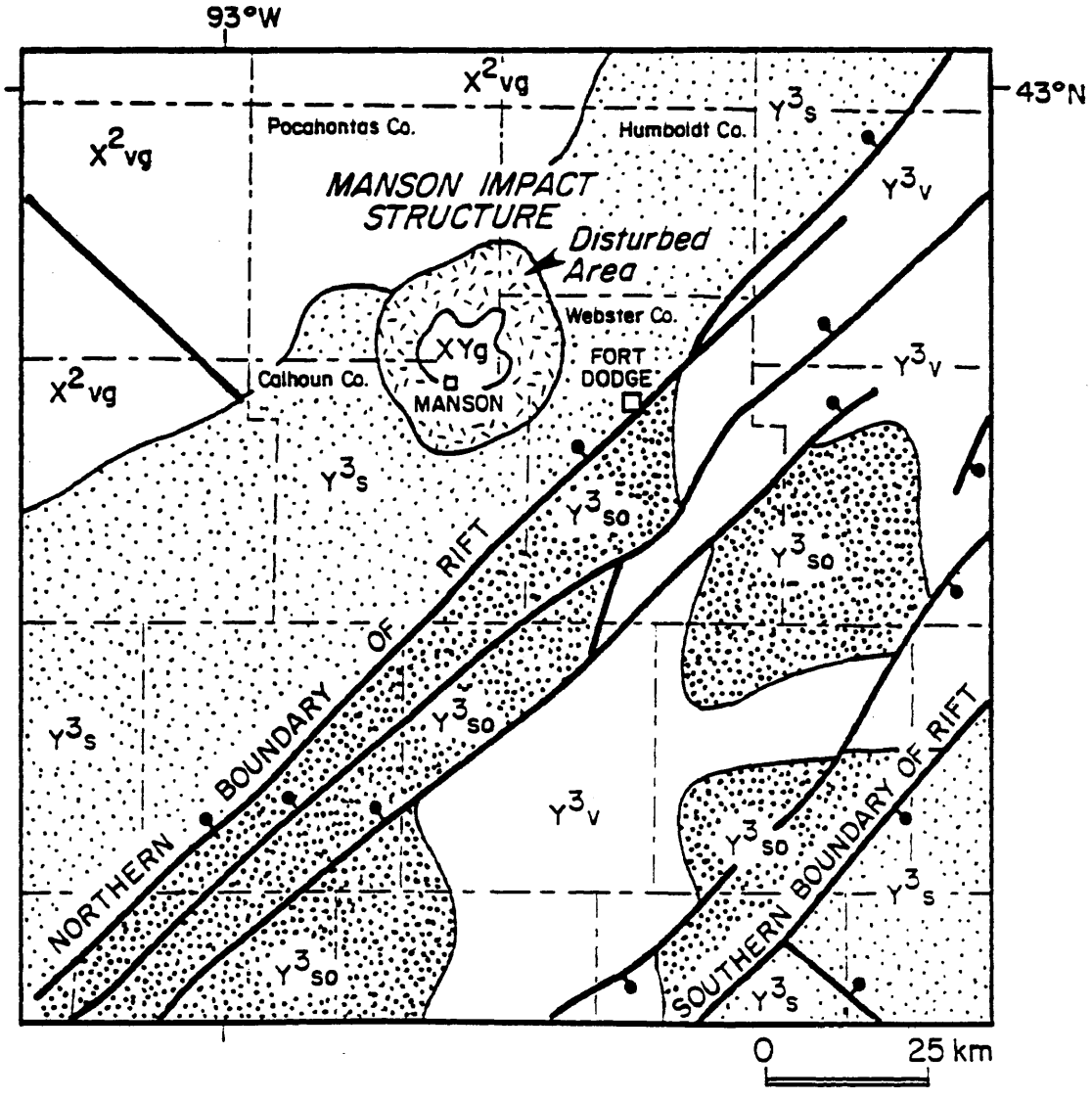
93°W
43°N
$X^2_{vg}$
$X'^2_{vg}$
Pocahontas Co.
Humboldt Co.
Webster Co.
Calhoun Co.
MANSON IMPACT STRUCTURE
Disturbed Area
XYg
MANSON
FORT DODGE
$Y^3_s$
$Y^3_v$
$Y^3_{so}$
NORTHERN BOUNDARY OF RIFT
SOUTHERN BOUNDARY OF RIFT
0
25 km

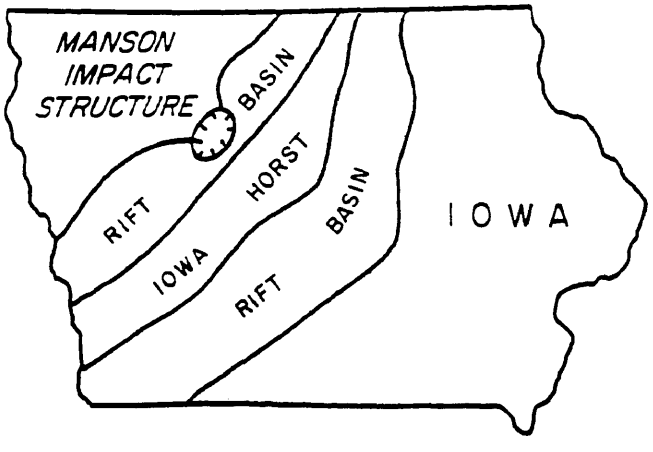
MANSON IMPACT STRUCTURE
BASIN
RIFT
IOWA
HORST
BASIN
RIFT
IOWA

Figure 2-23: Optical micrographs of shock-induced microstructures from the basement rocks of the Manson structure. A. Decorated planar features in quartz showing a curved habit from subsequent deformation after shocking. B. Shock mosaicism and planar fracturing in feldspar. C. Decorated multiple intersecting sets of planar features in quartz with a primary set trending NNW, and a second smaller set trending WNW. D. Shock mosaic structure in quartz showing significant recovery, but preserving single sets of planar features in some domains.

A

65 µm

B

400 µm

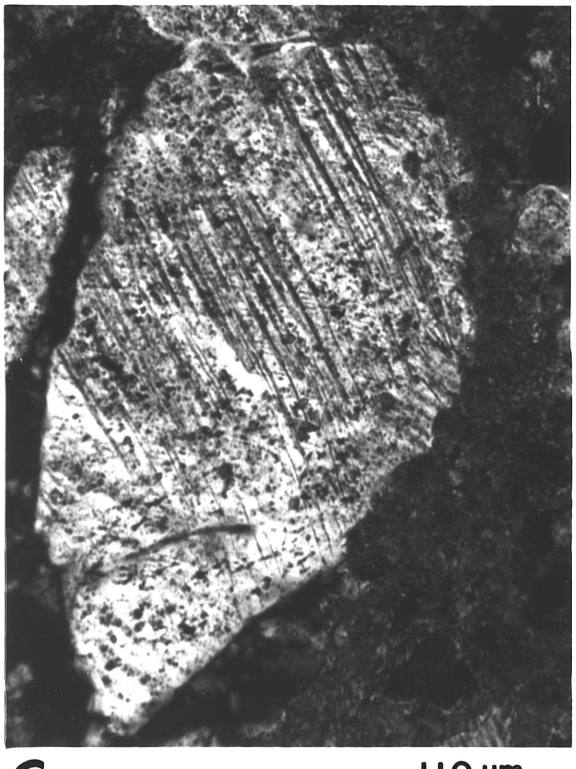

C

110 µm

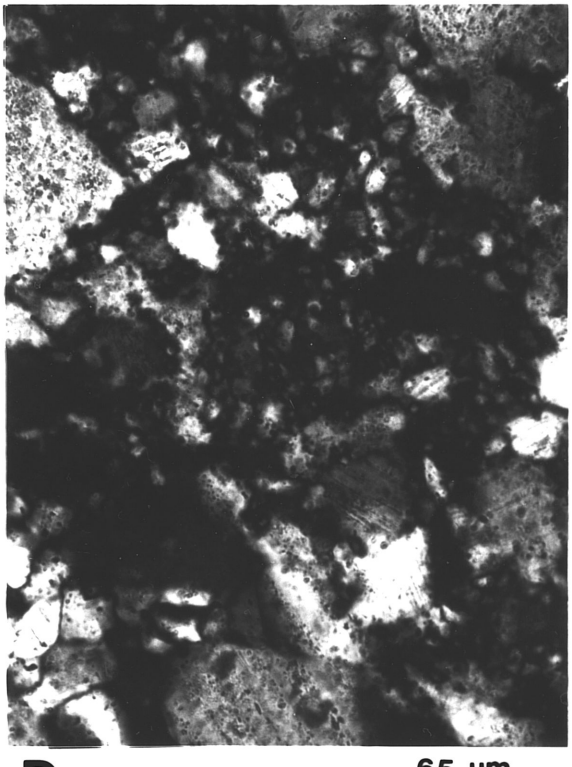

D

65 µm

planar features, planar fractures, and significant post-shock recovery and annealing. The presence of these microstructures indicates that Manson is an impact structure and that a significant degree of thermal metamorphism and tectonic deformation occurred after the impact event. In sharp contrast, petrographic analysis from the lower Cretaceous shales and Proterozoic clastic rocks from well cuttings in the ring structure show no evidence of shock microstructures (Officer and Carter, in press). This observation emphasizes the need for further work to explain some of the apparently contradictory evidence in the Manson area.

## Discussion

The data for the volcanic materials, high-temperature experiments, and natural materials from the KTB demonstrate several important results that are applicable directly to the KTB problem. First, the results for the volcanics indicate that the use of shock-induced microstructures as an exclusive diagnostic indicator of impact is incorrect. The presence of the shock mosaic structure and single sets of planar features in the volcanics supports the contention that moderately high pressures can be attained during high-strain-rate events in volcanic systems. The absence of multiple intersecting sets of planar features in quartz in the volcanics may indicate that (1) the pressure conditions during deformation in the volcanics are different than those which obtain during impact so that multiple sets of features are not produced; (2) the high temperatures during volcanic shock events prevent the formation of multiple sets of features at pressure conditions similar to impact; or (3) they simply have not yet been discovered for the several reasons discussed above. The constraints on the eruption process may support the first

assertion since it is unlikely that pressures over 20 GPa can obtain during volcanic eruptions; however, coupled effects of elevated temperature and reduced strain rate on peak stresses required are not yet resolved although stress reduction is clearly indicated (see chapter 4).

Results from the shock-recovery experiments of Reimold and Hörz (1986a) on quartzite reveal that pre-shock temperature does have a marked effect on the distribution and orientation of planar features as well as the shock mosaic structure. The great decrease in numbers of planar features indicates that the plastic strains and phase transformations that occur during the shock event are being fundamentally altered by the elevated temperatures, and that the mechanisms of strain-energy accommodation are probably shifting from heterogeneous to more homogeneous ones. It is hoped that refinement of observations such as these can provide essential insight into the thermodynamics and kinematics of high-strain-rate deformation

Results from the Raton KTB samples indicate that the character and statistical nature of the observed microstructures are more compatible with a high-temperature, moderate shock-stress event (P<25 GPa), than an impact event as proposed in the Alvarez theory. Additionally, the stratigraphic distribution of shock deformation across the K/T transition from Gubbio is in accord with an event of extended duration lasting on the order of $10^5$ to $10^6$ years, which is also supported by the geochemical data from the sites studied.

# CHAPTER III

## CHEMISTRY AND MINERALOGY ACROSS THE CRETACEOUS-TERTIARY BOUNDARY AT DSDP SITE 527, WALVIS RIDGE, SOUTH ATLANTIC OCEAN, AND ODP SITES 689B AND 690C, MAUD RISE, WEDELL SEA

## Introduction

The landmark paper by Alvarez et al (1980) has stimulated a tremendous amount of research on Cretaceous-Tertiary (K/T) boundary sections around the world. The proposal that a protracted period of intense volcanism (Officer and Drake, 1985) caused the K/T mass extinctions and the differences in duration of volcanic versus impact scenarios require that analytical work on K/T sections extend well above and below the boundary clay. Recent work on sediments from Gubbio (Carter et al, 1990) and at Maud Rise (Huffman et al, 1988) suggests an extended duration of shock deformation and iridium deposition (Crocket et al, 1988; and Rocchia et al, 1989) spanning a period of about $5 \times 10^5$ years. The problem of temporal resolution at K/T time and distinction of multiple events across the boundary can be resolved only through detailed and extended stratigraphic analysis of many marine and terrestrial sections. The marine K/T boundary section at DSDP Site 527 along the Walvis Ridge in the South Atlantic Ocean was selected for a detailed study of chemical changes and evidence for shock deformation across the boundary.

The purpose of this study was to analyze for trace-elements by neutron activation and for shocked minerals from a 10 meter section across the K/T boundary at Site 527. The results are correlated to determine what K/T related

events are recorded at this site, and how these events fit into the various hypotheses for the K/T mass extinction.

## The K/T Transition at Maud Rise, Wedell Sea

The results for shock deformation and Ir at Gubbio were sufficiently intriguing to warrant similar studies on other K/T sections. At the time the Gubbio work was being completed, samples from ODP Holes 689B and 690C from the Queen Maud Rise, Wedell Sea were made available to our group. Inasmuch as Barker et al (1987) reported continuous sedimentation associated with appreciable thicknesses of alleged volcanogenic material across the KTB at both localities, these two sites seemed ideal for this type of study.

For our preliminary analyses, 21 specimens were obtained at 0.5 m intervals of 5 m sections, bisected by the KTB, from holes 689B and 690C. Approximately 2 $cm^3$ of each sample were treated with dilute (10%) HCL to remove calcium carbonate and treated sonically to disaggregate the clay fraction. The acid was then neutralized by dilution and addition of sodium carbonate, and the remaining solids were separated by wet sieving into fractions greater and less than 63 microns. The fine fraction was subjected to a series of Stoke's settling tests to remove the clay fraction (<20 microns). The remaining material fractions (i.e. >63 and 20-63 microns) were dried and mounted in Epokwik epoxy for preparation of polished thin sections.

Total carbonate content of each sample was determined by fusion of about 200 mg of sample powder in a LECO WR12 carbon analyzer (Appendix I). Working under the assumption that all carbon occurs as carbonate in these

samples, the average carbonate content of hole 689B in the interval sampled is 92 wt%, and the range is 87.1 to 95.3%. For hole 690C, the average is 82 wt% and the range is 63.0 to 92.4 %. A second aliquot of sample material was analyzed for iridium by Dr. James Crocket., McMaster University using the Radiochemical Neutron Activation Method. Separate splits of sample were also analyzed by INAA for other trace elements, but the high carbonate content of the samples made the interpretation of any apparent trends questionable due to the large correction factors and their errors which must be applied.

Polished thin sections of both size fractions from the Maud Rise samples were studied to determine the structural state of quartz and feldspar grains. The deformational state of grains transected in linear traverses of the sections was characterized as either: (1) undeformed or deformed tectonically; or (2) deformed by dynamic deformation. Dynamically-deformed grains showing the shock mosaic structure, commonly partially recovered, were observed in all of the sections. Their frequency as a function of stratigraphic location relative to the KTB is shown in figure 3-1. Inasmuch as there was no systematic difference between frequency of shocked silicates in the two size fractions, the 1633 observations plotted in the histogram (figure 3-1) represent the combined total number of observations for each specimen. Single sets of planar features parallel to $\omega$ were observed only in three quartz grains in the specimen 0.5 m below KTB in hole 689B.

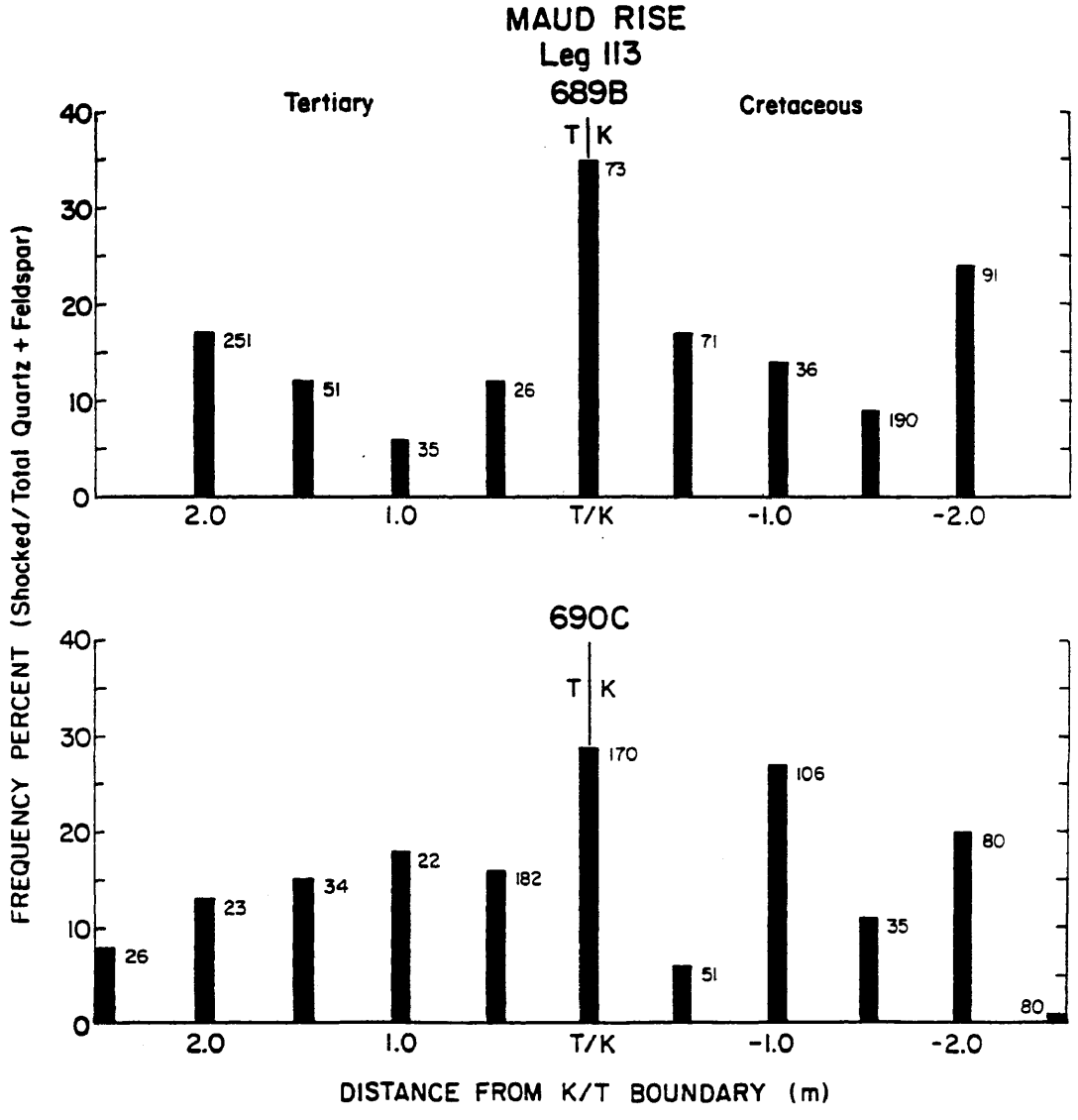


Figure 3-1: Distribution of shocked quartz and feldspar across the KTB at ODP holes 689B and 690C, Maud Rise, Wedell Sea. The number of observations for each sample are listed next to the histogram for each stratigraphic location.

The maximum shock frequency of quartz and feldspar, near 30%, occurs at or near the palynological KTB for both holes (figure 3-1). Shock frequencies vary appreciably both above and below the KTB to at least 2 meters, with especially strong concentrations at -2.0 m and -1.0 m in hole 690C and +2.0 m in hole 689B. The occurrence of 79 (of 80 total grains) unshocked grains in the specimen 2.5 m below the boundary in 690C suggests that background is being approached. To confirm that background is reached away from the KTB, additional samples from the lower Paleocene (13.0 m above KTB) and Upper Maastrichtian (10.5 m below KTB) from hole 690C, and from the lower Paleocene (16.1 m above KTB) and the Upper Maastrichtian (13.0 m below KTB) for hole 689B were analyzed. No evidence of shock deformation was observed in these four samples, which confirms that the data close to the KTB at Maud Rise do represent a significant increase in dynamic processes across the K/T transition.

The shock frequency pattern for the Maud Rise samples compares well with that for Gubbio, and suggests that while peak shock activity occurs at or near the KTB, appreciable shock deformation of silicates took place during events both prior to and following the KTB. Correlations between the shock frequency data and the iridium data (figure 3-2) reveal significant enrichments of Ir roughly coincident with the maximum shock frequency at the KTB. The use of carbonate-free Ir values at this site does not improve the correlation and is problematic because of the very large multipliers which result from carbonate values above 80 wt%. Another concern is the role of bioturbation in these sections, which is undefined at this time. The primary significance of the data for Maud Rise, however, is that they support the observations from Gubbio and other K/T localities, and support the contention

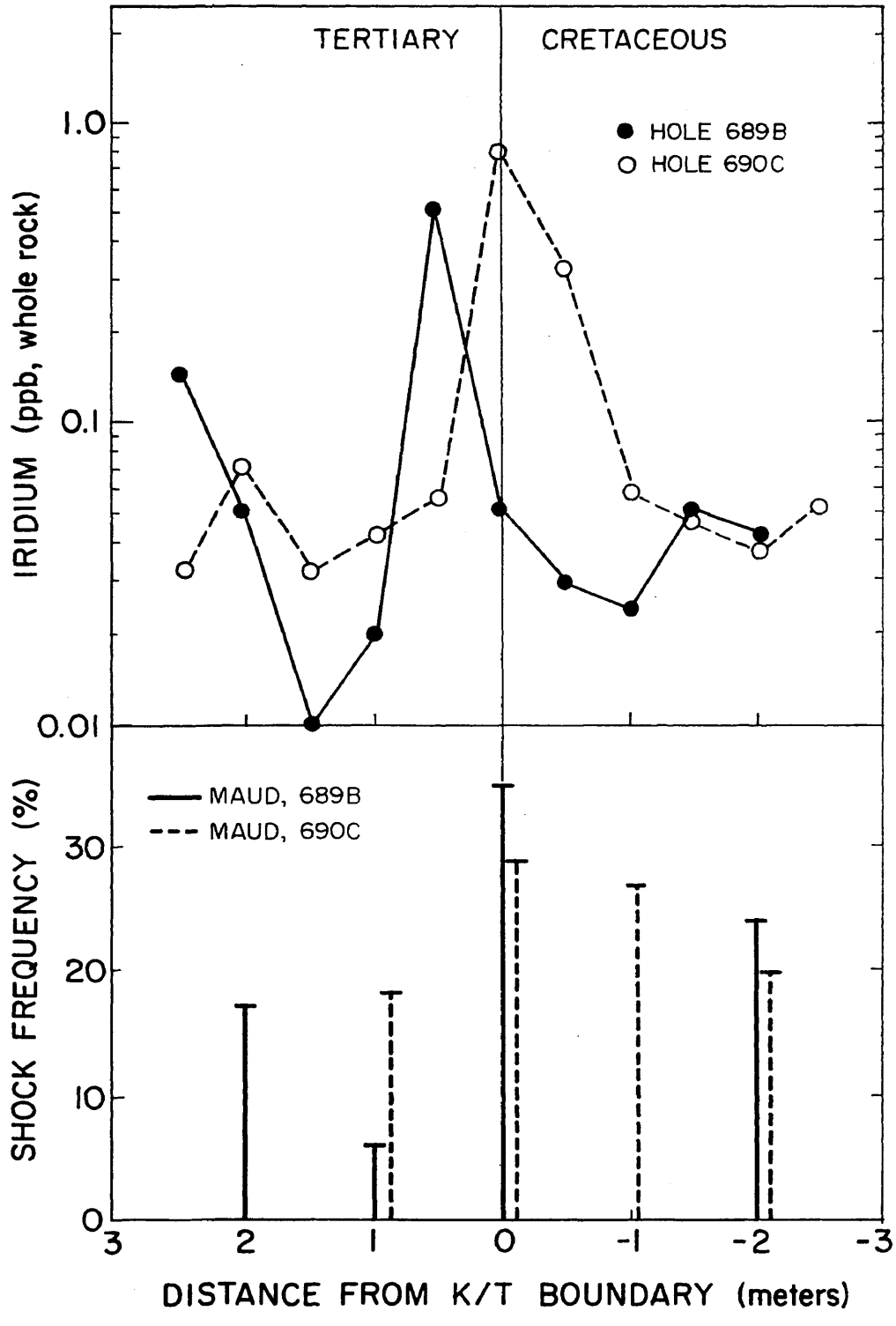


Figure 3-2: Correlation between shock frequency distribution and iridium data for holes 689B and 690C, Maud Rise, Wedell Sea.

that the K/T transition, as defined by shock deformation and iridium enrichments, is most likely not a single instantaneous event, but rather one of extended duration.

## Walvis Ridge, S. Atlantic Ocean

The Walvis Ridge is a roughly linear structural feature which runs SSE off the coast of Africa and divides the Angola and Cape Basins (figure 3-3 inset). The sedimentary section on the Walvis Ridge was sampled on Leg 74 of the Deep Sea Drilling Program (Moore et al, 1984a) at Sites 525 through 529. Geophysical surveys across the Walvis Ridge indicate the presence of magnetic anomaly 32 near the ridge crest with older anomalies present off the ridge axis (Rabinowitz and LaBrecque, 1979; Rabinowitz and Simpson, 1979). These data, along with seismic and gravity data (Chave, 1979; Detrick and Watts, 1979) support the contention that the Walvis Ridge formed in the late Mesozoic by sea floor spreading processes as Africa and S. America rifted apart. A complete description of the geologic and physiographic setting of the Walvis Ridge is provided by Moore et al (1984b).

### Site 527

DSDP Site 527 is the deepest site drilled at Walvis Ridge. It is located in 4437 meters of water off the axis of the ridge to the WNW in the Angola Basin (figure 3-3 inset). The interval recovered at the site begins in the late Maastrichtian with interbedded basalts and sediment and terminates in Pleistocene deposits at the sea floor. A complete K/T boundary sequence was recovered.

Figure 3-3: Paleoreconstructed world map showing the location of land masses at 65 Ma (base map after Alvarez et al, 1982). The stippled areas represent sea floor that has been subducted between 65 Ma and the present. Three major hot spot volcanic centers are shown as smoking volcanoes and include the Deccan Traps of India, the Brito-Arctic volcanic region in the North Atlantic, and the Hawaiian-Emperor hot spot. The inset shows the locations of DSDP Sites 525 to 529, which were drilled during Leg 74. Note that the Walvis Ridge and the Indian subcontinent were both in the southern hemisphere at K/T time.

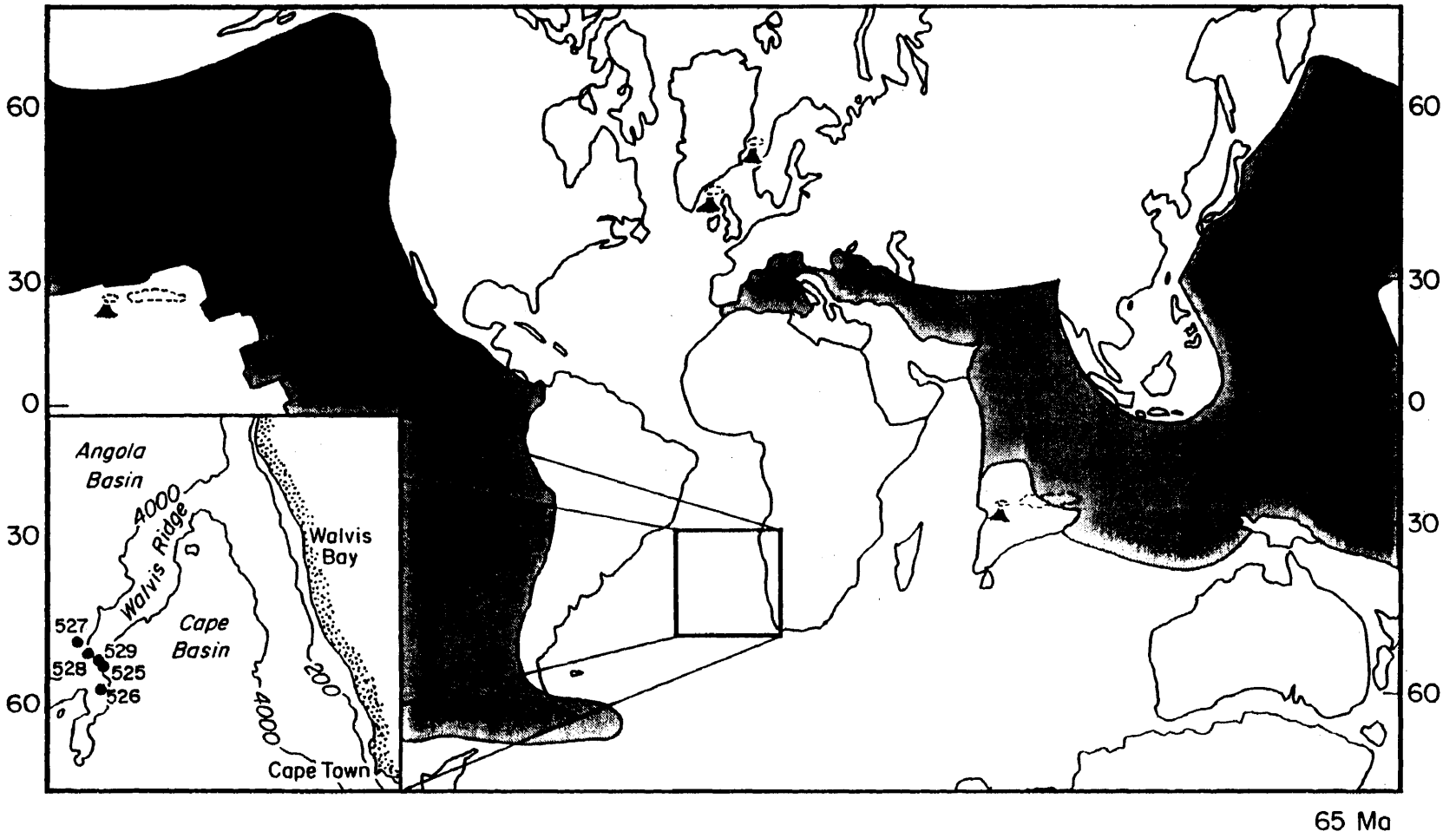
60
30
0
30
60
Angola
Basin
4000
Walvis Ridge
Walvis
Bay
527
529
528
525
526
Cape
Basin
200
4000
Cape Town
60
30
0
30
60

65 Ma

The K/T boundary at Site 527 occurs at 280 meters below sea floor (mbsf; Core 32, section 4, interval 48-52 cm), and is marked by a distinct gray ash deposit followed by an abrupt color change above the boundary (Moore et al, 1984b, see figure 3-4). The abrupt color change is accompanied by a major decrease in rate of deposition from 22 m/Ma below the boundary to 4 m/Ma above the boundary, and a marked decrease in carbonate content (Moore et al, 1984b). Paleomagnetic data indicate that the K/T boundary deposit occurs about three quarters of the way up section in Chron 29R. The age estimate for the boundary deposit is 66.45 Ma (Shackleton et al, 1984), based on paleomagnetic data and estimated rates of sedimentation.

Below the K/T boundary, the sediments are generally buff to medium brown in color, and show signs of macroscopic bioturbation. The only deviation from this character occurs from 1.75 to 2.00 meters below the boundary (281.75 to 282.00 mbsf), where an abrupt change to dark brown clay occurs. Above the K/T transition (280.00 mbsf), the sediments again become darker and vary from medium and rust brown to dark brown. Signs of macroscopic bioturbation are present here also. It has been proposed (Borella, 1984) that the color variations across the K/T interval at Site 527 may be related to local fluctuations in $fO_2$ in the environment; this type of variation is unique to the K/T interval. Some color changes are also related to episodic deposition of volcanic ash during the late Maastrichtian (Boersma, 1984).

The dominant component of sediments below the K/T boundary in Core 32 is carbonate (40-80%). Above the K/T boundary, the carbonate content drops substantially, averaging about 40% with one sample containing only 4% carbonate (figure 3-4). The non-carbonate mineralogy at Site 527 from the

upper Maastrichtian to lower Paleocene consists of 0-10% chlorite, 5-55% illite, trace to 25% mixed layer clays, 10-70% smectite, trace to 10% kaolinite, 0-15% palygorskite, trace amounts of sepiolite, along with small amounts of feldspar, goethite, and quartz (Maillot and Robert, 1984). The most significant change in clay mineralogy at the K/T boundary is a major increase in smectite content directly above the boundary deposit (Chamley et al, 1984). The sharp change to smectite-rich clays at Site 527 indicates a significant change in the character of source areas on the African landmass (Chamley et al, 1984).

## Biostratigraphy

Data available for calcareous nannofossils, planktonic foraminifera, and calcareous dinoflagellates suggest that the K/T extinctions of these calcareous marine microorganisms were not instantaneous or exactly synchronous, and occurred over an interval from 81 cm below the K/T boundary (280.81 mbsf) to 1.70 m above the boundary (278.30 mbsf), which is equivalent to roughly 0.5 Ma of deposition.

Danian calcareous nannofossils first appear at 10 cm below the gray ash layer which marks the K/T boundary. From this location (280.10 mbsf) to the boundary, Upper Cretaceous species are mixed with a typical Danian assemblage. The boundary layer itself contains mostly Cretaceous forms (Manivit, 1984). Immediately above the K/T boundary, the majority (90%) of nannofossils are redeposited Cretaceous forms, with very few Paleocene fossils occurring until much further into the Danian (Alcala-Herrera, 1989). Some Cretaceous coccoliths actually survive the extinction horizon and diversify rapidly into the lower Danian section. The species across this horizon also

show a change from tropical/subtropical to mostly temperate, supporting the contention of global cooling across the K/T boundary. The coccoliths recovered from the extinction over a 1.5 Ma period (Alcala-Herrera, 1989).

Planktonic forams are generally not well preserved at Site 527. The gray boundary layer contains a unique foram assemblage which is better preserved at nearby Site 528. This assemblage contains small specimens of A. mayoroensis zone fossils, along with *Hedbergella monmouthensis* and morphotypes of *Pseudoguembelina excolata* (Boersma, 1984). The foram tests in the boundary layer have significant amounts of pyrite embedded in them. The Paleocene foram assemblage above the boundary contains mainly *P. eugubinus* with a dominance of heterohelicids. The first occurrence of *P. eugubinus* is 10 cm above K/T (279.90 mbsf).

In contrast to the nannofossils and forams, the Cretaceous calcareous dinoflagellates continue into the Danian with the last species surviving up to 1.70 m above the boundary (278.30 mbsf; Futterer, 1984). The four Cretaceous species of Pithonella which occur in the late Maastrichtian start to disappear well before the K/T boundary layer was deposited. *P. cylindrica Pflaumann* is last reported at 5.10 m below K/T (285.10 mbsf), and is absent at 81 cm below the boundary (280.81 mbsf), suggesting that the first dinoflagellate extinction occurred from 250,000 years to 50,000 years before K/T. The species *P. sp. 1* and *P. globosa* are last observed at 10 cm below K/T (280.10 mbsf) and 12 cm above K/T (279.88 mbsf) respectively. The species *P. krasheninnikovi Bolli* persists until 1.70 m above K/T where it is replaced finally by the first Danian species, *P. parva*, which persists up section into the Pleistocene (Futterer, 1984).

## Analytical Methods and Sample Preparation

45 samples (10 $cm^3$ each) were taken at 30 cm intervals across a 10 meter section straddling the K/T boundary, and at 15 cm intervals within 2 meters of the boundary. Each sample was taken from the core using plastic tools and rubber gloves to avoid contamination. The samples were split with one set (5 $cm^3$) dedicated to Instrumental Neutron Activation Analysis (INAA) and studies of the deformational state of the silicates and the other set for Radiochemical Neutron Activation Analysis (RNAA) and clay mineralogy. The RNAA and carbon fusion analyses were performed by Dr. James H. Crocket of McMaster University.

### Sample Preparation for INAA and Shock Deformation

The 5 $cm^3$ (10 gm) samples used for INAA and microstructural work were split into two fractions, 2 gm for INAA and 8 gm for microstructural analysis. The 2 gm INAA split was powdered in an agate mortar using clean room procedures. After crushing, the powders were dried in an oven at 110°C for 24 hours and placed in a dessicator. The samples were homogenized using a sample splitter and a 200 mg aliquot was analyzed for carbonate content by fusion in a LECO WR12 carbon analyzer. The remaining portion of the split was used for INAA.

Samples (70 mg) and duplicates were weighed in a Mettler microbalance and sealed in polyethylene vials with a hot iron. The samples were counted by a 3-step process which permits analysis of 40 elements. Samples were irradiated in a pneumatic tube facility at the Texas A&M University (TAMU)

Research Reactor for 30 seconds at a thermal Neutron flux of $10^{13}$N/cm$^2$/sec, and were counted for 500 seconds after a 15 minute delay. Multi-element standards used in the analysis were USGS G-2 granite and NBS 1633A Coal Flyash. The samples were later irradiated in an aluminum rotisserie for 14 hours at the TAMU Research Reactor. The samples and standards were counted after a 7-day delay (1000 sec count) and 21-day delay (4000 sec count) for intermediate- and long-lived isotopes respectively. Estimated errors for the analyzed elements are less than 10% for Na, Mg, Mn, Ca, Al, La, Lu, Sm, Yb, Ce, Co, Cr, Cs, Eu, Fe, Nd, Rb, Sc, Tb, and Zn; about 10% for Ti, V, Dy, As, Sb, Ba, Sn, Sr, and Ta; and 10-20% for U, Ni, Zr, and Se. Carbonate content was calculated from percent carbon determined by fusion and, based on the assumption that organic carbon was negligible, has an estimated error of ±3%.

The remaining 8 gm fraction of raw sample was treated in 75% HCl to remove carbonate, and then subjected to a series of Stoke's settling tests to separate the clastics (>20 μm size) from the clay fraction. The clastic grains were separated into two size fractions of >63 microns and 20-63 microns. Nearly all the recovered material fell into the finer fraction in most samples. The volume of clastics, which consisted almost entirely of quartz and feldspar, was less than 5% of total volume in all samples, and was less than 1% in most cases. Doubly polished thin sections (20 microns thick) were prepared from each separate for optical microscopy.

Radiochemical Neutron Activation Analysis

Iridium was determined by radiochemical neutron activation analysis (RNAA) using a tellurium co-precipitation method to collect noble metals. The

procedure is similar to that described by Stockman (1983). In the present application this procedure was optimized to determine only iridium.

Samples of approximately 250 mg were sealed in General Electric high-purity fused-quartz tubing and irradiated together with standards in the McMaster University Nuclear Reactor in a thermal neutron flux of 8 to 9 x $10^{13}$ neutrons/$cm^2$/sec for time periods of 24 to 48 hours.. Iridium standards were prepared from Johnson Matthey Spec-pure grade iridium salts, usually ammonium chloroiridate. After irradiation a decay period of 4 to 5 weeks was allowed prior to radiochemical processing. Where INAA for long half-life elements was also performed, appropriate rock standards were included in the irradiation package, and counting was performed immediately prior to RNAA.

Iridium was counted on a gamma spectrometer system consisting of a coaxial intrinsic germanium detector (peak-to-compton, 47:1; resolution, 1.9 KeV at 1.33 MeV; Canberra Ltd.) shielded by 10 cm of lead, a Canberra Model 2020 spectrometer amplifier and a Canberra Series 35 multichannel analyzer. Spectra were taken on the MCA and transferred to a microcomputer where photopeaks were analyzed with a gamma spectral analysis program, MicroSAMPO (Koskelo et al, 1981). Two iridium photopeaks were recorded, at 316 and 468 KeV. The count period was set so that either $10^4$ counts were accumulated in the 316 KeV spectral region or the sample was counted for a period of 12 hr.

# Results

## General Chemostratigraphy

Results from INAA, RNAA, and carbonate analysis were plotted versus depth to determine chemical variations across the K/T boundary and any possible relation to the evidence for shock deformation. Data for carbonate and aluminum content (figure 3-4, and Appendix I) indicate that a marked decrease in carbonate content begins at the boundary, with additional decreases at 53 cm and 1 m above the boundary and reaches a minimum at 1.40 meters above the boundary. Another sharp change in carbonate content occurs at 3 m above the boundary. The first major reductions in carbonate content, concomitant with increases in Al content, are synchronous with the three major negative excursions in $\partial^{13}C$ recorded by Shackleton and Hall (1984; figure 3-6 and appendix I). The carbonate minimum at 278.6 meters correlates well with the maximum excursion of the $\partial^{13}C$ value, supporting the concept that the $\partial^{13}C$ excursion is related to productivity collapse (Shackleton and Hall, 1984; Tappan, 1968). The carbonate and $\partial^{13}C$ data indicate that the collapse in primary productivity at Walvis Ridge occurred in three stages. Based on the age data of Shackleton and Hall (1984), these events occurred at approximately 280 mbsf (66.45 Ma) at the K/T boundary, at about 279.47 mbsf (66.40 Ma), and at 278.6 mbsf (66.285 Ma) with the first two events being followed by a short period of recovery. After the third event, the amount of carbonate increases and the $\partial^{13}C$ value recovers steadily into the Paleocene. However, it has been suggested that the $\partial^{13}C$ data simply reflect the redeposition of Cretaceous coccolith tests (Alcala-Herrera, 1989). These tests, which make up the majority of the carbonate material for the 1 meter of

Figure 3-4: Data from Site 527, Core 32 across the K/T boundary. The K/T boundary is located at 280.00 mbsf in magnetic Chron 29R. Panel 1 shows the paleontological, lithologic, and paleomagnetic data for the interval sampled (data from DSDP Initial Reports, Site 527 core barrel sheets). Age estimates in panel 1 are from Shackleton and Hall (1984). Panel 2 displays the shock- and tectonic-deformation stratigraphy, with frequency of planar features in black, frequency of mosaicism in light stipple, and frequency of tectonic microstructures in white. Dots below the zero line signify samples which showed no evidence of any deformation. Panel 3 shows percent carbonate calculated as $CaCO_3$ from total carbon fusion data. Panel 4 shows percent Al from INAA.

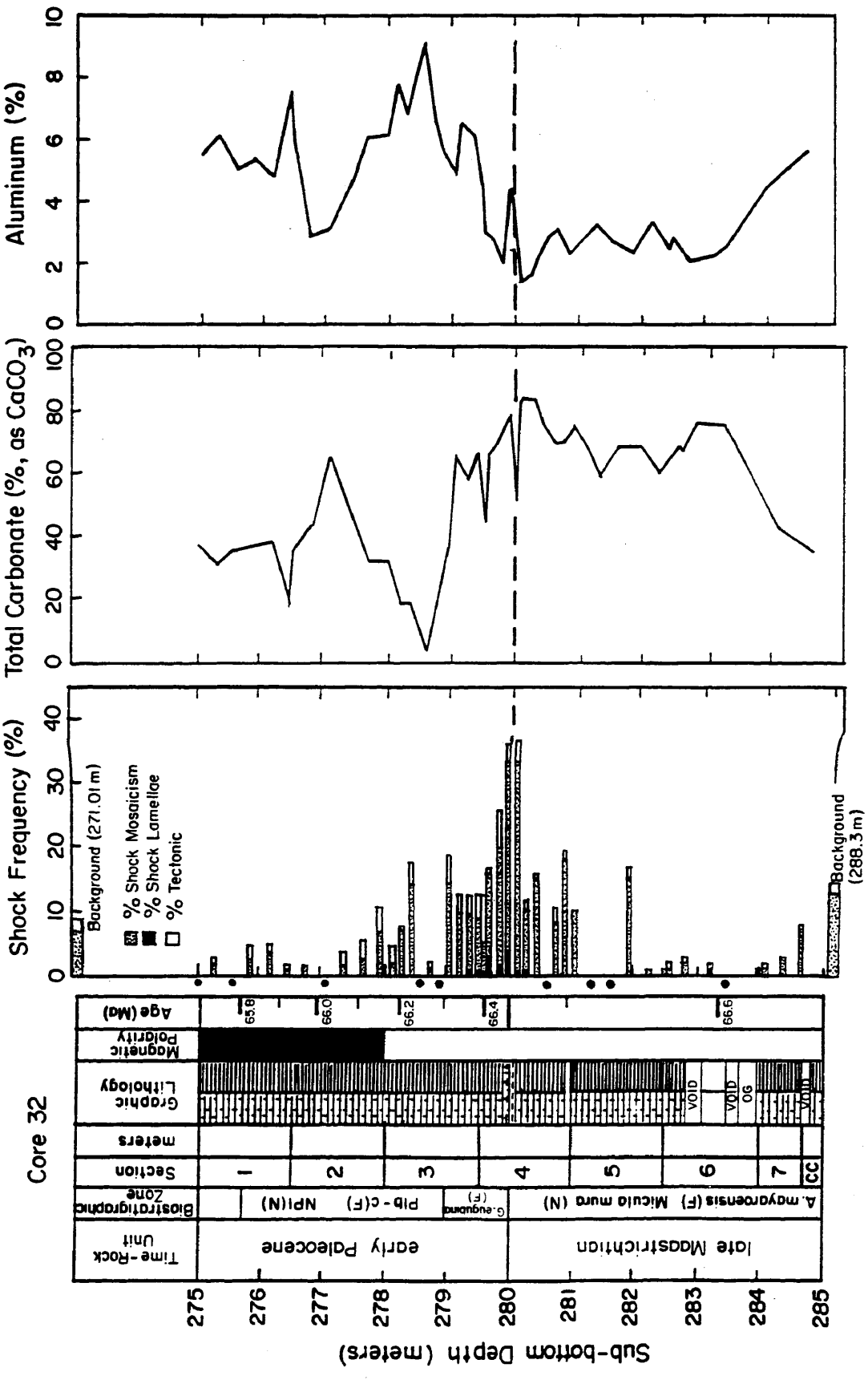
Core 32
Time-Rock Unit
Biostratigraphic Zone
Section
meters
Graphic Lithology
Magnetic Polarity
Age (Ma)
late Maastrichtian
early Paleocene
A. mayaroensis (F) Micula mura (N)
G. equidens (F)
Plb-c(F) NPl(N)
1
2
3
4
5
6
7
CC
VOID
OG
65.8
66.0
66.2
66.4
66.6
Shock Frequency (%)
% Shock Mosaicism
% Shock Lamellae
% Tectonic
Background (271.01 m)
Background (288.3 m)
Total Carbonate (%, as CaCO3)
Aluminum (%)
Sub-bottom Depth (meters)
275
276
277
278
279
280
281
282
283
284
285

sediment directly above the extinction horizon, would cause an artificially slow decline in $\partial^{13}C$ as their numbers decreased into the Danian. If this interpretation is correct, then the changes in carbon isotopes and total carbonate were probably more abrupt than is reflected by the whole-rock data.

The $\partial^{18}O$ data of Shackleton and Hall (1984) (figure 3-6) indicate a slow cooling of about 2°C over 1.4 x $10^5$ years in the late Maastrichtian, followed by a period (about 6 x $10^4$ years) of rapid cooling to 50 cm above the boundary, and then rapid warming and return to Cretaceous $\partial^{18}O$ values. This extended period of cooling and warming may be a secondary climatic effect from volcanism or impact. The boundary events may have acted as forcing agents for an abrupt climatic change which lasted significantly longer than the duration of the causative events (Crowley and North, 1988).

Trace elements at Site 527 can be divided into 3 categories, those elements that follow carbonate, those that follow the clays, and those that follow neither of these components consistently. The elements that follow carbonate are Ba, Sn, and Sr. Those that follow the clays are Cr, Cs, Fe, Rb, Sc, Se, Th, Ti, U and Zn. Those that appear to be independent of either major fraction or show significant enrichments above background are As, Ce, Co, Ir, Mg, Mn, Ni, Sb, and Zr. Chemostratigraphic plots of selected data and their carbonate-free values (figure 3-5) suggests that Ir, some of the siderophile (Fe, and Co) and lithophile (Cr, Cs, and Sc) elements along with selenium, and the chalcophiles (As and Sb), each display different enrichment patterns. The only large enrichment of Ir and Ni is nearly coincident with the boundary as are the largest concentrations of As and Sb. However, the siderophiles,

Figure 3-5: Chemostratigraphy for selected elements from Site 527. The ordinate is elemental concentration as shown in each plot, and the abscissa is depth in meters below the sea floor (mbsf). The open symbols are whole rock values and the closed symbols are carbonate-free data based on a multiplier of [100/(100-% carbonate)].

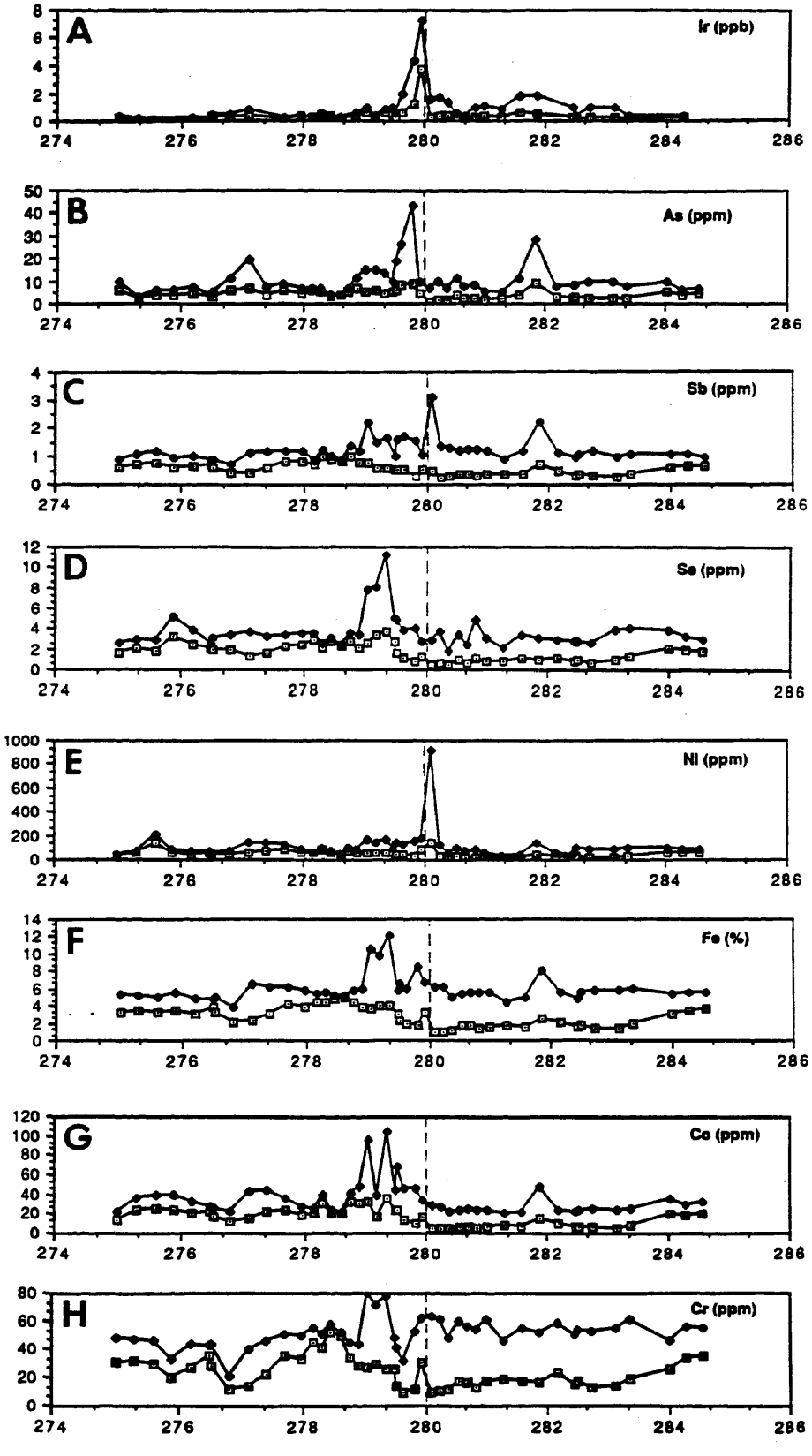
A
Ir (ppb)
B
As (ppm)
C
Sb (ppm)
D
Se (ppm)
E
Ni (ppm)
F
Fe (%)
G
Co (ppm)
H
Cr (ppm)
Depth (mbsf)

lithophiles, and selenium also show strong enrichments (carbonate-free basis) over background to 1.0 meters above the boundary and moderate enrichments below the boundary. Ir, Fe, Co, As and Sb show appreciable enrichments over background at 1.87 m below the boundary (281.87 mbsf), which may correlate with a small negative excursion in $\partial^{13}C$ (figure 3-6).

Large multipliers required for recalculation of carbonate-free values when carbonate is high (>80%) are problematic because small errors in carbonate values can cause major changes in the multiplier. In contrast, the data for Al are well constrained, and may be used to determine the enrichment of other elements. Ratios to Al content (Figure 3-6) of some selected elements reveal that some of the enrichments above the K/T boundary are confirmed (Co and Fe) while others (Cr, Cs, Sc, and Se) are not. The lack of enrichments for Cr, Cs, Sc, and Se ratiod to Al supports the contention that they are following the clay content. Confirmed enrichments for As, Fe, Ir, and Sb suggest that these elements are enriched relative to both the clay and carbonate fractions. These Al-normalized representations of the chemistry show more clearly the similarities in enrichment patterns of these elements. The Mg/Fe ratios (figure 3-6A) suggest a change to less magnesian material at Site 527 coincident with the elemental anomalies at 281.87 mbsf, and also just above the boundary at 279.82 mbsf. These changes in Mg/Fe ratio, which are also reflected in lower Mg/Al ratios, may be related to changes in clay chemistry or changes in mineralogy due to basaltic volcanic ash or sulfide deposition. In particular, the strongest decrease in Mg/Fe, which is coincident with enrichments in other trace elements at 1.87 meters below K/T (281.87 mbsf), is in the middle of a 25 cm thick zone of dark brown to nearly black sediment surrounded by light brown to buff sediments. This sudden change to

Figure 3-6: Chemostratigraphy for Mg/Fe ratio, selected elemental ratios to Al, and the $\partial^{13}C$ and $\partial^{18}O$ data of Shackleton and Hall (1984).

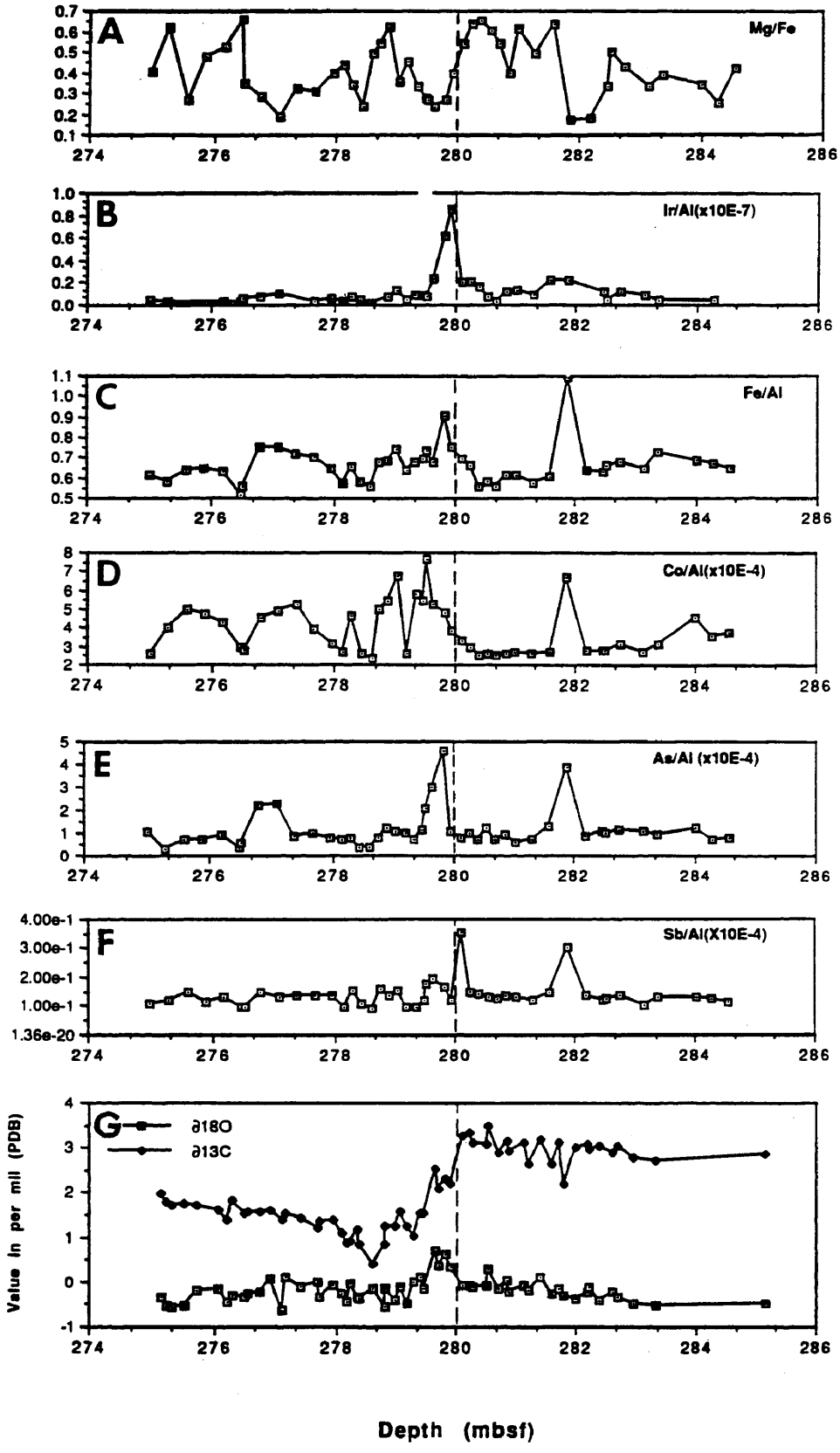
A
Mg/Fe
B
Ir/Al(x10E-7)
C
Fe/Al
D
Co/Al(x10E-4)
E
As/Al (x10E-4)
F
Sb/Al(X10E-4)
G
δ18O
δ13C
Value in per mil (PDB)
Depth (mbsf)

much darker material may reflect an influx of volcanic ash with Mg/Fe and Mg/Al ratios lower than the Cretaceous clays, and may correlate with a black volcanic sand deposit which occurs below the boundary at Site 528 nearby.

Chemistry of the Boundary Plug

Very late in this study, we obtained a sample of the gray boundary plug sufficiently large to complete INAA. The analysis (Appendix I, not plotted in figure 3-5 and 3-6) revealed that most elements are present in concentrations at background or transitional between the Maastrichtian and Danian sediments. In particular, background levels for As, Ni, and Sb indicate that the enrichments for these elements just above and below the boundary are distinct. Co, Cr, Cs, Fe, Rb, and Sc values are similar to the sample just above the boundary, while Ba. Mn, and Zr are very low. In contrast, Se and V show significant enrichments relative to the rest of the section, with Se enriched by a factor of 3 and V by a factor of 4 over the highest values found elsewhere in the section. Iridium was not analyzed.

The data for As, Sb, Se, and V indicate that there are multiple but distinct chemical anomalies across the K/T transition. The fact that these anomalies are sharp and occur across a sequence of well-defined sedimentary color changes indicates that the boundary sequence is relatively unaffected by bioturbation or other disturbances. The sequence of distinct enrichments also argues against secondary mobility from a single source layer and supports the contention that each enrichment is distinct in time.

Evidence for Shock Deformation

Quartz and feldspar grains in each section were examined petrographically to assess the microstructural state of these silicates. All deformation features, both tectonically- and shock-induced were recorded for each of the first 100 grains per section intersected in linear traverses. The nature of the clastic fraction, which was predominantly in the size range less than 63 microns, made distinction between the smaller (< 20μm) quartz and feldspar grains difficult. Quartz planar features (figure 3-7D) are rare, having been observed equally in single and multiple sets in only 15 of 4700 grains (0.3%). The maximum concentration (2%) occurs at K/T and 12 of the 15 grains containing lamellae occur to 53 cm above K/T. By contrast, tectonic lamellae occur over the entire interval studied (figure 3-4). Lamellar features were also observed in several feldspar grains (figure 3-7B) but were not included in the analysis.

Mosaicism (figure 3-7A), commonly partially recovered (figure 3-7C), is the dominant shock-induced microstructure in the Walvis samples, in accord with results of analyses of Maud Rise , Gubbio, Italy, Starkeville South section of the Raton Basin and of Toba ignimbrites and Bishop Tuff (e.g. Carter et al, 1990). Shock frequency levels (figure 3-4), as reflected primarily by the mosaic structure, are highest (36%) within 15 cm of the paleontological K/T boundary, dropping to between 10 and 18% within 1 m above and below the boundary. Other high shock frequency levels occur at about 1.5 m above the boundary and at 1.87 m below it; the latter peak coincides with anomalous enrichments of most of the elements (figure 3-5 and 3-6). Values of 7 and 13% (Appendix I) occur at 9 m above (271.01 mbsf) and 8.3 m below (288.30 mbsf)

Figure 3-7: Photomicrographs of shock deformation in Walvis Ridge sediments. A. Intense mosaicism in quartz in the gray plug at the paleontological K/T boundary (280.0 mbsf). B. Polycrystalline potassium feldspar grain (SEM/EDAX analysis) with intense mosaicism and single and multiple sets of planar features (same location as A). C. Partially recovered, mosaicism in quartz from 1.87 meters below the K/T boundary (281.87 mbsf). D. Quartz grain containing a single set of planar features from 6 cm above the K/T boundary (279.94 mbsf).

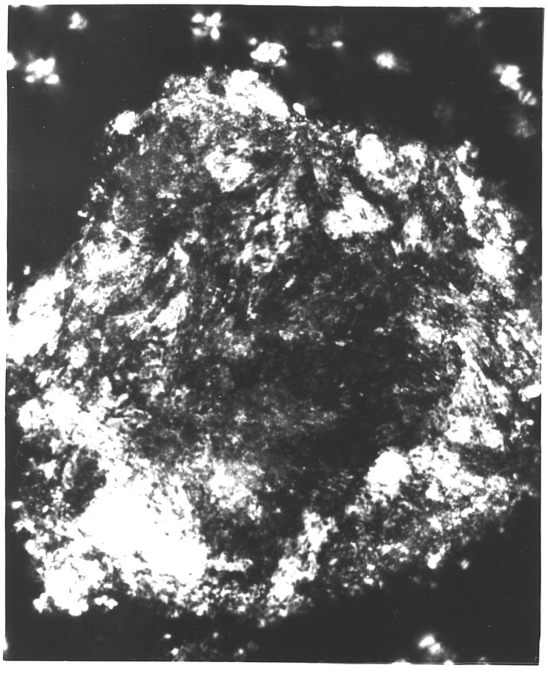

A

70 µm

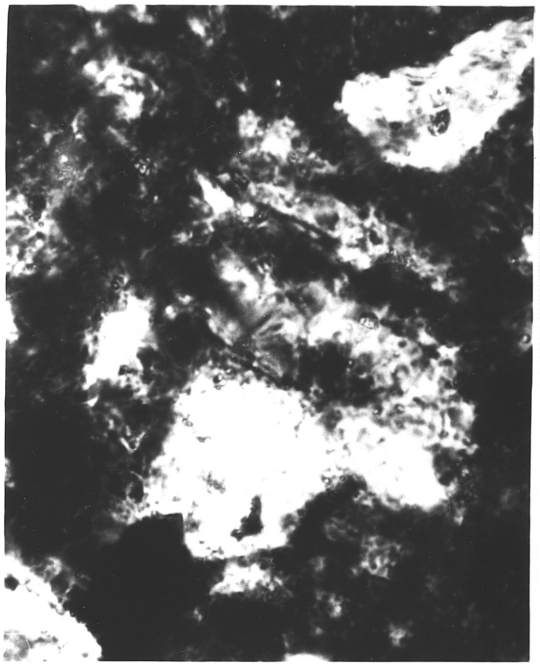

C

30 µm

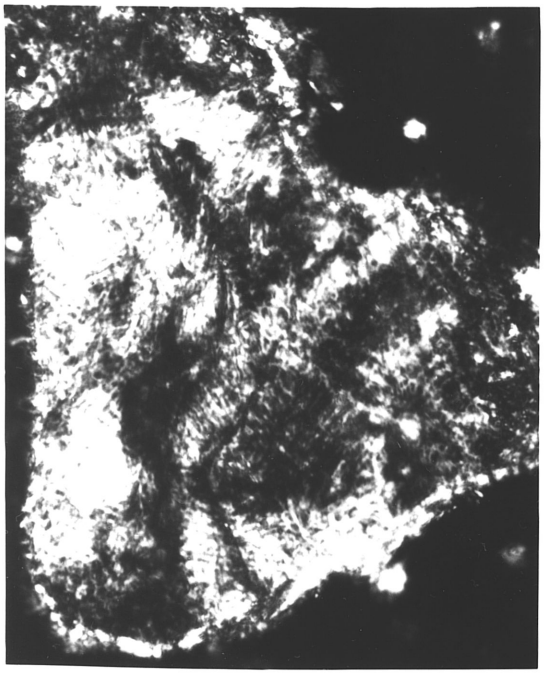

B

50 µm

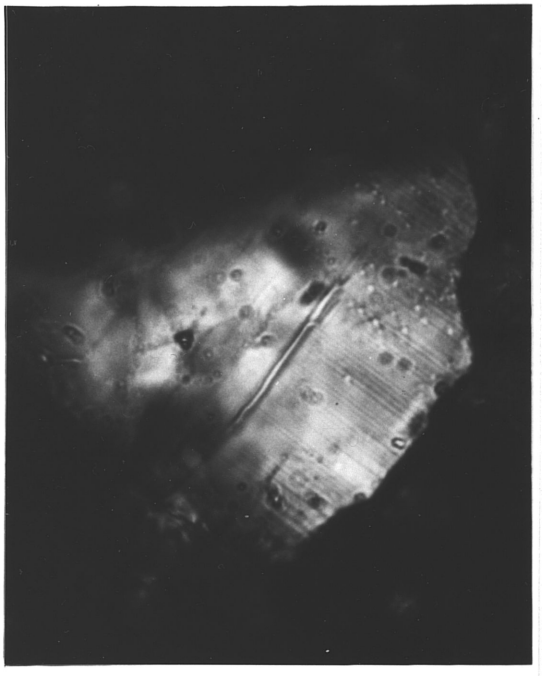

D

30 µm

the boundary, respectively, and chemical data at these horizons (Appendix I) indicates that these samples are similar to other background samples above and below K/T. Caution must be exercised is making use of recovered mosaicism as a moderate-level shock criterion as Sharpton and Schuraytz (1990) found that domains in one mosaic feldspar crystal from Toba (Carter et al, 1986) have formed by disequilibrium compositional zonation. The extent to which this type of chemical zoning affects the results given in figure 3-4 is not known but it is expected to be small as: 1) quartz is not affected by this problem; and 2) grains showing total recovery were not counted as shocked because the recovery could result from tectonic processes.

## Discussion

Analysis of the shock data and chemistry for Site 527 indicates that several events occurred across the K/T transition, including a single large shock event at the boundary with an associated Ir spike, and a series of enrichments of chalcophile and some siderophile elements (figures 3-5 and 3-6). As most of these elements tend to follow the clay content in general, plotting elemental ratios to Al (see figure 3-6) augments the various enrichment peaks. Mg/Fe ratios (figure 3-6) suggest several episodes of influx of Fe-rich clay or basaltic material. These decreases in the Mg/Fe (and Mg/Al) ratios correlate with enrichments of several other elements. The fact that ratios of these trace elements to Al content show strong enrichments suggests that they are not associated with changes in the clay content, and must represent either changes in clay chemistry, aerosol and ash emissions from basaltic volcanic eruptions (either regional or far-field), or changes in

mineralogy secondary to variations in pH and $fO_2$ across the boundary (Borella, 1984). Recent work by Hansen et al (1987), Schmitz (1985), and Graup (1989) suggests that the concentrations and distribution of certain elements at the K/T transition may depend primarily on terrestrial processes and the distribution of specific phases such as carbon black or sulfides. The observation that some foram tests at the boundary contain embedded pyrite (Boersma, 1984) may be of great significance here as sulfides would act as excellent concentrators for Fe and the chalcophile elements.

The suggestion that basaltic eruption events are recorded at Walvis Ridge is particularly important as concerns the proposed link between mass extinctions and flood basalts (Chapter 6 of this work). Courtillot et al (1988) have proposed that the Deccan Traps erupted in several distinct phases beginning in Chron 30 N in the late Maastrichtian. Their estimate of the timing and duration of these eruptive phases includes a pulse of Deccan activity just below K/T, and one at the K/T boundary, both in reversed Chron 29R. These two pulses correlate approximately with the 2 enrichments of chalcophile elements recorded at Site 527. The enrichments of chalcophile and siderophile elements at these times suggest that if basaltic emissions are a viable source, they must be a mixture of ash and volcanic aerosols, as aerosols alone are not enriched in all of these elements (Zoller et al, 1983; Olmez et al, 1986; Crowe et al, 1987). Work is currently underway to see if the Deccan pulses in Chron 30 N and 29N are also represented at Site 527. It is important to note here that the South Atlantic mid-ocean ridge was near Site 527 at K/T time. Therefore, a local source for the elemental enrichments at Site 527 cannot be ruled out. One other possibility is that the volcanic signature at Site 527 is related to local volcanism along the Walvis Ridge itself. Core photos

from the Leg 74 DSDP volume reveal several black sand layers at Site 528 (Core 37, section 4) which may represent ashfalls at shallower water depths related to the elemental enrichments at Site 527.

A small negative excursion of $\partial^{13}C$ (figure 3-6) which occurs below the K/T boundary at 281.87 mbsf correlates exactly with the first chalcophile enrichment event. Correlations between $\partial^{13}C$ changes and volcanic events imply that the latter affect productivity in the oceans. The basaltic eruptions may outgas sufficient volumes of $CO_2$ with strongly negative $\partial^{13}C$ values that affect the atmospheric and oceanic reservoirs; this would require that the basalts and their aerosols have extremely light $\partial^{13}C$ values such as those observed at Kilauea (Allard, 1983) .

The pattern of mosaicism frequency at Site 527 is similar to that observed over a 4 m interval, bisected by K/T, at Maud Rise (Leg 113, hole 689B and 690C; figure 3-1) and at Gubbio (figure 2-17); planar features are also rare at these sites. With one exception (ODP Site 689B; Michel et al, 1990) the maximum occurrence of mosaicism at all these sites coincides with the maximum iridium concentration. At Gubbio, anomalous concentrations of Ir (Crocket et al, 1988) begin at 2 m below the boundary, correlating with high frequency of mosaicism, and remain anomalous to 1.5 m above the boundary where the frequency of mosaicism is also high (figure 2-19). Furthermore, where the Ir data at Gubbio decrease to background away from the K/T boundary, the frequency of mosaicism also approaches zero. The Ir data of Crocket et al (1988) have remained controversial, although they have recently been confirmed by an independent study using different samples (Rocchia et al, 1989).

## Conclusions

Evidence of shock deformation, the chemical trends, and correlations between these data, the biostratigraphy, and the isotopic data of Shackleton and Hall (1984), indicate that the K/T transition at Site 527 is complex. Enrichments of chalcophile and other trace elements at 1.87 meters below and nearly coincident with the elevated levels of Ir and shock deformation at the boundary, suggest that at least two pulses of basaltic volcanism are recorded at Site 527. These pulses of volcanism may be related to the Deccan Traps which were erupting during the K/T transitional period, with a maximum in volcanic activity at K/T, or they may be related to regional volcanic activity from the Walvis and/or Mid-Atlantic eruption centers. The presence of coincident siderophile and chalcophile anomalies implies that either the basaltic emissions were a variable mixture of aerosols and fine ash, or that the enrichments are due to changes in mineralogy secondary to local pH and $fO_2$ changes caused by the volcanism. However, the correlations between the mineralogy, chemistry, biostratigraphy, and isotope data suggest that the decline in marine productivity associated with the K/T transition occurs over an extended period of time, and is probably related only indirectly to the basaltic signatures observed at Site 527. In addition, the extended distribution of light to moderate shock frequency levels across the apparently undisturbed boundary sequence may be accounted for either by a single event of extended duration or by multiple shock events, the cause(s) of which are not yet discernable.

# CHAPTER IV

# HIGH-EXPLOSIVE SHOCK-RECOVERY EXPERIMENTS ON GRANITE AND QUARTZITE AT ELEVATED TEMPERATURES

## Introduction

The presence of high-strain-rate microstructures in known volcanic rocks, diatremes, and landslides (Carter et al, 1986; Carter et al, 1990; Carter and Officer, 1990, and this thesis) and the differences between these features and classic impact-induced microstructures indicates that the endogenous microstructures may be generated in an environment that is quite different from impact. Microstructural data from the Hospital Hill quartzite experiments further indicate that pre-shock temperature may be of fundamental importance to the character of high-strain-rate microstructures at specific peak shock pressures. The notion that the development of shock-induced microstructures is a function of temperature also raises the question of what other parameters might influence microstructural development? It has long been recognized that parameters including temperature, stress, strain rate, confining pressure, pore pressure, and defect chemistry affect the mechanical response of silicates deformed in the laboratory and in tectonites (e.g. Carter, 1976). High-temperature creep is a rate process; however, rate process theory has not been applied to shock deformation because of the exceedingly high strain rates.

To date, nearly all shock recovery experiments have been done at ambient temperature, at strain rates of $10^6$ to $10^8$/sec, peak stresses from 10 to 50 GPa, and durations of loading from 0.5 to 2.0 microseconds. The primary

reason for this narrow range of experimental conditions has been technological limitations on available apparatus. To determine whether shock-induced microstructures are sensitive to parameters other than peak shock pressure, these technological limitations must be overcome. The purpose of this chapter is to (1) describe the background history and basic physics of shock waves and recovery experiments; (2) describe the design and experimental program completed in this research project; and (3) suggest some improvements for future shock recovery experimentation based on the results of this program.

## Physics of Shock Waves

A shock wave is a transition between an initial energy-pressure-volume (EPV) state, to a higher-energy and pressure, and lower-volume, compressed state (figure 4-1). Because of this change of state, the shock wave actually travels faster than the acoustic velocity in the undeformed medium (Duvall, 1968). A shock wave differs from a seismic wave in that it alters the physical properties of the propagating medium through which it travels. Another unique characteristic of shock waves is the nature of the rarifaction, or release, which follows the compression front. Because the particles behind the shock front are accelerated relative to the shock itself, the rarifaction actually travels faster than the shock front This causes the shock front to decay more rapidly than it would otherwise do, leading to very rapid decreases in the level of shock attained as a function of distance from the source. The general factors that affect the behavior of shock waves include (1) the wave-generation characteristics (i.e. the source function) of the source, (2) the propagation distance, (3) the geometry of the source and the target, and (4)

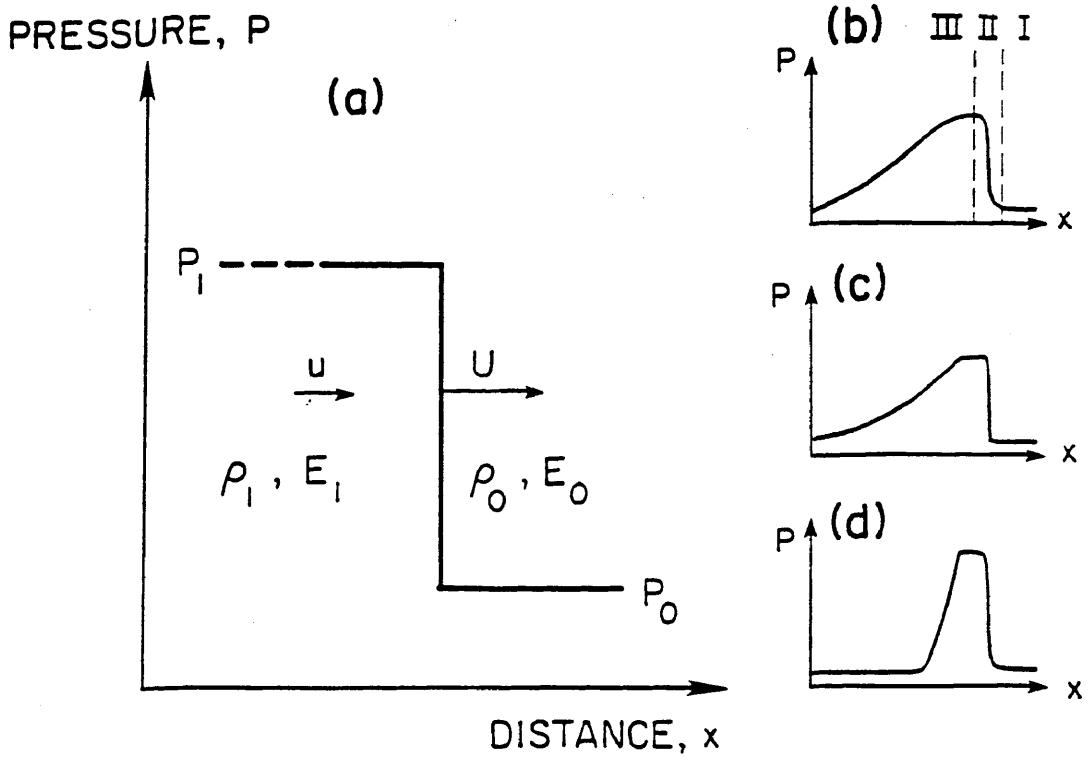


Figure 4-1: Schematic diagram of a shock transition from an initial density ($\rho_0$), pressure ($P_0$), and energy ($E_0$), to a shocked state ($\rho_1$, $P_1$, $E_1$). Insert b, c, and d represent the various shapes that a shock transition can have due to changes in rise time, pulse length, and release time. Diagram after Stöffler (1972).

the physical properties and impedance contrasts that exist in the propagating media. As a shock front compresses a medium, it produces a multitude of effects including, among others (Duvall, 1968):

- Changes in electronic energy states in atoms
- Atomic rearrangement
- Changes in the equilibrium partitioning of energy in the medium
- Changes in crystal structure (phase transitions)
- Changes in electrical conductivity
- Releases of electric currents in many piezoelectric, ferroelectric, and insulating materials
- Creation of vacancies and dislocations in solids
- Changes of fast reactions in gases
- Elevated temperatures due to compressional heating

The Hugoniot Elastic Limit

As an elastic wave increases in amplitude, the particle velocity and stress field associated with the wave also increase. In every material, there is a limit beyond which the elastic strength of the material is exceeded and permanent plastic strain and fracturing occur. This limit is usually called the yield limit or elastic strength for the material. In strong waves, the stress value at which plastic yielding occurs is called the Hugoniot Elastic Limit (HEL). As a shock wave strains a material above the HEL, the energy of the shock is partitioned into an elastic precursor and a second, strongly nonlinear plastic wave (Melosh, 1989). This plastic wave follows the elastic wave front and travels at a slower velocity. As the strength of a shock wave increases, the velocity of the plastic wave will also increase along with the higher EPV state

of the compressed material. For strong shock, the plastic wave travels faster than the elastic precursor, and develops into a very abrupt transition front (shock front) that takes the initial material to its compressed state almost instantaneously. Strong shock fronts in gases, for example, have thicknesses of roughly 10 microns (Melosh, 1989). In complex solids, however, the shock front can be affected by other rate-dependent processes that will spread out the shock transition. In rocks, where pore crushing, compaction, and brittle phenomena accompany the shock, the thickness of the transition may range up to several meters.

## The Hugoniot Equations

A complete description of a shock wave can be derived from the conservation of mass, momentum, and energy across a discontinuity. The equations relate the pressures in the unshocked medium ($P_o$) and the compressed state ($P_1$), the particle velocity in the compressed state ($u_p$), the velocity of the shock front ($U_s$), the initial and final densities ($\rho_0$ and $\rho_1$), and the specific internal energy for the initial state ($E_o$) and the final shocked state ($E_1$). These relations, which were first derived by P. H. Hugoniot in 1887, are written as

$$\rho_1 (U_s - u_p) = \rho_0 U_s \tag{4.1}$$

$$(P_1 - P_0) = \rho_0 u_p U_s \tag{4.2}$$

$$(E_1 - E_0) = (P_1 + P_0) (V_0 - V_1)/2 \tag{4.3}$$

where $V_1=(1/\rho_1)$ and $V_0=(1/\rho_0)$, and are called the Hugoniot equations (Melosh, 1989). In these equations, the initial particle velocity of the unshocked

medium is always assumed to be zero so that this reference frame must always be used to apply the equations properly. It is also assumed that the effect of body forces can be neglected, and that no dissipative processes occur during the shock event. To specify completely the state of the shocked versus the unshocked material, an equation of state (EOS) such as the Mie-Grüneisen EOS, which is written as

$$P = C_B^2 ( \rho_1 - \rho_0) + (\gamma - 1)\rho_1 E \qquad (4.4)$$

where $C_B$ is the bulk sound velocity and $\gamma = C_p/C_v$ , the ratio of the specific heat at constant pressure to the specific heat at constant volume, must be introduced. This EOS relates the scalar pressure, internal energy, and specific volume, and addresses all the atomic, molecular, and crystalline properties that affect the response of the material. Once an EOS is specified, the shocked state can be defined completely. A useful form of the resulting equations specifies the variables V, P, $U_s$, and $u_p$ in terms of each other, and is written as

$$u_p = [(P_1 - P_0)(V_0 - V_1)]^{1/2} \qquad (4.5)$$

$$U_s = V_0 [(P_1 - P_0) / (V_0 - V_1)]^{1/2} \qquad (4.6)$$

$$V = 1/\rho_0 = (U_s - u_p)/\rho_0 U_s \qquad (4.7)$$

$$P_1 = P_0 + \rho_0 u_p U_s \qquad (4.8)$$

where P is the component of compressive stress in the direction of shock propagation. The locus of points that are defined in E-P-V space by these relations is called the Rankine-Hugoniot curve for the specified material (figure 4-2). It is important to emphasize that this curve does not represent

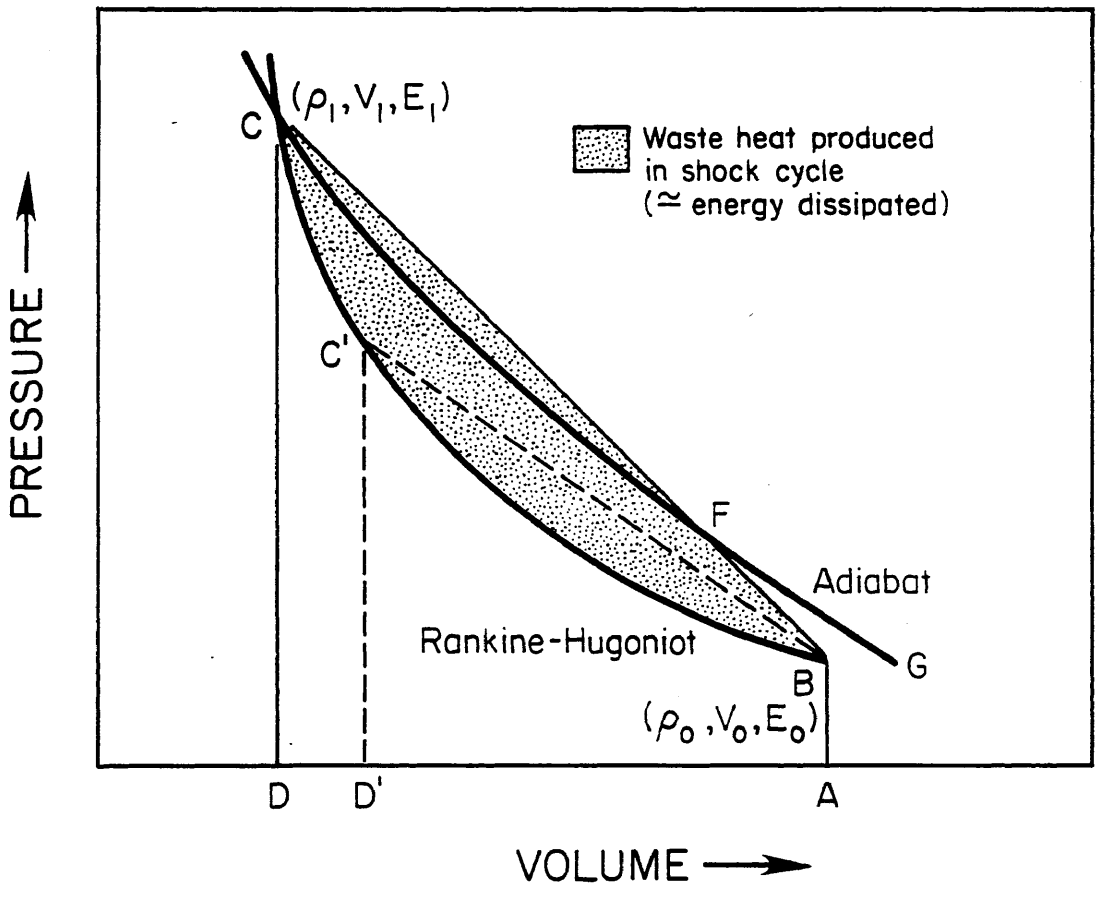


Figure 4-2: The Rankine-Hugoniot curve for a hypothetical material in P-V space. Shock states are achieved by a direct compression along lines such as BC or BC', which are called Rayleigh lines for the shocked states C and C' respectively. The stippled area between the Rayleigh line and the Rankine-Hugoniot is the heat generated by dissipative processes during compression from the initial state to the shocked state. Diagram after Duvall (1968).

the path taken during shock, but is a curve representing the states that can be achieved by shock compression.

An important result of shocking a material is the production of waste heat. For example, when a material is shocked in figure 4-2 from pressure B to pressure C, the path taken is the line BC which is called the Rayleigh line for that shock transition. The area under the Rayleigh line and above the Rankine-Hugoniot curve represents the waste heat produced by the shock cycle. Therefore, as the intensity of shock is increased, waste heating and the resulting residual temperatures will increase.

Shock Wave Interactions

As noted earlier, shock waves are affected by the geometry and properties of the medium through which they propagate. Rhinehart (1968) describes in detail the results of stress-wave interactions in complex solids. These interactions include: (1) spalling from reflections of stress waves off of free surfaces with amplitudes greater than the tensile strength of the material; (2) notch stresses caused by the presence of voids or other low impedance sources within the solid; (3) hoop stresses from highly-curved wave fronts that produce large tangential stresses. In geologic materials which are frequently polycrystalline in character, the presence of grain boundaries, dislocations, and porosity all produce stress interactions that lead to complex behavior. Also, the presence of several phases (e.g. quartz, feldspar, and biotite in granite) with differing impedance can enhance greatly the complexity of shock propagation in these materials.

## Shock Wave Experiments on Geologic Materials

The first interest in shock propagation in geologic materials resulted partially from the recognition of impact as a terrestrial process (McIntyre, 1962), and also because of defense concerns relating to the strength of natural materials under loading from nuclear weapons. The study of shock in manmade materials actually dates back to before 1900, with the primary interest having been for military and industrial uses of explosives and shock-hardened substances (Duvall, 1968). As the state of technology improved in the 1950's, the ability to measure the effects of shock waves in situ enhanced greatly this area of research, leading to the first direct laboratory evidence for specific compositions for the earth's deep interior.

A variety of methods have been developed for producing shock waves in the laboratory. These methods include: (1) high-explosive shock-wave generators; (2) artillery cannons; (3) the two-stage gas gun; (4) implosion-tube generators; and (5) underground nuclear or chemical blasts. Experimental shock wave research in geologic materials is divided into three areas, equation-of-state (EOS) experiments, cratering studies, and shock-recovery experiments. EOS research permits the definition of the E-P-V states that can be achieved through the shock transition for a particular material. These data are used to determine the Hugoniot for materials of interest as well as to study the effects of shock propagation in real time. Cratering studies utilize hypervelocity impact of projectiles in the laboratory to study the mechanics of crater and ejecta formation (Roberts, 1968; Gault et al, 1968), and the penetration characteristics of projectiles for military uses.

Equation-of-State Experiments on Quartz and Feldspar

The EOS of quartz has been studied extensively. and has been well characterized (Wackerle, 1962; Ahrens and Rosenberg, 1968). The results for single crystal quartz and Arkansas Novaculite (figure 4-3) reveal that quartz responds elastically at shock states up to 10 to 15 GPa. Above the HEL, quartz compresses progressively up to shock states of 30 to 40 GPa where it attains a density and volume consistent with stishovite. The complete conversion to the stishovite state appears to occur at lower pressures in single crystal quartz than in polycrystalline material, reflecting the difference in response due to the presence of grain boundaries and other flaws and boundaries in the material. The observation that quartz does not convert abruptly to a high pressure form but rather does so progressively with increasing pressure indicates that the region between 10 and 35 GPa contains a mixture of quartz and stishovite. For this reason, this region of the deformational Hugoniot has been called the "two-phase region".

Another observation relates to the release adiabats in P-V space (figure 4-3). For shock states at or below the HEL, the release adiabats reflect a return to the initial volume for quartz. However, as the shocked state exceeds the HEL, this condition is no longer valid. For pressures in the range from 15 to 30 GPa, the release curves show a steep release that follows the trend of the coesite, and later the stishovite isotherms. These release curves suggest the presence of amounts of both high-pressure polymorphs in the shocked state, with some of both polymorphs being preserved in the more dense final material at room pressure. At shock states above 30 GPa, the release curves change yet again, and reflect a dominance of stishovite in the shocked state. The release curve

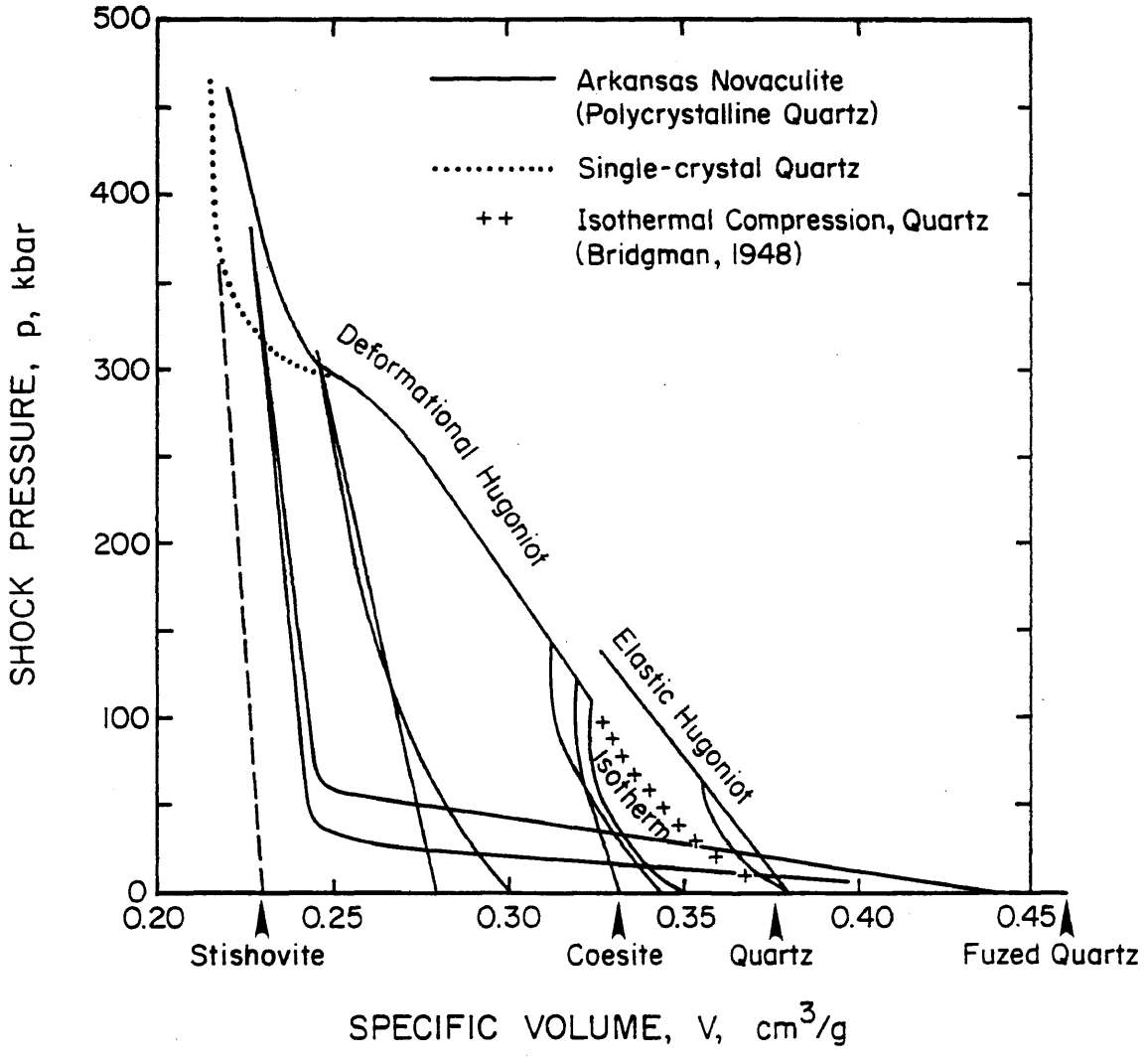


Figure 4-3: Hugoniot and release curves for single-crystal quartz and Arkansas Novaculite in P-V space. Note the change in the release curves for pressure above 30 GPa. At very high pressures, temperatures in the shock transition increase dramatically and the entire sample is converted to stishovite or a short-range-order analog to stishovite. Upon release, this phase reverts to a low-density fused quartz. Diagram after Ahrens and Rosenberg (1968).

in this pressure range reflects a nearly isothermal decompression of a stishovite-dominated material, followed by reversion to fused quartz as the release curve crosses the lower stability pressure of 9.0 GPa for stishovite.

The release curves for quartz imply that coesite and stishovite should only be preserved in materials shocked from 15 to 30 GPa. The release to a fused quartz volume for shock states above 30 GPa suggests that post-shock temperatures during strong shock above 30 GPa are too high to permit preservation of the high-pressure polymorphs. These observations of release behavior are in accord with the results of Kieffer et al (1976), which suggest that stishovite and coesite are not preserved in rocks shocked to peak pressures above 30 GPa at Meteor Crater in Arizona.

Hugoniot data for feldspars reveal that the HEL for these silicates ranges from 3.5 to 4.5 GPa (Grady and Murri, 1976; Ahrens et al, 1973; Borg, 1972). Above the HEL, the feldspars also undergo a progressive decrease in specific volume with increasing shock state, reflecting a progressive conversion to a more dense phase, which is similar to the observed response of quartz. Since no high-pressure polymorphs for feldspars have been discovered in shock-deformed rocks, the resulting structure has been assumed to be a short-range-order glass with higher density than the unshocked material. However, it is also possible that the final state is similar to the high-pressure polymorph of the germanate orthoclase analog reported by Kume et al (1966), or a hollandite-type structure in which silicon changes from tetrahedral to hexagonal close packing with oxygen (Ringwood et al, 1967).

## Shock-Recovery Experiments on Quartz and Feldspar

Shock-recovery experiments, which were first developed in the late 1950's (Gray, 1990), are designed specifically to preserve a sample subjected to a shock wave so that it can be studied for physical evidence of the shock event. Ideally, the experiment is designed to (1) produce either a predetermined or measurable shock history so that the final state of the material may be compared to the deformation history and (2) produce no post-shock annealing, radial release waves, or other collateral damage. Shock recovery is accomplished routinely using the powder gun (e.g. Hörz, 1968), high explosives (e.g. McQueen, 1963; and Müller and Defourneaux, 1968), and in nuclear tests where samples are collected by post-mortem drilling or sampling from a resulting crater (Cummings, 1968; and Short, 1968a, b; and Borg, 1972). Although implosion tubes have also been used for recovery work (Deribas et al, 1966; Hamann, 1966), this method produces a spherical front which prevents recording of the P-T history of the specimen, and also produces large hoop stresses that can cause additional collateral damage compared to plane shock waves. These factors prevent a quantitative estimate of the shock history of the sample and thus make implosion-tube experiments less reliable for recovery experiments.

The most important factor in successful shock-recovery work is confinement of the sample during and after the shock event. This problem has been solved through the use of "momentum trapping" which prevents the sample from experiencing significant release fracturing, recovery, and other collateral damage. Momentum trapping is accomplished by surrounding the sample with a shell of material. Ideal trapping uses a shell of similar

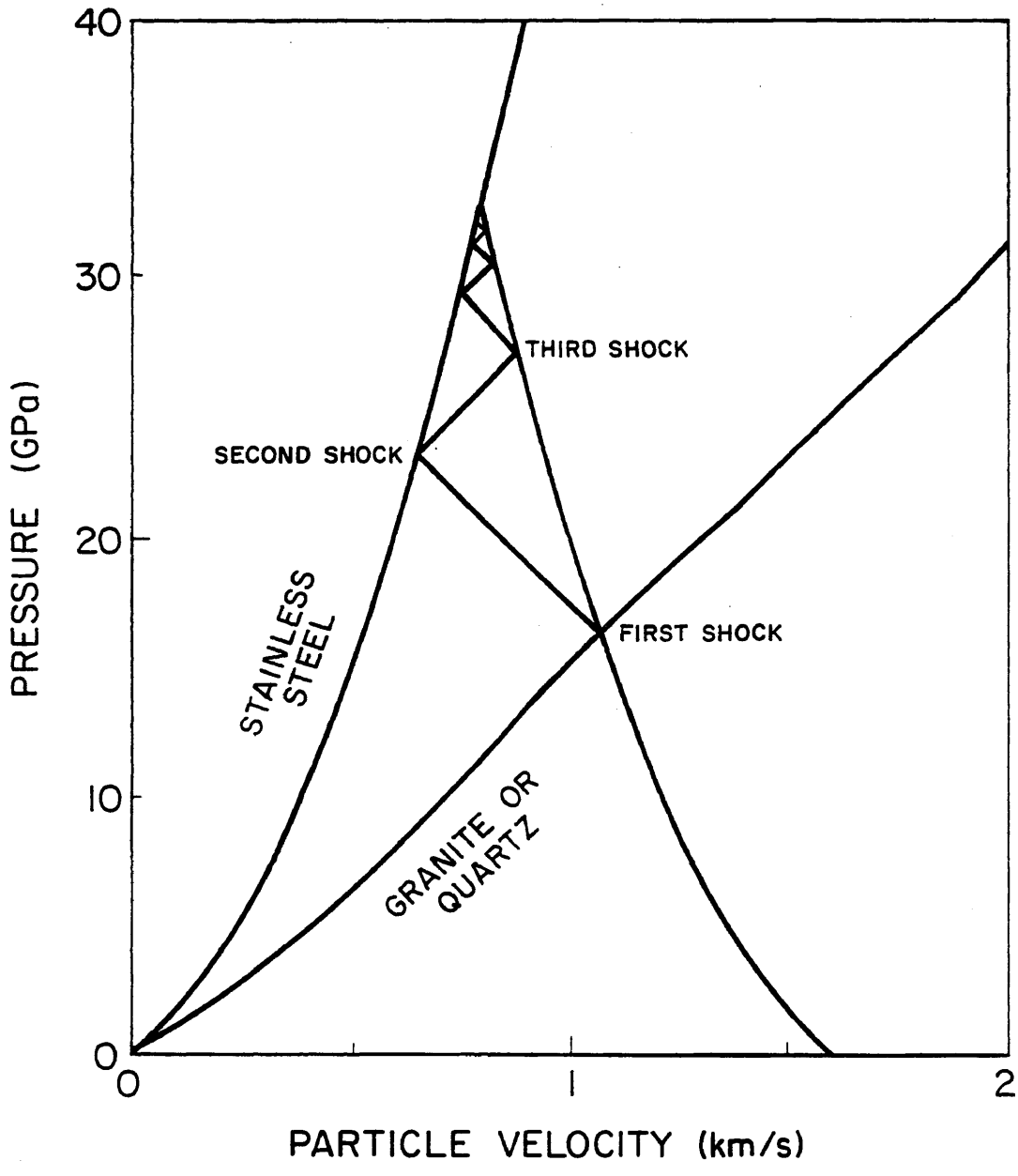


Figure 4-4: Impedance matching method for determining shock states across an interface between a higher impedance material (stainless steel) and a lower impedance material (quartz or granite). The first shock in steel produces a lower shock state in the quartz where the reflection of the steel Hugoniot crosses the quartz Hugoniot. Higher shock states in the quartz are achieved by reverberations along the quartz Hugoniot until the resulting shock state equals that in the steel.

impedance to the sample, which prevents spallation and other undesirable shock interactions. This impedance matching method for momentum trapping works well for metals and certain other substances, but presents a difficult problem for brittle ceramics and silicates. In these materials, the inability of a brittle ceramic momentum trap to survive a shock experiment has required that metal momentum traps with an impedance mismatch relative to the sample be used for effective recovery. Thus, most recovery experiments on silicates have used steel momentum traps and a reverberation method of obtaining the maximum shocked state. In impedance mismatched materials (figure 4-4), the shock wave travels through a steel shell, shocking the steel to a specified pressure on the steel Hugoniot. A sample of silicate material, which is sandwiched between the steel, also undergoes shock compression, but attains a lower pressure than the steel that is determined by the intersection of the reflection of the steel Hugoniot with the silicate Hugoniot. Because the silicate is sandwiched between steel, the reflected shock trapped in the silicate produces a reverberation that follows the slope of the silicate Hugoniot and eventually drives the shock state of the sample to the state of the steel momentum trap.

In theory, the reverberations in the silicate sample will always attain the same shock state as the steel. However, in actual experiments, where a flyer plate of finite thickness is used, the flyer plate also shocks up, and releases as the shock reflects off the back surface of the flyer (figure 4-5). This release wave, which travels slightly faster than the shock itself, catches up with the reverberating shock in the silicate and prevents the sample from achieving the maximum shock state depicted in figure 4-4. Thus, the configuration and thickness of the flyer, base plate, and sample, and the

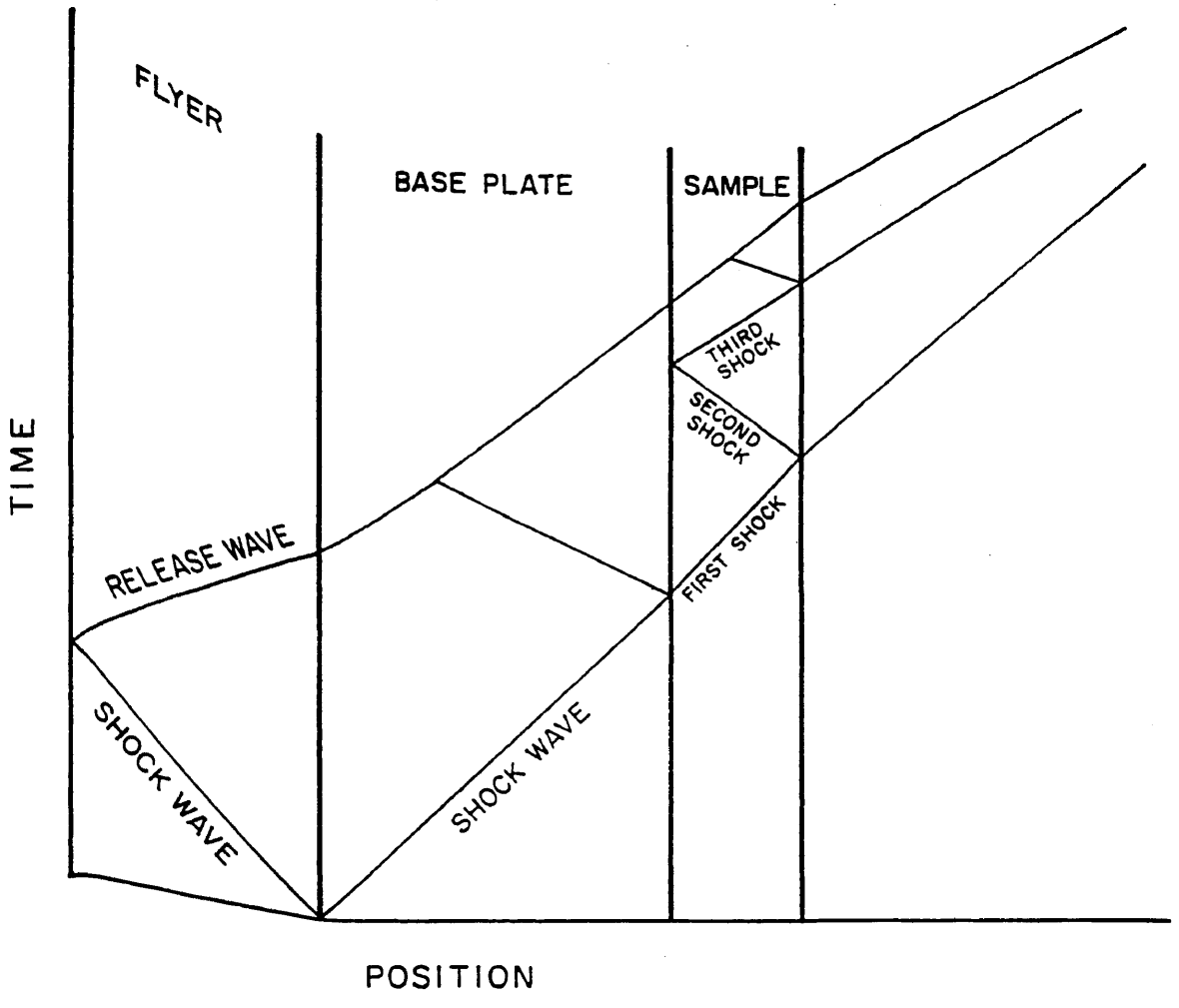


Figure 4-5: Impedance matching in a shock recovery experiment. As the flyer plate strikes the base plate, a shock front propagates into the base plate and back into the flyer plate. When the shock enters the sample, it follows a reverberation path as shown in figure 4-4. The reflected wave from the back of the flyer plate also propagates back into the assembly as a release wave, and truncates the reverberation process at some shock state below that initially achieved in the steel.

impedance matching, all play critical roles in the final shock state attained in the recovery experiment.

Previous recovery experiments performed at room temperature in the powder gun (Hörz, 1968; Kleeman and Ahrens, 1973; and Reimold and Hörz, 1986a, b) and using HE methods (e.g. Grothues et al, 1989) reveal that the general progression of shock-induced microstructures in quartz can be calibrated to specific ranges of shock pressure (figure 4-6). The microstructural development in these samples progresses from fracturing below the HEL, to mosaicism and planar fracture, mosaicism and planar features, isotropization, and finally to a short-range-order diaplectic glass. Several features of this progression are worthy of comment. First, the laboratory data matches the observed progression of shock-induced microstructures from known impact structures (Engelhardt and Stöffler, 1968; Engelhardt and Bertsch, 1969; and Kieffer et al, 1976). Second, except for the work of Kleeman and Ahrens (1973) and Ashworth and Schneider (1985), reports of experimental shock-produced stishovite and coesite have not been reported. Kleeman and Ahrens (1973) detected stishovite in all of their samples of Brazilian quartz shocked from 9.0 to 26 GPa. Kieffer et al (1976) observed that stishovite was not preserved at shock states above 28 to 30 GPa at Meteor Crater, which is in accord with the data of Kleeman and Ahrens (1973), who observed decreasing preservation of stishovite at shock states above 23.4 GPa in their samples.

The pressure range for isotropization of quartz in room-temperature experiments is 30 to 40 GPa. Detailed measurements of the changes in refractive index of quartz shocked parallel to *m* (Grothues et al, 1989) reveal

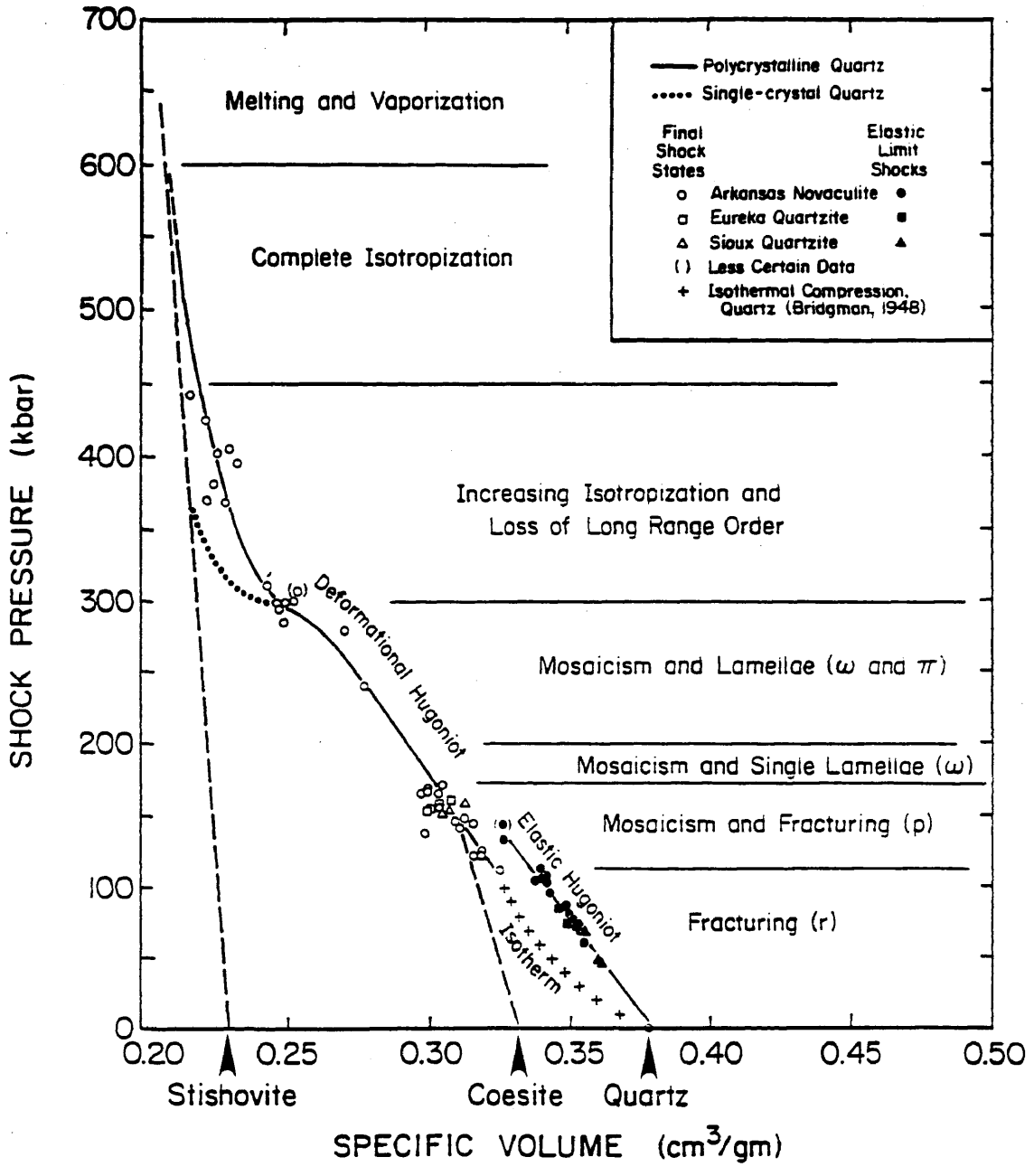


Figure 4-6: Onset pressures for specific shock-induced microstructures in quartz. These onset pressures are a synopsis of the data available from previous shock-recovery experiments at room temperature. Note that type-A {0001} planar features are not included in this diagram, but are believed to form at pressures from 9 GPa. Diagram after Ahrens and Rosenberg (1968).

that the entire change from normal quartz to isotropic quartz occurs between 30 to 35 GPa (figure 4-7). In contrast, refractive index data from naturally-shocked quartz from the Ries and Lappajarvi structures (Xie and Chao, 1987) document that these samples show the onset of isotropization at 10 to 15 GPa with total isotropization being accomplished at pressures below 30 GPa. The natural samples were calibrated to shock pressure using cell expansion parameters. Assuming that this is a valid calibration, the data imply that there may be differences between the naturally-shocked materials and those produced in the laboratory.

Problems With the Shock-Recovery Database

The limited range of conditions under which shock-recovery experiments have been completed raises some questions regarding extrapolation to various pressure, temperature, pulse duration, and strain-rate settings. In particular, there are several concerns relating to the various shock parameters that must be addressed.

The data for single crystal quartz and Arkansas Novaculite (figure 4-6) suggest that polycrystalline aggregates require slightly higher shock states to achieve the stishovite configuration compared to the single crystals. This suggests that the presence of grain boundaries, porosity, and random orientation of polycrystalline materials may change the shock response. This effect may be explained partially by the anisotropic response of quartz to loading. In single crystal shock, the orientation of the crystal may affect the shock pressure required to achieve the stishovite polymorph. In random polycrystals, the anisotropy becomes significant as a source of impedance

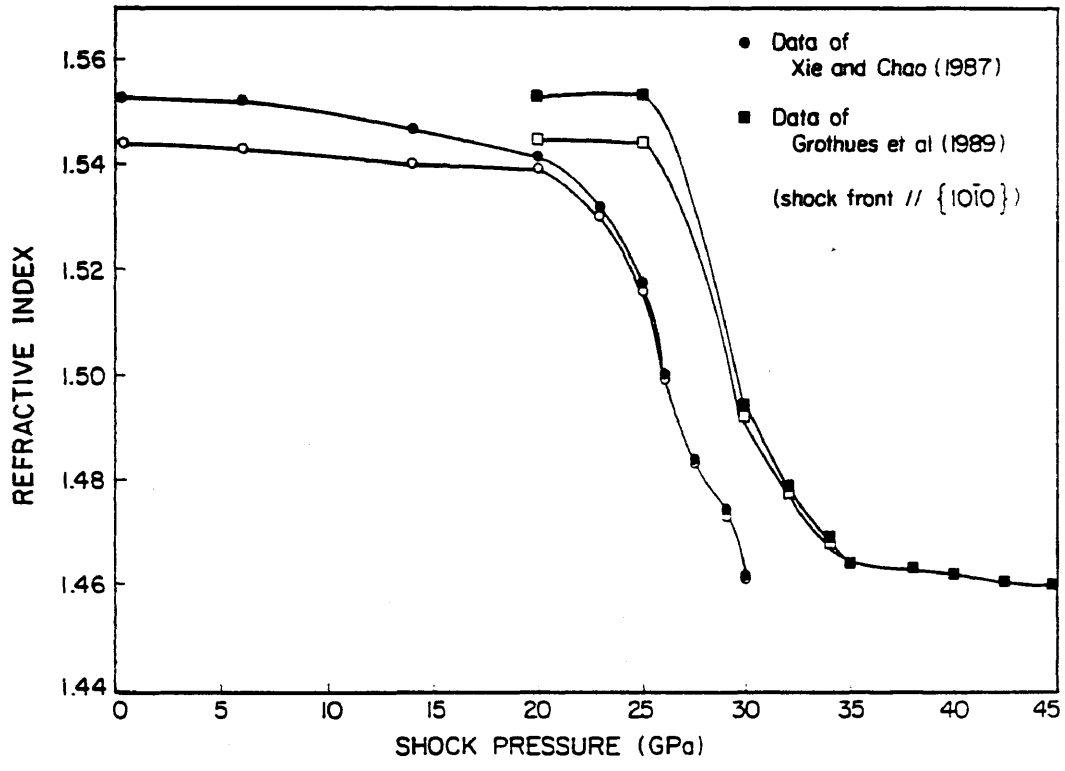


Figure 4-7: Changes in refractive index of quartz as a function of shock pressure. The data of Grothues et al (1989) are for shock-recovery experiments, while the data of Xie and Chao (1987) are for naturally-shocked quartz from the Ries Crater, Germany, and the Lappajarvi Crater, Finland. Provided that the pressure calibration of Xie and Chao (1987) is valid, the data indicate that the natural samples reflect more intense shock damage than the lab samples at the same pressures.

contrast along grain boundaries. The differences in impedance between the a and c directions in quartz may cause a significant amount of scattering and destructive interference during propagation of shock waves in quartz. An easy test of this theory would be a comparative test of an isometric material, such as garnet, whose fourth-order $S'_{33}$ surface is nearly spherical. If impedance contrast is the cause of the observed differences as opposed to just the presence of grain boundaries, the garnet polycrystal should respond in much the same way as the garnet single crystal. If the differences are caused by dissipative losses along grain boundaries, then the garnet will also show differences between single crystal and polycrystalline response to shock compression.

As noted in figure 4-1(B-D), not all shock transitions are the same. Because of the many ways of generating shock in the laboratory, the general path taken by a particular shock, and the specific rise and decay time of a shock may be critical as these processes must be compensated for by thermal and mechanical processes that have a limited response time. The classic example of this problem is the formation of planar features. If these features form by shear heating during the shock transition as proposed by Grady (1980), then the rate of shear heating should be coupled directly to the rise time of the shock. Also, since quartz will melt in response to this heating, and the amount of melt formed is a result of the balance between frictional dissipation and conductive heat transfer away from the planar feature, the amount of glass produced should also be sensitive to the rise time of the shock.

The decay time of the shock becomes important in terms of post-shock fracturing, recovery, and collateral damage. A sudden relaxation from the

shocked to unshocked state is undesirable because it will cause spalling, fracturing, and other damage. In fact, properly designed recovery experiments attempt to achieve a "soft recovery" where the shock stress declines rapidly but not so fast that additional work is done to the sample after shocking.

To date, all shock-recovery experiments have correlated the intensity of deformation and specific microstructures to the peak shock stress achieved. In contrast to this simple approach, studies of tectonic deformation mechanisms have attempted to look at the affects of path dependency on the resulting deformations (e.g. Handin et al, 1986; Russell et al, 1990). The issue at hand is two-fold and includes the problems of (1) threshold stress versus the pressure-time history as the appropriate parameter for correlating shock microstructures, and (2) duration of loading in nature versus the laboratory (figure 4-8).

Despite the fact that shock deformation is an irreversible, path-dependent process, it has often been argued that only the peak stress is important in determining the final state of a shocked material. However, the intensity of the shock mosaic structure, which is a plastic response of a solid to shock-loading, should be affected directly by the duration of loading. Therefore, it may be appropriate to consider a more general parameter for shock deformation analysis, such as the integral of the simulated pressure-time curve for a given event. Where particle velocities are also estimated by simulations, it may be possible to correlate the microstructures to the estimated total work performed during a shock event. The onset of isotropization may also be sensitive to the total work done, so that events such as impacts (figure

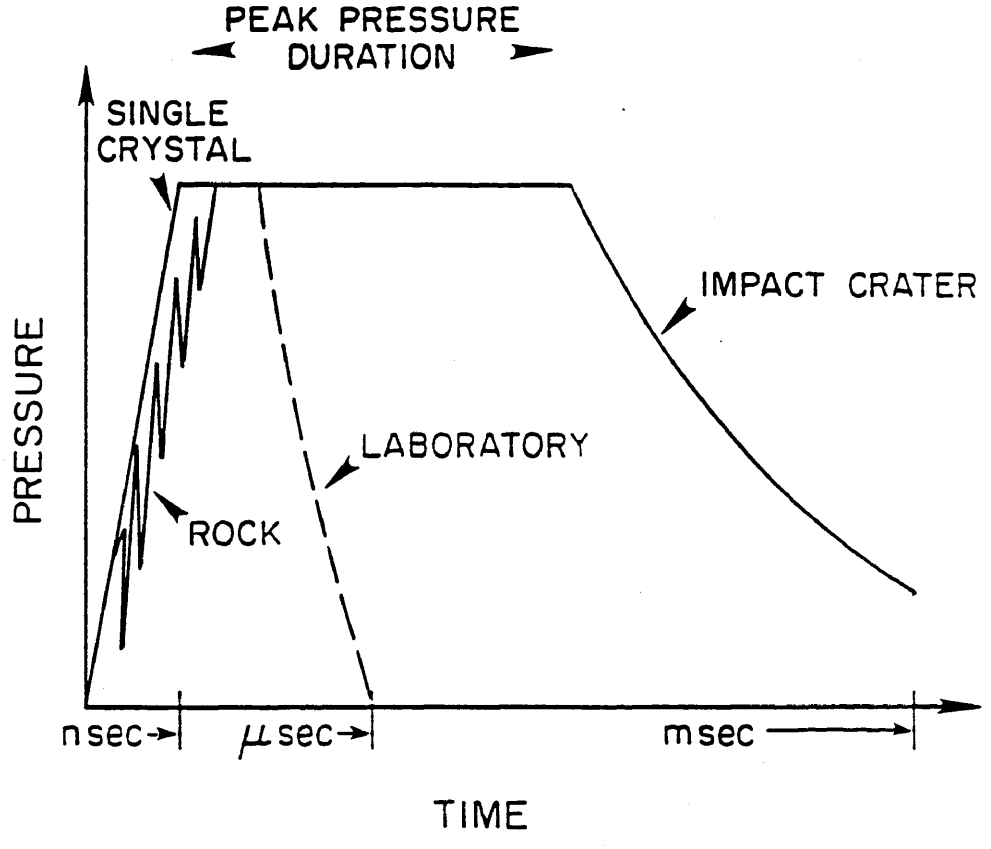


Figure 4-8: Differences in the duration of shock loading in the laboratory and natural impact events reflects the potential problem in extrapolating laboratory data to the real world. The difference in response of single crystals versus polycrystalline aggregates is also shown. Diagram after Kieffer (1971).

4-8), which have durations of loading up to $10^6$ times longer than laboratory experiments, might produce isotropization at much lower pressures (e.g. figure 4-7).

The second problem relating to duration of loading involves the formation of high-pressure polymorphs such as coesite and stishovite. Other than the work of Kleeman and Ahrens (1973) and Ashworth and Schneider (1985), no preservation of stishovite and/or coesite has been achieved in laboratory shock studies. If the polymorphs form from a melt or short-range-order glass phase in the planar features as proposed by Schmitt and Ahrens (1989), the duration of loading becomes critical in determining whether these phases will be preserved. The ability to form the polymorphs is a function of the peak stress and temperature achieved during the shock. Schmitt and Ahrens (1989) note that the formation of stishovite appears to initiate at about 9.0 GPa, and continues up to 34 GPa, although preservation of detectable amounts of the polymorph ceases above about 26 GPa. The duration of loading becomes critical in polymorph preservation because maintenance of high pressures allow: (1) the polymorph to nucleate and grow large enough to be preserved as a shock product; and (2) thermal conduction to transfer heat away from the hot zone around the planar features, which will help prevent reversion of the stishovite to glass as the shock state relaxes (Schmitt and Ahrens, 1989). Considering the balance between shock, conduction, transformation, and crystallization processes, it can be predicted that stishovite will form in a wider range of pressures at the longer durations of loading in nature versus the microsecond-scale pulses in the laboratory. Although coesite has never been observed in laboratory shock products, the

presence of coesite in static experiments suggests that the same general argument should apply to this polymorph as well.

Another factor that has not been addressed in shock recovery or EOS experiments is the role of ambient (pre-shock) temperature in development of shock microstructures. It has been recognized that temperatures generated during shock events are quite high (Lyzenga and Ahrens, 1983; Boslough, 1988) as are the residual temperatures due to dissipative heating during the shock event. The role of ambient temperature is of special concern in light of the presence of high-strain-rate microstructures in volcanic rocks and diatremes that probably formed at temperatures > 600°C. It is also important for large-body impacts where shock compression of middle to lower crustal rocks is achieved at initial temperatures to 800°C. The classic example of this problem is the Vredefort structure in South Africa, which has been exumed from a depth of 10 to 15 km (e.g. Schreyer, 1983), and displays shock-induced microstructures that appear quite different from typical impact microstructures (Reimold, 1990). Recognizing that a particular shock event in quartz will generate a specific amount of shock heating, the effect of ambient temperature in shock compression can be predicted on the quartz phase diagram (figure 4-9). Progressively higher ambient temperatures to 750°C will shift the Rayleigh line for a specific shock event (e.g. 12 GPa) from the room temperature final shock state of 12 GPa and 2200°C, to a new final state of 12 GPa and 2950°C. The release curves will remain essentially the same, but will end up at higher temperatures reflecting the pre-shock condition of the material.

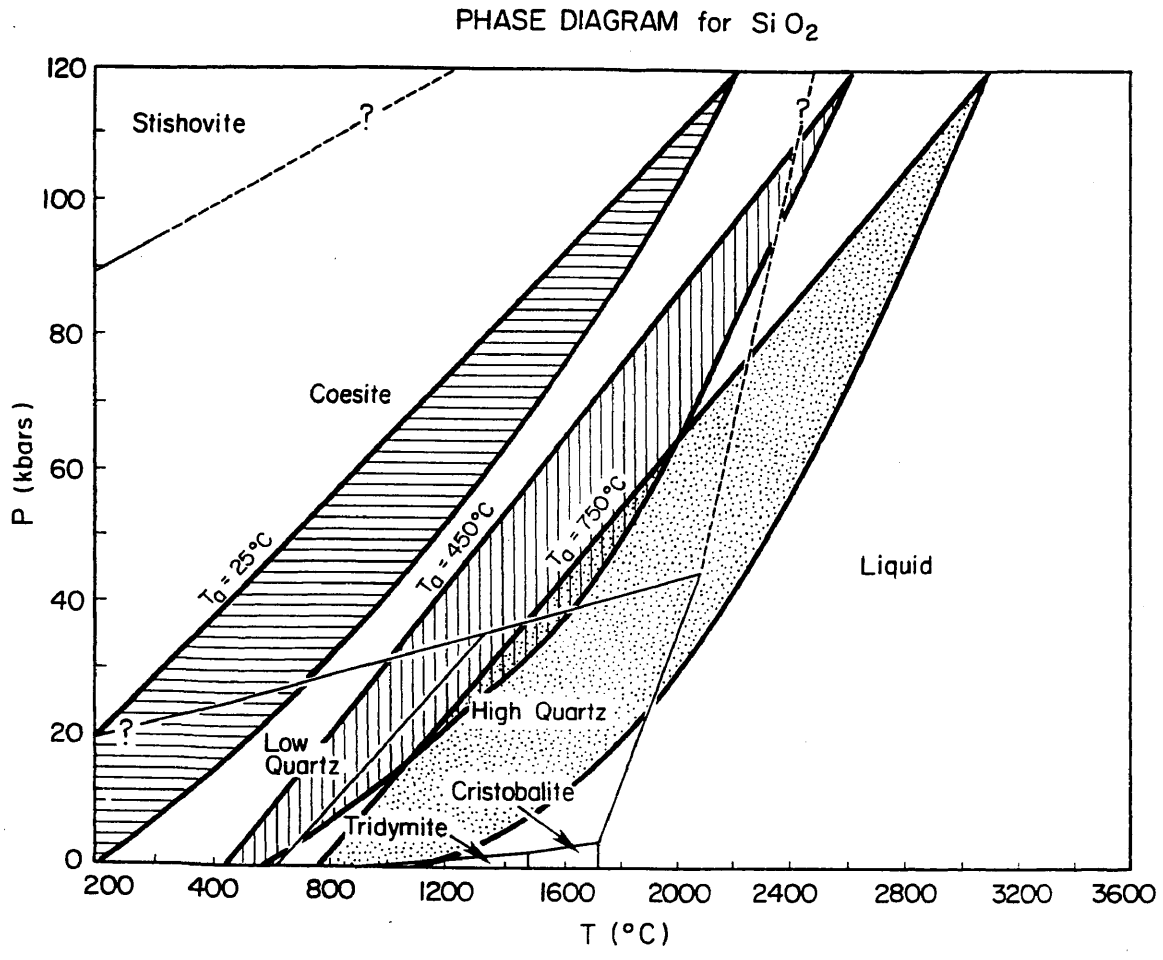


Figure 4-9: Estimate of the final shock state achieved for experiments initially at ambient temperatures ($T_a$) of 25°, 450°, and 750°C. Note that the release from a high-temperature test should produce melting where the 25°C test should not. The possibility of cristobalite and/or tridymite production also exists for high-temperature experiments.

The two important observations in this predicted behavior are that (1) the preservation of high-pressure polymorphs will probably be suppressed despite the assistance of higher temperatures in the nucleation and growth process, and (2) the release path for shock at elevated temperatures may produce melting at shock pressures much lower than in room-temperature experiments, as well as formation of high-temperature polymorphs such as tridymite and cristobalite as the material cools rapidly during unloading. It is also anticipated that high ambient temperatures will enhance development of the shock mosaic structure and recovery processes that occur after the shock event. The effect on the formation of planar features can be predicted under the assumption of a specific model for their formation.

It has long been recognized that the strain rate applied to a material affects the character of deformation (figure 4-10). Strain rates from $10^{-1}$ to $10^{-8}$/sec generated by triaxial apparatus produce stresses on the order of 1 to 100 MPa in geologic materials, and reflect the processes of fracturing, faulting, frictional sliding, semi-brittle behavior, and plastic creep of silicates. Strain rates from $10^{-1}$ to $10^{2}$/sec produced by hydraulic or Hopkinson Bar techniques can yield stresses up to 2.0 GPa representing the low-velocity end of the dynamic loading range. In contrast to these deformation regimes, shock-recovery work has been accomplished in the strain-rate range from $10^{6}$ to $10^{8}$/sec, and at stresses form 3.0 to 50 GPa. The general relationship between stress and strain rate for dynamic loading in this strain-rate range has been determined to be a power-law relation with a stress exponent of about 4 (Grady, 1981; Swegle and Grady, 1985), and is written in the general form

$$\text{Strain Rate} = a\, P_h^4 \qquad (4.9)$$

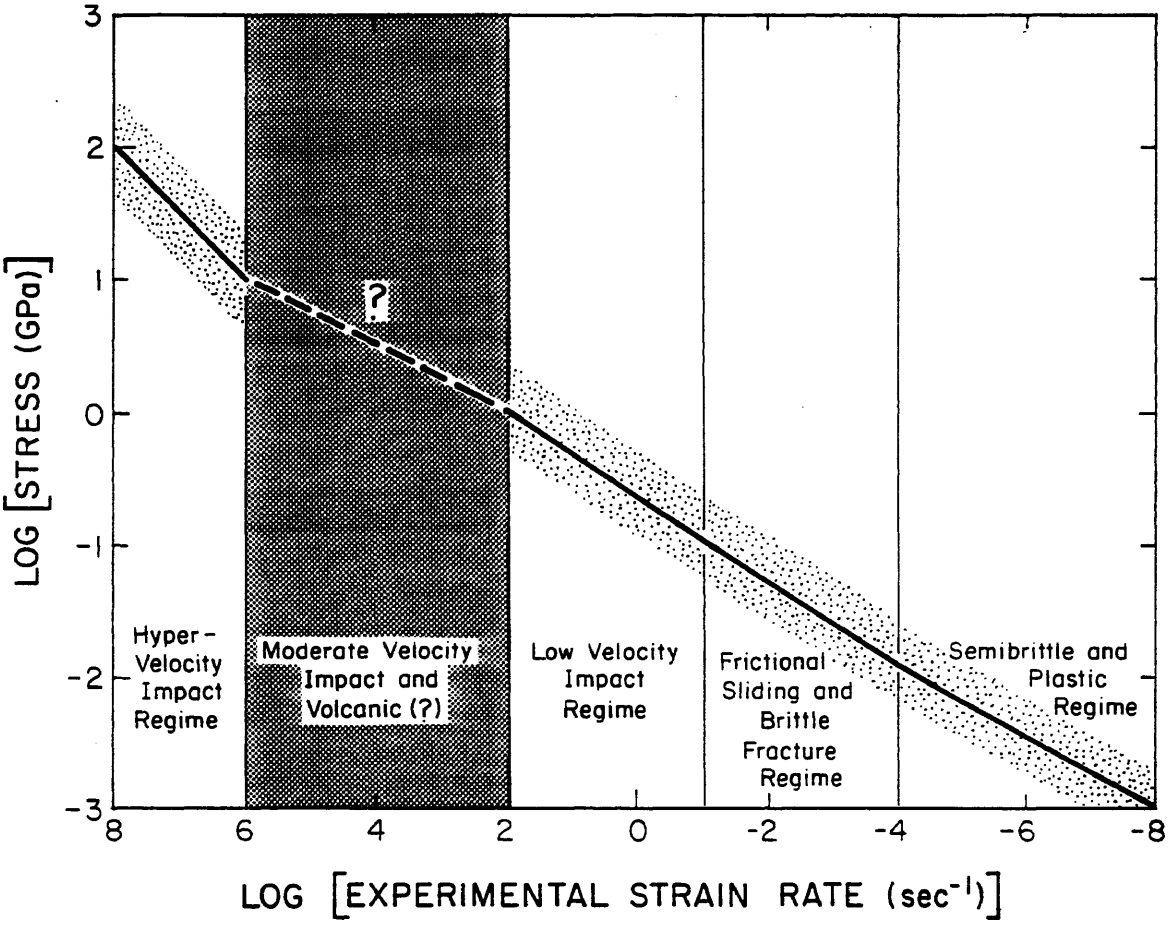


Figure 4-10: The range of available strain rates in experimental rock deformation reveals a gap from $10^2$ to $10^6$/sec, which reflects limitations of present apparatus. The inherent problem with this gap is that most natural dynamic events probably occur in this strain-rate range where no analog recovery experiments are available for comparison.

where a is a coefficient in $(GPa^4sec)^{-1}$. The data from hypervelocity impact studies, which are represented by this range of strain rates, suggests that stresses in quartz do not exceed 3 GPa at strain rates of $10^5$/sec. However, no shock-recovery data are available for strain rates below about $10^6$ and above $10^2$/sec, so that no microstructural data for this moderate velocity regime are available. The paucity of data in this range is due primarily to limitations on laboratory apparatus. The concern, however, is that most terrestrial dynamic events probably occur in this strain rate range, and with pulse durations on the order of seconds (volcanic jetting) to $10^2$ seconds (large landslides; e.g. Scott and Drever, 1953; Heuberger et al, 1984). The recognition of high-strain-rate features in volcanics (Chapter 2 of this thesis) ,from major landslides (e.g. Koefels; Surenian, 1988), and diatremes (Officer and Carter, 1990), raises a question as to whether there may be a wide spectrum of dynamic deformation features that change in character as a function of strain rate, stress, and temperature. This idea would not be intuitively unreasonable considering the similar observation for tectonic and frictional strain rates where a wide variety of features are observed.

## The Experimental Program

To determine whether ambient temperature and pulse duration affect the character of shock-induced microstructures, a series of high-explosive (HE) shock-recovery experiments were completed using the firing range at Los Alamos National Laboratory (LANL), Group M-6, at Ancho Canyon. The conditions selected for the experiments were temperatures of 25°, 450°, and 750°C, and pressures from 5 to 30 GPa in increments of 5 GPa. The materials selected for the program were Westerly granite and Hospital Hill Witwaters-

rand quartzite. The granite was selected because (1) it is a well-characterized material with known physical properties, (2) it contains quartz, plagioclase, and K-feldspar which are of primary interest for the development of shock-induced microstructures, and (3) it is an acceptable coarse-grained analog for a glassy to cryptocrystalline high-silica rhyolite which is a common rock type involved in explosive volcanic eruptions. The Hospital Hill quartzite was selected specifically for comparison with the same material used in the shock-recovery experiments described by Reimold (1988) and discussed in chapter 2 of this work.

Momentum-Trap and Furnace Design

The first task in the experimental program was the design and construction of a momentum trap suitable for the proposed experiments. The use of HE as an energy source allows the use of either internal or external furnace assemblies. Because the HE destroys the assembly, an external furnace was deemed to be too costly, so an internal furnace was designed using 0.010" molybdenum foil as a heating element (figure 4-11). The foil was designed in a wrap-around configuration with power leads that were welded to 12-gauge copper wire using high-temperature silver solder. The sample was a 0.10" thick wafer of rock, 0.35" in diameter, and ground to a 600-grit, plane-parallel finish. The furnaces were wrapped around the sample and sandwiched between layers of 0.01" mica to insulate the assembly from the steel momentum trap.

The momentum trap itself was constructed from 303 stainless steel bar stock that has a known Hugoniot (figure 4-4). The assembly was designed as a

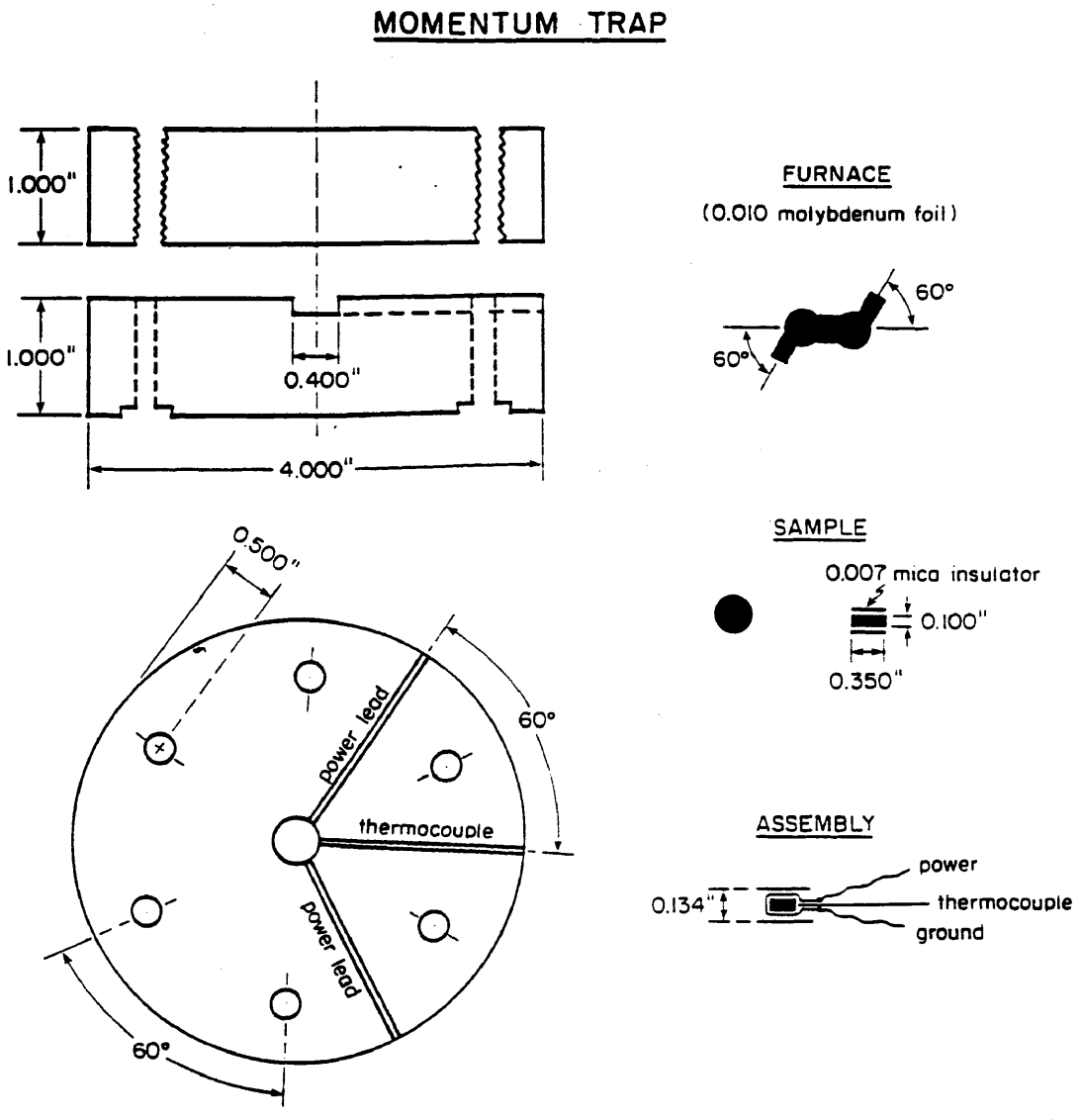


Figure 4-11: Momentum trap design with internal molybdenum foil furnace for shock-recovery experiments at high ambient temperatures and pressures to 15 GPa. Diagram is not to scale.

Figure 4-12: Momentum trap design with modifications to allow shock pressures to 30 GPa. Note the thinner base plate (A), and the notched spall ring (C). The range of flyer plates (D3-D6), and spall plates (D1-D2) are also shown. Diagram is not to scale.

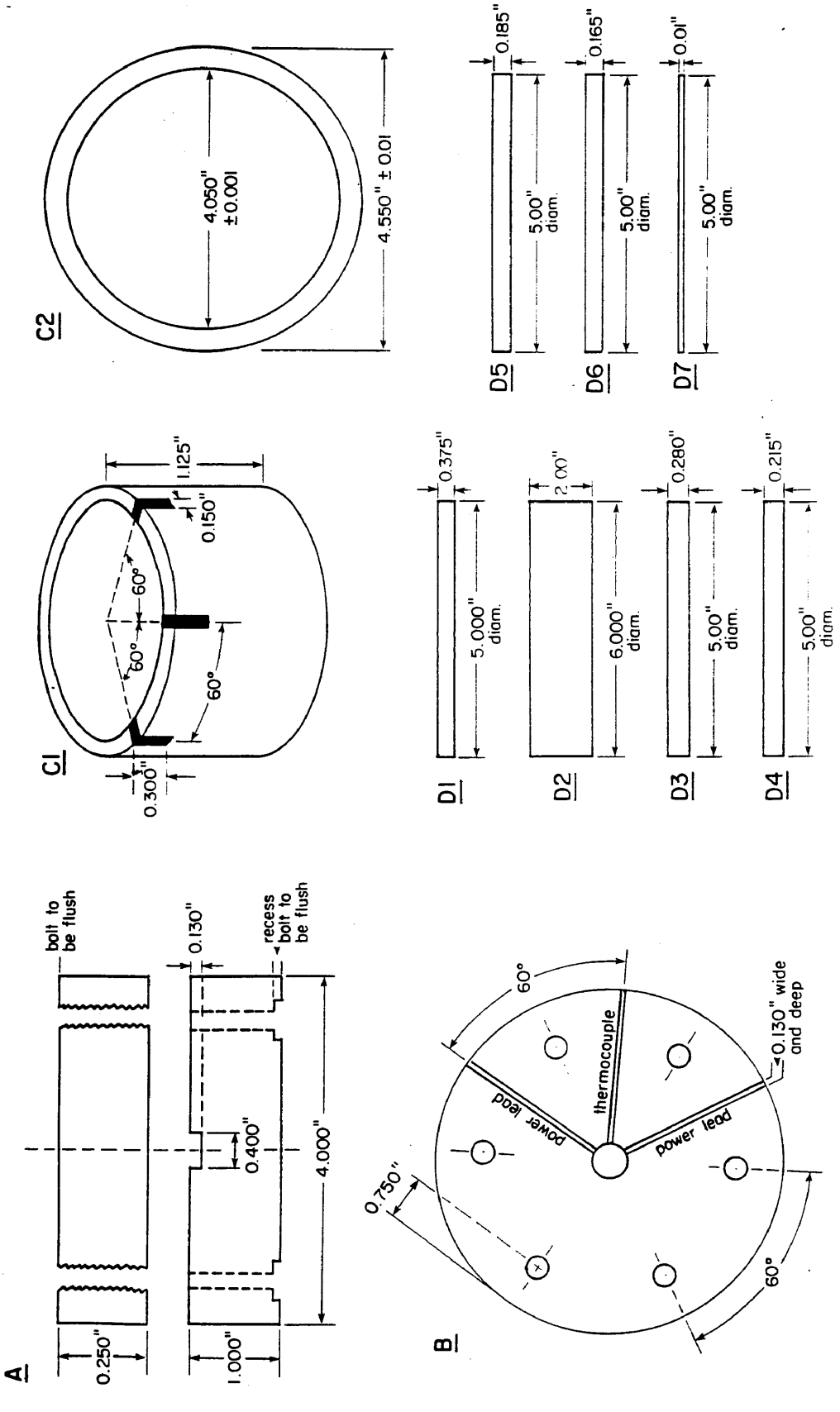
A
bolt to be flush
0.130"
recess bolt to be flush
0.400"
4.000"
0.250"
1.000"
B
60°
thermocouple
power lead
power lead
0.130" wide and deep
0.750"
60°
C1
1.125"
0.150"
60°
60°
60°
0.300"
C2
4.050" ±0.001
4.550" ± 0.01
D1
0.375"
5.000" diam.
D2
2.00"
6.000" diam.
D3
0.280"
5.00" diam.
D4
0.215"
5.00" diam.
D5
0.185"
5.00" diam.
D6
0.165"
5.00" diam.
D7
0.01"
5.00" diam.

sandwich of two steel discs, which were bolted together using hardened steel bolts with the heads machined to be flush with the back surface when assembled. An assembly diameter of 4.0" was chosen to assure that any side rarifactions of diffracted waves from the corners of the assembly would converge behind the sample and would not affect the loading history at the geometric center of the assembly. In the low pressure (5-15 GPa) configuration, the "base plate" which separates the sample from the flyer plate, was 1.0" thick. The lower plate, which was also 1.0" thick, contained a recess for the sample assembly, along with tracks for the two copper power leads and a chromel-alumel thermocouple for monitoring of temperature before detonation of the HE. For the high-pressure (20-30 GPa) configuration, the assembly was redesigned (figure 4-12) with a thinner base plate (0.25"), and a 1015 cold-rolled-steel spall ring was added to transfer the energy from radial expansion of the assembly and suppress radial fracturing during the experiment.

Each experiment was assembled carefully to assure that the furnace, power leads, and thermocouple were placed properly and insulated from the steel trap. The sample, furnace, and mica were placed in the lower plate recesses with the copper wires and thermocouple insulated in 0.125" I.D. alumina tubing. Additional mica strips and Sauerizen resistor cement were used to insulate any remaining places in the assembly and also to fill any voids. The thermocouple was placed in direct contact with the side of the sample (figure 4-11). The assemblies were bolted together and the furnace circuit was checked to determine if it was complete and insulated properly. Furnaces constructed and insulated in the correct way produced a circuit resistance of 1.0 to 1.1 ohms at room temperature. Cross-checking of a circuit

from the furnace through the steel trap yielded resistances of 15-20 Mega-ohms in properly constructed assemblies. Each assembly was baked in an oven at 110°C for 24 hours to dry the resistor cement and drive any moisture from the assembly.

Estimation of Peak-Shock Pressure

After the design of the momentum trap was completed, the next step was to determine what flyer plate thicknesses were required to produce a specific peak-shock pressure in the sample. An equation describing flyer plate velocity ($V_f$) versus flyer plate thickness ($h_f$) for the specific P-40 HE plane-wave generator used at Los Alamos is written as

$$V_f = 2.23 - 6.15\ h_f + 5.9\ h_f^2 \qquad (4.10)$$

The Hugoniot equations for 303 stainless steel, which are written as

$$U_s = 4.48 + 1.51\ u_p \qquad (4.11)$$

$$P_s = 7.93\ u_p\ U_s \qquad (4.12)$$

where $u_p$ = particle velocity, $U_s$ = shock velocity, and $P_s$ = peak shock pressure may be combined with equation 4.10 and the equation relating $V_f$ and $u_p$, which is

$$u_p = V_f / 2 \qquad (4.13)$$

to derive an equation for shock pressure in the steel. This equation is written as

$$P_S \text{ (GPa)} = 54.498 - 191.351\ h_f + 296.79\ h_f^2 - 217.228\ h_f^3 + 104.194\ h_f^4 \qquad (4.14)$$

with $h_f$ in inches. The resulting curve (figure 4-13) predicts the peak shock pressure achieved in the steel, which will be the same in the sample provided that the release wave doesn't truncate the reverberation process before it reaches the peak pressure defined by equation 4.14. Calculation of the arrival of the release wave at the sample, and hence the actual shock pressure and pulse duration achieved, will be discussed later in this chapter.

Calibration of Thermocouple Readings

Because the thermocouple was not placed in the sample, and because of the strong temperature gradient from the furnace to the steel trap at high temperature, it was necessary to calibrate the thermocouple using a reference thermocouple. To accomplish this, a special base plate with a hole drilled down its axis was machined. A complete momentum trap was assembled using this base plate. After assembly, a 3 mm microdrill was used to drill through the furnace and into the sample, and a reference thermocouple was placed through this hole (figure 4-14). As power was applied to the furnace, readings were recorded from both thermocouples. A plot of these readings (figure 4-15) reveals that when the reference thermocouple produced readings indicative of temperatures of 450° and 750°C, the sample thermocouple produced readings of 9.6 and 11.2 mV respectively. These readings were used as calibrations for achieving these temperatures on the firing point.

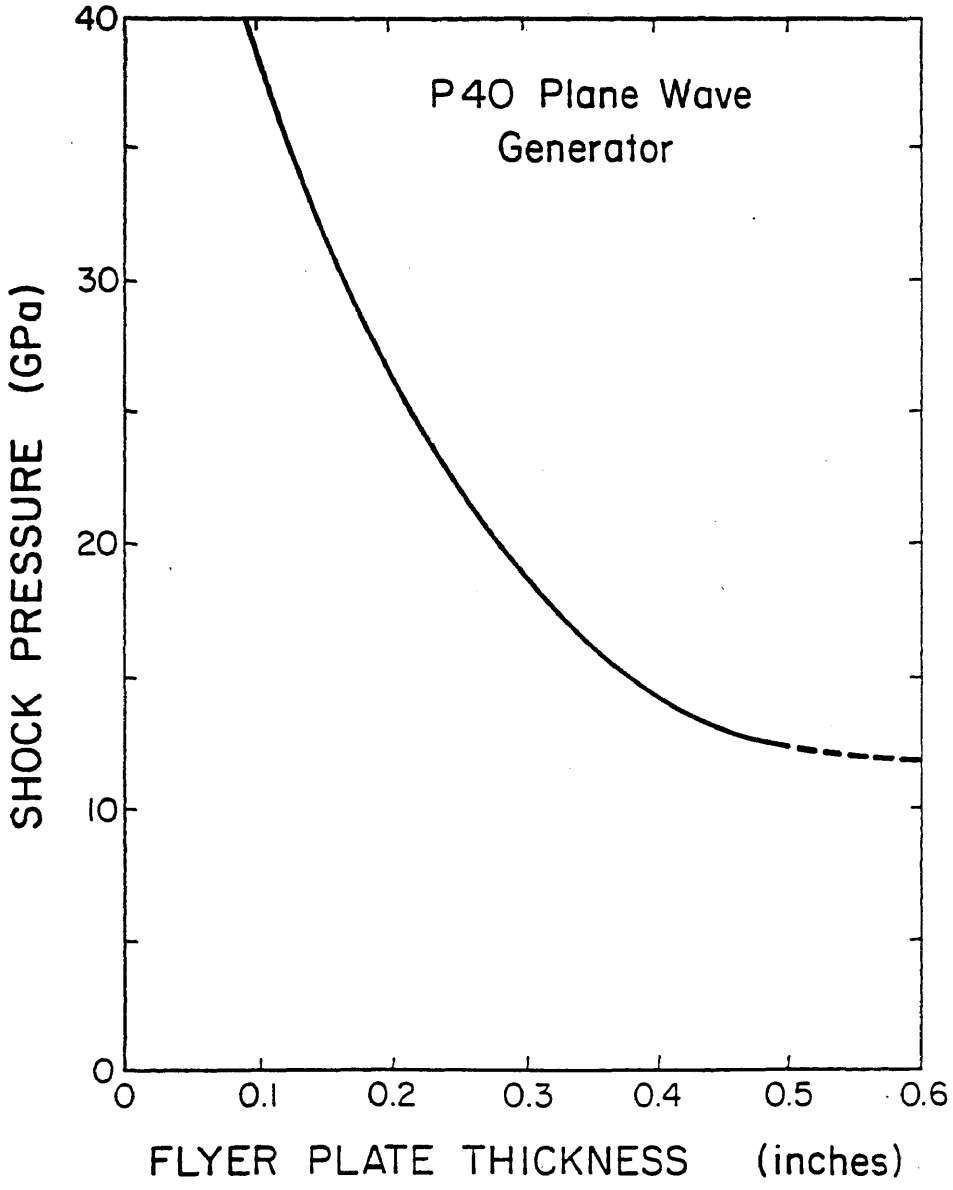


Figure 4-13: Shock pressure calibration curve for impedance-match solution in stainless steel. This pressure assumes that the granite achieves the same shock state as the steel by reverberation as shown in figure 4-4 and 4-5. This shock pressure estimate is called the "nominal" shock pressure.

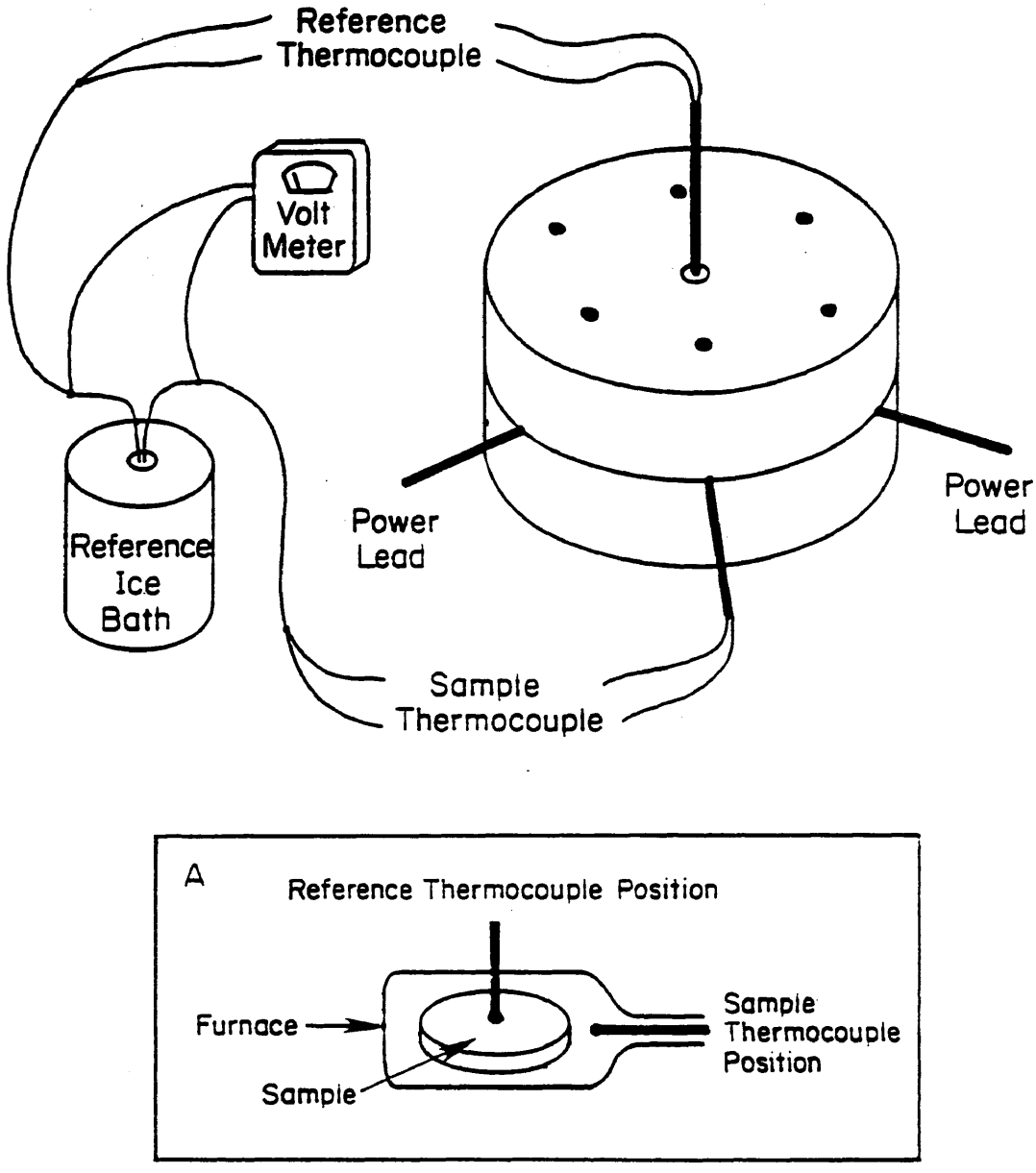


Figure 4-14: Schematic of the configuration used for thermocouple calibration. Insert A shows the relative positioning of the reference and sample thermocouples.

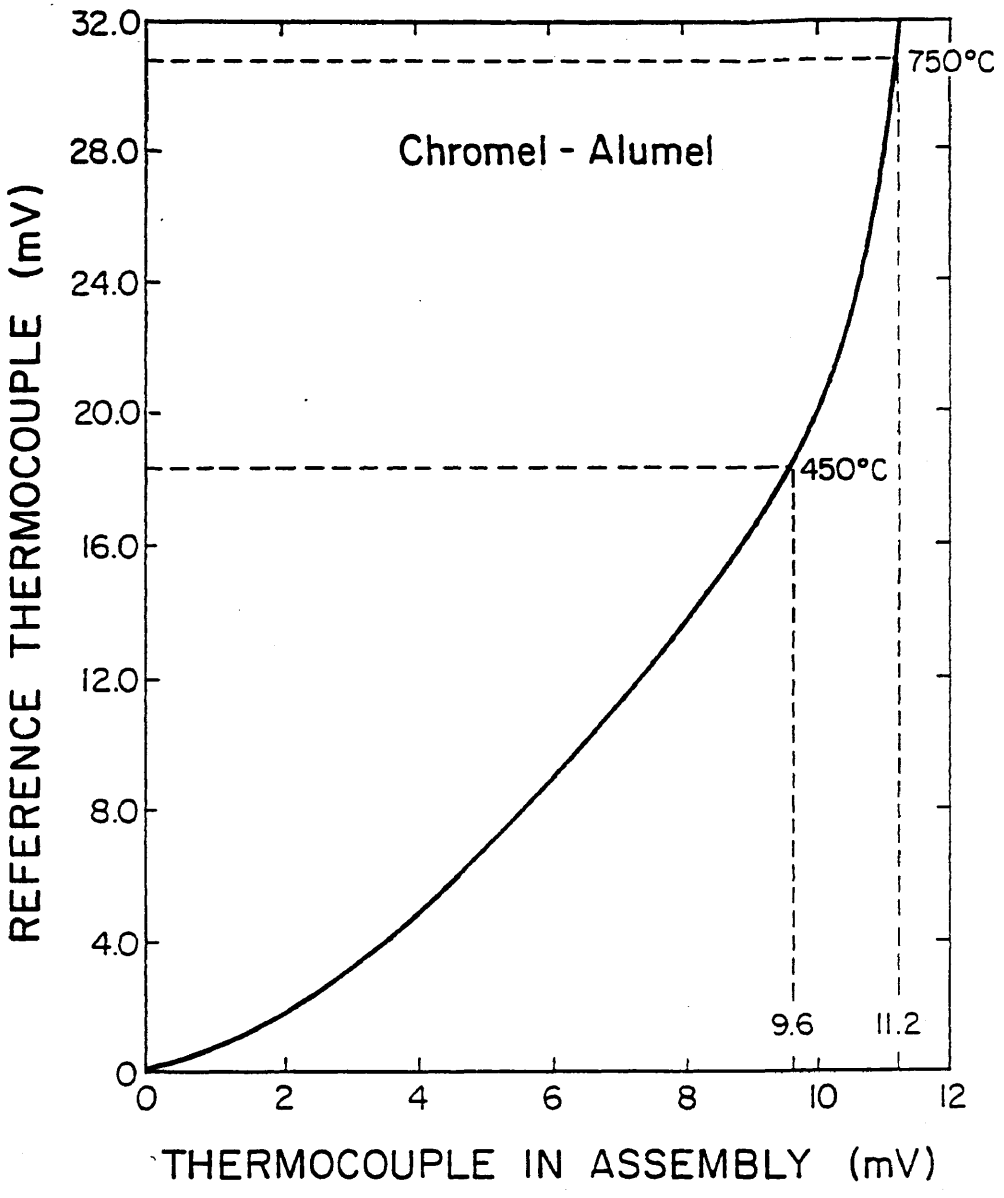


Figure 4-15: Calibration curve for the sample thermocouple based on the configuration shown in figure 4-14.

Experimental Field Configuration

The shock-recovery experiments were completed in two phases during August, 1988, and January 1989. The sample configuration for each experiment (listed in Appendix II) utilized either a driver plate in contact with the assembly base plate, or a free-run method with the flyer plate and explosive separated from the assembly base plate by a 1.0" ring of styrofoam (figure 4-16).

The explosive used for all the experiments was a P-40 plane-wave generator used routinely at LANL for such experiments. The P-40 consists of a machined shell of fast-burning Composition-B explosive and a core of slower-burning Baratol explosive. The geometry of the explosives is designed to produce a planar shock front that will drive the flyer plate straight downward into the assembly. The explosive was elevated above the flyer plate using a sheet of 0.01 polyethylene and a set of 2 mm spacers. The sample assembly was placed below the explosive and styrofoam ring along with several steel spall plates (figure 4-17). These spall plates were used to transfer the shock wave energy and prevent free-surface reflections which could result in spallation and destruction of the assembly. The specific thicknesses of the components in each experiment are listed in Appendix II. The entire experiment was suspended over a bucket of water and then sandbagged to prevent the assembly from escaping during the experiment.

The power source for the furnace used a 110 V powerstat, a 20:1 stepping transformer, and 4.0 gauge welding cable. The powerstat was used to feed power by 12-gauge single-strand wire from inside the firing bunker to the

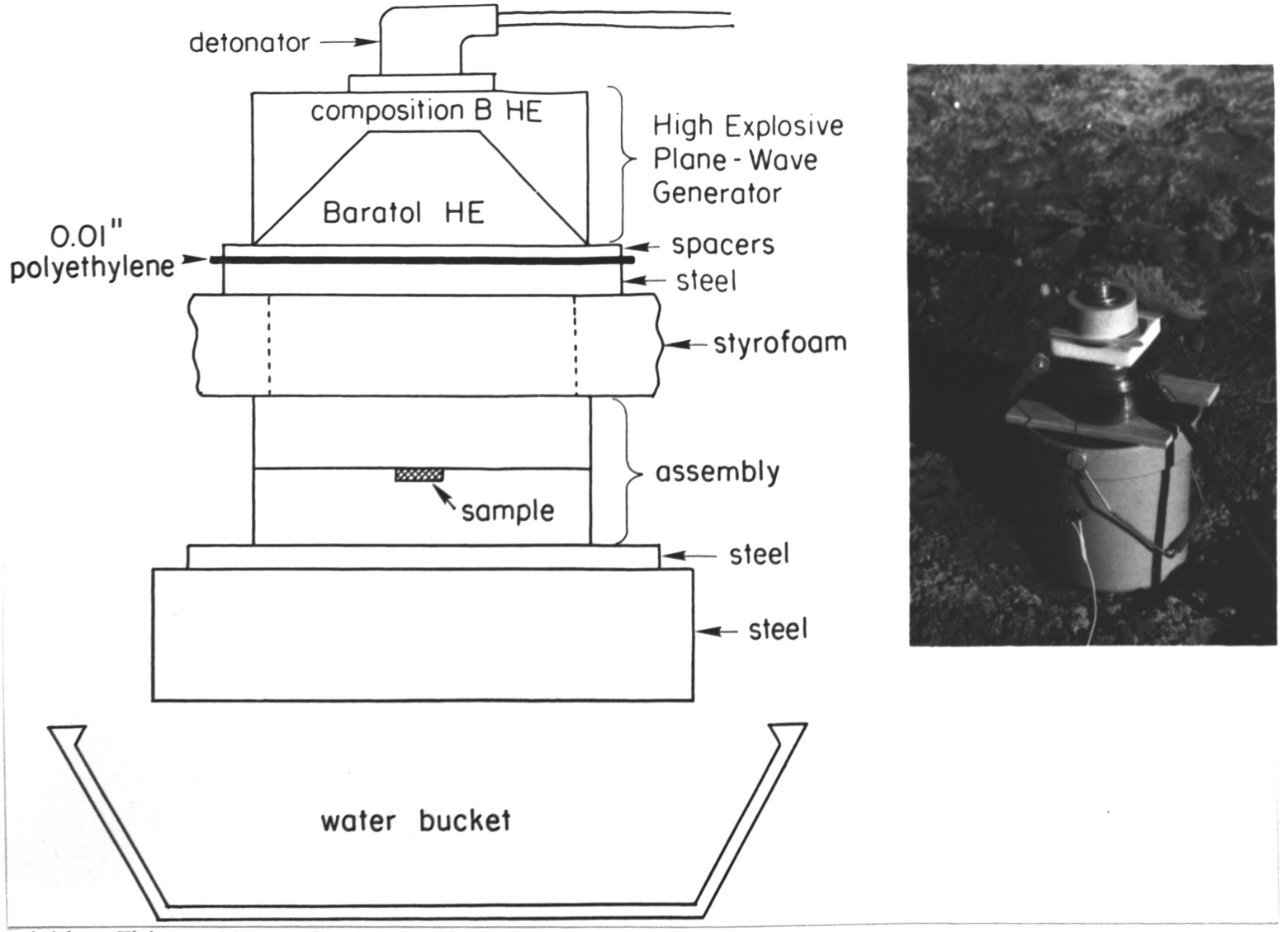




**Figure 4-16:** Firing table configuration for a free-run shock-recovery experiment. The photo insert shows the assembly on the firing point with power leads, thermocouple, and explosive in place. The configuration for a contact driver plate is the same except for the absence of the styrofoam spacer.

explosion table. The stepping transformer was placed at 5 meters from the firing point and was sandbagged to protect the power system from blast effects and debris. The power from the transformer to the furnace was conducted through 4.0 welding cable, which was necessary to transmit up to 800 Watts (200 amps at 4.0 volts) without significant power loss. The 4.0 cable was hooked up to the transformer using welding clamps, and was bolted to the assembly power leads using copper welding eyes and metal nuts and bolts (figure 4-16, photo insert). The cables were sandbagged to prevent damage to all but the last five feet, which was replaced after each shot. Power consumption of the furnace circuit was monitored using an ammeter and voltmeter between the assembly and the transformer. The output was monitored from inside the firing bunker by the use of meters built into the powerstat unit.

## The Experiments

The first series of 16 experiments were completed in August, 1988, and included shots at nominal pressures of 5, 10, 12, and 15 GPa. These experiments, which are identified by '88' and the shot number (e.g. 88-1) included successful experiments on 3 quartzite and 9 granite samples (table 4-1; and Appendix II). Because this was the first attempt at doing this type of experiment, the configuration was varied to determine the best way to recover the assemblies intact. Shots 88-1 through 88-8 were completed using the 1.0" base plate (figure 4-11), and a driver plate in contact with the assembly (i.e. no free-run). The results using this method were only partially satisfactory, with four of the eight shots yielding no recovery due to complete failure of the assembly. The dominant cause of failure was radial fracturing along the power-lead and thermocouple tracks, and through the bolt holes. The

remaining eight experiments were performed using the free-run method and the configuration shown in figure 4-16. All of these experiments were completed successfully with recovery of completely intact assemblies from each shot. The molybdenum furnaces performed well with only one furnace failure in a shot for which the sample was lost as well.

The second series of 15 experiments were completed in January, 1989, and included shots at nominal pressures of 20, 25, 28, and 30 GPa. These experiments, identified by '89' and the shot number included 4 experiments on quartzite, nine experiments on granite, and two stand-alone shots on dunite (table 4-1; and Appendix II). All the shots in this series were completed using a 0.25" base plate as shown in figure 4-12A, and a free-run method. To suppress the radial fracturing problem encountered in the first series of shots, a spall ring made of 1015 cold-rolled steel was added to the assembly (figure 4-12C and 4-17A). These design changes led to 100% recovery in 12 of 15 experiments, and only one shot with no recovery due to assembly failure. One furnace failed (shot 89-1), and all others worked sufficiently well to complete the desired matrix of experiments.

Other problems encountered during the experiments were minor. The major concern was the effectiveness of the water bucket for quenching the assemblies. The small size of the bucket was ill-suited to the task and failed to catch the assembly in sufficient water for proper quenching. To deal with this problem, a large barrel of water was placed adjacent to the firing point. After each shot, the assembly was retrieved quickly using an asbestos glove, and immersed in water to cool the momentum trap. The temperature of the steel was estimated to be between 200° to 300°C after shocking, which was

Table 4-1: Shot table showing experiment identification numbers, sample type, and the experimental conditions including the nominal shock pressure ($P_n$), the estimated shock pressure ($P_a$) in GPa, the ambient temperature before shocking ($T_a$) in °C. Sample type is either Westerly granite (WG), Hospital Hill quartzite (HHQ), or Balsam Gap Dunite (BGD). (* indicates no recovery)

| Experiment Number | Material | $P_n$ | $P_a$ | $T_a$ |
|---|---|---|---|---|
| 88-1 | WG | 10 | 12 | 25 |
| 88-2 | WG | 10 | 12 | 450 |
| 88-3 | WG | 10 | - | 450 |
| 88-4 | WG | 5 | 5 | 750 |
| 88-5 | WG | 10 | 12 | 750 |
| 88-6* | WG | 10 | - | 450 |
| 88-7* | WG | 20 | - | 25 |
| 88-8* | WG | 20 | - | 450 |
| 88-9 | WG | 12 | 8 | 750 |
| 88-10 | WG | 12 | 8 | 450 |
| 88-11 | HHQ | 12 | 8 | 100 |
| 88-12 | HHQ | 12 | 8 | 450 |
| 88-13 | HHQ | 12 | 8 | 750 |
| 88-14 | WG | 15 | 15 | 750 |
| 88-15 | WG | 15 | 15 | 450 |
| 88-16 | WG | 15 | 15 | 25 |
| 89-1 | BGD | 25 | 23 | 300 |
| 89-2* | BGD | 25 | 23 | 900 |
| 89-3 | WG | 30 | 25 | 450 |
| 89-4 | WG | 25 | 23 | 750 |
| 89-5 | WG | 25 | 23 | 450 |
| 89-6 | WG | 20 | 18 | 750 |
| 89-7 | WG | 30 | 25 | 750 |
| 89-8 | HHQ | 25 | 23 | 750 |
| 89-9 | HHQ | 28 | 24 | 750 |
| 89-10 | HHQ | 28 | 24 | 450 |
| 89-11 | HHQ | 28 | 24 | 25 |
| 89-12 | WG | 20 | 18 | 450 |
| 89-13 | WG | 30 | 25 | 25 |
| 89-14 | WG | 25 | 23 | 25 |
| 89-15 | WG | 20 | 18 | 25 |

Figure 4-17: Photographs of the momentum trap before shocking. A. Momentum trap and spall ring showing the 0.25" base plate on top. B. Momentum trap showing recessed bolts in the lower plate. Note the insulated copper power leads and thermocouple. C. Assembly and spall ring in place over a 0.375" and 2.0" set of spall plates and the water bucket.

A

B

C

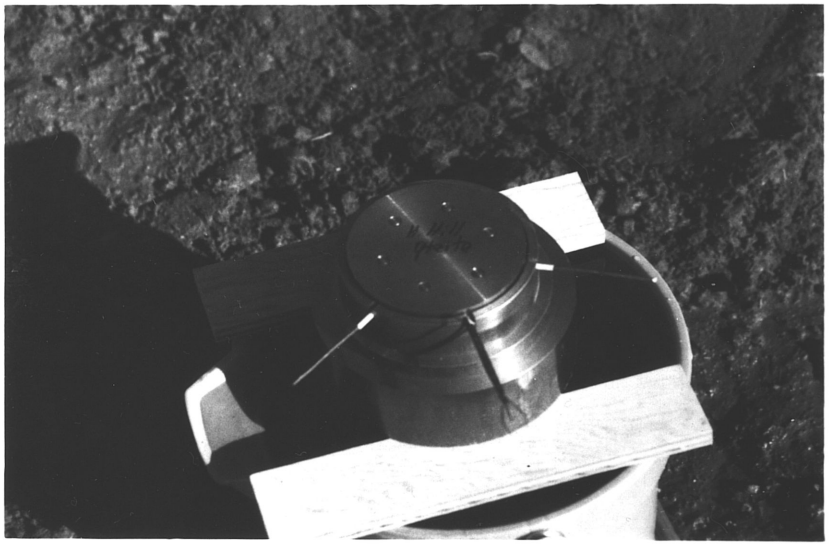

reflected in a short duration (about 30 seconds) of surface boiling upon immersion into the water bath. These temperature estimates are also born out by the fact that the assemblies did not scorch the asbestos glove.

Post-Mortem Procedures

After each series of shots were completed, the assemblies were transported back to Texas A&M for recovery of the samples. Each assembly was photographed to document its condition after shocking, and was then machined or pried open to retrieve the sample. Each assembly was rephotographed after opening to document any internal damage that occurred as well. Each sample was placed in a glass vial for further processing, which will be described in chapter 5.

The general condition of the assemblies after shocking indicated that the free-run configuration worked as expected. Each assembly shocked in this manner showed a symmetrical, bowl-shaped depression from the bolts inward, and a clean zone of shear deformation in the base plate from the bolt holes outward to the assembly perimeter. This character of deformation in the steel indicated that the flyer plate impacted the base plate in a nearly flat and parallel orientation, which is necessary to achieve uniform shocking of the samples.

The use of a spall ring turned out to be the most important design change as indicated by the resulting assemblies. All assemblies shocked with the spall ring showed significantly less radial fracturing and flow, in spite of the fact that the samples with spall rings were shocked to much higher

pressures. The thickness of the spall plates behind the assemblies also turned out to be critical to the success of the shots. Those shots which used the largest and heaviest spall plates resulted in the poorest recovery, probably due to the inability of the explosive to accelerate the larger plate along with the assembly. In the shots that used the thickest spall plates, the assemblies essentially bounced off of the spall plates and fragmented as the assembly continued to ring up without the presence of the spall plate in contact. The best results were obtained when a moderate thickness (2.375") of spall plate was used (Appendix II).

## One-Dimensional Hydrocode Simulations Using MACRAME

As noted earlier, the nominal peak shock pressures for the experiments were determined assuming an impedance mismatch between stainless steel and the samples, and a complete reverberation to allow the sample to reach the shock pressure in the steel (figure 4-4). However, because of the release wave, the maximum shock pressure is not always achieved. To estimate the peak-shock pressure, pressure-time history, pulse duration, and particle-velocity history for each experimental configuration, a series of simulations were completed using a 1-D, finite difference discrete-wave simulation program called MACRAME (Fritz, 1987). MACRAME is designed to track specific wave-wave and boundary-wave interactions in a solid that is subjected to a shock wave. The code uses an impedance-match solution in the $P_s$-$u_p$ plane for each interaction, and calculates the new state at the interaction point, and the new wave, and/or new interface, created by the interaction. As the shock process progresses, the code follows each wave, and according to how fine one wishes to set $\partial P_s$ and $\partial u_p$, the code will calculate the $P_s$ history, $u_p$ history, and

lagrangian and eulerian x-t plots for the modeled interactions, including any spalls or other new interfaces created by the shock process. The impedance-match solutions used in MACRAME are based on the EOS database from Group M-6 at LANL.

The results of the simulations for the nominal 10, 12, 15, 20, 25, and 30 GPa experiments (figure 4-18) revealed that the nominal peak pressures were too high in most cases. The simulated pressure estimates, and the pulse duration for each nominal pressure (listed in Appendix II) were critical for comparison of the microstructures produced in the experiments, especially in the nominal 10 and 12 GPa shots, which turned out to have estimated peak pressures of 12 and 8 GPa respectively. The $u_p$-history for each simulation (figure-4-19) was also valuable in determining the deformation history of each sample configuration.

The simulations also served a useful purpose as a predictor of spallation and other collateral damage in the assemblies. For example, Plots of the wave interactions in lagrangian (y-t) and eulerian (x-t) coordinates for the nominal 30 GPa configuration (figure 4-20 and 4-21 respectively) reveal that significant spallation should occur in the sample (y = 0.0 to 4.0 mm). Other plots not shown here revealed spallation in the base plate and lower plate that were observed in the sample assemblies, demonstrating the usefulness of simulation codes such as MACRAME.

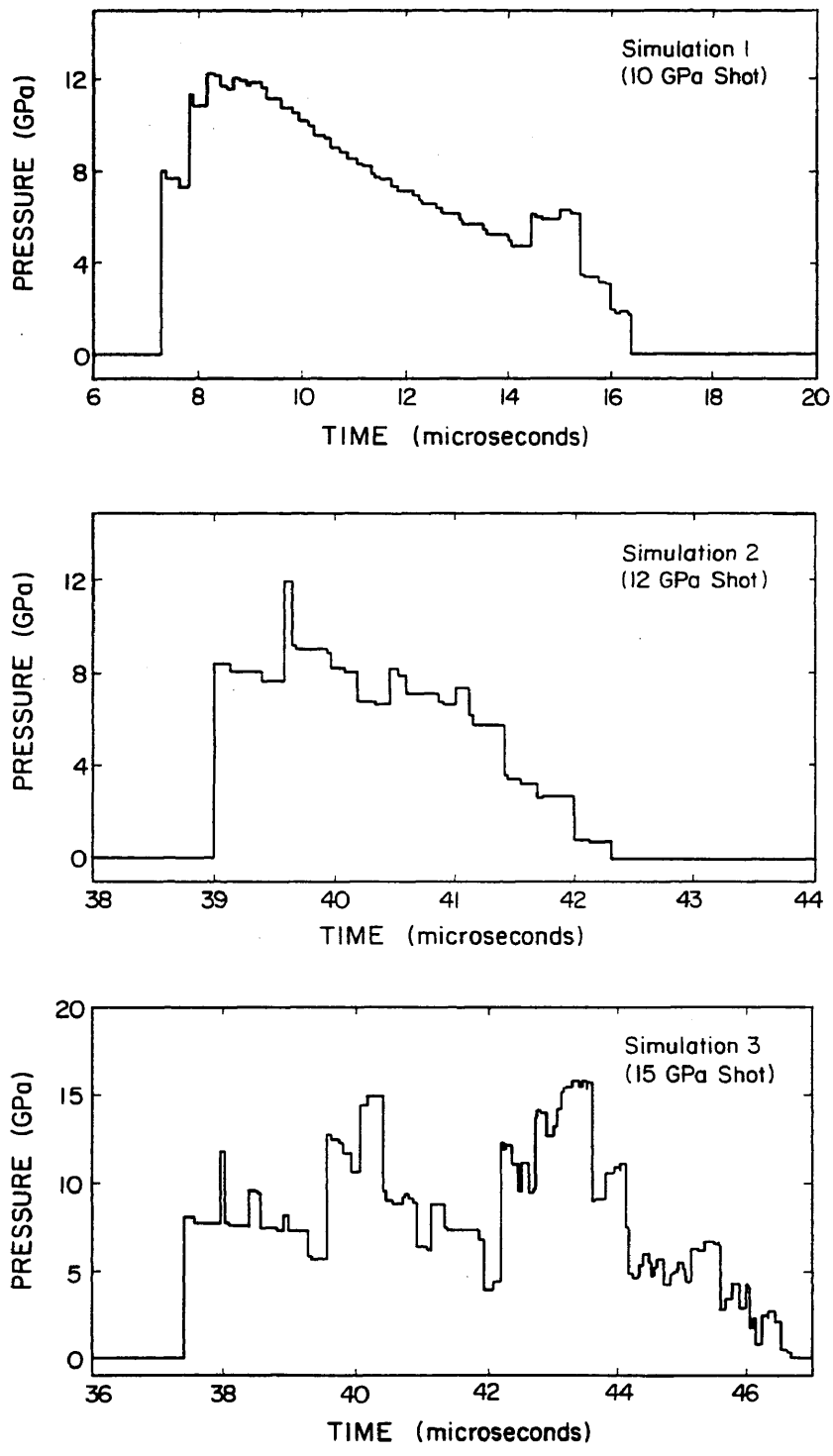


Figure 4-18: Estimates of actual shock pressure and pulse duration using the 1-D hydrocode MACRAME. The curves have been smoothed to remove short duration rattling with durations less than 0.1 microseconds that produces no significant effects. The pressures listed are the impedance match pressures.

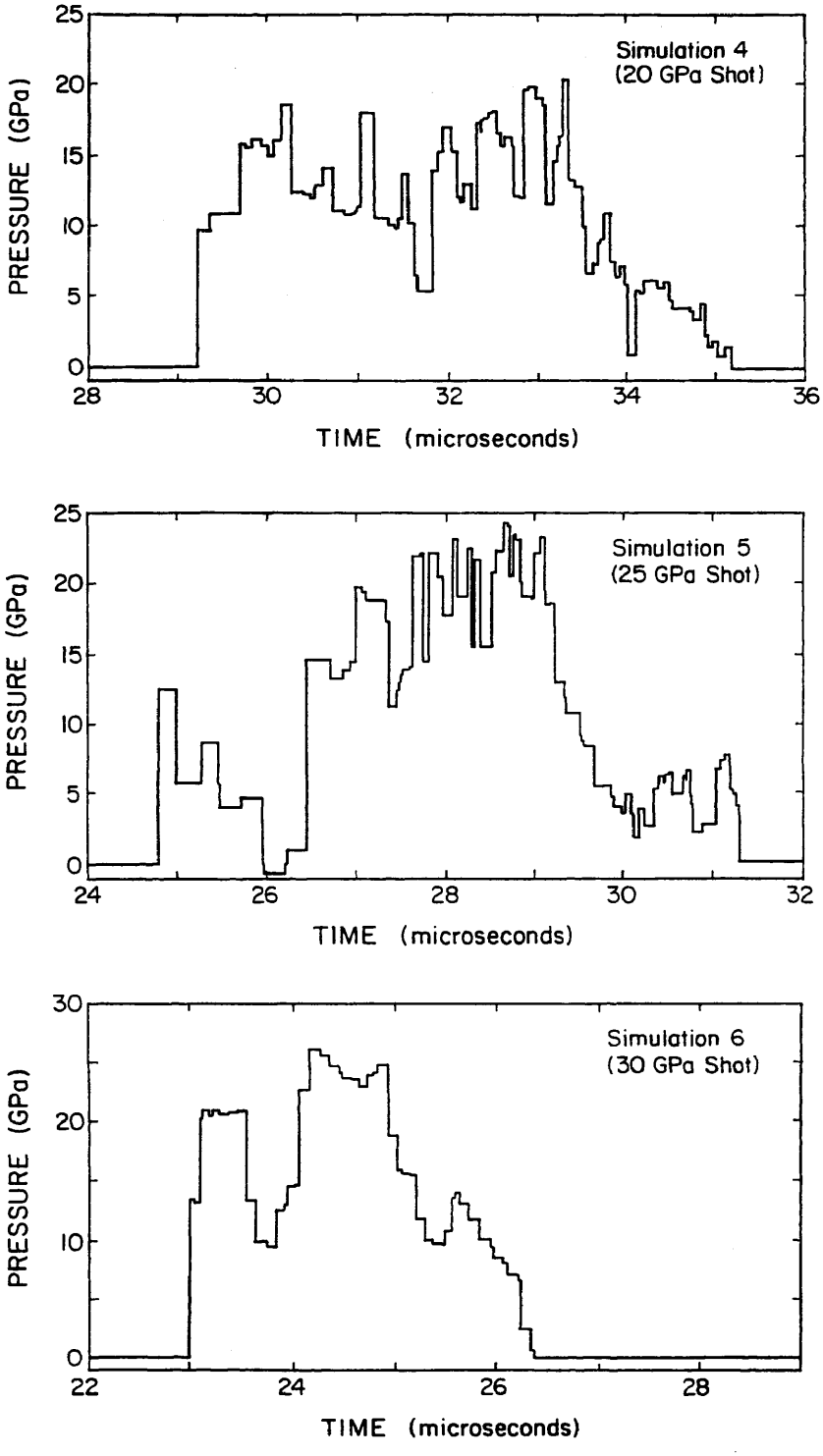


Figure 4-18 (Continued)

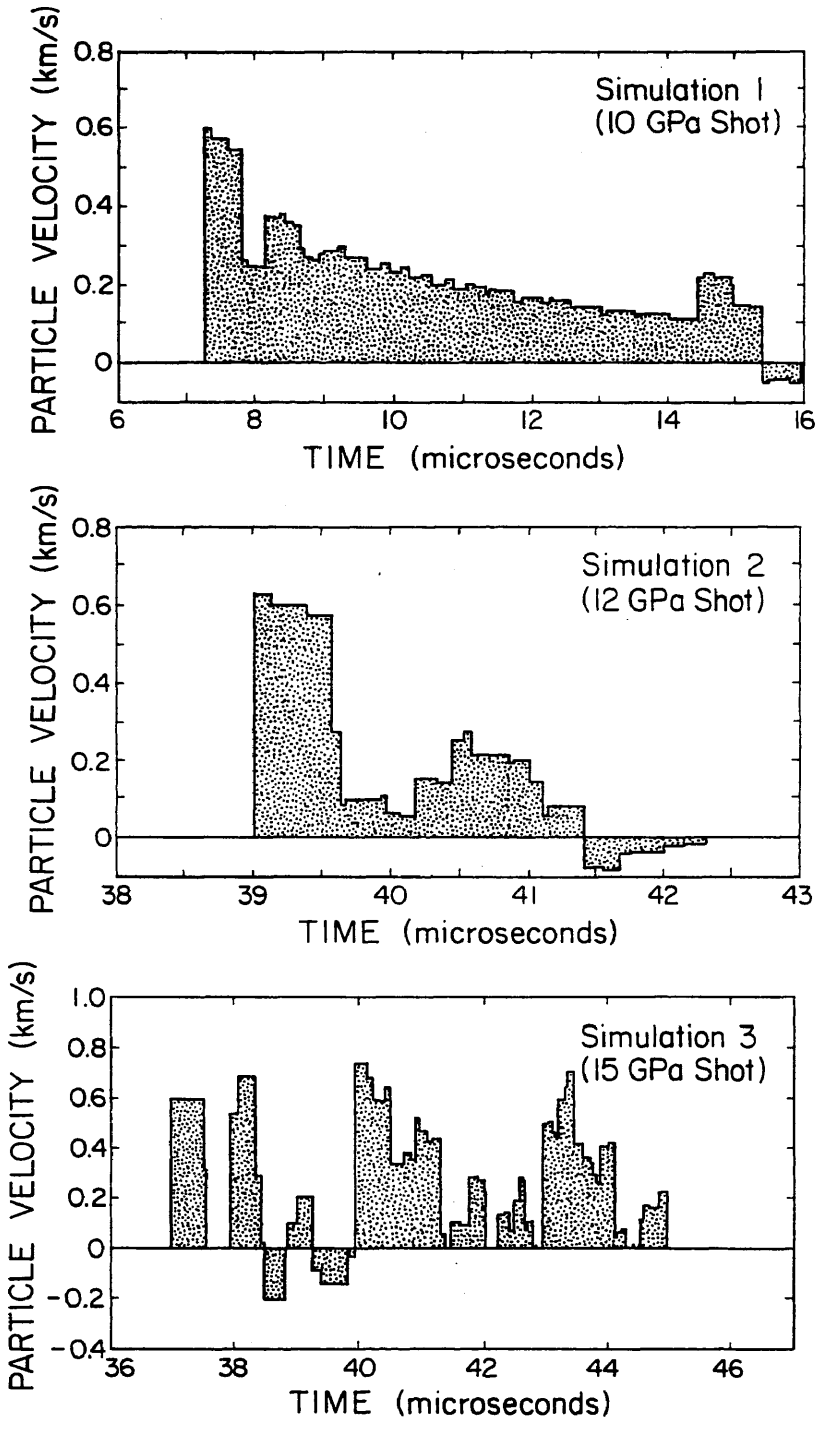


Figure 4-19: Estimates of the particle velocity in the sample during the shock pulse using the 1-D hydrocode MACRAME. The velocity curves have been smoothed to remove short-duration rattling that is mechanically insignificant.

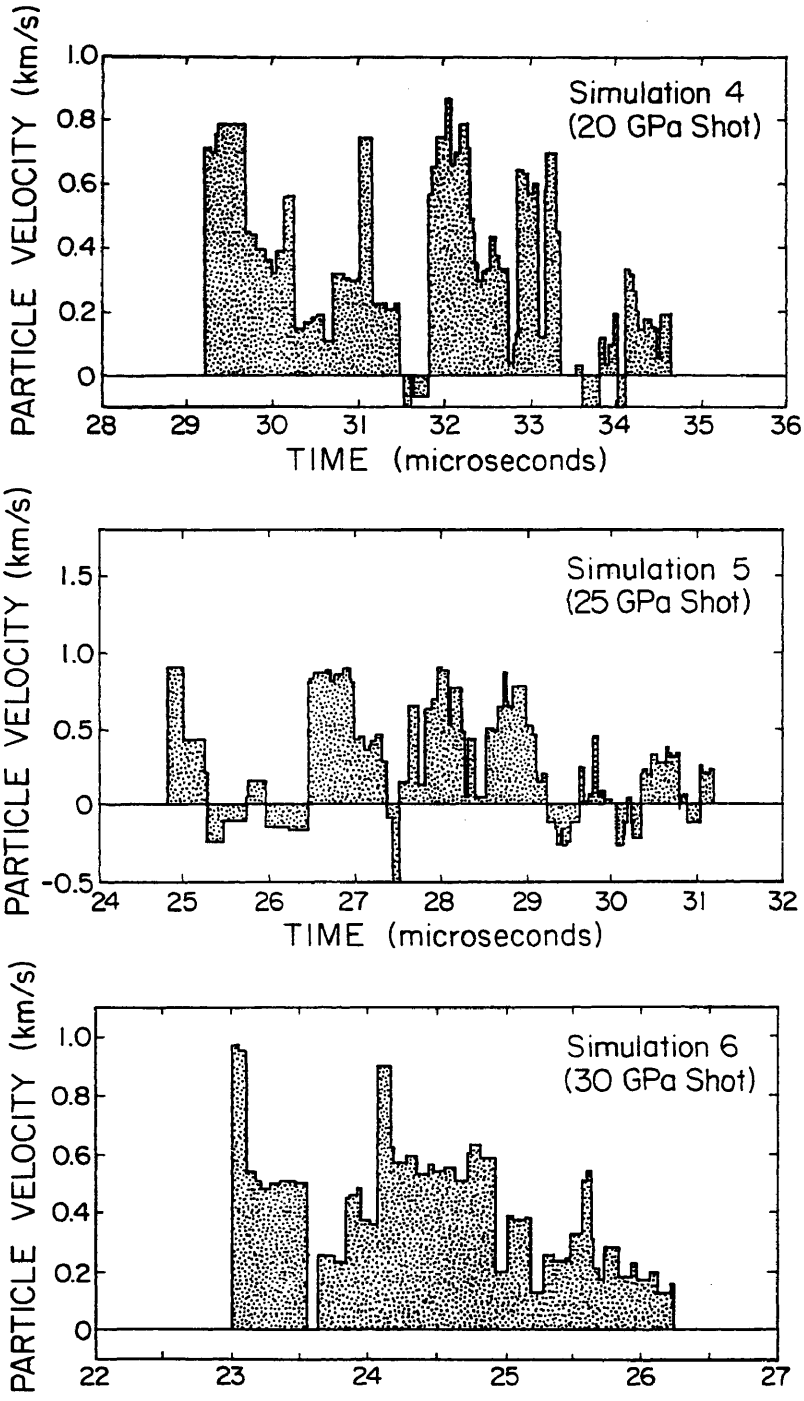


Figure 4-19: (Continued)

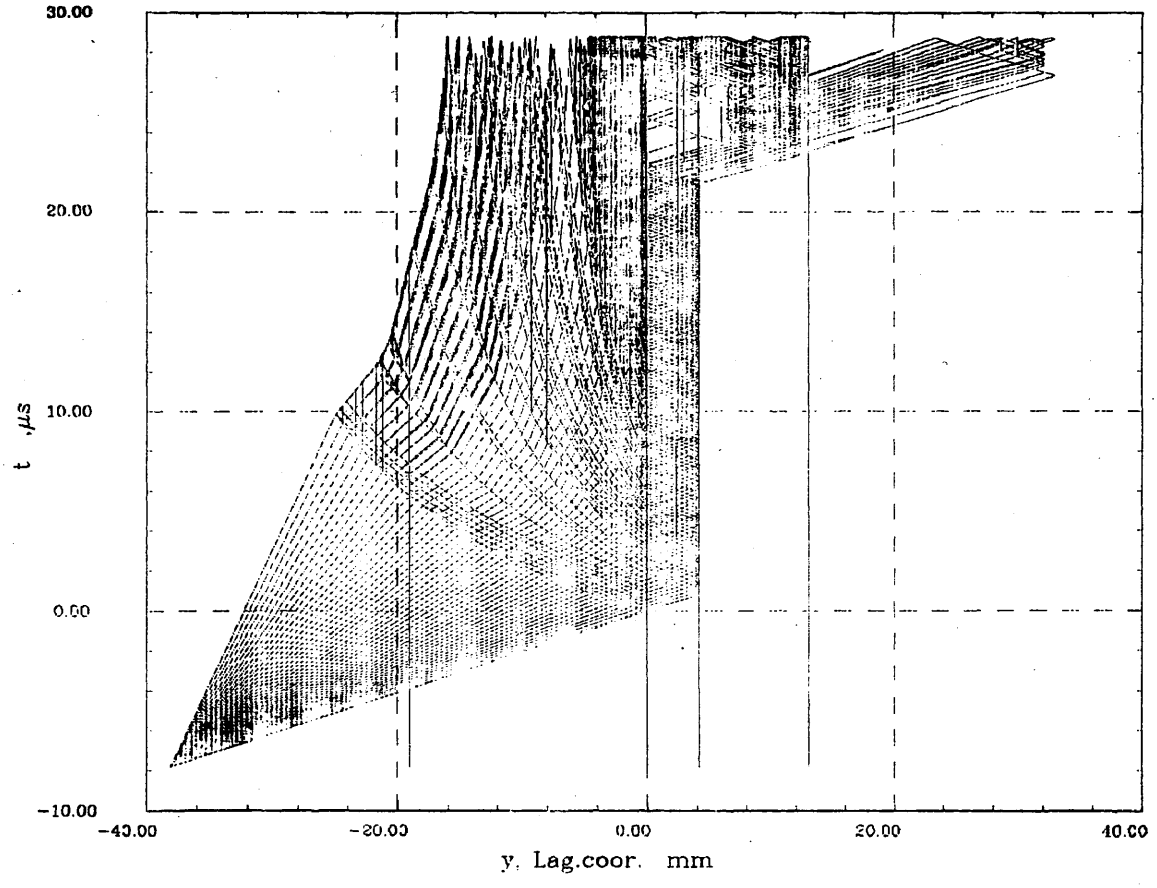


Figure 4-20: Y-t plot for simulation 6 (nominal 30 GPa pressure) in lagrangian coordinates showing the reverberations in the sample (0.0 to +4.0 mm), and the location of spalling in the sample, base plate, and lower plate shown by line and gap discontinuities.

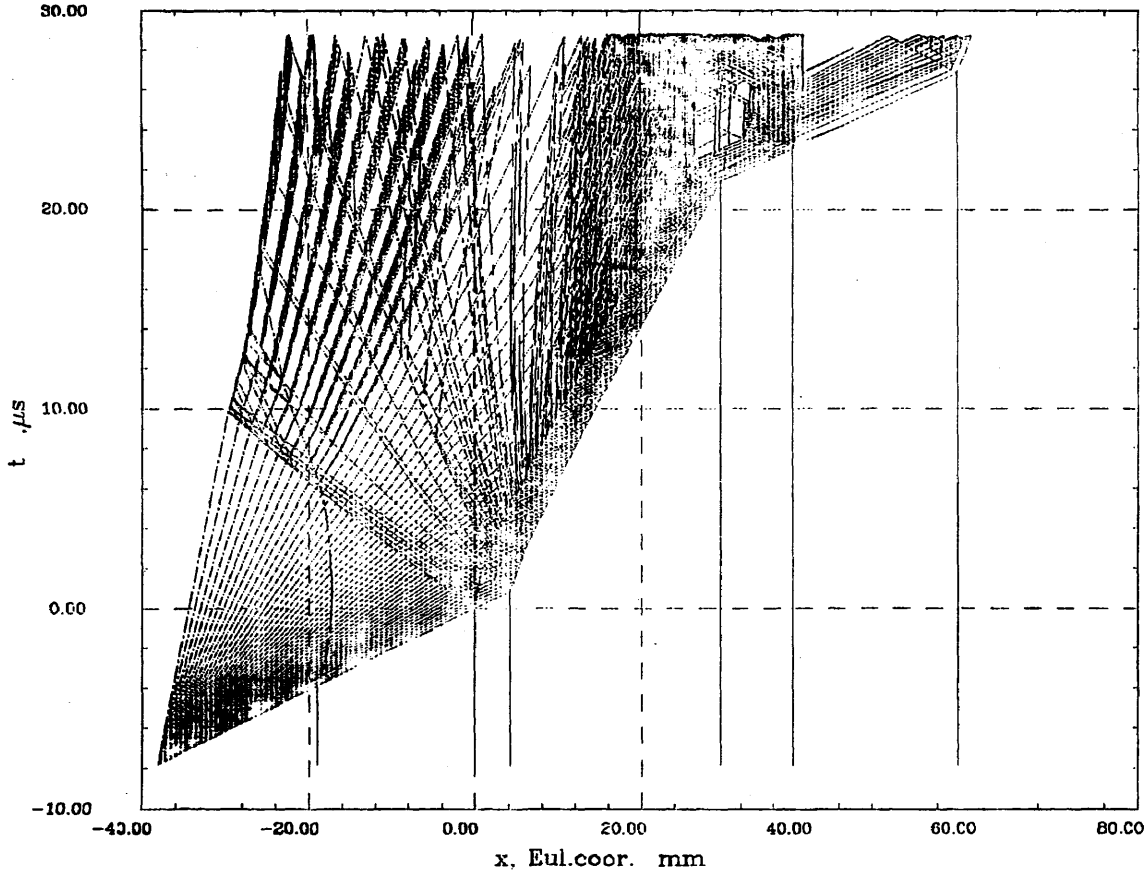


Figure 4-21: X-t plots in eulerian coordinates for the same simulation shown in figure 4-20. Note the change in location of the sample with time, which reflects the downward motion of the assembly during the experiment. The sample spall is also shown to be opening up with time.

## Discussion

The problems encountered during the experimental program and observations of the shocked assemblies indicate several improvements that could be made for future shock-recovery experiments. The furnace design used for this study was adequate, but can be improved significantly. The primary reason for furnace failures in pre-testing and during the experiments was burnout of hot spots in the narrow portion of the furnace at the weld zones. The decrease in cross-sectional area produced by this design flaw could be eliminated by using an external coil or strip heater furnace, or going to a coiled internal wire furnace that would maintain a constant cross-sectional area throughout its length. Provided that the coil furnace does not produce serious problems with the shock-wave propagation, this design might be successful and could attain much higher temperatures than the 100°C maximum temperature obtained during bench testing of the foil-furnace design. Another advantage of using an external furnace would be the elimination of the power lead and thermocouple tracks, which would prevent radial fracturing along these discontinuities in the assembly. The presence of hot spots in the furnaces also suggests that the temperature estimated for each experiment should only be treated as approximate values with errors of ±50°C.

The character and intensity of damage in the steel assemblies suggests that future experiments should utilize a slightly modified design. The thin base plate seems to work better than the thick one. A thicker lower plate along with a larger assembly diameter will decrease the degree of damage from fracturing and spalling in this plate, and will permit larger bolts to be used as well. The spall ring used in the second series is essential to suppress

the development of radial fracturing, and could be thickened slightly. Another design change that would suppress the radial fracturing is the use of a "star" trap as proposed by workers at Sandia National Laboratory (M.B. Boslough, personal communication, 1989), who use a polygonal outer surface. This geometry prevents the radial component of the shock from reflecting back into the assembly by causing destructive interference of the reflected phases, thus eliminating radial fracture effects.

The proposed enlargement of the assembly will also allow larger samples to be used in future experiments. Increasing the volume of sample is desirable and will provide more material for post-mortem analysis. However, the desire for more shocked material must be balanced with the desired shock conditions since, for example, changes in sample thickness will change the resulting shock pressures achieved.

The presence of radial effects such as fracturing and large permanent lateral strains during flattening of the assembly suggest that a 1-D simulation of shock recovery experiments is not adequate. Along with design changes to mitigate radial effects, future work should be modeled using 2-D simulation programs; better control on stress, strain, velocity, and pulse duration histories may be achieved in this way.

The use of elevated temperatures in shock-recovery experiments raises another question regarding the equation-of-state of the materials involved in an experiment. Since temperature does affect the micromechanical response of the materials, the standard method of simulating a shot using room-temperature Hugoniot data may be invalid. Although the effect of temperature

on the Hugoniot is believed to be negligible (J. M. Brown, personal communication, 1989), it is suggested that future recovery work be coupled to EOS experiments with similar initial conditions to assure that the pressures achieved are accurate.

Problems encountered with quenching of the shocked assembly is mitigated easily by some simple changes in the experimental configuration. The width and depth of the water tank needs to be enlarged to allow capture of the entire assembly and spall plates. Burial of the tank will also eliminate water losses due to penetration damage from flying debris. This design change is easily accomplished on the explosion table.

# CHAPTER V

# TEMPERATURE AND PULSE-DURATION DEPENDENCE OF SHOCK-INDUCED MICROSTRUCTURES IN QUARTZ AND FELDSPAR

## Introduction

Following successful completion of the shock-recovery experiments, the assemblies were photographed to document the degree of damage as a function of experimental conditions. After being photographed, each assembly was machined or pried open to retrieve the sample, which was then stored in a glass vial (table 5-1), and the assembly was photographed again to document the character of internal deformation of the momentum trap.

Each sample was analyzed using optical microscopy, and critical samples were selected for transmission electron microscopy (TEM), electron diffraction analysis, and energy dispersive x-ray analysis (EDAX). The purpose of this chapter is to: (1) document these results and compare them to previous recovery experiments; (2) discuss the results in light of models for the development of shock-induced microstructures; and (3) discuss the relevance of the results to natural shock deformation in impacts, volcanics, and at the K/T boundary.

Table 5-1: Shot table showing experiment identification numbers, sample type, the estimated shock pressure ($P_a$) in GPa, the ambient temperature before shocking ($T_a$) in °C, and the percent sample recovered. Sample type is Westerly granite (WG), Hospital Hill quartzite (HHQ), or Balsam Gap Dunite (BGD). Dashed lines in the $P_a$ column are experiments that were not simulated.

| Experiment Number | Material | $P_a$ | $T_a$ | % Recovered |
|---|---|---|---|---|
| 88-1 | WG | 12 | 25 | 10 |
| 88-2 | WG | 12 | 450 | 100 |
| 88-3 | WG | - | 450 | 100 |
| 88-4 | WG | 5 | 750 | 100 |
| 88-5 | WG | 12 | 750 | 50 |
| 88-6 | WG | - | 450 | 0 |
| 88-7 | WG | - | 25 | 0 |
| 88-8 | WG | - | 450 | 0 |
| 88-9 | WG | 8 | 750 | 100 |
| 88-10 | WG | 8 | 450 | 100 |
| 88-11 | HHQ | 8 | 100 | 100 |
| 88-12 | HHQ | 8 | 450 | 100 |
| 88-13 | HHQ | 8 | 750 | 100 |
| 88-14 | WG | 15 | 750 | 100 |
| 88-15 | WG | 15 | 450 | 100 |
| 88-16 | WG | 15 | 25 | 100 |
| 89-1 | BGD | 23 | 300 | 100 |
| 89-2 | BGD | 23 | 900 | 0 |
| 89-3 | WG | 25 | 450 | 50 |
| 89-4 | WG | 23 | 750 | 20 |
| 89-5 | WG | 23 | 450 | 100 |
| 89-6 | WG | 18 | 750 | 100 |
| 89-7 | WG | 25 | 750 | 50 |
| 89-8 | HHQ | 23 | 750 | 100 |
| 89-9 | HHQ | 24 | 750 | 100 |
| 89-10 | HHQ | 24 | 450 | 100 |
| 89-11 | HHQ | 24 | 25 | 100 |
| 89-12 | WG | 18 | 450 | 100 |
| 89-13 | WG | 25 | 25 | 100 |
| 89-14 | WG | 23 | 25 | 100 |
| 89-15 | WG | 18 | 25 | 100 |

## Analysis of The Hydrodynamic Simulation Data

Simulations were performed to estimate the loading history of samples shocked to nominal pressures of 10, 12, 15, 20, 25, and 30 GPa. As noted in chapter 4, the results of the simulations indicated that the nominal peak shock pressures calculated simply from the impedance match between steel and sample were not attained precisely in any of the samples. In every case except for the nominal 10 GPa shot, all the samples attained pressures lower than that calculated from the impedance match (figure 4-18). The nominal 10 GPa simulation actually attained a peak pressure of 12 GPa (figure 4-18A). The results of the simulations, which include a pressure-time plot (figure 4-18) and a particle velocity-time plot (figure 4-19), allow some crude calculations to be made for comparison of the optical and TEM results. For each simulation, estimates of the peak shock pressure, peak shock duration, total pulse duration, and average shock pressure were determined (table 5-2). The $P_S$-t plot and $u_p$-t plots were smoothed to eliminate chattering, and were integrated manually to obtain estimates of the $P_S(t)$ and $u_p(t)$ for each simulation, and then multiplied to estimate the total work done in each experimental configuration (table 5-2).

The results of this analysis reveal that although the total pulse durations ranged from 3 to 8 microseconds, the duration of the peak shock pressure in each simulation was only 0.8 to 2.0 microseconds. The average shock pressure achieved across the entire pulse length varied from 8 to 15 GPa as compared to a peak pressure range from 8 to 25 GPa. This narrow range of average pressures indicates that the majority of a pulse achieves pressures that are much lower than the peak value.

Table 5-2: Results of analysis of the $P_s(t)$ and $u_p(t)$ simulation data from MACRAME. $P_n$ is the nominal peak pressure in GPa from impedance matching, $P_s$ is the actual peak pressure in GPa estimated by MACRAME, $D_{pm}$ is the duration of the peak pressure in microseconds, $D_p$ is the total pulse duration in microseconds, $P_a$ is the average shock pressure in GPa attained across the total pulse duration, $\int P_s(t)$ is the integral of the area under the $P_s(t)$ curve in MPa-sec x $10^{-3}$, $\int u_p(t)$ is the integral of the $u_p(t)$ curve in mm, and $\int P_s(t)u_p(t)$ is the product of the two previous columns in MPa-mm-sec.

| Simulation Number | $P_n$ | $P_s$ | $D_{pm}$ | $D_p$ |
|---|---|---|---|---|
| 1 | 10 | 12 | 2 | 8 |
| 2 | 12 | 8 | 2 | 3 |
| 3 | 15 | 15 | 1.5 | 6 |
| 4 | 20 | 18 | 0.8 | 4 |
| 5 | 25 | 23 | 1.5 | 4 |
| 6 | 30 | 25 | 1.0 | 3.3 |

| Simulation Number | $P_a$ | $\int P_s(t)$ | $\int u_p(t)$ | $\int P_s(t)u_p(t)$ |
|---|---|---|---|---|
| 1 | ~8 | 71.8 | 1.84 | $1.32 \times 10^{-1}$ |
| 2 | ~6 | 20.8 | 0.63 | $1.31 \times 10^{-2}$ |
| 3 | ~10 | 73.9 | 2.28 | $1.68 \times 10^{-1}$ |
| 4 | ~14 | 66.0 | 1.78 | $1.17 \times 10^{-1}$ |
| 5 | ~15 | 66.5 | 2.16 | $1.44 \times 10^{-1}$ |
| 6 | ~15 | 53.3 | 1.29 | $6.88 \times 10^{-2}$ |

The area under the $P_s(t)$ and $u_p(t)$ curves reflects the balance between the shock velocity achieved at specific pressures and geometry of the assembly. As shock pressure increases, the concomitant increase in shock velocity causes the pulse duration, and hence the $P_s(t)$ and $u_p(t)$ integrals to decrease. In addition, scrutiny of the $P_s(t)$ diagrams (figure 4-18) reveals that the samples shocked to nominal pressures of 15, 25, and 30 GPa were actually shocked twice because of the assembly, flyer plate, spall plate configuration.

In comparison to previous shock-recovery experiments by Kleeman and Ahrens (1973) and those on Hospital Hill quartzite (Reimold and Hörz, 1986a, b; chapter 2 of this work), the experiments reported herein attained pulse durations from 8 to 16 times longer. Kleeman and Ahrens (1973) reported pulse durations to 2.0 microseconds, and the experimental configuration of Reimold and Hörz (1986a) produced durations of 0.5 to 0.6 microseconds.

## Observational Results of Shock-induced Microstructures

### Sample Preparation and Analytical Procedures

After being separated from the furnace and mica, each sample was mounted in a disc of Epokwik epoxy resin. The solidified disc was then removed from the mold, cut to size, and ground on a lap wheel using SiC 600 size grit until the surface was flat. The ground surface was subsequently hand-ground on a glass plate using 5.0, and 1.0 micron alumina, and polished using 0.3 micron alumina powder on a felt pad. The polished surface was mounted to a frosted thin section glass using Lakeside thermal cement, and the

excess epoxy was removed so that a wafer of epoxy and sample about 2 mm thick remained on the glass. The wafer was then ground to 200 microns using a 320-grit wheel on a Buehler Petro-thin sectioning machine. The section was hand-ground to 50 microns on a glass plate with 600 grit, and then polished using alumina as in the first stage of the preparation procedure. The resulting doubly-polished thin sections had a thickness ranging from 20 to 30 microns, which is suitable for microstructural analysis.

Each sample was studied optically on a Zeiss research polarizing microscope to determine the structural state of quartz and feldspar. All observed features were documented photographically, and recorded as a function of peak shock pressure, temperature, and pulse duration. Following the optical analysis, selected areas of the thin sections were prepared for transmission electron microscopy (TEM). Areas of interest were cleaned to remove any immersion oil residues left from optical analysis, and a nickel foil and copper cover ring were bonded to the thin section using 5-minute epoxy. The sample and foil were lifted from the thin section by scribing around the foil with a sharp razor blade. After being washed in acetone to remove Lakeside cement, the foils were thinned using a Gatan Dual-Gun Argon Ion Thinning Mill. The thinned foils were coated with ~100 Å of carbon to prevent charging in the electron beam.

TEM, electron diffraction, and EDAX analyses were completed using a Phillips 400T Transmission Electron Microscope equipped with a two-axis stage. All images obtained in the TEM were coupled with a selected area diffraction (SAD) pattern and an EDAX analysis, which was done semi-quantitatively to estimate the composition of the viewed area for comparison to the SAD

analyses. An attempt was made to index each SAD to determine the phase present and the orientation of any substructures observed.

Initial Materials

As discussed in chapter 4, the materials selected for the shock-recovery experiments were Westerly granite and Hospital Hill quartzite. Westerly granite is an equigranular rock consisting of quartz, plagioclase feldspar ($An_{17}$), potassium feldspar, and small amounts of biotite and other accessory minerals. The modal mineral composition is quartz ~27.5%, plagioclase~35.4%, K-feldspar~31.4%, and biotite and accessory minerals 4.9% (Brace, 1965). Westerly granite displays an average grain size of 300 microns, and very low porosity (<<1%). Optical evidence for tectonic deformation in the block of Westerly granite used in this study included some fractures in the feldspars (figure 5-1A), subgrains in quartz (figure 5-1B), and mechanical twins in plagioclase.

Hospital Hill quartzite is a well-cemented orthoquartzite with very low porosity (<<1%), and very weak preferred crystallographic orientations. The average grain size in the material supplied by F. Hörz for this study was about 75 microns (figure 5-1C), with some larger grains extending to 200 microns. The samples used in this study showed virtually no secondary phases, and evidence of tectonic deformation was restricted to occasional weak subgrain development and rare tectonic (Böhm) lamellae (figure 5-1D).

Figure 5-1: Photomicrographs of the starting materials used in the shock-recovery experiments. A. Westerly granite showing granular texture and interlocking grains of plagioclase, quartz, and K-feldspar. B. Subgrain development in quartz in Westerly granite indicative of tectonic deformation. C. Hospital Hill quartzite showing a crystalline granular texture with very low porosity, and grain sizes ranging from 50 to 100 microns. D. Tectonic (Böhm) lamellae in quartz in Hospital Hill quartzite showing curviplanar and discontinuous habit.

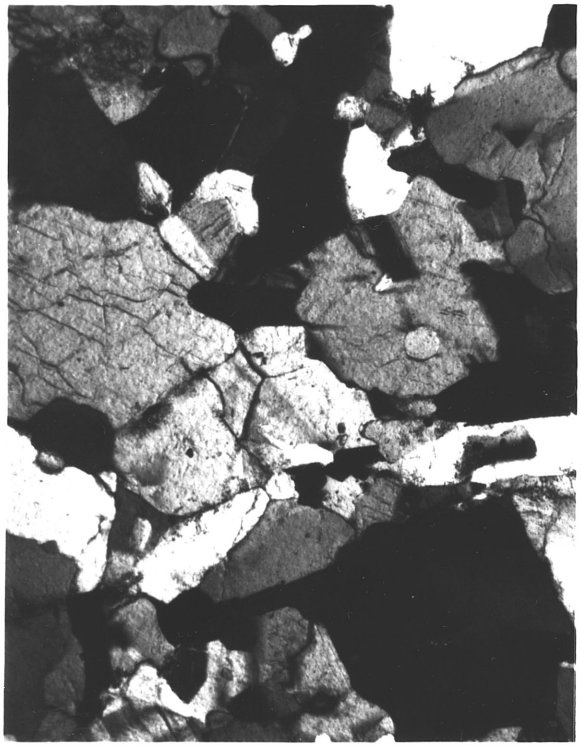

A

225 µm

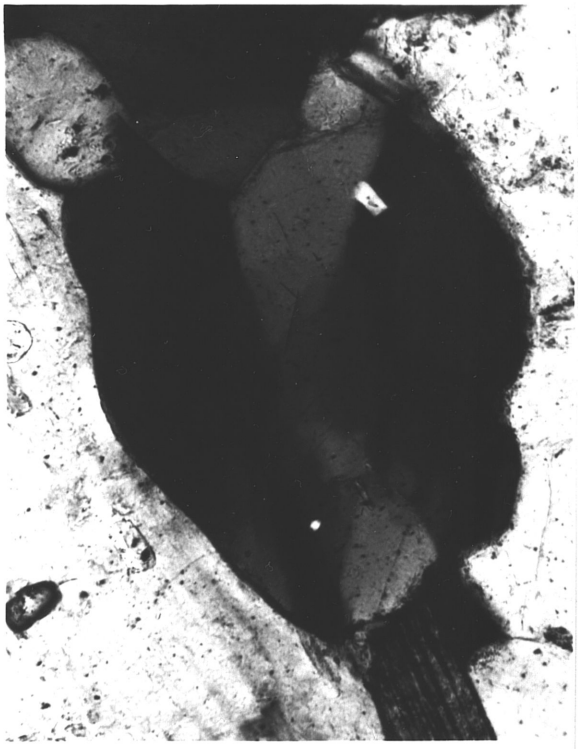

B

65 µm

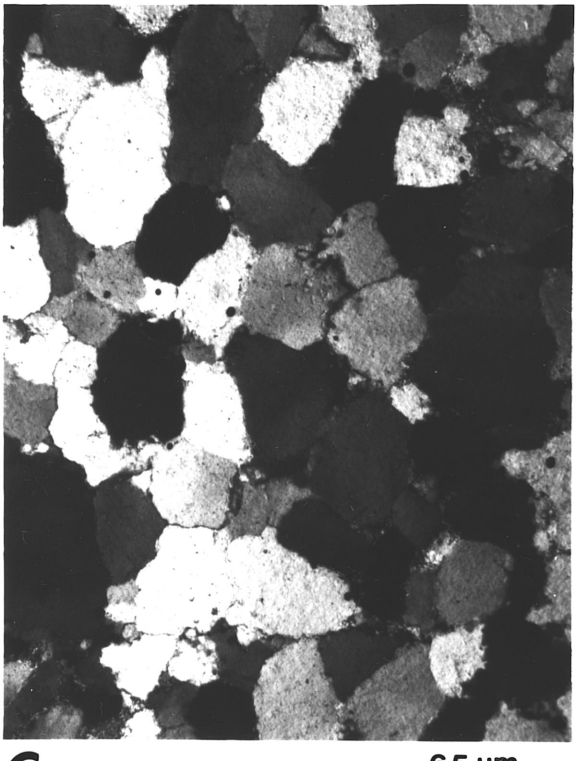

C

65 µm

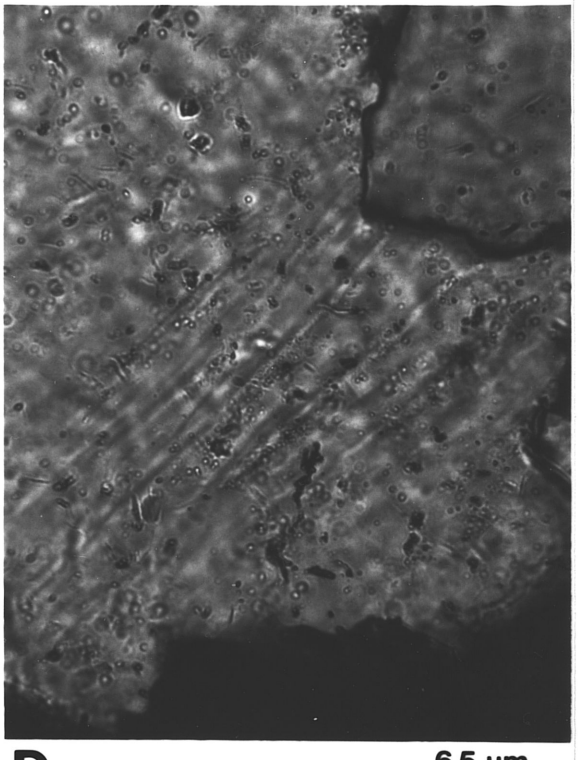

D

65 µm

Figure 5-2: Transmission electron micrographs of quartz in Hospital Hill quartzite (unshocked) and quartz from the Lameta Beds below the Deccan Traps in India. A. Dislocations in Hospital Hill quartzite. B. Dislocations and planar defects in Hospital Hill quartzite. C. Dislocations in Lameta Bed (sample 5BL) quartz. D. Dislocations, a planar defect, and a bubble trail (NW-trending feature) in Lameta Bed quartz.

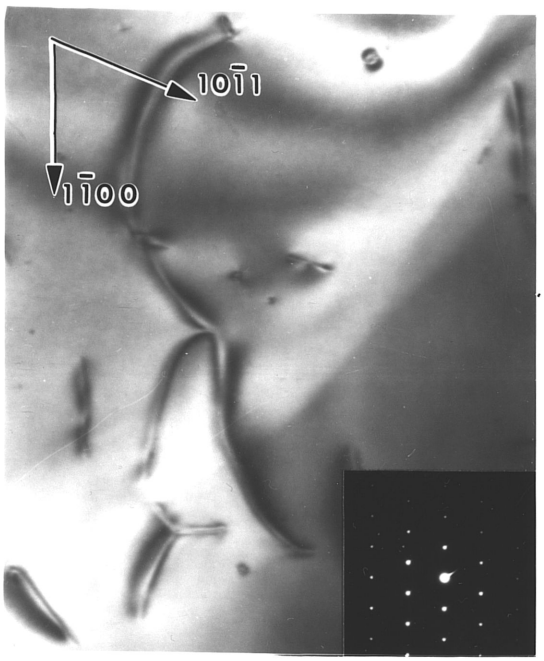


A

0.5μm

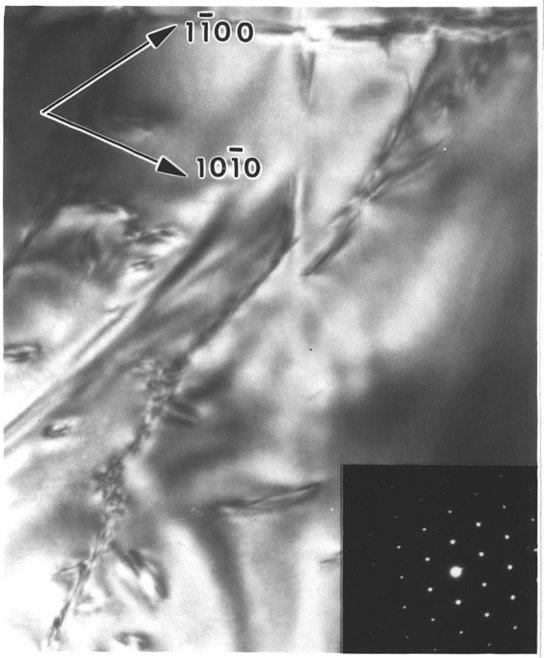


B

0.5μm

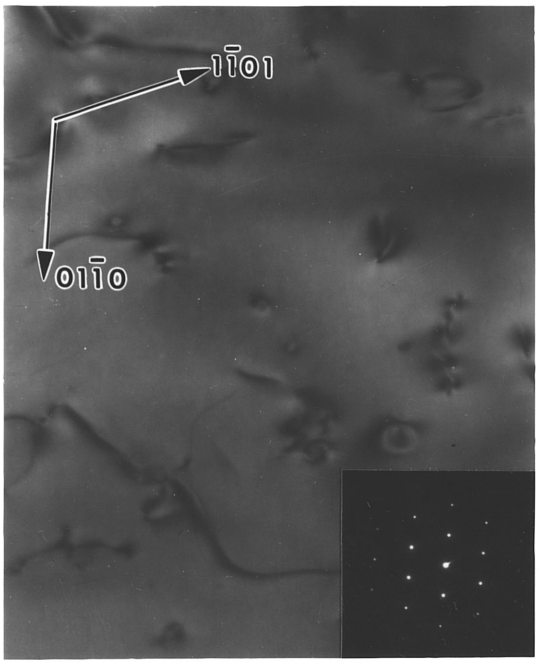


C

0.5μm

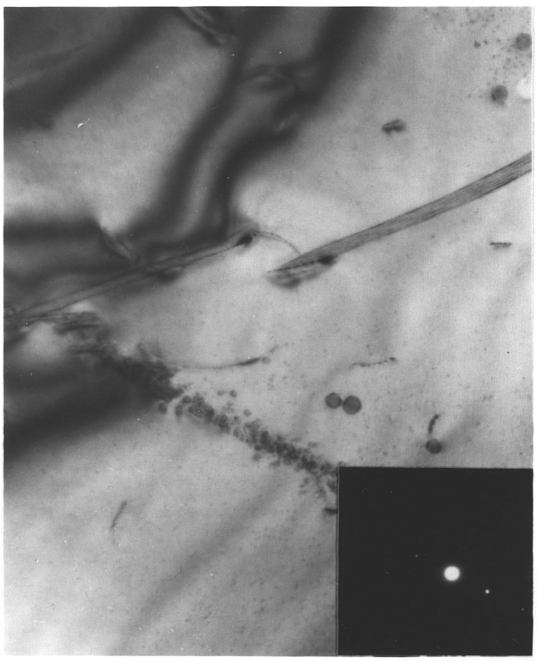

D

0.5μm

TEM observations of the starting materials revealed substructures indicative of creep processes, including free dislocations, dislocation tangles, stacking faults, and fine bubble trails that are inferred to represent healed microfractures (figure 5-2A, B). In particular, the quartzite sample showed typical dislocation substructures (figure 5-2A) with estimated free dislocation densities ranging from $10^8$ to $10^9$ $cm^{-2}$ (TEM estimate), which is within the range of densities observed in tectonically- and experimentally-deformed quartz. Similar dislocation substructures were also observed in samples of Lameta Sandstone from India (figure 5-2C, D), which is believed to have a similar tectonic history with optical evidence of subgrain development and numerous Böhm lamellae; in the Lameta material, there is no evidence of the shock deformation purported by Basu (1988).

Results From Optical Microscopy of The Shocked Material

Each thin section of the experimentally-shocked material was studied in detail to document all shock-induced microstructures that were present. The results (compiled in Appendix III) reveal the classical progression, with increasing shock intensity in quartz and feldspar, from random fracture (figure 5-3A), to development of the mosaic structure (figure 5-3B) and planar fracture (figure 5-3C), single sets of planar features (figure 5-3D) to multiple sets of features (figure 5-4B), and finally to isotropization and partial melting (figure 5-4C, D). Combinations of specific microstructures were observed commonly in all minerals and included mosaicism and planar features (figure 5-3D), planar fracture and planar features (figure 5-4A), and relict planar features in completely isotropic grains (figure 5-4C). Melting was characterized as either absent, fracture melting, or massive melting; a general

Figure 5-3: Photomicrographs of representative microstructures in quartz and feldspar at 5, 8, and 15 GPa peak shock pressures. A. Random fracturing in quartz and feldspar shocked to 5 GPa at 750°C. B. Shock mosaicism in feldspar shocked to 8 GPa at 450°C. C. Planar fracture in quartz shocked to 15 GPa at 25°C D. First development of rare single sets of planar features in quartz shocked to 15 GPa at 750°C.

A

190 µm

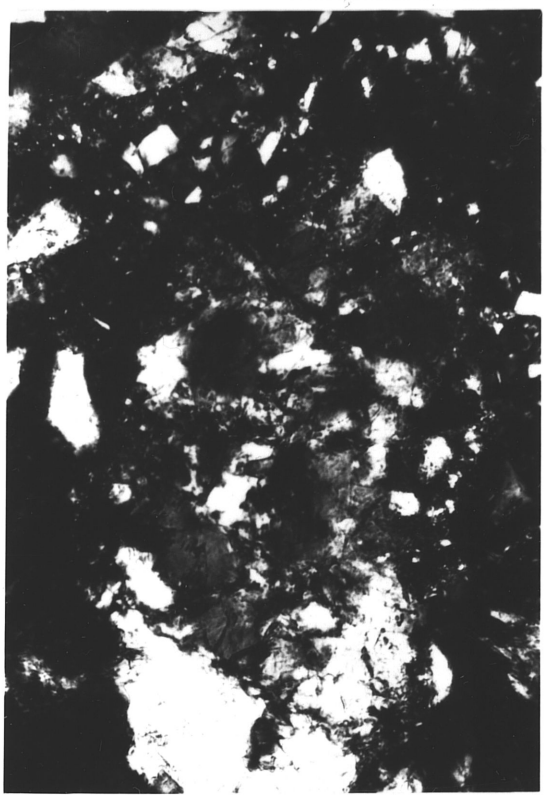

B

145 µm

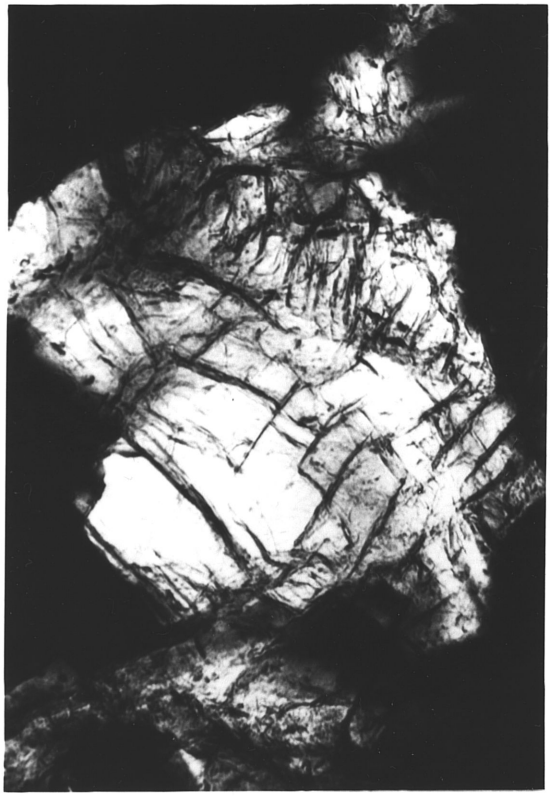

C

120 µm

D

90 µm

Figure 5-4: Photomicrographs of representative microstructures in quartz and feldspar at 18 and 23 GPa peak shock pressure. A. Planar fracture and planar features in quartz shocked to 18 GPa at 25°C. B. Multiple intersecting sets of planar features in quartz shocked to 18 GPa at 25°C. C. Relict multiple sets of planar features in an isotropicized quartz grain shocked to 23 GPa at 25°C. D. Advanced domainal isotropization and fracture melting in granite shocked to 18 GPa at 450°C. The birefringent material is quartz that still displays some single sets of planar features. The isotropic areas are feldspars.

A

70 µm

B

45 µm

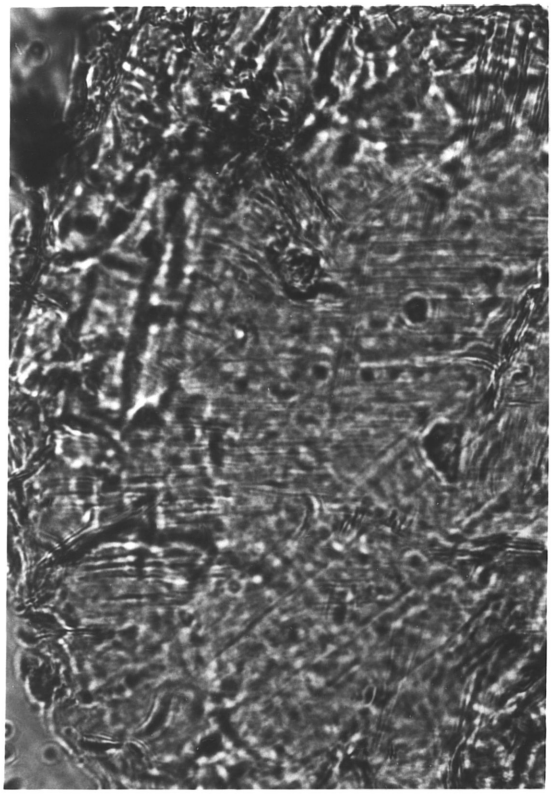

C

45 µm

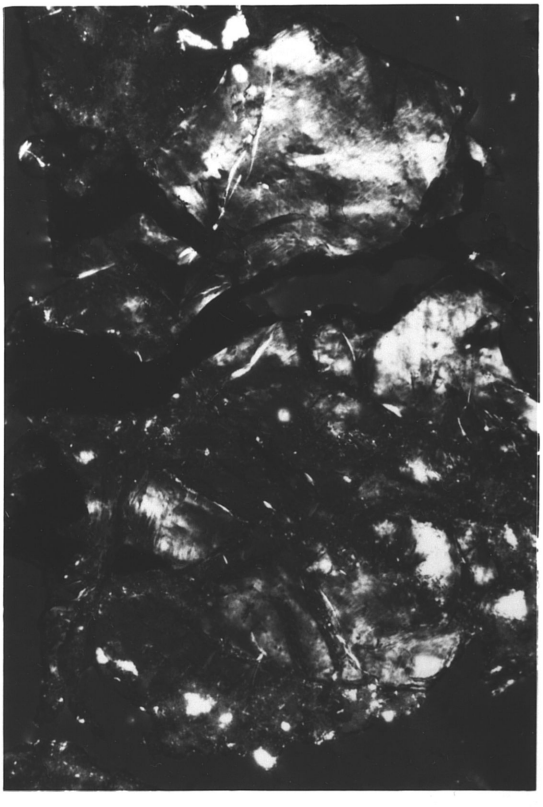

D

190 µm

progression from no melting at low temperatures and pressures to massive melting at high shock pressures and temperatures was observed. Samples shocked at high temperatures and pressures above 15 GPa show changes in sample thickness indicative of bulk flow and large strains (>50%), with the largest strains occurring in the high-temperature samples. This observation suggests that as the samples exceed the HEL of quartz, they begin to respond to the shock by bulk flow, as opposed to an elastic and brittle response.

## The Effect of Pre-Shock Temperature

The optical results were divided into quartz and feldspar features so that direct comparison between specimens could be made as a function of pre-shock temperature and the estimated shock pressures from MACRAME. The results for quartz (figure 5-5) indicate that the general progression of microstructures as a function of increasing shock pressure is confirmed. However, when temperature is added to the system, the results reveal clearly that the onset pressures for specific features decrease. The most dramatic change occurs for the onset of isotropization and melting; at 750°C, both show decreases of about 10 GPa in onset pressures. Less dramatic is the effect of temperature on the onset pressure for the shock mosaic structure which is moderately developed at 12 GPa and 25°C, and weakly developed at 8 GPa and 450°C. The shock mosaic structure in quartz shows two distinct characteristics as a function of increasing temperature. First, the samples at high temperatures show subtle recovery compared to the room-temperature tests. Second, the mosaic structure is better developed at high temperatures for the same shock pressure. This suggests that the greater energy of the starting material at high temperature may have enhanced the plastic response

Figure 5-5: Shock-induced microstructures in quartz as a function of peak-shock pressure and pre-shock temperature. The lower limit of the HEL for quartz is approximated by the dashed line. The upper limit is about 15 GPa. The solid lines represent estimated onset pressures for various microstructures and are grouped based on the simplest divisions possible. A. Onset pressures for random fracture, planar fracture, planar features, and isotropization. B. Onset pressures for mosaicism and isotropization. Symbols used are for random fracture ( ● ), planar fracture ( ◒ ), shock mosaic structure ( □ ), planar features ( ○ ), and isotropization ( X ). The symbols in parentheses on the diagram are from the Hospital Hill quartzite. All other symbols are from Westerly granite.

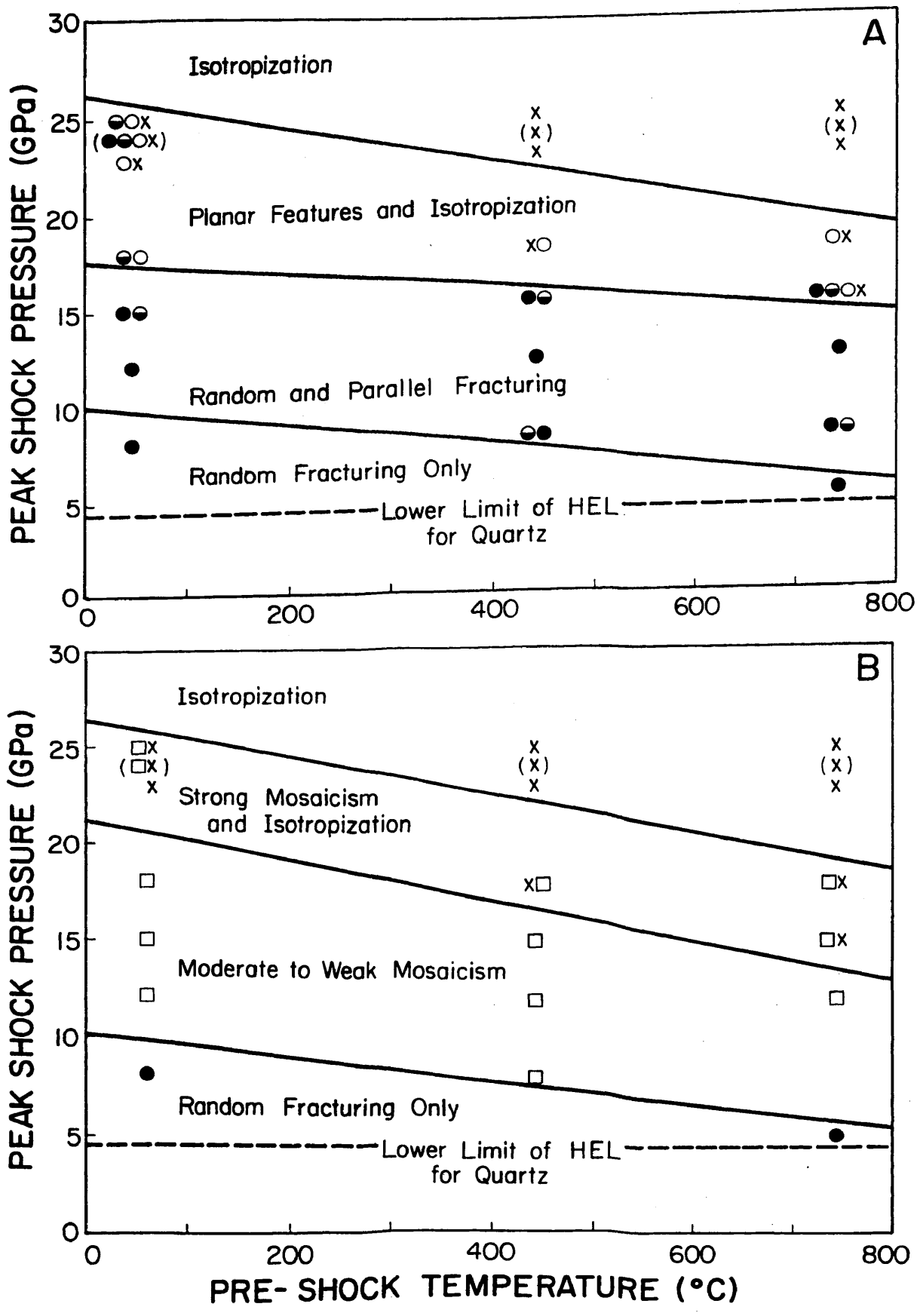
A
Isotropization
Planar Features and Isotropization
Random and Parallel Fracturing
Random Fracturing Only
Lower Limit of HEL for Quartz
PEAK SHOCK PRESSURE (GPa)
0
5
10
15
20
25
30
0
200
400
600
800
B
Isotropization
Strong Mosaicism and Isotropization
Moderate to Weak Mosaicism
Random Fracturing Only
Lower Limit of HEL for Quartz
PEAK SHOCK PRESSURE (GPa)
PRE- SHOCK TEMPERATURE (°C)

of the crystal structure ,permitting more plastic strain to accumulate during specific pulse durations at specific pressures.

In terms of onset pressure, the microstructure that is least affected by temperature is planar feature development. The first sets of planar features are observed at 18 GPa in room-temperature experiments, and include both single and multiple sets; they occur only as rare single sets in quartz shocked to 15 GPa at 750°C. In sharp contrast to the onset pressures, the changes in character of planar features with temperature is marked. At 18 GPa and 25°C, planar features in quartz show roughly equal numbers of multiple and single sets. At 450°C, the number of multiple sets decreases significantly until at 750°C, no multiple sets of planar features are observed, and only occasional single sets are present. The occurrence of isotropization at lower pressures in the high-temperature experiments suggests either that the samples begin responding homogeneously before large numbers of planar features develop, or that they formed in very dense arrays prior to complete isotropization during the shock transition or in the compressed state. The presence of relict planar features in quartz shocked to 23 GPa (figure 5-4C) suggests that the reverberations produced during the experiment may produce superposed shock-induced microstructures. This apparent path dependency on microstructural development may eventually prove useful in determining the sequence of development of the microstructures. The presence of relict planar features provides strong evidence that they form in the shock transition before the isotropization, not during the release phase as proposed by Gratz et al (1988).

Microstructural changes in plagioclase and K-feldspar probably occurred simultaneously since they are not significantly different in their response to shock waves (figure 5-6). Unlike quartz, the feldspars show much stronger development of the shock mosaic structure at 5 to 8 GPa (figure 5-3B). This is not surprising considering that the HEL for feldspars is much lower than for quartz. Like quartz, the feldspars show stronger mosaicism at elevated temperatures in the pressure range from 5 to 15 GPa, indicating enhanced plastic flow caused by pre-heating. The character of mosaicism in feldspars changes sufficiently at pressures from 8 to 15 GPa to justify differentiating between weak and strong mosaicism. In general, weak mosaicism occurs just above the HEL along with fracturing, mostly of random orientation, and is superseded at higher pressures by development of planar features and strong mosaicism.

As in quartz, the change of onset pressure for isotropization and melting in the feldspars is affected dramatically by initial elevated temperatures. The change in onset pressures for these microstructures is as high as 10 GPa in the temperature range studied. Also, as in quartz, the onset pressure for development of planar features is least affected by temperature, with the first sets of features observed at 18 GPa at 25°C, and at 15 GPa at 750°C. The general change at 18 GPa from multiple sets of features at 25°C to rare single sets at 750°C is also observed in the feldspars. Unlike the quartz, however, the conversion from mosaicism and planar features to isotropization in feldspars appears to occur at lower pressures, which suggests isotropization of feldspars occurs more readily under shock loading than for quartz.

Figure 5-6: Shock-induced microstructures in plagioclase and K-feldspar as a function of peak-shock pressure and pre-shock temperature. The HEL for feldspars is approximated by a dashed line. The solid lines represent estimated onset pressures for various features and are grouped based on the simplest divisions possible. A. Onset pressures for random fracture, planar fracture, planar features, and isotropization. B. Onset pressures for mosaicism and isotropization. Symbols used are for random fracture ( ● ), planar fracture ( ◒ ), shock mosaic structure ( □ ), planar features ( ○ ), and isotropization ( X ).

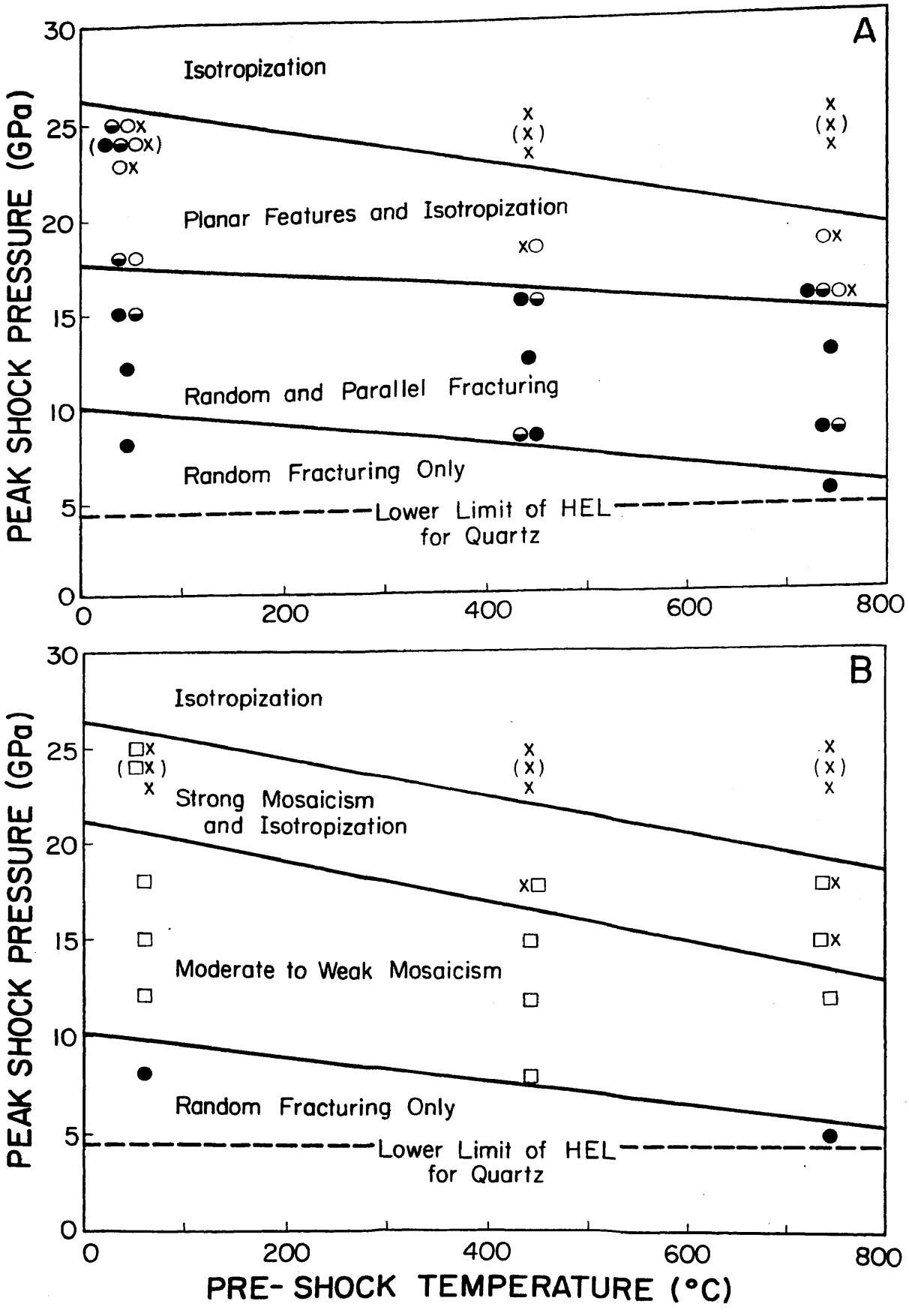
A
Isotropization
Planar Features and Isotropization
Random and Parallel Fracturing
Random Fracturing Only
Lower Limit of HEL for Quartz
PEAK SHOCK PRESSURE (GPa)
0
5
10
15
20
25
30
0
200
400
600
800
B
Isotropization
Strong Mosaicism and Isotropization
Moderate to Weak Mosaicism
Random Fracturing Only
Lower Limit of HEL for Quartz
PEAK SHOCK PRESSURE (GPa)
PRE- SHOCK TEMPERATURE (°C)

Because of the predicted role of elevated temperatures in release melting following shock compression (figure 4-9), the character of melting in the Westerly granite samples was also studied. With increasing pressure and temperature, a general trend from no significant melting, to melting in irregular fractures and veins, and finally to massive melting was observed (figure 5-7). The results suggest that elevated temperatures do play a major role in the development of melt structures. Optically, the melts often show islands of crystalline material which are being resorbed into the melt. The orientations of these islands normally show optical continuity of extinction across regions up to several hundred microns within relict grains, which suggests that bulk flow of the sample had ceased before most of the melting occurred. At moderate P-T conditions where fracture melting is dominant, no significant offsets across fractures were observed. These observations suggest that the melting occurs during the release phase of the shock, not during the compression phase, which is in accord with the predicted behavior from figure 4-9.

## The Effect of Pulse Duration

Hospital Hill quartzite samples shocked in this study were compared to the results for Hospital Hill quartzite shocked in the 20-mm powder gun at NASA. For samples shocked at room temperature (figure 5-8) at 8 GPa, the sample deformed for 0.5 microseconds produced only random fracturing, whereas the sample shocked for 3.0 microseconds showed planar and random fracturing and weak mosaicism. The sample shocked to 24 GPa for 3.5 microseconds showed microstructures similar to the sample shocked to 28 GPa for 0.5 microseconds, although the 24 GPa sample showed significantly more

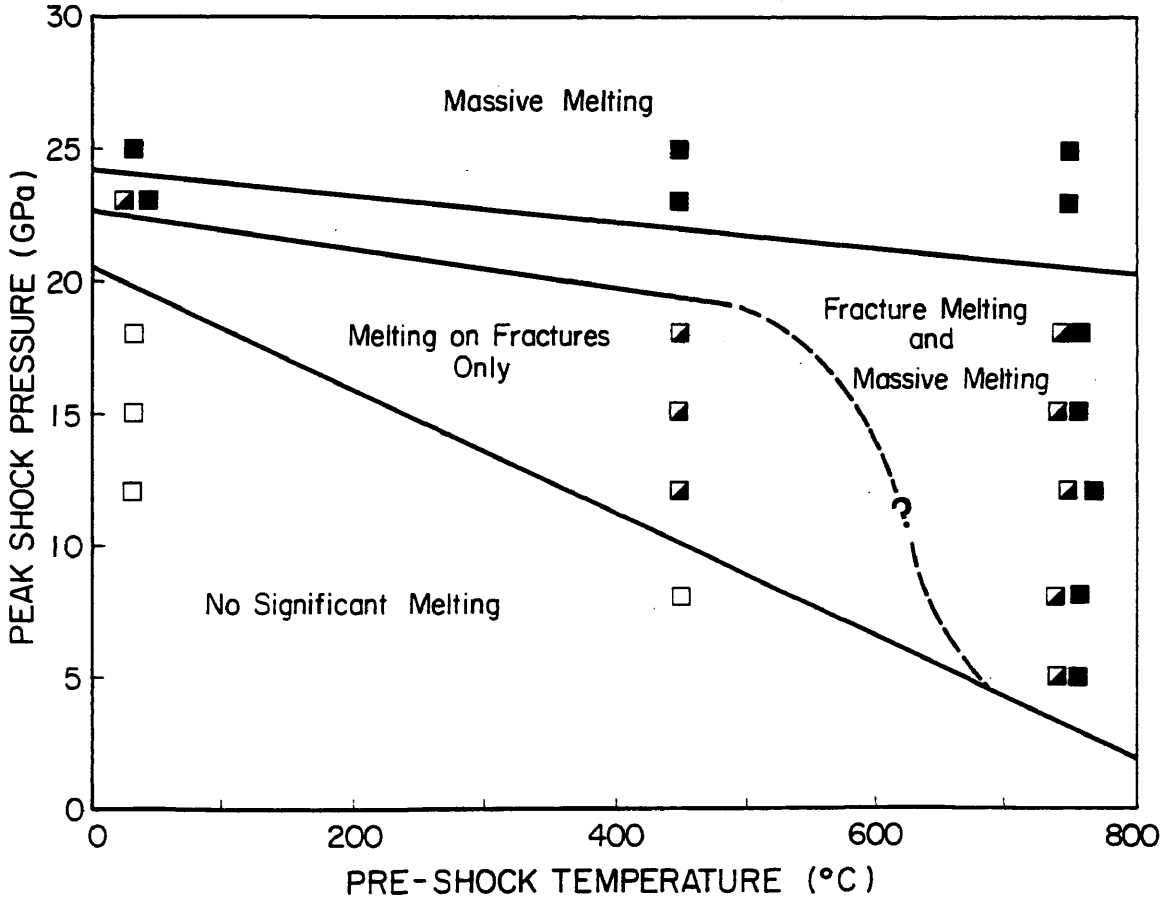


Figure 5-7: Melting behavior as a function of peak-shock pressure and pre-shock temperature. Solid lines represent estimated onset pressures for specific types of melting. Symbols used are for no melting (□), fracture melting (◪), and massive melting (■).

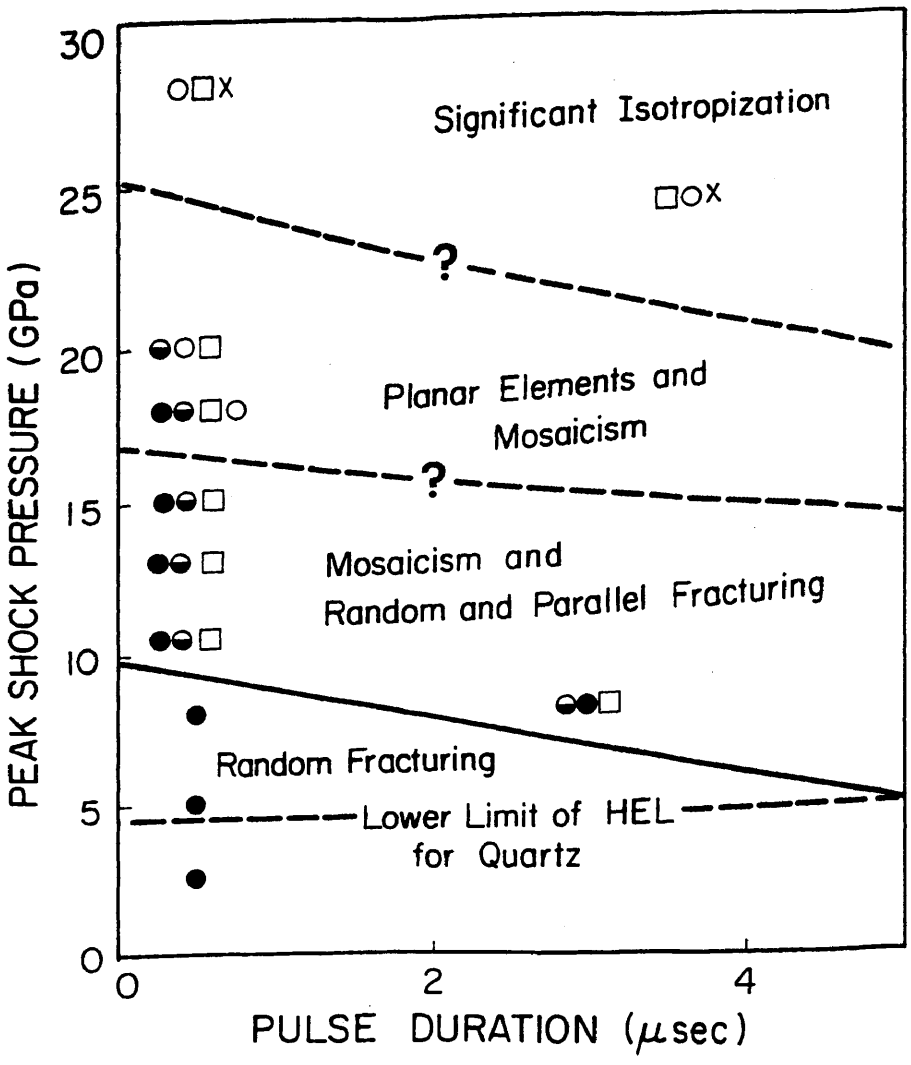


Figure 5-8: Shock-induced microstructures in Hospital Hill quartzite as a function of peak-shock pressure and pulse duration. The lower limit of the HEL for quartz is plotted as a dashed line. The upper limit of the HEL is about 15 GPa. A solid line is used to estimate the onset pressure for mosaicism and planar fracture. Because of lack of data control, the other onset pressure lines are only quesses based on the available observations from the granite samples, and are denoted by dashed lines. Symbols used are for random fracture ( ● ), planar fracture ( ◒ ), shock mosaic structure ( □ ), planar features ( ○ ), isotropization ( X ), and melting ( ■ ).

isotropization. Although patchy, these results may suggest that longer pulse durations result in higher total strains and deformation that are reflected primarily in the development of mosaicism, planar fracture, and isotropization at lower pressures. Results for quartz from the Westerly granite samples indicate that multiple sets of planar features are more prevalent in the sample shocked to 18 GPa for 4 microseconds than in the quartzite shocked to 18 to 20 GPa for 0.5 microseconds. Thus, longer pulse durations may allow more sets of optically-visible planar features to develop at a particular shock pressure. More experiments with a wider range of pulse durations at the same pressure are required to confirm this observation.

The increase in isotropization with pulse duration is of particular significance in light of the apparent discrepancy between the results of Grothues et al (1989) for experimentally-shocked quartz, and those of Xie and Chao (1987) for naturally-shocked quartz (figure 4-7). The shock pressures in the natural quartz of Xie and Chao (1987) were determined by x-ray precession and transmission-Laue measurements of shock-induced anisotropic cell expansion calibrated to similar data from experimentally shock-recovered quartz. Results for longer pulse durations and higher temperatures from this study fall very close to the results of Xie and Chao (1987) whereas the results of the powder gun experiments are closer to the results of Grothues et al (1989). This shift to greater isotropization with longer pulse durations and higher temperatures emphasizes the need for caution in extrapolating from the laboratory to nature.

TEM Substructures In Quartz and Feldspar

The general progression of shock-induced microstructures observed optically is also noted at the TEM scale. Detailed study of submicron-scale substructures in quartz, plagioclase, and K-feldspar reveal some features not detected optically which are quite heterogeneous in character.

In quartz, deformation substructures are generally nonexistent at 5 GPa except for local development of twinning along boundaries (figure 5-9A). These twins are quite common in quartz in samples shocked to 15 GPa, and occur in both low- and high-temperature experiments. The orientations for these features with twin planes of *m* and *r* suggest that they could be either secondary Dauphine or Brazil twins, and are interpreted as Brazil twins based on their morphology. The presence of these features in the low-temperature experiments (e.g. 88-11) rules out the possibility that they are Dauphine twins produced by thermal shocking since residual temperatures from 8 GPa experiments always lie below the alpha-beta transition where this type of twinning has been observed (Frondel, 1962). In addition, their presence along grain boundaries and other discontinuities is a habit commonly observed in deformed quartz (Christie and Ardell, 1976).

At pressures of 8 GPa, the first hint of the mosaic structure is observed along with fine twins, fracturing, and possible thin planar features (figure 5-9B). At 15 GPa, planar fractures and mosaicism are well developed (figure 5-9C) along with planar features showing small amounts of glass in zones less than 10 nannometers across. Also present in quartz at 15 GPa and 750°C are large zones of glass which have partially resorbed the host quartz, indicating

Figure 5-9: Transmission electron micrographs of experimentally-shocked quartz exhibiting changes in microstructure with experimental conditions. A. Twinning (Brazil Law?) in Westerly granite shocked to 5 GPa at 750°C. The twins are adjacent to virtually undeformed quartz, demonstrating the heterogeneity of the process. The SAD is from the undeformed quartz adjacent to the twins. B. Disruption, twinning, and first onset of planar features (?) in Hospital Hill quartzite shocked to 8 GPa at 100°C. C. Intensely deformed quartz in Westerly granite shocked to 15 GPa at 750°C, displaying massive melting, mosaicism, and thin planar features in intersecting sets. D. Completely melted quartz in Hospital Hill quartzite shocked to 24 GPa at 450°C.

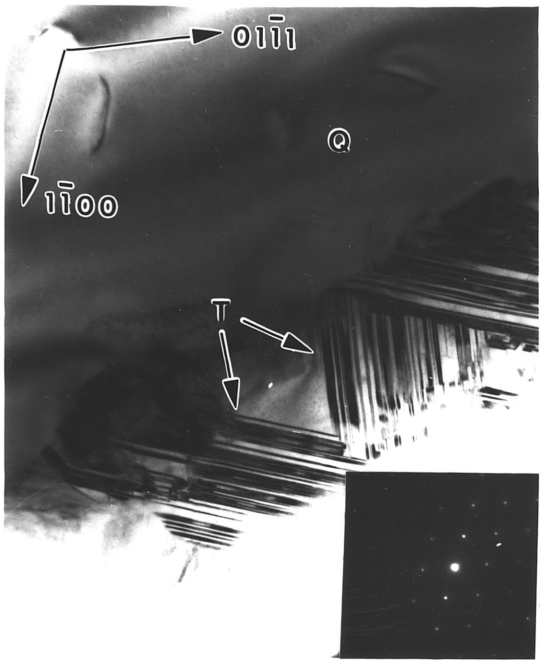


A

0.5μm

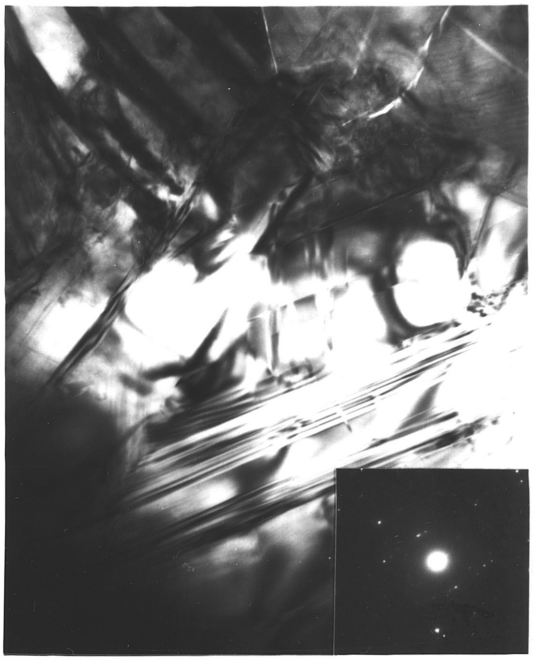

B

0.5μm

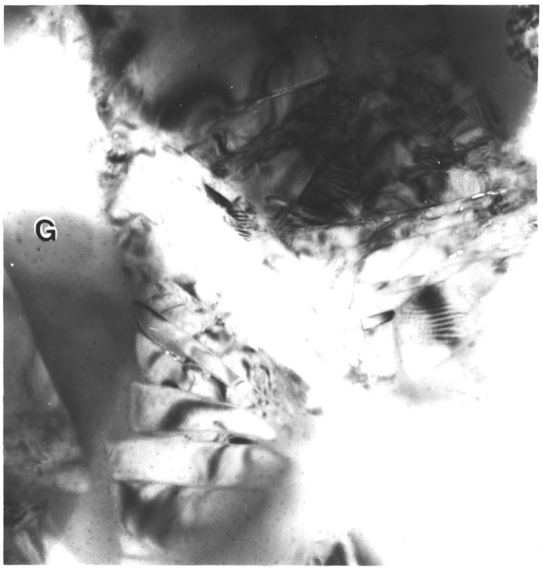


C

0.5μm

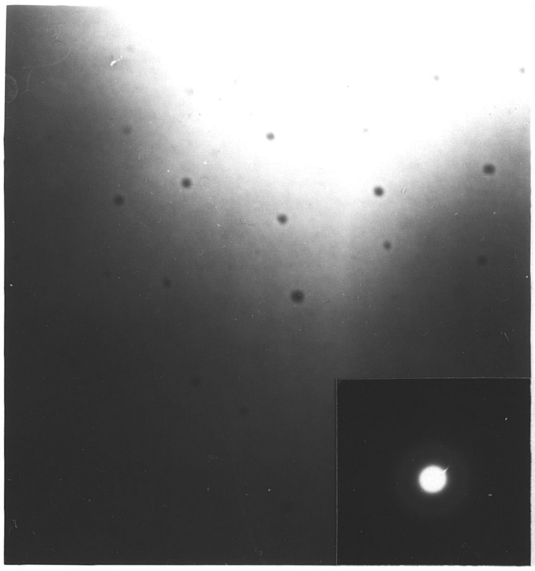

D

0.5μm

some post-shock melting (figure 5-9C, upper left). The coherency of the crystalline material reflects this process as does the absence of these features at 25°C.

Above 15 GPa, the substructures in quartz reflect the dominance of mosaicism, planar features, and progressive isotropization. As noted in chapter 2 (figure 2-14), the primary difference between the high- and low-temperature experiments is the multiplicity and width of the planar features. At low temperatures, quartz substructures are characterized by both multiple and single sets of fine planar features filled with short-range-order glass, and widths from 0.001 to 0.05 microns (figure 2-16B). At elevated temperatures, the planar features show a dominance of single sets displaying widths from 0.05 to 0.10 microns (figure 2-16C, D). This shift from fine multiple sets of features to thicker single sets of features appears to be the typical result of higher temperatures and may reflect changes in the mode of planar feature development. As shock pressure and temperature increase, the quartz displays a change from heterogeneous development of planar features to a dominance of isotropization. This shift from apparently heterogeneous to homogeneous deformation may reflect either a true change to homogeneous isotropization, or a coalescence of many planar features to produce a material that appears isotropic at the optical scale. Finally, at the highest P-T conditions achieved, the quartz becomes completely isotropic and melts upon release as indicated by the small exsolved bubbles in the resulting glass (figure 5-9D).

Orientations of planar features in quartz from this study demonstrate the heterogeneity of the shock process. Features were observed parallel to the basal *c* plane, along with the *r*, $\pi$, *a*, and *s* planes. Surprisingly, no $\omega$ features

were observed at the TEM scale used in this study (i.e. 36,000X), although they clearly dominate in the optical observations of the high-temperature samples. The absence of ω features at the high magnifications is probably a scale-dependent problem. The viewing area at 36,000X is approximately 1 $\mu m^2$, which is actually within a single optically-visible planar feature. Thus the features observed in TEM in this study represent the variety of substructures that collectively form individual optically-visible ω planar features. Recent TEM analyses at lower magnifications (3600X; Doukhan and Goltrant, personal communication, 1990) reflects this scale-dependent heterogeneity, and suggests that future work on the micromechanical response of silicates to shock must include both low-magnification TEM, and high-magnification TEM.

TEM analysis of plagioclase reveals substructures that are quite different from quartz. The sample shocked to 8 GPa at 750°C displayed fine mechanical twins in otherwise strain-free crystal (figure 5-10A). At higher shock pressures, plagioclase responds to shock through intense mosaicism and crystallographic faulting (figure 5-10C), and also by formation of planar features and glass (figure 5-10D). The disorientations are very pronounced in the electron diffraction patterns which reveal significant spot broadening at 15 GPa. At elevated temperatures, the response of the plagioclase to a 15 GPa shock is quite different and shows much larger mosaic domains surrounded by localized zones of intense deformation (figure 5-10B). Although some of this may be due to post-shock annealing, it is suggested that high temperatures may suppress the microfaulting observed at low temperatures (figure 5-10C, D), and permits the mosaic structure to accommodate most of the strain by localized plastic flow along mosaic domain boundaries. A sample shocked to 15 GPa with indexible diffraction patterns revealed that planar features in

Figure 5-10: Transmission electron micrographs of experimentally-shocked plagioclase feldspar in Westerly granite showing changes in microstructure with experimental conditions. A. Fine mechanical twins in a sample shocked to 8 GPa at 750°C. B. Shock mosaic structure with large domain size and relatively undeformed cores in a sample shocked to 15 GPa at 750°C. C. Intense mosaicism and distortional strain in plagioclase shocked to 15 GPa at 25°C, showing severe blurring of the diffraction spots. D. Mosaicism, disruption, and planar features in a sample shocked to 15 GPa at 25°C.

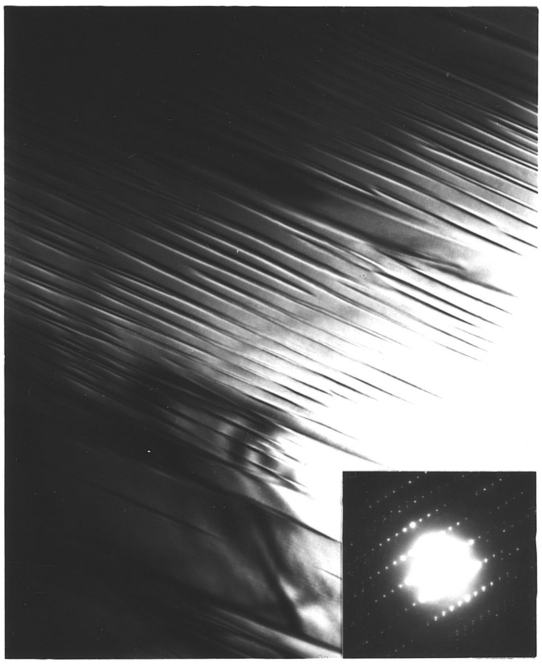

A

0.5μm

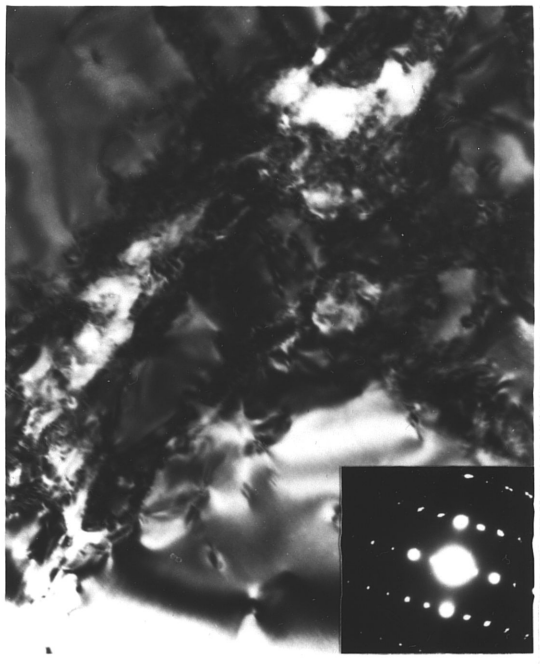

B

0.5μm

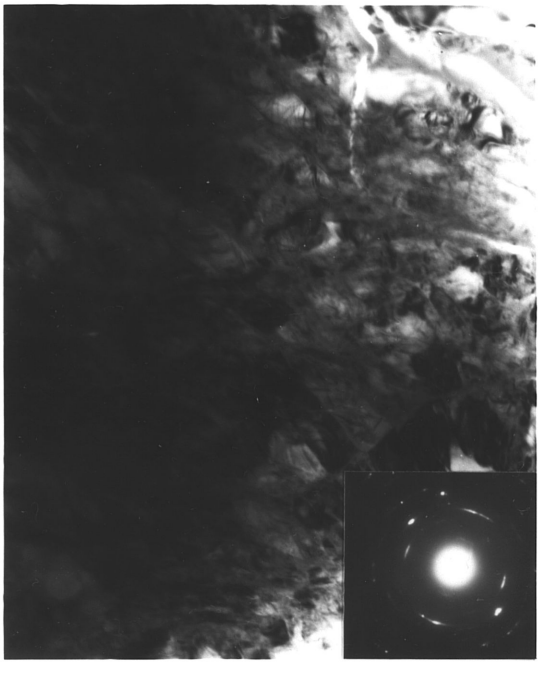

C

0.5μm

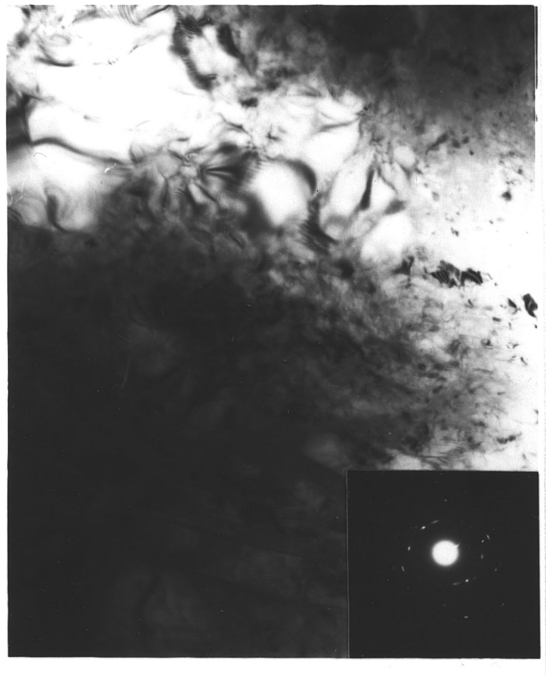

D

0.5μm

plagioclase show a wide variety of orientations including (001), (021), $(1\bar{1}1)$, and $(\bar{1}31)$, which are similar to optical observations on andesine and labradorite from the Ries Crater breccias (Stöffler, 1972). At pressures of 23 GPa, no crystalline plagioclase was observed in TEM, suggesting that the 23 GPa shock was sufficiently intense to induce short-range order and/or melt plagioclase.

TEM analysis of K-feldspar reveals that this mineral deforms much more readily at low pressures than does either quartz or plagioclase. K-feldspar shocked to 5 and 8 GPa at 750°C (figure 5-11A) reveals intense microfracturing and shock mosaicism under conditions at which quartz and plagioclase are only mildly deformed. The difference in relative intensity is demonstrated by the electron diffraction pattern which shows extreme disorientation of the K-feldspar. At 23 GPa and 25°C, K-feldspar deformation is characterized by discrete zones of crystal with high distortional strains that are bordered by microfaults and/or planar features that contain glass (figure 5-11B, C). The presence of thin zones of melt with vesiculation (figure 5-11B) suggests that the release path from 23 GPa for a material initially at 25°C, is just above the solidus for this mineral. In striking contrast, the sample shocked to 23 GPa at 750°C reveals no crystalline K-feldspar, only melt (figure 5-11D). EDAX analysis of this region (marked A and B) indicates a composition intermediate between K-feldspar and plagioclase, and may represent two melted feldspars in close proximity to each other.

Figure 5-11: Transmission electron micrographs of experimentally-shocked K-feldspar in Westerly granite showing changes in microstructures with experimental conditions. A. Intense mosaicism and microfracturing in a sample shocked to 8 GPa at 750°C. B. Mosaicism, crystallographic faulting, and planar features in a sample shocked to 23 GPa at 25°C. C. Intense mosaicism, crystallographic faulting, and distortional strain in a sample shocked to 23 GPa at 25°C. D. Completely melted zone of feldspar shocked to 23 GPa at 750°C. The bubbles are actually zones of the region of lower contrast (A) trapped in a film of the higher contrast material (B).

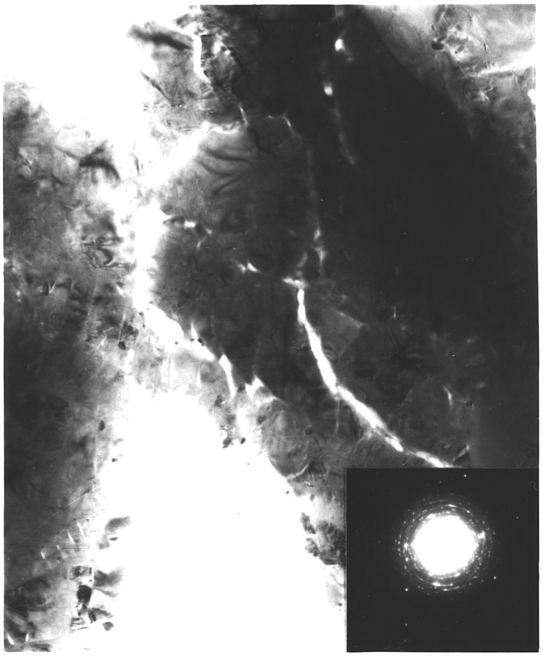

A

0.5μm

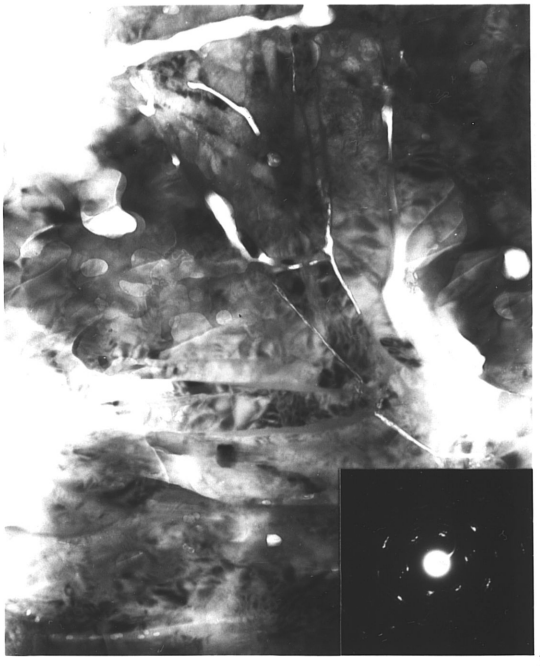

B

0.5μm

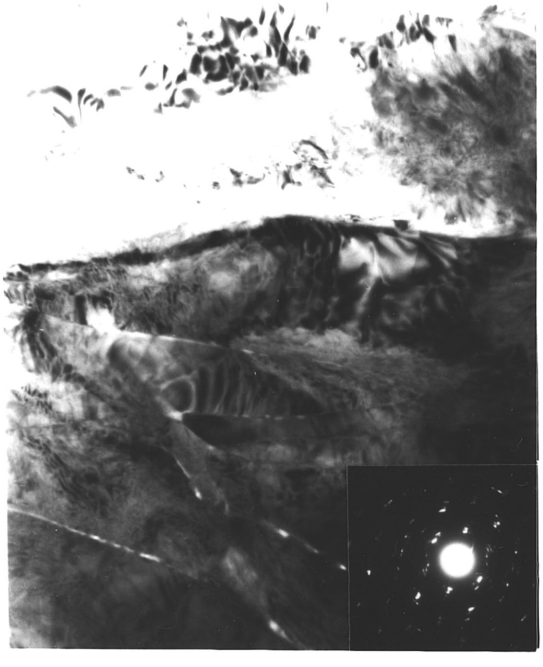

C

0.5μm

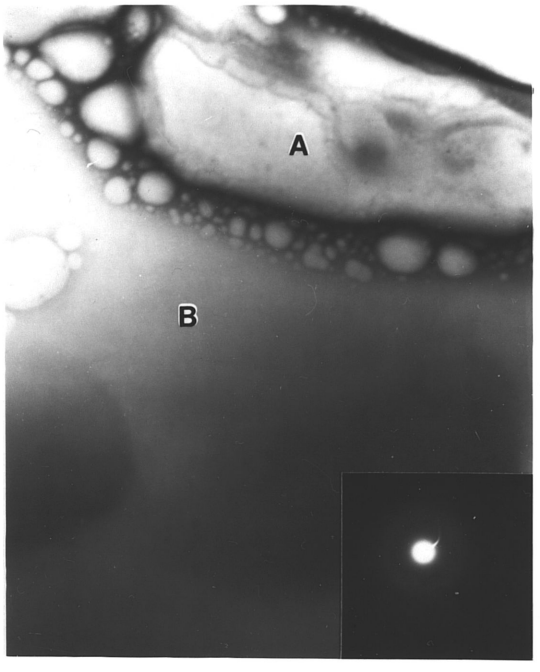


D

0.5μm

## Discussion

The results from this study indicate that shock-induced deformation occurs in four modes including brittle failure, plastic yielding, phase transformation, and pressure-release melting. The brittle response of the material includes the formation of random and planar fractures during compression along with additional fracturing that occurs during the release phase as the sample decelerates from the shocked state. The plastic response of the samples also occurs during the compressional phase of the shock and includes shock mosaicism and possibly bulk flow along grain boundaries after the initial compression to the shocked state is achieved. Phase transformations occur heterogeneously in the shock transition at low pressures by collapse parallel to specific planes of the crystal structure to form short-range-order silica, followed by development of complete isotropization at higher pressures. Melting occurs primarily during the release phase, but also in compression at the highest temperatures and pressures.

The results from the pre-heated experiments suggest that the development of planar features is very sensitive to the thermodynamic state of the sample. The observation of mostly single sets of thick planar features at the TEM scale in high-temperature experiments suggests that the kinetics of glass development are increased at high temperatures. Increased temperatures may also suppress collapse of the less compressible planes so that the resulting strains are localized on sets of thicker features that form at pressures lower than those at 25°C.

The change from heterogeneous to homogeneous phase transformation, as reflected in the onset of isotropization, is also a function of pre-shock temperature. The progression from single to multiple sets of planar features and then to isotropization at low initial temperatures is replaced by mostly single sets of features followed directly by isotropization at high temperatures. This change in behavior suggests that silicates begin to respond by homogeneous collapse at high temperatures before the phase transformation can become localized along more than a single set of planar features. This change in response may be due, in part, to the fact that quartz starts out in the beta-form in the 750°C experiments. The increase in the kinetics of glass formation in the first planar features to develop probably also assists in the isotropization process at high temperatures, as do the longer pulse durations in the experiments performed in this study versus those completed by Reimold and Hörz (1986a).

The lower pressures for the onset of isotropization and other microstructures at increased pulse durations raises a serious concern regarding the use of experimental pressure calibrations of microstructures as a piezometer for naturally-induced microstructures. Pressures required for complete isotropization in this study are much lower than in other experiments of much shorter duration (figure 4-9), and are very close to those observed in naturally-shocked quartz (Xie and Chao, 1987), which were calibrated to shock pressure using cell-expansion data. This may reflect the larger amount of mechanical work performed at the longer pulse durations, and suggests that the pressures for natural shock microstructures have been overestimated because of the differences in pulse duration.

Another striking difference between the experiments of Reimold and Hörz and those in this study is the amount of bulk flow that occurs. Reimold and Hörz (1986a) document some crushing and brecciation along grain boundaries in their samples shocked to 28 GPa. In comparison, the sample shocked to 24 GPa at 25°C in this study showed significant bulk flow identified by large zones of comminuted quartz along grain boundaries, separating cores of shocked quartz. This observation indicates that much of the strain in the longer experiments is achieved by bulk flow of the compressed material along grain boundaries and other macroscopic flaws in the sample, leading to large areas of intensely deformed material.

The apparent lack of coesite or stishovite in the high-temperature experiments results from post-shock residual temperatures much too high to permit preservation of either polymorph. The most thorough study of high-pressure polymorphs in shocked Coconino sandstone from Barringer Crater (Kieffer et al, 1976) reveals that coesite and stishovite are probably transformed directly from quartz or from a hot precursor phase such as amorphous silica. The absence of either phase in the low-temperature samples studied by TEM suggests that the transformation must have finite nucleation and growth rates that are too slow to preserve domains of sufficient size to be observable at the TEM scale. The large differences in duration of loading between the laboratory ($10^{-6}$-$10^{-5}$ sec) and the Barringer Crater shock event ($10^{-3}$-$10^{-2}$ sec) and the size of the largest grains of coesite (~5 microns) and stishovite (~1 micron) preserved at Barringer crater versus their absence in the laboratory, suggests that the kinetics of crystallization for coesite and stishovite are very slow relative to the durations of loading in the laboratory.

Figure 5-12: Recovery microstructures of the shock mosaic structure in samples of Hospital Hill quartzite shocked to 8 GPa at 100°C (A), and 750°C (B), and shocked to 28 GPa at 25°C (C), and 440°C (D). The 8 GPa shots were performed using HE methods and the 28 GPa shots are from the experiments of Reimold and Hörz (1986a). Note the larger, more well-defined domains in the high-temperature experiments.

A

0.5μm

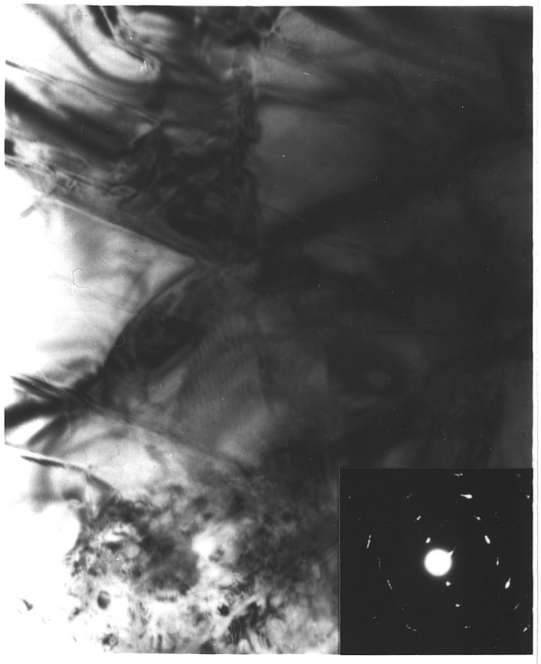

B

0.5μm

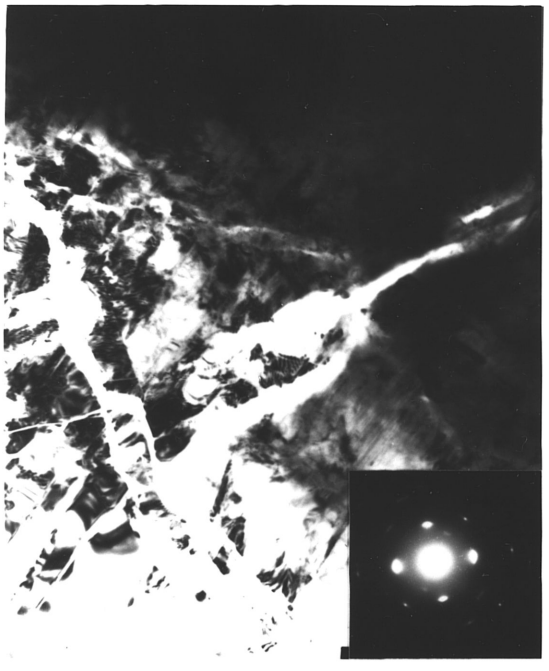

C

0.5μm

D

0.5μm

Another difference observed in experiments performed at low and at high temperature is the degree of recovery at equal shock pressures that is related to immediate post-shock annealing. Samples shocked to 8 GPa in this study (figure 5-12A, B) and to 28 GPa by F. Hörz (figure 5-12C, D) reveal that the high-temperature experiments (figure 5-12B and D) display reduced distortional strains and larger domain sizes in quartz. These microstructural changes may represent thermally-assisted recovery of the strains in the mosaic domains after the shock event. Electron diffraction patterns reflect a change from short-range distortional strains at room temperature by uniform diffuse streaks, to larger recovered domains at high temperature by concentrations of spots within less pronounced diffuse streaks.

Models For Development of Planar Features

The first detailed analysis of shocked quartz single-crystals (Hörz, 1968) revealed that samples shocked parallel to *c* and normal to *m* and *r* (figure 2-1C) produced planar fractures in planes of high shear stress. Brannon et al (1984) performed experiments on *a*-cut quartz and observed heterogeneous emission of radiation along planes at 25°, 35°, 47°, and 72° from the *c*-axis. These planes of high radiance, which produce high temperatures due to shear heating, were observed at pressures as low as 5 GPa and are equivalent to the fractures observed by Hörz (1968). In crystals shocked parallel to *c*, Hörz (1968) observed optically visible planar features dominantly parallel to ω at 16.2 GPa, additional sets parallel to $\pi$ at 21.1 GPa, and equal numbers of ω and $\pi$ at 26.2 GPa The major difference in the planar feature development relative to the shock propagation direction is that the ω features first appear in large numbers at 16.2 GPa in the *c* experiments, whereas they first occur in large

numbers in the *m* and *r* experiments at 21.3 and 21.9 GPa, respectively. Planar features parallel to $\pi$ develop in appreciable numbers at pressures greater than 25 GPa in all three orientations with lesser concentrations parallel to basal, rhombohedral and prism planes in the *m* and *r* experiments. The orientation data for the Hospital Hill quartzite samples shocked to 28 GPa at 25° and 440°C indicate that the orientation of planar features is virtually random with respect to the shock propagation direction (figure 2-12).

Grady (1980) proposed a model of planar fracture development by shear failure in the compressed state (figure 5-13A), which is in accord with the fracture data of Hörz (1968), and the radiance observations of Brannon et al (1984). Schmitt and Ahrens (1989) further proposed that shear heating during shock compression results in the formation of melted quartz within planar fractures that crystallizes to form stishovite and/or coesite, provided that the pulse duration is sufficiently long (figure 5-13A). Schmitt and Ahrens (1989) argue that this model is in agreement with the presence of stishovite in experiments observed by Ashworth and Schneider (1985), Kleeman and Ahrens (1973), and DeCarli and Milton (1965).

Gratz et al (1988) have proposed that planar features are produced by injection of melt into tensional cracks formed during the release phase of the shock (figure 5-13B). The only evidence in support of their model is the observation that all planar features observed at the TEM scale in their synthetic single crystals shocked in the *a* direction have normals nearly 90° from the shock propagation direction (figure 5-13B); that is, the features contain the shock direction and lie in planes of low to zero shear stress.. This model, which contradicts the more detailed work of Hörz (1968) and this study,

Figure 5-13: Models for the development of planar fractures (microfaults) and planar features in quartz. A. The model of Schmitt and Ahrens (1989) for development of microfaults and crystallization of high-pressure phases in the compressed state. The model is a modification of the shear-heating model of Grady (1980) for microfault formation. B. Model for development of planar features in tension during the release phase of a shock (Gratz et al, 1988). The experimental configuration with the shock in the *a* direction is also shown. C. A preferred model for development of microfaults and planar features in compression. The microfaults (bold lines) form by shear failure of the crystal along planes of high shear stress. Within each microfault domain, planar features develop along $\omega$, $\pi$, and other planes independent of the shock direction. Optically-visible planar features (stippled features) represent the coalescence of a TEM-scale heterogeneous phase transformation in the solid state, which causes a lowering of the refractive index that is observable at the optical scale. D. TEM-scale view of a single optically-visible planar feature surrounded by crystalline quartz. The planar feature is filled with fine planes of short-range-order silica (black) sandwiched between layers of crystalline quartz. The glass coalesces to produce an optically-detectable decrease in refractive index. Diagrams after Grady (1980), Schmitt and Ahrens (1989), and Gratz et al (1988).

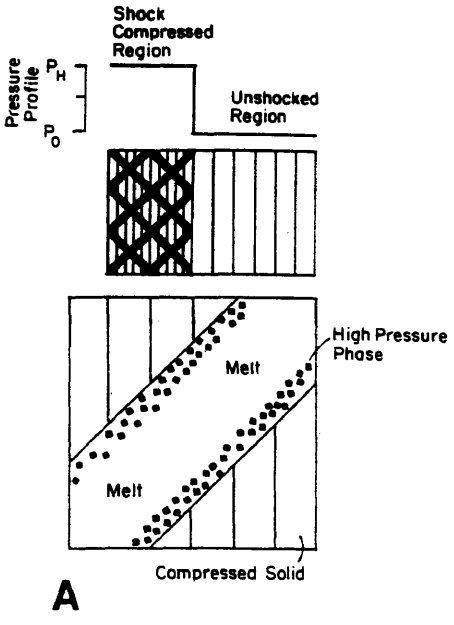
Shock Compressed Region
Pressure Profile
$P_H$
$P_O$
Unshocked Region
Melt
High Pressure Phase
Melt
Compressed Solid
A

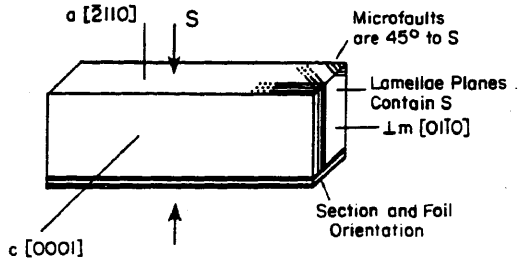
a [2̄110]
S
Microfaults are 45° to S
Lamellae Planes Contain S
⊥m [01̄10]
c [0001]
Section and Foil Orientation

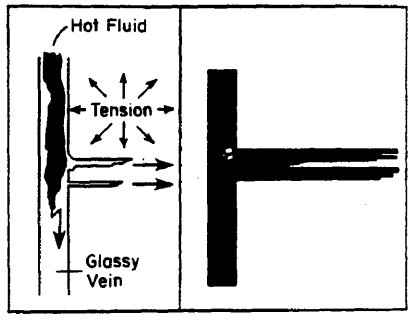
Hot Fluid
Tension
Glassy Vein
B

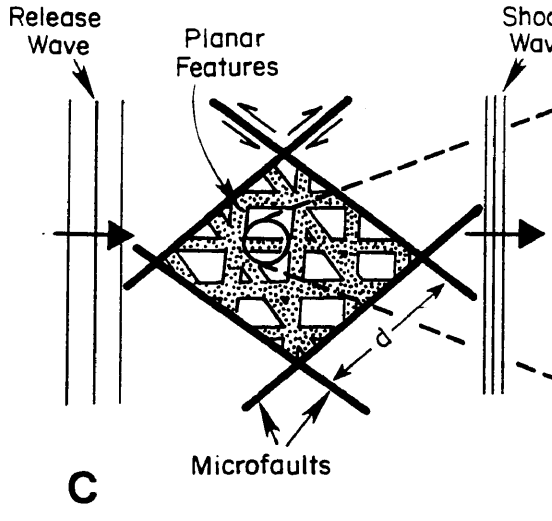
Release Wave
Planar Features
Shock Wave
d
Microfaults
C

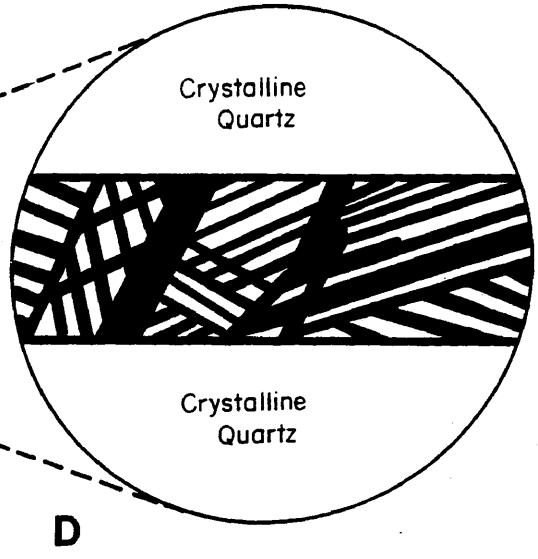
Crystalline Quartz
Crystalline Quartz
D

is questionable since the only thin sections studied by Gratz et al were cut perpendicular to the shock propagation direction, which makes observation of the planar features at high angles to the shock propagation direction virtually impossible. Their model also ignores the presence of stishovite in the shocked glasses reported by other workers (listed in the previous paragraph), which requires that the planar features form during the compressional phase, not the release phase. Gratz et al (1988) also observed that planar features seem to nucleate and grow on crystal defects in quartz. Although this observation was not confirmed clearly by this study, the presence of many TEM-scale *r* planar features in Hospital Hill quartzite samples from this study does correlate with the large number of dislocations observed trending along *r* in the starting material (figure 5-2).

Gratz et al (1988) reported a dominance of *c* features at 12 GPa at the TEM scale, whereas Hörz (1968) observes appreciable concentrations of these features at 22 and 27 GPa in the *r* experiment. The absence of these features at the optical scale in the experiments of Reimold and Hörz (1986a) may reflect either the lack of pulse durations sufficient to localize these features at the optical scale, or experimental conditions that allow homogeneous development of the features at the TEM scale. The presence of such well-developed *c* features in the 12 GPa experiment of Gratz et al may reflect either shock-crystal orientation relations or differences between synthetic and natural quartz.

The TEM results from this study do not support the notion that large shear strains in silicates are responsible for glass formation in planar features. Furthermore, the presence of multiple sets of planar features at all

orientations with respect to the shock direction in naturally- and experimentally-shocked silicates, and the presence of stishovite and high-density, short-range-order silica in the planar features rules out their formation exclusively by tensional failure during release from the shocked state. A third alternative that can explain the observations of Hörz (1968), Gratz et al (1988) and this study is heterogeneous solid-state collapse of the structure under shock compression to form a high-pressure polymorph or dense short-range-order silica. In this model, the quartz structure responds to the shock by collapsing preferentially on planes of progressively lower compressibility. At low pressures (9-15 GPa; Schmitt and Ahrens, 1989) where the shock possesses insufficient energy to produce large amounts of stishovite or coesite, the material compresses to a short-range-order silica with 6-fold coordination, and temperature increases. The preferred orientation for this first collapse is the *c* direction, which is also the first orientation to form glass-filled planar features at pressures above about 9 GPa. The high temperatures generated in this pressure range are insufficient to produce melting of the compressed zones, but are high enough to allow small amounts of stishovite to form by direct crystallization from the glass during the compressional phase of the shock. At pressures above 15 GPa, it is suggested that the shock may contain sufficient energy to cause collapse parallel to $\omega$, followed by collapse parallel to $\pi$ above 20 GPa. Finally, collapse of the less compressible *m*, *z*, and *a* orientations (Birch, 1966) occurs; this is the sequence observed by Hörz (1968).

In the model of solid-state collapse, the number and thickness of individual planar features is a function of the temperature at a given pressure. As specific planes collapse, they thicken and coalesce with the

assistance of locally elevated temperatures caused by the compression. Thickening of individual features (figure 5-13D) progresses until the features are sufficiently broad to give rise to an optical signature (figure 5-13C). At progressively higher shock pressures and temperatures, the various orientations of features produced coalesce so that homogeneous deformation is achieved, giving rise to large-scale isotropization of the material. The fundamental difference between this model and those of Grady (1980) and Gratz et al (1988) is that planar features represent a heterogeneous form of phase transformation, which is quite distinct from the micromechanical (shear or tensional) response of the crystal to loading represented by planar fracturing. The frequent observation of planar fracture (microfault) domains that contain sets of planar features (figure 5-13C) suggests that the planar fractures form as the quartz crosses the HEL, followed by the development of planar features in the two phase region of the plastic Hugoniot. Small shear offsets observed across planar features can also be accounted for by the phase transformation model. The transformations from quartz to coesite and quartz to stishovite produce volume changes of 10.2% and 61.5% respectively. Collapse from quartz to stishovite on planes inclined at 45° to the shock direction will produce apparent shear displacements of 0.06 microns for a 0.1 micron planar feature; the largest displacements observed at the TEM scale are of this order. Shear displacements accompany phase transformations parallel to any plane of non-zero shearing stress.

The model can account for the apparent lack of control that shock propagation direction exerts on the orientation of planar features (figure 2-12), and supports the contention of Hörz (1968) that the primary factor influencing their development is the crystallography of the host crystal. This

model also explains the temperature dependence of planar feature development since elevated temperatures tend to favor a more homogeneous phase transformation. The absence of optically-visible $\pi$ planar features at high temperatures reflects homogenization of planar feature development at the TEM scale, not the absence of TEM-scale $\pi$ features. This also explains why rare optically-visible $\omega$ features are followed directly by isotropization at elevated temperatures. In theory, this change in transformation behavior should be reflected in the compressibility surface for the crystal at elevated temperatures, especially in quartz which occurs in the ß-form above 573°C; such data are not currently available. A simple test of this model for planar feature development would be to shock oriented single crystals and determine if any planar features develop parallel to planes that are perpendicular to the shock propagation direction. It should also be possible to distinguish between high-density glass produced in compression and fused silica with a density lower than quartz, provided that the former does not convert during release. This distinction should reveal high-density glass in planar features, and fused silica in post-shock fractures as suggested by Kieffer et al (1976) and Ashworth and Schneider (1985).

## Application of The Results to Natural Shock Processes

The results of this study are directly applicable to the interpretation of microstructures observed in nature, including the KTB and volcanic rocks. The dominance of intense mosaicism in feldspar, weak mosaicism in quartz (both with partial recovery), and rare single sets of planar features oriented parallel to $\omega$ in known volcanic rocks are as predicted by the experimental results. Samples shocked to < 18 GPa at 750°C in the laboratory reveal strong

mosaicism in K-feldspar and plagioclase, moderate mosaicism in quartz, and rare single sets of planar features in both quartz and feldspar. The absence of significant isotropization or multiple sets of planar features in the volcanic rocks rules out the possibility of shock pressures greater than 18 GPa, and probably represent pressures below 15 GPa. This pressure limit is based on limitations on eruption dynamics, and the much longer pulse durations, which should obtain in high-strain-rate volcanic events, that lower the pressure thresholds for the observed microstructures even further. The high temperatures of volcanic events also preclude the preservation of detectable amounts of coesite or stishovite in shocked quartz. Volcanic shock events will tend to drive the magmatic system back across the liquidus to even higher temperatures so that any high-pressure polymorphs, if formed, most likely revert to a fused silica phase following shock. However, the enhanced kinetics of shock for material initially at elevated temperature for long durations might favor more rapid growth of the high pressure polymorphs at moderate shock pressures. Unlike impactites, techniques involving dissolution of very large quantities of quartz to concentrate tiny quantities of coesite and stishovite have not been used on any silicic volcanics to the knowledge of the author.

The results of this study also emphasize a critical point regarding mosaicism as a diagnostic indicator of shock damage in silicates. The shock mosaic structure is but one plastic response of the silicate structure to shock compression and is quite different from planar feature formation. Shock mosaicism should occur at all pressures above the HEL for a specific material, which means that mosaicism should be observed in feldspars shocked above 4 GPa and in quartz shocked above 5 to 15 GPa. These pressures are much lower

than those required for development of single and multiple sets of planar features parallel to $\omega$ and $\pi$, about 15 and 20 GPa respectively. Thus, there is a pressure range from 4 to 15 GPa where shock mosaicism and crystallographically-oriented fracturing will be the only microstructures induced by weak to moderate shock waves, along with some basal *c* planar features.

This result dispels the myth that only multiple sets of planar features are diagnostic of shock deformation in quartz. It also reveals shock mosaicism as a diagnostic indicator of shock deformation in quartz and feldspar, which represent shock pressures > 5 and < 15 GPa when observed in the absence of planar features. The development of the mosaic structure should be enhanced in volcanic rocks by elevated temperatures, and in all natural shock events where longer pulse durations permit greater plastic strains to be achieved. The high temperatures should also enhance the recovery of the mosaic structure as reflected in the volcanic samples. It remains to be seen whether or not high pre-shock temperatures actually lower the HEL for silica and silicates.

The results can also be used to answer some questions regarding the KTB debate. The paucity of multiple sets of planar features in the high-temperature experiments along with the complete absence of multiple sets in volcanic rocks is very different from the more frequent multiple sets of planar features observed at the Raton Basin localities. The presence of multiple sets of planar features at Raton indicates that the shock event recorded in the KTB clay layer is more likely a low- to moderate-temperature impact event at pressures to 20 GPa. The presence of partially-recovered shock mosaicism in the boundary clay also requires that the shock event

occurred at moderate temperatures. In addition, the presence of stishovite in the Raton deposits (McHone et al, 1989) suggests that the boundary deposits are not of volcanic origin, which leaves an impact event as the only explanation for the shocked minerals at the KTB proper in North America. Regarding the distribution of rare sets of planar features and frequent, partially-recovered shock mosaicism across the K/T transition at Gubbio, Walvis Ridge, and Maud Rise, it is proposed that these deposits represent a major increase in volcanism across the K/T transition that begins long before the KTB impact event and is completely unrelated to the impact event.

## Conclusions

The results of the experimental program reveal that pre-shock temperature and pulse duration exert a first-order influence on the character of shock-induced microstructures in silicates at specific shock pressures. This includes a dramatic decrease at elevated temperatures in pressures for the onset of shock mosaicism and isotropization, and a marked change in the development of planar features above 15 GPa. Elevated temperatures also produce release melting, initially along veins and fractures, and finally as massive melting throughout the sample. The degree of melting increases with pressure and temperature, and may initiate in the compressed state at the highest temperatures where the compression drives the system across the solidus. The very small effect of temperature on the onset pressure for planar features suggests that these microstructures form during the shock transition by heterogeneous solid-state collapse of the crystal structure, and that subsequent deformation in the compressed state occurs by intensification of the mosaic structure and bulk flow of the material. The planar features which

develop in planes of non-zero or finite shearing stress exhibit small shear displacements that result from collapse of the crystal structure.

At elevated temperatures, the dominant microstructures in shocked quartz and feldspar are fracturing, mosaicism, and isotropization, with rare planar features, all of which occur at pressures below 20 GPa. This is in sharp contrast to classical room-temperature microstructures which occur up to 30 GPa, with the pressure range from 15 to 30 GPa being dominated by planar features and shock mosaicism. The results also confirm shock mosaicism as a diagnostic indicator of shock processes, and is especially important at high temperatures where planar features are uncommon. However, the use of mosaicism in feldspars as a diagnostic for shock must take into account the unusual crystallization and exsolution textures that often occur in feldspars of igneous origin. Shock microstructures in volcanic rocks do represent high-temperature dynamic deformation which must be produced at peak pressures below about 15 GPa. Pressures greater than this drive the system back into the liquid state precluding preservation of microstructures.

# CHAPTER VI

## A MODEL FOR ENDOGENOUS CAUSATION OF MASS EXTINCTIONS

### Introduction

The hypothesis that the K/T and other mass extinctions were caused by bolide impact has now been actively studied for nearly a decade. Considerable and sometimes irreconcilable problems with this model still remain. These problems include evidence of accelerated extinction and geomagnetic reversal activity prior to the boundary, ambiguities concerning the specific type of extraterrestrial object and target necessary to produce the geochemical signatures, and uncertainties concerning mechanisms relating the K/T impact event to the selectivity of the extinctions and the cause of the climatic and sea level changes.

One of the most important developments in the impact hypothesis has been the suggestion that the K/T event is but one of a series of episodic or periodic phenomenon. Raup and Sepkoski (1984) and Rampino and Stothers (1984a, b) argue that mass extinctions occur periodically in approximately 30 million year (Ma) cycles. Since this discovery, Ir anomalies have been sought (and sometimes found) at other extinction boundaries, and hypotheses for periodic extraterrestrial impact have been proposed. When it became increasingly clear that many extinctions at the K/T boundary predated the terminal event, Hut et al (1987) proposed that the cause of this and other mass extinctions was cometary showers, resulting from perturbations of the Oort cloud, that occur at approximate 30 Ma intervals. It was speculated that such a

bombardment near the K/T boundary would cause a series of impacts spread over several Ma and thus account for the extinctions and climate changes that preceed the boundary. However, there is no evidence that comets can account for the Ir (Weissman, 1985, Crocket et al, 1988) and there is no evidence of multiple impact events near the K/T boundary that are separated in time.

It has also been observed that extinctions correlate well with changes in the frequency of geomagnetic reversals (Raup, 1985; Pal and Creer, 1986; Stothers, 1986), flood basalt eruptions (Rampino and Stothers, 1988), and other surface phenomena (e.g. Rampino and Stothers, 1988). Impact mechanisms have been proposed to explain these effects (e.g. Muller and Morris, 1986); however, they are highly speculative and not supported by any dynamo calculations. They also require that the reversals and basalt flows occur after impact, which is not supported by the evidence (Loper and McCartney, 1990).

The inability of the impact model to explain much of the evidence associated with the mass extinctions has led to the development of an alternate "endogenous" model (Loper and McCartney, 1986, 1988; Courtillot and Besse, 1987; Loper et al, 1988). This involves the lowermost part of the mantle, known as the D" layer, which may be related directly to geomagnetic reversal activity. An instability in this layer, which would be related to an increase in the frequency of geomagnetic reversals, causes a large amount of lower mantle material to rise diapirically through the mantle. Upon reaching the base of the lithosphere, this diapir could cause massive volcanism, crustal thinning, lithospheric breakup, and eustatic and climatic changes leading to gradual extinctions. Eventually a large volume of this material might reach the earth's surface in the form of extensive flood basalts. Ash, and aerosols laden

with sulfates, $CO_2$, halogens, and associated trace elements, would be emitted into the atmosphere, triggering a catastrophic climatic change leading to the terminal extinction event as found in the plankton record. The paleontologic, mineralogic and geochemical evidence lends some support to this mechanism. Furthermore, the sequence of events associated with the K/T boundary, including the change in geomagnetic reversal rate, support this mechanism.

The endogenous alternative has some advantages over the impact model, but is not without major problems of its own. In particular, there is not a generally-accepted mechanism for a volcanic explosion sufficient to produce and distribute the shocked quartz. The general, and possibly incorrect, presumption that only a bolide event is capable of producing this evidence is currently being challenged. In addition, the evidence for shocked quartz at the K/T boundary may represent a minor impact at Manson crater in Iowa (Izett, 1987b), and is clearly insufficient to have caused global extinctions at K/T time. In the following pages, the paleontologic, geochemical and mineralogic evidence found at the K/T boundary will be reviewed in the context of the plume model. A mechanism for how flood basalts might be related to specific extinctions and climatic effects will be proposed.

## Observations at The Cretaceous-Tertiary Boundary

### Paleontological Evidence

Recent research suggests that the K/T extinctions were much more complex than previously thought. In general, the extinctions can be separated into two distinct components. The first of these involves the macro-organisms, which often show a decline in the million or so years before the boundary, with accelerated decline in the last few hundred thousand years (see Sloan et al, 1986). Many of the marine micro-organisms show a different extinction history; these undergo a relatively abrupt extinction very near to or coincident with the boundary. Detailed study, however, has shown that both components are not always amenable to generalization (Hallam and Perch-Nielsen, 1990). The ammonite extinctions, for example, may be far closer to the boundary than originally believed (Ward and Macleod, 1988). On the other hand, the plankton extinctions that were previously considered to be sudden and synchronous are now known to be neither (e.g., Brinkhuis and Zachariasse, 1988).

For the macro-organisms, total extinction was suffered by the dinosaurs, flying and marine reptiles (except turtles), ammonites, and several carbonate-shelled clam groups including the inoceramids, rudistids, and Exogyra. The belemnites barely survived the K/T event, only to linger until the Eocene. All these groups were dominant in large parts of the Mesozoic, and declined considerably during the latter part of the Maastrichtian (Carpenter and Breithaupt, 1986; Wiedmann, 1986). The pre-boundary decline of the various macro-organisms is generally attributed to rapid sea-level regression

(Hallam, 1989) and climatic changes (Stott and Kennett, 1988) shortly before the terminal event. These would also explain the frequent presence of hiatuses near the boundary and the many discrepancies seen in the pre-boundary fossil record (Hallam, 1987). While there is little question that there were abundant pre-boundary extinctions, the timing of these extinctions seems to vary considerably from one region or latitude to another. Organisms that are extinct well before the boundary at some locations survive up to or near to the boundary at others.

Pre-boundary extinctions of many macro-organisms are much in contrast to the planktic microfossil record. The planktic extinctions are more abrupt, and are normally used to define the boundary itself. The extinctions are also highly selective, with those possessing calcareous skeletons being more affected than the others, although radiolarian extinctions were also considerable (Thierstein, 1982). However, the plankton extinctions were not instantaneous; the foraminifera and nannoplankton events are separated by several thousand years (Smit and Romein, 1985). Furthermore, foraminiferal extinctions predate the boundary (Brinkhuis and Zachariasse, 1988; Keller, 1988a-c); at El Kef in Tunisia, 13% of the planktic species become extinct 25 cm below the boundary and 17% at 5 cm below (Keller, 1988b). Among the planktic foraminifera, large complex species became extinct before the smaller, more primitive, morphologies (Keller, 1988b) and there is an abundance of abnormal foraminiferal tests below the boundary (T. Hansen et al, 1987).

The general sequence of planktonic extinctions across the K/T boundary (Hallam and Perch-Nielsen, 1990) implies a reduction of planktonic

foraminifera and nannoplankton prior to the boundary with the nannoplankton experiencing their main extinction several thousand years into the Tertiary. Dinoflagellates and diatoms are not affected seriously by the terminal event (Kitchell et al, 1986), possibly because they could survive by forming resting spores. Brinkhuis and Zachariasse (1988) propose that the K/T boundary itself represents a peak in sea level regression at the end of an extended regression lasting several Ma, although some sites (e.g. Brazos River; Jiang and Gartner, 1986) do not show any evidence of a marine regression at all. Whatever the cause of the K/T event, it affected the marine environment for a long time, as the recovery was extremely slow, lasting several Ma (Keller, 1988a,c); this is also seen in terrestrial plant studies (Lerbekmo et al, 1987). The hypothesis of impact-induced global darkness cannot explain why many photosynthetic protists, including some that do not have resting spores such as the silicoflagellates, survive the boundary event in relatively good order.

Study of other mass extinction events indicates that sea level regression and climate change often occur before the terminal extinctions (Stanley, 1988; Hallam, 1989) which is inconsistent with an impact. At the Mississippian/ Pennsylvanian boundary there is an extinction event coupled with a major eustatic regression (Saunders and Ramsbottom, 1986) and a coincident Ir anomaly that is not associated with other evidence of impact (Orth et al, 1986). Extinction, regression, and anomalous Ir can be found at the terminal Ordovician (Wilde et al, 1986) and Late Devonian as well (Playford et al, 1984); a eustatic transgression with an associated Ir anomaly is found also at the Cenomanian-Turonian boundary (Elder, 1987; Orth et al, 1988).

The paleontologic evidence is at odds with the impact model, which has maintained that the extinctions were sudden and synchronous. Later, when the record of gradual and unsynchronized extinctions was reiterated, Alvarez et al (1984) argued for extinctions "on two timescales: a slow decline unrelated to the impact and a sharp truncation synchronous with and probably caused by the impact." This required that an extraterrestrial event happened precisely at the time that an unrelated terrestrial phenomenon had reached its apogee. Hut et al (1987) attempted to accommodate the early extinctions by use of multiple cometary bombardment lasting several million years, even though there is no physical evidence to support their occurrence. It is more likely that the "stepwise extinctions" can be explained more adequately by terrestrial events or hiatuses in the geologic record; both the timing and the selective nature of the extinctions can be explained by endogenous mechanisms (McLean, 1978; Officer et al, 1987).

Geochemical Evidence

A tremendous analytical effort has been lavished on the K/T boundary since the first report of Ir by Alvarez et al (1980); enriched levels of Ir relative to an "average" crustal value of 0.02 ppb (Shaw et al, 1976) have been reported from some 75 sites. A number of these sites are indicated in figure 6-1. The concentration of Ir ranges over nearly three orders of magnitude, from 87 ppb at Stevns Klint, to values as low as 0.16 ppb in DSDP cores from the South Atlantic.

It is important to ask the question: What enrichment level constitutes an Ir anomaly relative to background? It is difficult to justify the

Figure 6-1 : A global map of the positions of the continents at *ca.* 65 Ma. Indicated are some of the localities for which Ir analyses have been done (adapted after Alvarez et al, 1982) : filled circles represent sites at which anomalous Ir was found; open circles represent sites where no anomalous Ir was found. Site #8 is a new section from southern Africa (Tredoux et al, 1989). The insets show chondrite normalized PGE plots for European (inset A) and New Zealand (inset B) K-T boundary samples. Information about the normalization procedure and the C-1 chondrite values can be found in Tredoux et al (1989).

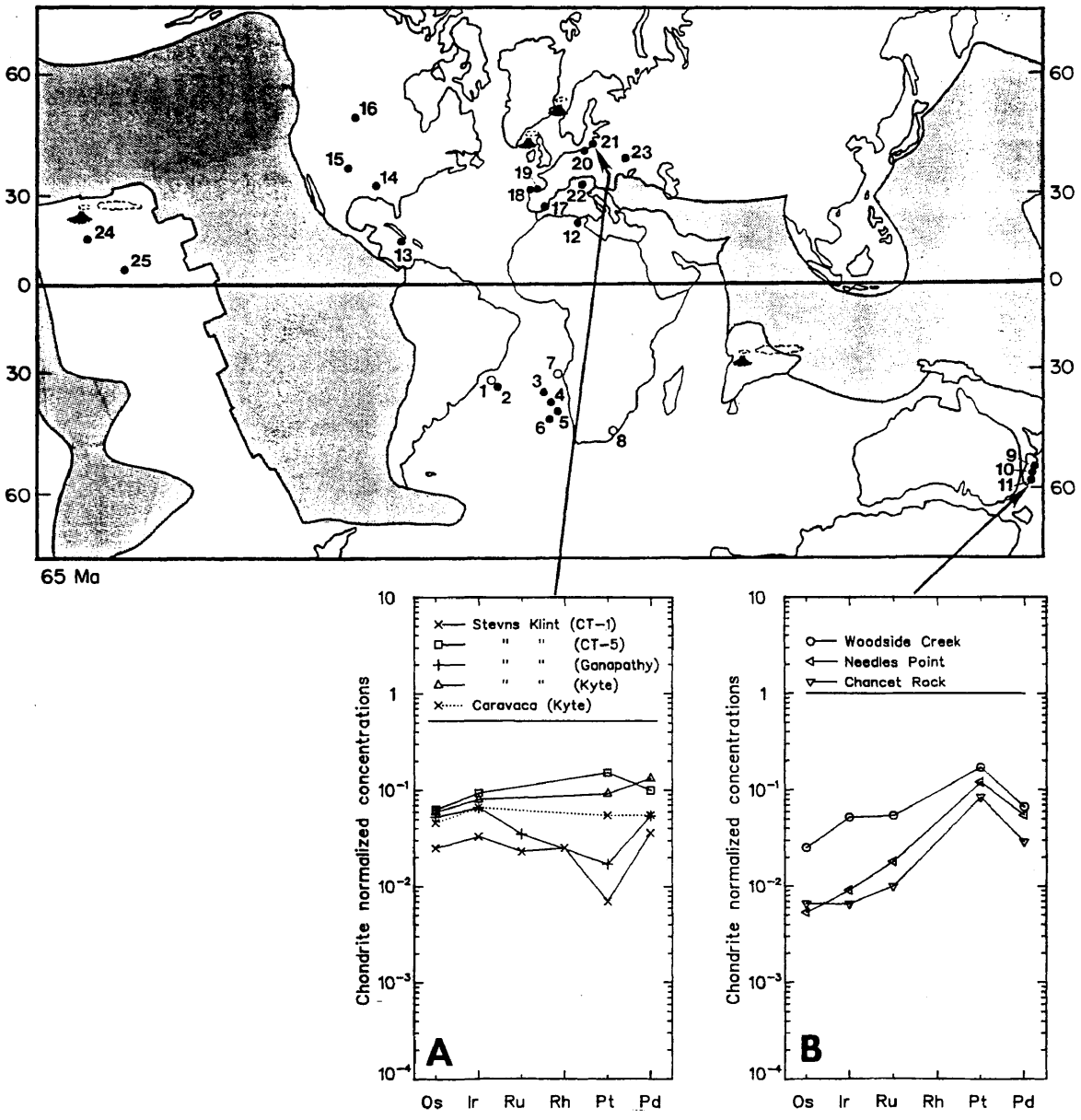
60
30
0
30
60
16
15
14
13
24
25
21
23
20
19
18
22
17
12
7
3
1
2
4
6
5
8
9
10
11
65 Ma
Stevns Klint (CT-1)
" " (CT-5)
" " (Ganapathy)
" " (Kyte)
Caravaca (Kyte)
Chondrite normalized concentrations
10
1
$10^{-1}$
$10^{-2}$
$10^{-3}$
$10^{-4}$
A
Os
Ir
Ru
Rh
Pt
Pd
Woodside Creek
Needles Point
Chancet Rock
B

classification of layers with <1 ppb Ir (e.g., DSDP sites in the South Atlantic) as anomolous, despite their substantial enrichment relative to the quoted crustal average of 0.02 ppb. This value pertains to Precambrian continental crust (Shaw et al, 1976), but Crocket and Kuo (1979) have shown that average Ir levels in 37 deep-sea sediments are in fact ten times higher (0.3 ppb). Also, although Gilmore et al (1984) report very low values (<0.04 ppb) in Cretaceous clays in the Raton Basin, Van der Flier-Keller and Fyfe (1987) found Ir concentrations ranging between 0.1-3.0 ppb in 30 of 61 studied Cretaceous coals and sediments in Canada. If the K/T boundary sections in North America (Orth et al, 1982; Gilmore et al, 1984; Lerbekmo et al, 1987) are evaluated in terms of these data, only some of the Raton Basin data (Gilmore et al, 1984) would constitute significant enrichments. A persistent observation from the KTB sequences in North America is that peak Ir levels often occur at the base of a coal seam (Gilmore et al, 1984; Lerbekmo et al, 1987). It is possible that the coal swamp environment may be responsible for significant acid leaching, elemental remobilization, and concentration of Ir. The very high Ir content in the Stevns Klint, Caravaca, and Woodside Creek sections also coincides with an organic layer (Schmitz, 1985). These observations led Lerbekmo et al (1987) to conclude that "the influence of the depositional environment must be isolated from that of the extraordinary event before a full understanding of the causal event can be gained".

The proponents of the impact model often integrate the Ir across a non-specific interval of sediment to calculate the total contribution of the presumed dust cloud at each site. This practice is based on the assumption that the Ir concentration is "primary", in the sense that it was established syn-depositionally and not altered or added to significantly during subsequent

weathering (e.g. Kyte et al, 1985; Strong et al, 1987). However, as mentioned above, Lerbekmo et al (1987) raise the point that depositional environment might be an important factor in the formation of the Ir anomalies. For example, Schmitz (1985) proposes a mechanism of upward migration and redeposition at a redoxcline, to explain the high values of the "terrestrial chalcophiles" and the PGE in the Stevns Klint and other boundary clays. Such models of secondary reconcentration and remobilization of Ir are probably important at the K/T boundary and cannot be ignored. Modeling of the behavior of the PGE in the sedimentary cycle is in its infancy and very little is known other than that organic layers and clay-rich sediments occasionally have elevated levels of Ir (and the other PGE) (Kucha, 1982; Van der Flier-Keller and Fyfe, 1987). It is important to note that models of Ir mobility in the crust are based on observations of weathering of meteorites and basic/ultrabasic rocks, in which the PGE occur as sulphides or alloys. There are currently no experimental or other data bearing on possible weathering patterns of the PGE if they should enter the sedimentary cycle as more reactive species (e.g. as fluorides as suggested by Zoller et al, 1983).

That the Ir/Au ratios of the Stevns Klint fishclay fall in the field of "extraterrestrial signature" (Palme, 1982) (Ir/Au >3.3, see Figure 6-2) has been used to indicate the presence of impact-derived material in these layers. However, we note that the Ir/Au ratios of mantle nodules also plot in this field (Palme, 1982; Morgan, 1986), which therefore denotes a "non-crustal" signature rather than an "extraterrestrial" one. Also plotted on figure 6-2 are five samples from a Stevns Klint section (data listed in Table 6-1). Note that ratios of all these samples plot close to the Ir/Au = 3.3 line. Boundary sample (CT-5) is therefore not unique, but merely shows maximum enrichment of a

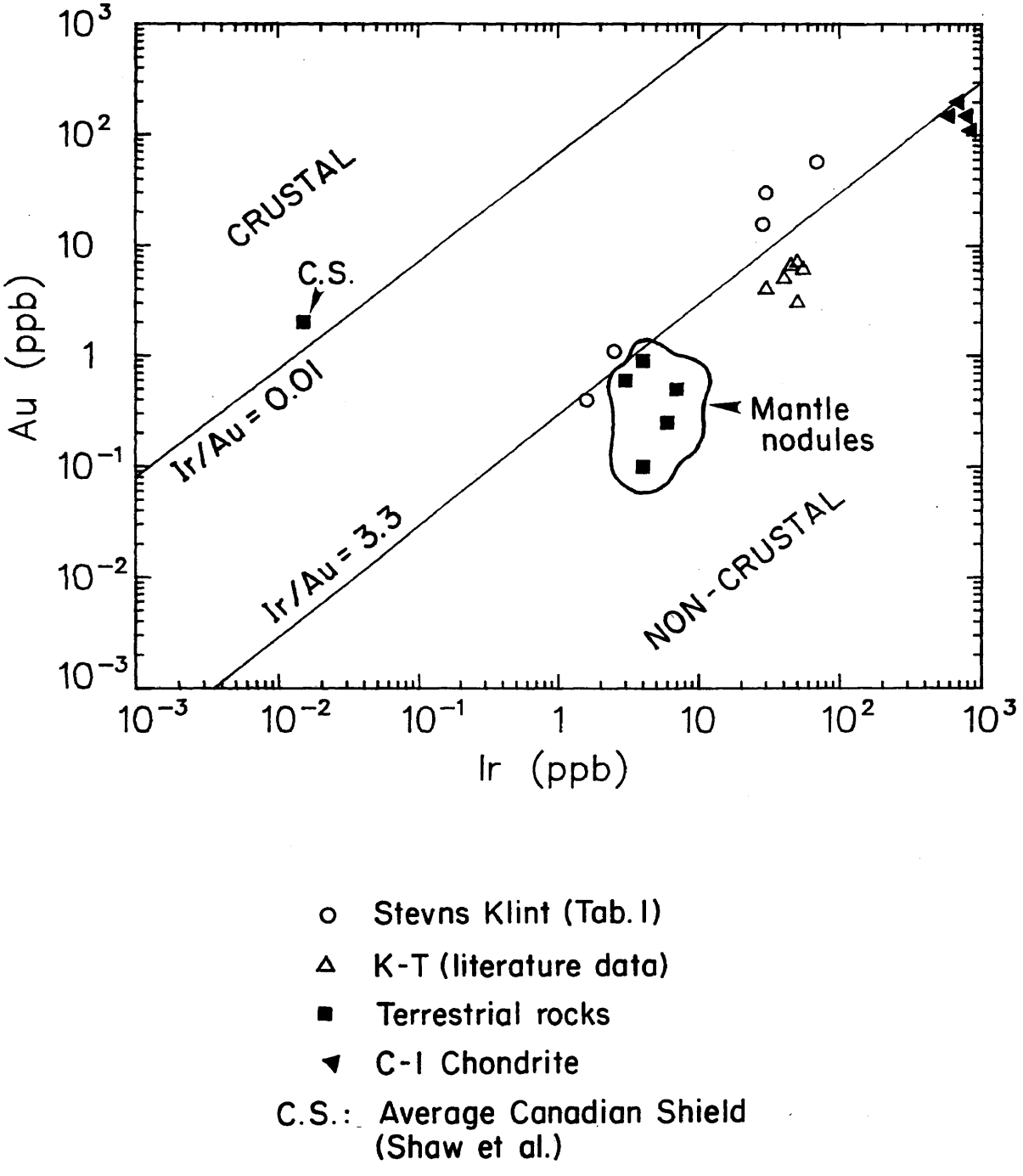


Figure 6-2 : A plot of Au/Ir ratios of some K/T boundary samples (modified after Palme, 1982). The open circles represent a series of analyses from Stevns Klint (Tredoux et al, 1989), and in increasing gold content, are for CT-3, CT-7, CT-6, CT-4, and CT-5. The stratigraphic positions of these samples are given in Table 6-1.

Table 6-1 : Inter-element ratios for six samples across the K-T fishclay at Stevns Klint. Stratigraphic position, relative to the boundary (CT-5), is also indicated. Also listed are data for southern hemisphere K/T boundary sites, average terrestrial basalt, iron meteorite, and chondrite meteorite. Data from Davies and Tredoux (1985) and Tredoux et al (1989).

| | Stratigraphic Position | Ir/Au | Ir/Pt | Ir/Os |
|---|---|---|---|---|
| CT-3 | -0.5 m | 2.8 | 0.3 | 1.3 |
| CT-4 | -0.1 m | 1.2 | 0.3 | 1.2 |
| CT-5 | 0.0 m | 1.8 | 0.3 | 1.5 |
| CT-6 | +0.5 m | 0.7 | 0.6 | 1.4 |
| CT-7 | +1.0 m | 0.7 | 0.4 | 1.3 |
| Woodside Creek [a] | - | 0.7 | 0.16 | 1.9 |
| Needles Point [b] | - | 0.9 | 0.04 | 1.6 |
| Mantle [a] | - | 0.97 | 0.2 | 1.03 |
| Basalt [b] | - | 0.11 | 0.02 | - |
| Iron Meteorite [a] | - | 1.17 | 0.4 | 0.86 |
| Chondrite [a] | - | 1.07 | 0.5 | 0.93 |

a=data from Tredoux et al (1989)
b=data from Davies and Tredoux (1985)

component that is already present in the sediments at 0.5 meters below the boundary. This is also true of the other inter-PGE ratios (Table 6-1). The impact model would probably ascribe this observation to large-scale bioturbation but it might as easily be putative evidence that the PGE enrichments in the K/T clays are not geochemically exotic in those stratigraphies.

The Ir/Os ratios of the Stevns Klint section are closer to mantle values (>1) than meteorite values (<1) (see Table 6-1). Os isotopic studies of the K/T boundary clay at Stevns Klint ($^{187}Os/^{186}Os$ = 1.65) and in the Raton Basin, Colorado ($^{187}Os/^{186}Os$ = 1.29) (both values from Luck and Turekian, 1983) show that these Os isotopic ratios are significantly higher than those of meteorites (~ 1) (Luck and Turekian, 1983). Both these ratios correspond to that of the Bushveld Complex (1.44; Allegre and Luck, 1980) which was derived from the upper mantle. Luck and Turekian (1983) have interpreted their data in terms of impact-derived Os, with some crustal contamination, although they concede that a model of mantle-derived Os would also satisfy the data.

Multiple Ir peaks have been reported a few meters above and below the boundary at the Gubbio section by Crocket et al (1988), and Rocchia et al (1987); in the Lattengebirge section (Graup et al, 1989), and at Brazos River (Ganapathy et al, 1981; Huffman et al, 1989). Increased concentrations of Ir, Pt and Au occur some distance below the K/T boundary in the Raton Basin (York Canyon site) (Orth et al, 1982). Crocket et al (1988) report that, beside the discrete Ir peaks at Gubbio, a broad zone (4 m) across the boundary is actually enriched in Ir. They conclude that the PGE enrichment event was of a

protracted nature and that a volcanic model is more compatible with the evidence than a single impact. This is in accord with the Stevns Klint Ir/Au data (Figure 6-2 and Table 6-1), and with the observation of H. Hansen et al (1987) that carbon staining at Stevns Klint correlates with Ir enrichments and is associated with many generations of encrusting bryozoans. H. Hansen et al (1987) conclude that the carbon and Ir were deposited together in pulses over 50,000 years and may be related to pulsed fluxes of volcanic origin as evidenced by a succession of stained and unstained bryozoan remains in and below the Fish clay at Stevns Klint. These workers also suggest that the carbon black is the primary carrier for the Ir.

Alvarez et al (1980), Smit and Kyte (1984), and Strong et al (1987) stated categorically that a volcanic model cannot account for the Ir enrichment . However, studies of aerosol emissions from Kilauea (e.g., Crowe et al, 1988), and of Cenozoic volcanic ash deposits in Antarctica (Koeberl, 1988) indicate that Ir-enriched aerosols (up to 7.0 ppb) may be associated with hotspot and alkaline volcanism. Furthermore, one of the largest basalt provinces of the Phanerozoic, the Deccan flood basalts of India, began erupting shortly before the K/T boundary (e.g., Courtillot et al, 1988). The Ir signature found at the K/T boundary could have come from the Deccan flood basalt if its aerosols had an iridium enrichment similar to that measured at Kilauea (Olmez et al, 1986). Recent work by Toutain and Meyers (in press) indicates that Piton de la Fournaise volcano on Reunion Island does emit excess iridium and other elements similar to the signatures observed at Kilauea. The significance of this observation is that the Reunion hotspot is believed to be the source for the Deccan basalts. Zoller et al (1983) and Olmez et al (1986) speculated that Ir expelled from subaerial hotspot volcanos occurs principally in the form of

$IrF_6$ gas. The presence of Ir in the atmosphere as a reactive gaseous phase might provide another mechanism for the widespread distribution of Ir at the K/T boundary and may be a viable alternative to global dispersion of vaporized meteoritic material.

Alvarez et al (1980) estimated that the global fallout of Ir was about 200 kilotons based on the concentrations at Gubbio. A 10 km diameter meteorite with density of 3.0 $gm/cm^3$, distribution efficiency of 0.22, and Ir=500 ppb, yields 173 kilotons of Ir, which is approximately sufficient to produce the K/T signature at Gubbio. Using Kilauea basalt (BHVO-1) as a proxy for the Deccan, and assuming an efficiency of 0.1 for Ir dispersal, the volume of basalt required to produce the K/T Ir as a primary signature is $1.4 \times 10^6$ $km^3$, which is in the range of volume estimates currently accepted for the Deccan Traps (Table 6-2). The basaltic aerosols also have an advantage over a meteoritic source since they are enriched in many of the other anomalous elements in the K/T sediments, including As, Sb, and Se, as well as Ir.

Aerosol emissions from non-hot spot volcanic provinces (e.g. Mt. St. Helens, El Chichon, Augustine, Arenal, Poas, and Colima; Zoller et al, 1983) show no Ir anomaly, suggesting that the only documented volcanic sources of Ir enrichment are hotspot-related volcanics. Typical mid-ocean ridge basalts (MORB), which are produced at an annual rate of about 20 $km^3$, are not a viable source for atmospheric Ir dispersal because most of these lavas are erupted below the sea surface which prevents aerosol emissions. Also, it has been recognized for some time that MORB is usually depleted in trace elements relative to hot spot magmas, which originate at greater depths (e.g. Hanson, 1980). Based on these data, it is proposed that the only recognized volcanic

source for Ir enrichment are hotspot-related and deep alkaline melts which originate in regions of the mantle that have not been previously depleted by significant partial melting.

The Deccan event is the only possible volcanic contributor to the PGE enrichment of the K/T sediments; the Late Cretaceous was a period of increased volcanism on a global scale (Vogt, 1972; White et al, 1987). Vogt (1972) points out that many near-equatorial hot-spot provinces were very active in the Late Cretaceous and early Tertiary. If conditions similar to those which cause some modern volcanic aerosols to be enriched in Ir and Au relative to the associated basalts (Zoller et al, 1983; Koeberl, 1988) also prevailed for some of the Late Cretaceous episodes, a worldwide Ir enrichment in the sediments deposited at times of intense volcanic activity might be expected. Subsequent leaching of the PGE from such layers and secondary enrichment in reduced overlying sediments, as suggested for the Stevns Klint fishclay by Schmitz (1985), would result in anomalous zones which are essentially condensed manifestations of long periods of previous volcanism. In this interpretation, the PGE signature can then be neither a unique identifier of the source of enrichment, nor of a time-specific event. The secondary processes could also alter the elemental ratios sufficiently that use of these signatures (e.g. Au/Ir ratio) as an indicator of source character would be rendered useless (Zoller et al, 1983). Such a model would offer more satisfactory explanations than the impact model for the features of the PGE anomaly as discussed above, as well as the inter-hemispheric variation of the chondrite normalized patterns (figure 6-1), the differences in Ir concentration within and between sites, and the uniformity of inter-element ratios across the boundary at Stevns Klint.

Sharp negative $\partial^{13}C$ (e.g. Shackleton and Hall, 1984), positive $\partial^{18}O$ (e.g. Shackleton and Hall, 1984) and positive $\partial^{87}Sr$ (Hallam, 1987; Koepnick et al, 1985; and MacDougall, 1988a) excursions occur across the K/T boundary; the carbon excursion has been attributed to decreased productivity (Tappan, 1968; Zachos et al, 1988). The data for $\partial^{13}C$ from basalts indicate that normal basalts range from -8 to -5 permil, while some hotspot magmas (e.g. Kilauea and Mauna Loa) range from -27 to -13 permil (Allard, 1983). If carbon and sulfur from Deccan emissions are as voluminous as proposed herein, these emissions might affect significantly the atmospheric and oceanic reservoirs of carbon and sulfur. This could explain why some negative excursions in $\partial^{13}C$ occur where no apparent change in productivity has been identified, such as at Walvis Ridge from 54 to 58 Ma (Shackleton and Hall, 1984). At Walvis Ridge, a major excursion of $\partial^{13}C$ correlates well with the eruption of the Brito-Arctic (Greenland) flood basalts (Rampino and Stothers, 1988), but not with a significant productivity decrease. Although current understanding of carbon and oxygen isotopes suggests that flood basalts cannot cause changes in the oceanic reservoirs for these isotopes (M. Arthur, personal communication, 1989), it is suggested here that some negative carbon excursions, and correlated excursions for sulfur and other isotopes, may be related in some way to the eruption of flood basalts. Where these eruptions coincide with productivity decreases and other climatic effects, the excursions will be more extreme as in the Deccan K/T event.

The positive excursion for $\partial^{87}Sr$ in marine sediments from a late Cretaceous value of ~0.7077 to a K/T peak values ~0.7079, indicates an influx of continental material into the oceans, perhaps either due to increased land exposure from sea-level regression (Hallam, 1987) possibly aided by acid rains,

and/or injection of large volumes of acidic volcanic debris with high Sr ratios. The timing for Sr injection indicates that it began up to 3 Ma before K/T time (Koepnick et al, 1985), and thus cannot be linked to any instantaneous event such as a single impact. Tectonic reconstructions for the terminal Cretaceous indicate that levels of volcanism may have been higher than at present (Zonenshain et al, 1985). Most silicic volcanics and continental crust have $\partial^{87}Sr$ values that are higher than the Cretaceous ocean sediment values (e.g. Hanson, 1980). Also, some of the Deccan flows display more evolved isotope signatures, with especially high $\partial^{87}Sr$ values in some eruptive units indicative of severe crustal contamination or mantle isotopic heterogeneity (Murali et al, 1987). Injection of large volumes of volcanic particles with elevated $\partial^{87}Sr$, coupled with increased erosion from acid rain and sea-level fall, can account easily for the K/T isotope signature.

Depressed concentrations of the Rare Earth Elements (REE) in K/T boundary samples from Caravaca and Stevns Klint have been used by Smit and ten Kate (1982) as evidence of the presence of meteoritic material. This argument is not generally supported: most workers infer that the variation of the REE between the different sections indicates that local detritus and terrestrial processes exert the dominant influence on these elements (e.g. Kyte et al, 1985). Sm-Nd isotopic data for sanidine microspherules from the Caravaca boundary clay are consistent with derivation of the REE from seawater (De Paolo et al, 1983) or volcanic detritus (Shaw and Wasserburg, 1982).

Negative Ce anomalies occur in all Stevns Klint and Gubbio samples (e.g. Schmitz, 1985), and at Walvis Ridge (this work). Such patterns are usual for

deep-sea sediments and for biological marine sediments, notably ones which contain fishbone debris and the plankton genera Globigerina (Henderson, 1984). It is therefore reasonable to assume that the negative Ce anomaly, where present, is caused by equilibration with seawater and/or the presence of some biological remains. The Spanish K/T sections do not have negative Ce anomalies (Smit and ten Kate, 1982) and, like the continental section from Alberta (Hildebrand and Boynton, 1987) and the outer shelf section from the Brazos River (Huffman et al, 1989), shows patterns like those of average continental sediments (Henderson, 1984).

Mineralogical Evidence

Carbon black and soot concentrated at the KTB has been suggested to represent global wildfires that followed the blast effects of the K/T impact event (Wolbach et al, 1988). More recently, Gilmour et al (1988) have suggested that the carbon black, coupled with the presence of kerogen and retene in the soot, represents combustion of as much as 90% of the global biomass at the boundary. The paleontological evidence (Hickey, 1984; Johnson and Hickey, 1988) indicates that only the angiosperm plants were devastated in restricted areas of North America and Northeastern Eurasia, with less severe effects over the rest of the globe. Considering that the presence of retene indicates combustion of coniferous biomass, this correlation between the organic chemistry and paleontological evidence may have some merit, although the estimates of combusted volume seem to be extremely high. Also. H. Hansen et al (1987) found that the carbon black is distributed over 3.5 meters below K/T at Stevns Klint, and is actually the staining color in the chalk. H. Hansen et al (1987) estimate that this 3.5 meter section represents

50,000 years of deposition, and may be related to pulsed fluxes of volcanic origin as evidenced by a succession of stained and unstained bryozoan remains in and below the Fish Clay at Stevns Klint. These workers also suggest that the carbon black is the primary carrier for the Ir.

India was just south of the Equator at K/T time (Figure 6-1), suggesting that it was probably covered with dense, tropical rainforests. The Deccan Traps covered an estimated 1 to 1.5 million $km^2$ of India (Courtillot et al, 1988): if the rainforests were set ablaze and pyrolized by the advancing flow fronts, they could account in part for both the volume and temporal distribution of carbon black at K/T time. Cisowski (1988a) made the observation that some of the K/T magnetic spherules are similar to flyash and may be related to K/T carbon black via combustion of fossil fuels. Cisowski (1988a) also points out that high Ir in the magnetic spherules is strong support for such a mechanism. Isotopic mixing of the combusted biomass with isotopically light, carbon-rich Deccan aerosols could also account for the $\partial^{13}C$ data for these deposits.

Spheroidal magnetite (Smit and Kyte, 1984) is not confined to the K/T boundary. McCabe et al (1987) report that similar deposits are common in many Paleozoic carbonate sequences and that they are also found in biodegraded oil. The dendritic texture of the K/T magnetite spheroids, used by Smit and Kyte (1984) to infer impact, is not diagnostic as it is also a common feature in volcanic glass (Shaw and Wasserburg, 1982). Smit and Kyte (1984) concede that their data do not exclude a volcanic source, but they reject this alternative because of the high siderophile element content of the magnetite spheroids. On the other hand, the high Ir contents of the K/T spherules is one

of the reasons why Cisowski (1988a) concludes that they are not impact related. This and several other mineralogical features caused Cisowski (1988a) to conclude that the K/T spherules are much more closely related to fly-ash spherules formed during the combustion of coal, rather than melt spherules formed during an impact event.

Sanidine microspherules (Smit and Klaver, 1981), platinum-rich grains and spinels (Margolis and Doehne, 1988), and spheroidal magnetite (Smit and Kyte, 1984) at the K/T boundary have been used to support an impact model. However, there is much debate at present about whether this approach is valid. For example, Naslund et al (1986) caution that microspherules are not unique to the K/T boundary and that they might be of diagenetic origin. This interpretation is corroborated by H. Hansen et al (1986) who show that the microspherules in the K/T boundary sediments at Stevns Klint were probably formed by secondary alteration of algal structures. Furthermore, microspherules have been found in aerosols from Mount Etna (LeFevre et al, 1986). Sm-Nd and Rb-Sr systematics of sanidine spherules from the Caravaca K/T section (Shaw and Wasserburg, 1982) are consistent with authigenic growth and/or a volcanic origin. In addition, the Cr- and Ni-rich spinels and platinum-rich metal grains can also be found in lherzolitic material from the terrestrial mantle (Keays et al, 1981; Mitchell and Keays, 1981), and are common constituents of placer deposits (Cabri, 1981). They are, therefore, not good indicators of extraterrestrial matter as suggested by Margolis and Doehne (1988). Hallam (1987) suggests that the K/T microspherules probably represent all the possible sources including secondary sedimentary, volcanic, and extraterrestrial, which makes them essentially useless as an indicator of the unique cause of the extinctions.

Perhaps the most crucial evidence in the impact versus endogenous debate is the occurrence of shocked quartz at the K/T boundary. The shocked grains are distributed over a wide area, including North America, Europe, New Zealand and the North Pacific (see Bohor, 1990) along with the discoveries in the Weddell Sea and at Walvis Ridge. Such grains with multiple intersecting sets of planar features are found commonly at impact craters but have not been recognized in volcanics.

Shocked quartz grains are often taken as conclusive evidence of impact, and are one of the criteria used for the identification of impact craters. Other workers (Stevenson and Stevenson, 1980; Schreyer and Medenbach, 1981; Riedel et al, 1982, Schreyer, 1983) argue, however, that shocked features are only indicative of very high strain rates and are not process-specific. The results of Carter et al (1986), Officer and Carter (1990), and this study reveal clearly the presence of shock-induced microstructures in volcanic rocks, and the differences between those microstructures and classical impact microstructures. An appropriate model for generation of shock waves using thermochemical detonation (Boslough, 1989) assisted by a gas-phase explosion (chapter 2 of this work) may result in shock pressures required to produce the observed microstructures, but at lower pressures, higher temperatures, and longer pulse durations than obtain during impact events.

The experimental results from this study, Reimold and Hörz (1986a, b), and Reimold (1988) support the idea that high-temperature, moderate-pressure shock deformation will produce dominantly shock mosaicism and single sets of planar features. In addition, the results show that the use of the mosaic

structure as a diagnostic indicator of shock is useful, and actually necessary for high-temperature shock where planar feature development is suppressed. These results, coupled with the work on volcanics by Carter et al (1986) and this study lead to the proposal that classic impact microstructures may be just one end-member in a broad class of high strain rate microstructures whose character is a function of thermodynamic and material properties.

The distribution of shock-induced microstructures across the K/T transition at Gubbio, Maud Rise, and Walvis Ridge, and the character of the mosaicism and planar features in these sections suggests the occurrence of multiple shock events of moderate intensity across the transition. The presence of mostly single sets of planar features along with partially-recovered mosaicism indicates that these shock events are of the moderate- to high-temperature type (400° to 700°C), that are probably due to volcanic activity. The KTB shock event, as preserved in the Raton Basin localities, shows sufficient numbers of multiple planar features and the presence of stishovite (McHone et al, 1989) which suggests that this deposit is of impact origin. Although the natural and experimental evidence for shocked quartz supports the hypothesis that a small impact may have occurred at K/T time, impact is not the only viable mechanism for the production of shocked minerals.

In spite of the apparent uncertainties regarding shock microstructures, the link between the character and size of shocked minerals (Bohor et al, 1987), and the location of the Manson impact structure (Izett, 1987a and b) is worth serious consideration. $^{40}Ar/^{39}Ar$ dating of shocked microcline from Manson drill cores yields an age of 65.7±1.0 Ma (Kunk et al, 1989), which

supports the assertion of a K/T impact at Manson. This age date is regarded as more reliable than the paleomagnetic work (Cisowski, 1988b), which indicates that the Manson event occurred during a normal magnetic polarity interval (the K/T occurs in reversed chron 29R). Petrographic analysis of Manson materials (figure 2-23) indicates that the granitic basement at Manson is intensely shocked and confirms that Manson is an impact structure. If correct, the source of the shocked quartz at the KTB in North America may be resolved; the small size of the Manson structure (~35 km, Hartung et al, 1988; Anderson and Hartung, 1988) precludes the possibility that the Manson event alone caused even regional extinctions. For comparison, the Ries crater, Germany (Heissig, 1986), and the Montagnais crater, Nova Scotia (Jansa et al, 1988) are of similar size or larger than Manson and show no indications of even regional extinctions related to these events. The Kara and Ust Kara craters, both of which are significantly larger than Manson, have been dated as close to K/T in age using K/Ar techniques (Badjukov et al, 1987), but Koeberl et al (1988) have placed an age of 70 to 73 Ma on these craters based on $^{40}Ar/^{39}Ar$ dating of similar samples. If the Ar/Ar dates are correct, they present the same problem as the Ries and Montagnais craters in that no mass extinction occurs at 70 to 73 Ma. Therefore, the search for a K/T crater of sufficient size must continue if impact is to become a viable cause for the extinctions.

## An Endogenous Mechanism For Extinctions

Vogt (1972) was the first to propose a relationship between mantle plumes and volcanism, reversals, regression, and faunal crises. He argued that the common cause was periodic generation of plumes at the base of the mantle,

but did not present a specific mechanism to relate these phenomena. The idea was taken further by Jones (1977), who argued that significant long-term variations in reversal frequency and intermittent generation of plumes may be the result of fluctuating temperatures at the core-mantle boundary. More recently Sheridan (1983) and McFadden and Merrill (1986) have produced variations of this idea; the latter authors suggested that convection in the D" layer (hereafter referred to simply as D"), a thin layer at the base of the mantle, is unsteady. The low viscosity material in this layer cannot remain static (Yuen and Peltier, 1980) and may serve as a steady source of hot mobile material for deep mantle plumes (Stacey and Loper, 1983; Loper, 1985).

Various workers (Loper and McCartney, 1986; Courtillot and Besse, 1987; Loper et al, 1988) have proposed that the thickness of D" varies periodically, undergoing both quiescent and active phases. According to the Loper model, the D" layer thickens by thermal diffusion until it becomes dynamically unstable. The thickness of D" controls the temperature gradient across the boundary between the outer core and the mantle, and is thus related directly to the frequency of geomagnetic reversals. Reversals of the magnetic field are most frequent when D" is thin and the temperature gradient is high. When the layer is thick, the temperature gradient across it is small and magnetic reversals are infrequent (as occurred during the Cretaceous Quiet Interval). There is, however, an upper limit to the thickness of D" where it becomes dynamically unstable (see Loper and Eltayab, 1986), initiating an active phase in which heat (either as thermal fronts or as diapirs of hot material) rises upward to the base of the lithosphere. With the loss of this heat and/or material, D" thins and the rate of geomagnetic reversals increases, thus beginning the cycle again. The interval between instabilities has been

calculated to be about 22 Ma (Loper and McCartney, 1986); this estimate suggests that instabilities in the D" layer might be a reasonable explanation for the slightly longer periodicities discussed earlier.

The amount of time that it takes for material rising from D" to reach the lithosphere is unclear Olson et al (1987) estimate that material confined to an established plume would traverse the whole mantle in only 4 to 8 Ma. Laboratory experiments indicate that the plume material travels much slower if it is establishing a new plume track. Richards and Duncan (1989) calculate the rise time to be 35 Ma for a diapir not within an existing plume track. Laboratory experiments further indicate that a wide range of rise times may exist according to the actual path taken by a specific diapir (Loper and McCartney, 1986; McCartney and Loper, 1989).

When the hot material reaches the base of the lithosphere, it could affect tectonism, sea level, and might cause intense volcanism. The magnitude of the surface effects would depend upon the mass of the diapir and its ascent history. Laboratory experiments with fluids of differing viscosities (Olson and Singer, 1985; Loper and McCartney, 1986; Loper et al, 1988) indicate that hot, low-viscosity material, which rises within a pre-existing plume, would cause an increase in non-explosive hotspot volcanism, because it can vent easily to the surface. However, if the diapir is outside an established plume, it rises at a much slower rate. This allows the diapir to become much larger, since it is continually fed by material from below. If the diapir continues this slow ascent all the way to the lithosphere, it could become quite large and the surface effects should be considerable (Olson and Nam, 1986). Under certain conditions, such as a rigid lithosphere in a state of compression, the hot

material would have to melt or hydrofracture a path to the surface (Neugebauer, 1987). Significant crystallization, fractionation, and anatexis of crustal material would occur during ascent through the lithosphere, concentrating the volatiles into the more highly evolved melt (Harris and Middlemost, 1969). This could set the stage for a very intense and voluminous volcanic event and would mark the initiation of a new hotspot at the surface. The nature of this event is still problematic, but could include kimberlites, carbonatites, and cryptoexplosion structures (Loper and McCartney, 1988; McCartney and Loper, 1989). Also, some large silicic calderas (e.g. Yellowstone; Smith and Braile, 1984), are related intimately with hotspot activity on continents, suggesting that the presence of a silicic component during the early phases of hot spot activity on continental lithosphere is probable. At the K/T boundary, the silicic and alkaline magmatism related to the Deccan basalts may provide the energetic component suggested above (Sethna and Battiwala, 1977; Krishnamurthy and Cox, 1980; and Lightfoot et al, 1987).

Flood Basalts as a Primary Kill Mechanism

The most important aspect of hot spot initiation, as it pertains to the extinction process, is the occurrence of flood basalt provinces at major extinction boundaries. The link between flood basalts and extinctions is such that every major extinction event in the last 250 Ma correlates in time with a flood basalt province (Table 6-2 and Figure 6-3). The two largest extinction events at the Permo-Triassic and Cretaceous-Tertiary boundaries correlate with the two largest flood basalt provinces, in Siberia and India, and both of these provinces erupted soon after major magnetic quiet intervals. Each flood basalt province is also linked to the proposed initiation of a known hot spot,

Figure 6-3: Locations of flood basalt provinces and their related hot spots. Diagram after Rampino (1989).

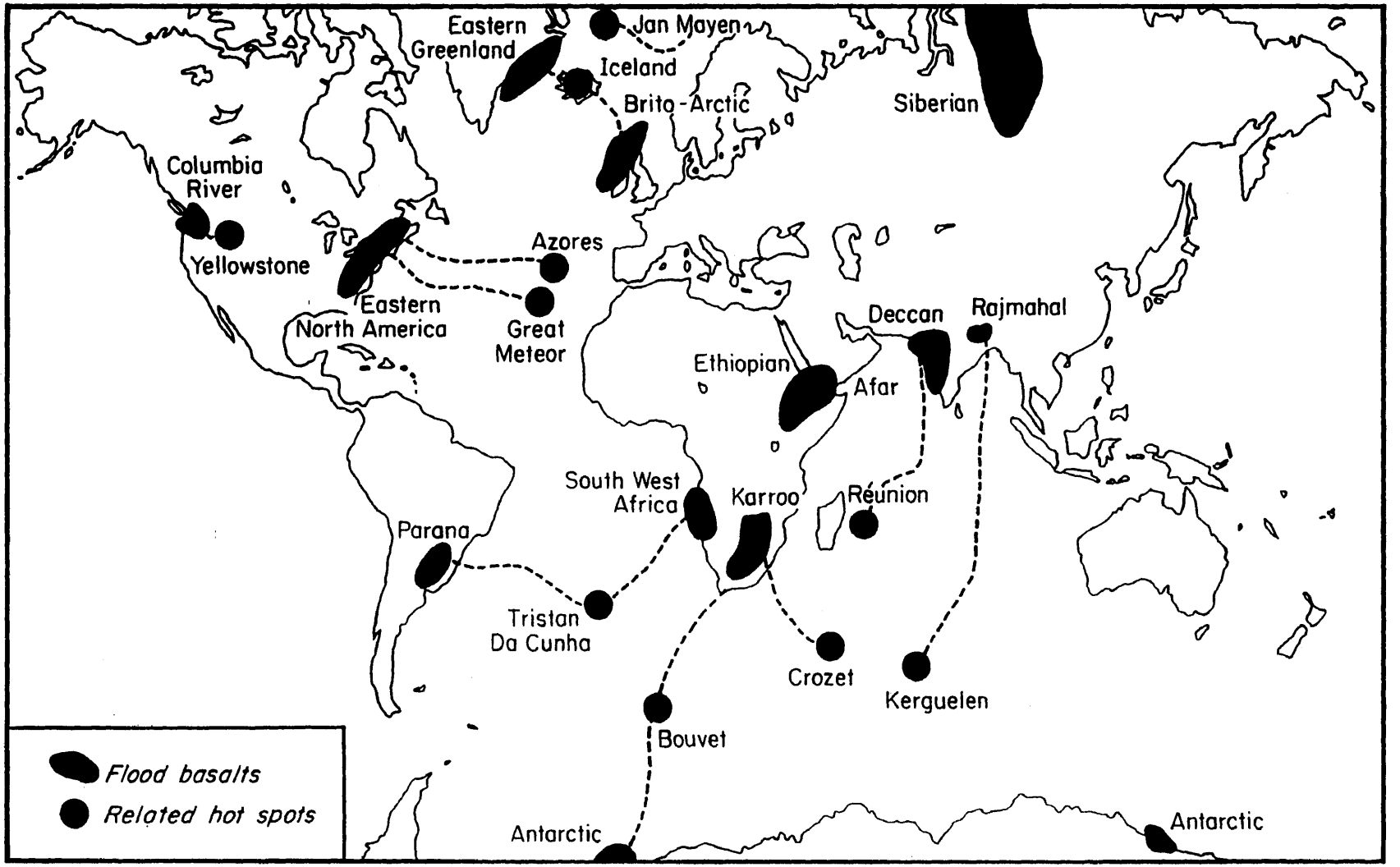
Eastern Greenland
Jan Mayen
Iceland
Brito-Arctic
Siberian
Columbia River
Yellowstone
Azores
Great Meteor
Eastern North America
Deccan
Rajmahal
Ethiopian
Afar
South West Africa
Karroo
Réunion
Parana
Tristan Da Cunha
Crozet
Kerguelen
Bouvet
Antarctic
Antarctic
Flood basalts
Related hot spots

Table 6-2: Possible correlations between mass extinctions, flood basalts, and hot spots over the last 250 Ma. Data for basalt volumes from Rampino and Stothers (1988) and MacDougall (1988b). Age data are from Rampino and Stothers (1988) and are based on a best fit estimate for initiation of volcanic activity from available K/Ar dates for each basalt province. The actual spread in the database used to obtain these values is significantly larger than the error values listed in the table, so that the correlation should be treated as approximate only.

TABLE 6-2

POSSIBLE CORRELATIONS BETWEEN FLOOD BASALTS AND MASS EXTINCTIONS

| Mass Extinction (Age) | Flood Basalt (Age) | Basalt Volume ($km^3$) | Related Hotspot |
|---|---|---|---|
| Mid Miocene (14±3) | Columbia River (16±1) | $4.5 \times 10^5$ | Yellowstone |
| Late Eocene (36±2) | Ethiopean (35±2) | $3.5 \times 10^5$ | Afar |
| Maastrichtian (65±1) | Brito-Arctic (62±3) | $3.0 \times 10^5$ | Iceland |
| Maastrichtian (65±1) | Deccan Traps (66±2) | $1.5 \times 10^6$ | Reunion |
| Cenomanian (91±2) | W. Pacific Seamounts (92±3) | $1.0 \times 10^6$ | Pacific Superswell |
| Aptian (110±3) | Rajmahal (110±5) | $2.0 \times 10^5$ | Kerguelen |
| Tithonian (137±7) | Parana (130±5) | $8.0 \times 10^5$ | Tristan Da Cunha |
| Tithonian (137±7) | Namibia (135±5) | ? | Tristan Da Cunha |
| Bajocian (173±3) | Antarctica (170±5) | ? | Bouvet |
| Pliensbachian (191±3) | Karroo (190±5) | $>1.0 \times 10^6$ | Crozet/Bouvet |
| Norian (211±8) | E. North Atlantic (200±5) | ? | Azores/Great Meteor |
| Dzulfian (249±4) | Siberian (250±10) | $2.0 \times 10^6$ | Jan Mayen? |

supporting the contention that flood basalts may be genetically linked to a deep-seated mantle process.

Short-term effects of historic volcanism have been well studied (Lamb, 1971; Pollack et al, 1976; Rampino and Self, 1982; Rampino et al, 1988). Volcanism causes lower temperatures and abnormal atmospheric circulation for the few years following the eruption, attributed primarily to the sulfate aerosols rather than ash or $CO_2$ (Rampino and Self, 1982; Devine et al, 1984). In terms of the extinction process, flood basalts should produce several primary and secondary effects. Based on data from known fissure eruptions such as the Laki eruption of 1783 (Devine et al, 1984), flood basalts should emit large volumes of sulfur, carbon, halogens, and ash into the troposphere and possibly the lower stratosphere. Using volatile budget data for Kilauea as an analog (Gerlach and Graeber, 1985), the Deccan Traps could have injected up to 3 x $10^{19}$ gm of $CO_2$, 6 x $10^{18}$ gm of sulfur, and 6 x $10^{16}$ gm of halogens into the atmosphere over a period of several hundred thousand years. Devine et al (1984) estimate that the emissions from the Laki eruption were much larger than predicted from scaling up of the Kilauean data, so that it is possible that the estimates listed above for the Deccan event represent a lower bound. Because some individual flood basalt flows may exceed 1000 $km^3$ in volume (e.g. the Roza flow alone at Columbia River is about 700 $km^3$), the potential emission of volatiles from a single 1000 $km^3$ eruptive unit is estimated at 1.6 x $10^{16}$ gm of $CO_2$ (81% of annual anthropogenic), 3 x $10^{15}$ gm of sulfur (46 times anthropogenic), and 3 x $10^{13}$ gm of halogens (Figure 6-4).

Such large volumes of volatiles injected into the atmosphere would have severe consequences for global climate and would produce acid rain, ozone

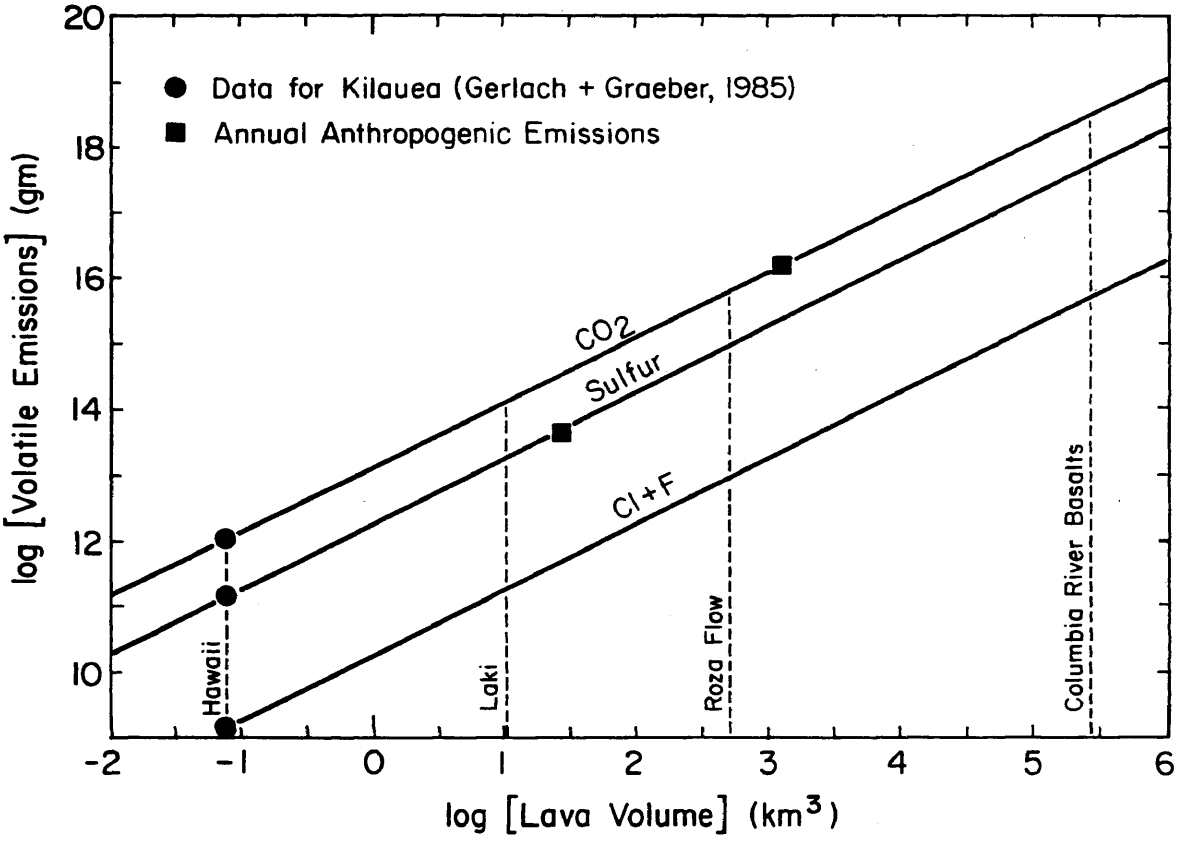


Figure 6-4: Emission of volatiles versus lava volume for basaltic eruptions based on the volatile budget data of Gerlach and Graeber (1985) for Kilauea. Volume estimates for the Laki eruption, the Roza Flow, and the Columbia River Basalts are shown for comparison, along with estimates of annual anthropogenic emissions of sulfur and $CO_2$.

damage, and increased reflectance of incoming solar radiation, leading to rapid cooling in the affected hemisphere (Handler, 1989). Devine et al (1984) developed an estimate of the climatic effect of volcanic sulfur emissions based on historic data. Extrapolation of their relationship between sulfur aerosols and cooling suggests that a 1000 $km^3$ basalt flow should produce a 3° to 5°C temperature decrease in the affected hemisphere (Figure 6-5). Residence time estimates for sulfur based on the El Chichon eruption (e.g. Pearson et al, 1988) indicate that such perturbations can last from 1 to 3 years, and are linked to climate change through changes in the Southern Oscillation (Handler, 1989), and probably through other phenomena as well.

The ability of a flood basalt to inject aerosols into the stratosphere is also very important in determining its effect on climate. Stothers et al (1986) determined that the atmospheric plume height for a basaltic fissure eruption is a function of the volume eruption rate per fissure length and the temperature change which occurs in the plume. The effectiveness of a plume is also regulated by the latitude of the eruption as the tropopause is lower in altitude at high latitudes. The calculations of Stothers et al (1986) revealed that large flows such as the Roza flow are capable of driving aerosols into the lower stratosphere, even at equatorial latitudes. Based on these calculations, it is evident that a flood basalt must erupt episodically in large volumes over very short time periods (i.e. 100's of $km^3$ over several weeks to months) if it is to affect global climate significantly in terms of mass extinctions.

In addition to global cooling from sulfur aerosols, the large volumes of $CO_2$, halogens (Figure 6-4) and ash will also affect the ecosystem adversely. In particular, the geological evidence suggests considerable changes in oceanic

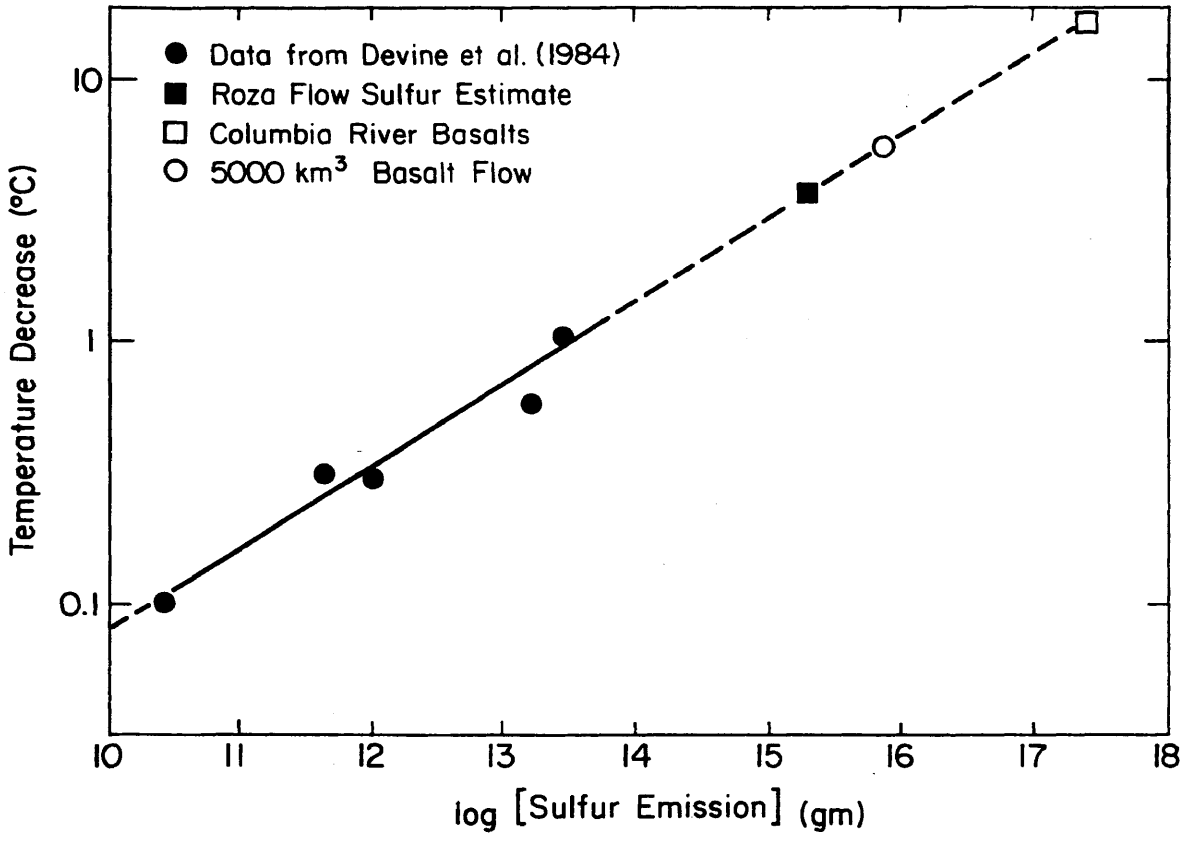


Figure 6-5: Estimate of climatic cooling from volcanic sulfur emissions based on historic data. The solid circles and solid lines are after Devine et al (1984). The Dashed line is an extrapolation which assumes no saturation limit for sulfur in the stratosphere.

processes at K/T time. It appears that the calcareous plankton were much more affected than other groups and there is abundant evidence of a carbonate crisis of some kind near the boundary (see, for example, Ekdale and Bromley, 1984). A mechanism for causing such a carbonate crisis is well known (Campsie et al, 1984; Ekdale and Bromley, 1984; McCartney and Nienstedt, 1986). The injection of a large amount of $CO_2$ into the oceans would cause a reaction with calcium carbonate to produce carbonic acid (see Arthur, 1982). The equilibrium reaction is as follows:

$$H_2O + CO_2 + CaCO_3 \rightleftharpoons Ca^{+} + 2HCO_3.$$

This reaction, coupled with halogenic and sulfuric acid rains, should change dramatically the chemistry of the oceans and place enormous environmental stress upon the calcareous marine organisms, particularly those that live in the surface waters, which is what is found at the K/T boundary.

Degassing of the Deccan basalt flows offers an explanation for the selectivity and sequencing of the K/T extinctions, which has been a special problem for the impact model. One attribute of the volcanic model is that the plankton extinctions need not be synchronous, as their tolerances to the developing crisis may differ. Officer et al (1987) have noted that as the pH of the surficial ocean waters decreased, the foraminifera would be the first to suffer, as they are inhibited below a pH of 7.6-7.8; small planktic foraminifera survive better in a lower pH environment and thus were affected later than the large species. Nannofossils would suffer extinction later as the pH decreased below 7.0-7.3. Siliceous organisms, which survive in even lower pH conditions, would be affected least. This sequence of large foraminifera, small

foraminifera, then nannofossils with siliceous organisms relatively unaffected appears to be the sequence found at the K/T boundary.

Microfaunal extinctions are spread over several thousand years, which suggests that both the event and its effects were prolonged. The dissolution of the foraminifera should balance the equilibrium at least somewhat and thus prevent the later nannofossil extinctions, unless more $CO_2$ and acid rain are introduced in the interim. The episodic eruption of massive flood basalt flows over a period of from $10^5$ to $10^6$ years should produce such a protracted event, thus explaining the extended duration of the K/T extinctions much better than a single impact or multiple impact scenario.

The length of time that it took for biotic recovery is another important piece of evidence. While a short period of global darkness might be devastating to the world ecosystem, survivors should repopulate the earth very quickly. Both the terrestrial plants and marine planktics, however, show very long recovery times that are not consistent with impact (Lerbekmo et al, 1987; Keller, 1988a,c). The lengthy recovery is not caused by a continuing carbonate crisis, since the crisis did not last long into the Paleocene; extensive dissolution is found below (and in) the boundary clay, but not above it (Hsü et al, 1982). However, as noted by McLean (1978), the demise of the calcareous nannoplankton would remove a large portion of the earth's plant biomass and thus keep atmospheric $CO_2$ levels high, and possibly cause a greenhouse effect. It is apparent now that massive carbon, sulfur, chlorine, and fluorine emissions, and thermal release from the flood basalts over a short time period (several hundred thousand years) could disrupt the terrestrial ecosystem, and

produce the observed effects across the K/T transition as well as other extinction horizons (McLean, 1988).

## Discussion

The effect of a large magmatic diapir impinging on the base of the lithosphere is postulated to be enormous. Richards and Duncan (1989) have constructed a simple quantitative model using reasonable plume bouyancy and mantle viscosity values to calculate that the Deccan basalts may have required a diapir up to 250 km in diameter. Such an arrival beneath the lithosphere should cause changes in rates of tectonism and volcanism, and thus could account for the climatic changes and extinctions that preceed the K/T boundary. The evidence at the K/T boundary itself, however, indicates a catastrophic event of even greater magnitude. This might, in part, be the result of a particularly intense, voluminous eruptive phase, which could also act as a forcing agent for abrupt and catastrophic changes in the global climatic system (Crowley and North, 1988) sufficient to cause a mass extinction. This model also explains the observation of stepped or gradual extinction through a model of gradually deteriorating climate and habitat, where different ecosystems are destroyed progressively as their tolerance limits to environmental stress are exceeded.

The volcanic model provides a different vantage point from which to view the evidence associated with the K/T and other mass extinctions. Extensive volcanism, perhaps related to a plume, alters atmospheric and marine chemistries. This affects both the accumulation of Ir and other exotic elements, and the biota; the demise of a large portion of the phytoplankton

may have further exacerbated the global environment through rapid changes in $CO_2$ buffering of the biosphere. A major attribute of the plume model is the inherent correlation between internal phenomena and their various surface manifestations, including an explanation for pre-extinction events, such as the increased reversal frequency. It is implicit in the plume model that subsurface events should predate surface events such as volcanism and deterioration of the atmosphere, but that they are all causally related. In terms of this model, the plume activity may also account for changes in the rate and direction of plate motions, episodes of lithospheric thinning and breakup, sea level changes and epierogeny, some episodes of vertical orogeny, and large-scale volcanic activity. Given this model, it is reasonable to expect that these phenomena might preceed the climatic and biotic changes; such cannot be said for impact.

## Conclusions

The results of this study suggest that the K/T transition was a period of intense volcanism and that a moderate-size accretionary event was superposed on the volcanism at the KTB proper. Recognizing that both events occurred, the issue remains which event caused the mass extinction? The evidence from the fossil record indicates that some extinctions and biotic decline definitely occurred before the KTB proper. It is also evident that volcanism can account for the chemical and mineralogical observations across the K/T transition. The data from historic volcanism supports the hypothesis that flood basalts can kill by climatic destabilization, and the apparent correlation between major flood basalt provinces and extinction events links these two processes together over the last 250 Ma. In contrast, the geologic record at other extinction

horizons does not show evidence that large-body impacts correlate with biotic crises.

The suggestion that flood basalt volcanism is responsible for mass extinctions is a major change from the temporal scale of extinction proposed originally by Alvarez et al (1980). Flood basalts and climatic destabilization as an extinction mechanism must be of grave concern to mankind since our industrial emissions, which are rich in Cl, F, $CO_2$, and $SO_2$, are not very different in composition from the emissions predicted for flood basalts.

The hypothesis that flood basalts are one manifestation of a deep-seated mantle process is important because it links surface phenomena with the dynamics of the earth's interior. Whether flood basalts are the result of melting at D" as proposed by Loper and McCartney (1986), or whether they are a manifestation of some other internal process is not a major concern. The key result is that hot-spot initiation and its associated effects including : (1) flood basalt eruptions; (2) episodic explosive silicic volcanism; (3) ozone depletion; (4) acid rain; (5) climatic instability; and (6) heavy metal toxicity may be a viable mechanism for many of the major biotic crises in the Phanerozoic.